



A GEOMECHANICAL ANALYSIS OF
THE FORMATION AND EVOLUTION
OF POLYGONAL FAULT SYSTEMS

Daniel Thomas Roberts MEng.(Hons).

Submitted in partial fulfilment of the requirements
for the degree of Doctor of Philosophy

Cardiff University

December 2014

DECLARATION

This work has not been submitted in substance for any other degree or award at this or any other university or place of learning, nor is being submitted concurrently in candidature for any degree or other award.

Signed Date

Statement 1

This thesis is being submitted in partial fulfilment of the requirements for the degree of PhD.

Signed Date

Statement 2

This thesis is the result of my own independent work, except where otherwise stated. Other sources are acknowledged by explicit references. The views expressed are my own.

Signed Date

Statement 3

I hereby give consent for my thesis to be available for photocopying and for inter-library loan, and for the title and summary to be made available to outside organizations.

Signed Date

Statement 4

I hereby give consent for my thesis to be available for photocopying and for inter-library loans **after expiry of a bar on access previously approved by the Academic Standards and Quality Committee.**

Signed Date

AUTHOR NOTE

At the time of submission sections of Chapters 4 and 5 have been presented as;

D.T. Roberts, A.J.L. Crook, J.A. Cartwright, M.L. Profit, J.M. Rance. Geomechanical Forward Modelling of the Genesis of Polygonal Fault Systems – EAGE International Workshop on Geomechanics and Energy: The Ground as Source and Storage, Lausanne, Switzerland, 26-28 November 2013.

The contents of this thesis are currently being prepared for submission as;

D.T. Roberts, A.J.L. Crook, J.A. Cartwright. A Geomechanical Analysis of the Formation and Evolution of Polygonal Fault Systems. *Journal of Structural Geology* (in preparation).

The following invited presentations have been given based on the work contained within this thesis;

D.T. Roberts, A.J.L. Crook, J.A. Cartwright, M.L. Profit, J.M. Rance. Geomechanical Forward Modelling of the Genesis of Polygonal Fault Systems – Bristol University Microseismicity Project, Bristol, UK, 23-24 November 2013.

D.T. Roberts, A.J.L. Crook, J.A. Cartwright, M.L. Profit, J.M. Rance. Geomechanical Forward Modelling of the Genesis of Polygonal Fault Systems – COMPSTRUCT JIP Meeting, Houston, USA, 17 February 2014.

Additionally, I have contributed to two other conference presentations that are not contained as part of this thesis;

J.M. Rance, M.L. Profit, S.J. Dee, **D.T. Roberts**. Predicting the Paleo Evolution of Overpressured Geological Structures – 47th American Rock Mechanics Association Symposium, San Francisco, California, USA, 23-26 June 2013.

D.A. Thornton, **D.T. Roberts**, A.J.L. Crook, J.G. Yu. Regional-Scale Salt Tectonics Modelling: Bench-Scale Validation and Extension to Field Scale Problems – Geological Society of America Conference, Minneapolis, Minnesota, USA, 09-12 October 2011.

ACKNOWLEDGEMENT

I wish to acknowledge a number of people who have provided guidance and assistance over the duration of this research project. The subject matter has presented a challenging, multidisciplinary topic and has required me to learn a great deal in a relatively short period of time. This has only been possible with the support I have received.

I want to thank Professor Joe Cartwright for his constant support and patient supervision, and in particular for the walks and lunches over which we had long discussions on the nature of polygonal faults. Joe is recognised as a world expert on polygonal faults, diagenesis, and subsurface fluid flow and I consider myself fortunate to have received his guidance. I am also grateful to Joe for encouraging me to immerse myself in new experiences, such as learning geological mapping skills and attending field trips, which I was not exposed to as a civil engineering graduate.

I would especially like to thank my other supervisor Dr Tony Crook, for the many hours he has devoted to explaining the finer details of geomechanical analysis and numerical methods, of which his knowledge is unparalleled. I am additionally thankful for his efforts in helping me to become a more effective researcher, and many of the practices he has encouraged me to adopt now form the foundations of my approach to research.

This thesis could not have been completed without the kindness, support and encouragement of both Joe and Tony.

My industry supervisor Dr Dean Thornton (now at Chevron ETC) is thanked for helping me during the early stages of the project, and my competency with the software owes much to his careful instruction. Dr Matthew Profit is thanked for continuing this role during the later stages of the project, as well as guiding code modifications and providing early reviews of the chapters contained within this thesis that greatly improved their quality. All of the staff at Rockfield are thanked for making me feel part of the team. I am grateful to Dr Jon Rance for allowing me to contribute to the COMPSTRUCT JIP which has broadened my knowledge of many aspects of constitutive modelling, structural geology and computational geomechanics.

Dr Attila Garai is thanked for assisting with code compilation and parallel processing issues. Dr Tiago Alves, Dr Dan Carruthers and Dan Morgan of the Seismic 3D Lab are thanked for stimulating discussions on a range of topics. Dr Maria Nikolinakou and Dr Gang Luo (University of Texas at Austin) are thanked for good times during their stay in Swansea and for discussions on the nature of salt-sediment interaction. Rockfield, Cardiff University and the European Social Fund (ESF) are acknowledged for financial assistance via the award of a Knowledge Economy Skills Scholarship.

I owe enormous thanks to my parents, Phil and Debs, for countless years of love and support, without which I would not have been in a position to undertake this work. I am grateful to my grandparents; Betty and Peter who have always encouraged me to do my best, and Mavis and Alwyn, who sadly passed before the completion of my undergraduate studies but who I know would have been very proud. I acknowledge my brothers, Jack and Joe, and many friends for providing welcome distractions throughout the duration of the project.

Finally, and most importantly, I am indebted to my partner Natalie for her unconditional love and support, particularly during the difficult times.

SUMMARY

The development of Polygonal Fault Systems (PFS) remains poorly understood despite extensive study for over two decades. These systems of exclusively normal faults are developed over wide areas of many basins worldwide and are believed to influence caprock integrity and hydrocarbon reservoir quality, whilst also potentially presenting shallow drilling hazards. A seemingly obvious conclusion from their layer-bound nature and significant lateral extent is that their origin must be governed by the constitutive behaviour of the host sediments. Establishing specific causative mechanisms has, however, proven difficult.

The aim of this research project is to first assess some existing arguments for PFS genesis and this is complimented by a review of modification of structure in soft rocks and discussion of how this facilitates changes in both shear and compaction. The approach in this work is to utilise geomechanical forward modelling to demonstrate how such changes might lead to PFS formation. The concepts of this approach are discussed with focus on the adopted computational framework and selected constitutive model.

An argument for polygonal fault genesis is presented that is founded on diagenetically induced shear failure, and the requirements for incorporating this into the constitutive model are described. Recovery of realistic PFS geometries is demonstrated as validation of the geomechanical argument and the competency of the computational approach. Conceptual sensitivity studies at the field scale are undertaken to better understand what processes, reactions and conditions might control fault genesis and propagation.

When observed in mapview polygonal faults commonly intersect bedding planes at a wide variety of azimuths which reflects an inferred horizontally isotropic state of stress. Occasionally, this so-called 'planform geometry' is modified by the presence of tectonic faults, slopes or salt structures. Therefore, there is the possibility that polygonal faults may be useful paleostress indicators. This is explored using the characterised materials in simple models featuring anisotropic horizontal stress conditions.

CONTENTS

Declaration.....	I
Author Note	II
Acknowledgement	III
Summary.....	V
Contents	VI
List of Figures.....	XII
List of Tables.....	XXII
Chapter 1 An Introduction to Polygonal Fault Systems	1
1.1 Rationale	1
1.1.1 Seal Integrity	2
1.1.2 Waste Repositories and Sequestration	3
1.1.3 Reservoir Compartmentalisation and Reservoir Quality	3
1.1.4 Hydraulic Stimulation.....	3
1.1.5 Summary	4
1.2 Characteristics of Polygonal Fault Systems.....	4
1.2.1 Global Distribution and Extent	4
1.2.2 Geometry and Lithology	4
1.2.3 Timing of Polygonal Fault Formation	8
1.2.4 Identification of a Polygonal Fault System.....	9
1.3 Suggested Mechanisms for the Genesis of Polygonal Fault Systems.....	9
1.3.1 Downslope Gravity Sliding.....	10
1.3.2 Overpressure Development.....	10
1.3.3 Density Inversion	11
1.3.4 Residual Friction on Fault Planes	12
1.3.5 Syneresis	13
1.3.6 Chemical Compaction.....	14
1.4 Summary	15

1.5	Objective and Scope of the Thesis	15
1.5.1	Primary Study Objectives	17
1.5.2	Secondary Study Objectives	17
1.6	Layout of Thesis	17
1.7	References	19
Chapter 2	Modification of Structure in Soils and Soft Rocks	22
2.1	Introduction to Structured Sediments.....	24
2.2	Processes that Influence the Level of Structure	29
2.2.1	Depositional Environment	29
2.2.2	Weathering	30
2.2.3	Thixotropic Hardening.....	31
2.2.4	Creep.....	32
2.2.5	Cementation	34
2.2.6	Diagenesis	37
2.3	Summary	41
2.3.1	Key Points.....	41
2.3.2	Relevance to PFS Genesis	42
2.3.3	Suggested Approach.....	44
2.4	References	45
Chapter 3	Computational Strategy and Constitutive Modelling.....	48
3.1	Methods for Investigating the Formation of Geological Structures.....	48
3.1.1	Conventional Approaches	48
3.1.2	Suggested Approach for Investigating Polygonal Fault Evolution.....	51
3.2	Computational Modelling.....	52
3.2.1	Potential Frameworks	53
3.2.2	Description of the Kinematics	55
3.3	ELFEN.....	56
3.3.1	Introduction.....	56
3.3.2	Finite Element Framework	57
3.4	Constitutive Models for Geomaterials.....	57
3.4.1	Background	57
3.4.2	Requirements for Elastoplastic Soil and Rock Models.....	58

3.5	Constitutive Model: Soft Rock 3 (SR3)	59
3.5.1	An Introduction to Critical State Soil Mechanics	59
3.5.2	Flow Rule Definition	64
3.5.3	Volume Change	64
3.5.4	Hardening Law and Poro-Elasticity	66
3.5.5	Elastoplastic Stress Update	67
3.6	Regularisation of the Material Softening	68
3.7	Conclusions	70
3.7.1	Studying Polygonal Faults	70
3.7.2	Computational Framework	71
3.7.3	Constitutive Modelling	71
3.8	References	73
Chapter 4	Incorporating the Influence of Burial Diagenesis at Shallow Depths	76
4.1	PFS Formation Due to Early Silica Diagenesis	77
4.1.1	Rationale	77
4.1.2	Mechanical Response to Silica Diagenesis	77
4.2	Geomechanical Argument	84
4.3	Methodology and Implementation	89
4.3.1	Modelling Burial Diagenesis	89
4.3.2	Considering the Influence on the Hydrostatic Intercept in Tension	92
4.3.3	Comments on the Modelling of Diagenesis	93
4.4	Material Characterisation	93
4.4.1	Mechanical Behaviour	94
4.4.2	Chemical Behaviour	94
4.4.3	Comments on Material Characterisation	96
4.5	K_0 Compaction - Single Element Test	96
4.5.1	Mechanical Compaction Results	98
4.5.2	Influence of Burial Diagenesis	100
4.5.3	Discussion of Results	107
4.6	Summary and Progression	110
4.7	References	112

Chapter 5 Field Scale Analysis of the Formation and Evolution of Polygonal Fault Systems.....	115
5.1 Field Scale Investigations Related to Opal A/CT Transformation	115
5.1.1 Two Dimensional Models	115
5.1.2 Three Dimensional Models.....	120
5.1.3 Comments on Opal A/CT Transformation Results	121
5.2 Sensitivity Study - Evolutionary Models.....	127
5.2.1 Two Dimensional Model Description.....	127
5.2.2 Three Dimensional Evolutionary Model	142
5.2.3 Comments	147
5.3 Investigation of Intraformational Faulting at Shallow Depth	147
5.3.1 Lake Superior.....	148
5.3.2 Boom Clay	148
5.3.3 Offshore West Africa.....	148
5.3.4 Approach for Conceptual Investigation	149
5.3.5 Results.....	153
5.3.6 Comments	157
5.4 Summary and Discussion.....	160
5.4.1 The Diagenetic Model for Genesis of Polygonal Faults.....	160
5.4.2 Fault Development at Shallow Depth.....	163
5.4.3 Horizontal Stress Reduction Hypotheses.....	165
5.4.4 Appraisal of Modelling Approach and Progression.....	166
5.5 References	168
Chapter 6 Polygonal Faults and the Influence of Horizontal Stress Anisotropy.....	171
6.1 Examples of Planform Geometry Polarisation Due to Horizontal Stress Anisotropy	171
6.1.1 Tectonic Faults	171
6.1.2 Slopes.....	173
6.1.3 Salt Structures	173
6.1.4 Anticlines and Fold Belts.....	173
6.1.5 Comments	175
6.2 Strategy for Conceptual Investigation.....	177
6.3 Results and Analysis.....	179
6.3.1 Intensity of Faulting.....	180

6.3.2	Fault Spacing	181
6.3.3	Fault Strike.....	187
6.3.4	Fault Length.....	191
6.4	Discussion.....	197
6.5	Estimating Paleostress	200
6.5.1	Concepts for a Workflow to Estimate Paleostress	200
6.5.2	Constraints on Use	202
6.5.3	Validation	204
6.6	Closing Comments.....	206
6.7	References	207
Chapter 7	Conclusions and Suggestions for Future Investigation.....	211
7.1	Approach for Investigating the Genesis and Evolution of Polygonal Faults ...	211
7.1.1	Chapter 2: Analysing the Behaviour of Sediments During Early Burial	211
7.1.2	Chapter 3: Utilising Computational Geomechanics	212
7.2	Chapter 4: The Diagenetic Mechanism for Polygonal Fault Formation.....	212
7.3	Chapter 5: Field Scale Modelling of the Formation and Evolution of a PFS ..	213
7.4	Chapter 6: Polygonal Fault Formation and Horizontally Anisotropic Stress States	215
7.5	Discussion.....	218
7.5.1	Diagenesis as a Trigger for Polyongal Fault Genesis	218
7.5.2	The Influence of Early Diagenesis and Brittle-Ductile Transitions.....	218
7.5.3	Trigger Beds.....	220
7.5.4	Polygonal Faults and Paleostress Estimation.....	221
7.6	Research Limitations	221
7.6.1	Subsurface Uncertainty and Validation.....	221
7.6.2	Complexity of Diagenetic Processes	222
7.6.3	Use of Geomechanical Forward Modelling.....	222
7.7	Extension of the Study and Future Work	223
7.7.1	Alternative Mechanisms and Improved Constitutive Modelling.....	223
7.7.2	Influence of Overpressure and Contribution from Diagenesis	224
7.7.3	A Unified Study Incorporating Explicit Modelling of Salt Diapir Growth	227
7.8	Closing Comments.....	228
7.9	References	230

Appendix Quasi-Static Explicit Adaptive Finite Element Framework and Application to Problems in Structural Geology	233
Explicit Finite Element Framework	233
Governing Equations and Semi-Discretisation by Finite Elements	233
Central Difference Time Integration	237
Stability Considerations and Mass Scaling	239
Remeshing Strategy	240
Entity-based model definition	240
Remeshing indicators	241
Regeneration of the Mesh and Mapping Procedure	241
References.....	243

LIST OF FIGURES

Chapter 1 An Introduction to Polygonal Fault Systems

- Figure 1-1: Petroleum system, Qiongdongnan Basin (Sun et al., 2010). The presence of polygonal faults overlying the anticlinal reservoir means that their potential influence as a seal-bypass system should be carefully considered.2
- Figure 1-2: Global Distribution of known Polygonal Fault Systems. As clearly demonstrated, the vast majority of the systems are observed on passive continental margin slopes.....5
- Figure 1-3: Examples of Polygonal Fault System planform geometries (Cartwright, 2011). Note the random fault orientation in all examples.....6
- Figure 1-4: Change in PFS planform geometry in the Central North Sea (CNS) due to the presence of a salt diapir (Davison et al., 2000).....6
- Figure 1-5: Cross-sections through typical Polygonal Fault Systems (a) Ideal Tier (b) Wedge Tier (c) Complex Tier (Cartwright, 2011).....8
- Figure 1-6: Overpressure model for PFS genesis. Sediment is consolidated to Point 1 along the K_0 stress path, thereafter the inability for the sediment to dewater leads to reduction in effective mean stress and eventual failure at Point 2. 11
- Figure 1-7: Proposed model for the residual strength mechanism, modified after (Gouly, 2001). Sediment is consolidated to Point 1 along the K_0 stress path which intersects the peak strength failure envelope and then softens to the residual state at Point 2. 12
- Figure 1-8: Proposed consolidation behaviour in the syneresis and chemical compaction models. Sediment is consolidated to Point 1 along the K_0 stress path, thereafter a reduction in the horizontal stress leads to a deviated stress path which intersects the failure envelope. 14

Chapter 2 Modification of Structure in Soils and Soft Rocks

- Figure 2-1: Typical compaction curves for Shales (Athy, 1930; Baldwin and Butler, 1985; Hudec et al., 2006).....22
- Figure 2-2: Comparison between compaction curves and trend observed in North Sea Wells (Baldwin and Butler, 1985; Hudec et al., 2006; Nordgård Bolås et al., 2008). 23
- Figure 2-3: 1-D Compression curves for six different clays (cf Burland, 1990). 27
- Figure 2-4: Compression curves for the clays in Figure 2.1 normalised to obtain the Intrinsic Compression Line, or ICL (cf Burland, 1990). 27
- Figure 2-5: Typical compression lines for a natural and destructured specimen. Note that the natural sample can sustain a higher void ratio for a given effective vertical stress. 28
- Figure 2-6: Conceptual model of Intrinsic State Boundary Surface (ISBS) and Structured

State Boundary Surface (SSBS). The state boundary surface for the structured material is larger than the equivalent destructured specimen, reflecting the influence of sedimentation and post sedimentation processes.	28
Figure 2-7: Stress-strain behaviour of kaolinite compacted by static and kneading methods (Mitchell and Soga, 2005). Note that when subject to sufficiently large axial strains the samples tend to the same residual strength, reflecting the intrinsic state. Prior to this the strengths and result deformation styles are markedly different.	30
Figure 2-8: Effect of macro-fabric on undrained response of Bothkennar Clay (Mitchell and Soga, 2005). Note the strength variation in the different samples depending on whether they exhibited mottled, bedded or laminated facies.	31
Figure 2-9: Modification of material strength due to thixotropy, (Mitchell and Soga, 2005). 32	
Figure 2-10: Hydrostatic Compaction of a chalk with creep stages (De Gennaro et al., 2003). Note that volume change continues to take place at constant mean stress during the creep stages.	34
Figure 2-11: Effect of creeping phases on soil structure (cf, Burland, 1990). Note that volume change continues when the stresses are held constant due to grain slippage and rotation. The material fabric is different after the creep stage which is reflected in the higher yield stress attained before resumed consolidation.	35
Figure 2-12: Behaviour of cemented and uncemented sands (Leroueil and Vaughan, 1990). 35	
Figure 2-13: Response of Carbonate samples in K_0 testing (Croizé et al., 2010). Note how samples do not yield and respond elastically to very high vertical stresses.	38
Figure 2-14: Comparison of K_0 testing on Kimmeridge Bay and Kimmeridge Westbury Clays. Note that for the same vertical stress there is a large difference in porosity of the two samples.	41
Figure 2-15: Assessment of criterion for structure development and PFS formation.	44

Chapter 3 Computational Strategy and Constitutive Modelling

Figure 3-1: Bench scale modelling of reactive diapirism. Taken from (Vendeville and Jackson, 1992b).	49
Figure 3-2: Regional scale kinematic restoration showing various stages in the evolution of the Kwanza Basin, offshore Angola. Restoration performed using the Geosec restoration software, modified after (Hudec and Jackson, 2004).	50
Figure 3-3: Bench scale modelling of polygonal fault genesis. Taken from (Victor and Moretti, 2006).	52
Figure 3-4: Continuum modelling approach.	53
Figure 3-5: Discrete modelling approach with particle method.	54
Figure 3-6: Comparison of continuum (left) and discrete (right) approaches for modelling the evolution of contractional geological structures (Gray et al., 2014).	55
Figure 3-7: The SR3 state boundary surface. (a) Principal stress space (b) Deviatoric (π) plane (c) Meridian plane (p' - q space).	63
Figure 3-8: Plastic potential in meridian plane.	64

Figure 3-9: Definition of dilation parameter, β^d	65
Figure 3-10: Hardening model.....	66
Figure 3-11: Demonstration of energy dissipation for a 1D brittle bar loaded axially. The region region designates the failed element.....	69
Figure 3-12: Force-displacement relationships for axial bar problem with differing mesh sizes.	69
Figure 3-13: Definition of material and element length scales for regularisation of fracture energy dissipation.	70
Figure 3-14: Observed and modelled stress strain responses using (a) two surface cap plasticity model (b) continuous surface model (Fredrich and Fossum, 2002).....	72

Chapter 4 Incorporating the Influence of Burial Diagenesis at Shallow Depths

Figure 4-1: Strength profiles across Opal A/CT transition zone (Ishii et al., 2011). The transition zone that straddles the interface between the Koetoi and Wakkanai Formations is observed to coincide with large variations in unconfined compressive strength (UCS), tensile strength and cohesion.....	79
Figure 4-2: Evolution of material state across Opal A/CT transition zone (Ishii et al., 2011).79	
Figure 4-3: Triaxial tests above and below the transition zone at the site of the URL at Horonobe. SEM images showing microstructure for (a) Diatomaceous mudstone just above transition zone (b) Transition zone (c) Siliceous mudstone just below the transition zone.....	80
Figure 4-4: Porosity profile for well 1173 (Spinelli et al., 2007).	83
Figure 4-5: Opal acting to cement pore-space (Spinelli et al., 2007). A shows an SEM image from a sample taken from the Upper Shikoku Basin facies. B indicates regions of inferred Opal cement.	83
Figure 4-6: Mechanical only response (normal consolidation behaviour). Final state boundary surface is shown with the solid line. Red line represents the stress path and the blue line represents the critical state line that separates shear and compaction.	85
Figure 4-7: Conceptual model of the effect of chemical compaction on material response. Final state boundary surface is shown with the solid line. Red line represents the stress path and the blue line represents the critical state line that separates shear and compaction.....	85
Figure 4-8: Consolidation data from Nankai Trough (Spinelli et al., 2007).....	87
Figure 4-9: Conceptual model for PFS formation (Laurent et al., 2012). A horizontal contraction causes a deviation from the K_0 line and leads to shear-enhanced compaction.	88
Figure 4-10: Treatment of tensile intercept on hydrostatic axis, p_t , incorporating mechanical and chemical behaviours.....	93
Figure 4-11: Yield surface in (a) principle stress space and (b) meridian plane (p - q space) and normalised with respect to the initial pre-consolidation pressure.....	97
Figure 4-12: Single element simulation setup with K_0 boundary conditions.....	98
Figure 4-13: Final geometries from single element tests for cases considering (a) mechanical compaction only and (b) mechanical compaction and an additional 20% porosity loss due to	

diagenesis.....	98
Figure 4-14: Mechanical only response (a) stress path and state boundary surface (b) stress ratio (c) evolution of principal stresses. A constant ratio between the horizontal (red) and vertical (green) stresses is maintained throughout the simulation. The value of 0.74 is typical of mudstones and claystones (Gouly and Swarbrick, 2005).....	99
Figure 4-15: Orthotropic diagenetic volume change. (a) After mechanical compaction (b) after diagenetic volume reduction. As shown in (b), in this case the volume change attributed to the diagenetic process is expressed principally in the vertical direction.	100
Figure 4-16: Evolution of stress ratio using the vertical compaction model for various chemical porosity changes expressed orthotropically (a) 5% (b) 10% (c) 20%.....	102
Figure 4-17: Stress path and state boundary surface evolution for various chemical porosity changes expressed orthotropically (a) 5% (b) 10% (c) 20%.....	103
Figure 4-18: Isotropic diagenetic volume change. (a) After mechanical compaction (b) after diagenetic volume reduction. As shown in (b), in this case the volume change attributed to the diagenetic process has a component in all three axes.	104
Figure 4-19: Evolution of stress ratio for various chemical porosity changes expressed isotropically (a) 5% (b) 10% (c) 20%.....	105
Figure 4-20: Stress path and state boundary surface evolution for various chemical porosity changes expressed isotropically (a) 5% (b) 10% (c) 20%.	106
Figure 4-21: Plot summarising the reduction in K_0 for various magnitudes of chemical volume change.	107
Figure 4-22: Evolution of the strength of diagenetic bonding for (a) uniaxial case with no destructuration predicted (b) volumetric case with destructuration predicted.....	108
Figure 4-23: Model data for 10% porosity reduction over geological time - see Figure 4-20(b) and experiment evolution of horizontal stress ratio for an induced volume reduction of 10% (Shin et al., 2008).....	109

Chapter 5 Field Scale Analysis of the Formation and Evolution of Polygonal Fault Systems

Figure 5-1: Geometry, boundary and loading conditions for 2D model. Gold layer is characterised as a generic mudstone. Overlying blue layer is characterised as diatomaceous mudstone.....	116
Figure 5-2: Fault evolution in 2D model. Contours of effective plastic strain at (a) 0My (b) 6My (c) 15My (c) 20My. Note how localised faults develop around 6My, are both synthetic and antithetic, and are confined to the chemically affected layer.	118
Figure 5-3: Final geometry from 2D model. (a) Material grid showing regions of intense deformation. Contours of accumulated vertical and horizontal displacement in metres are shown in (b) and (c) respectively.	120
Figure 5-4: Three dimensional model loading and boundary conditions. Gold layer is characterised as a generic mudstone. Overlying blue layer is characterised as diatomaceous mudstone. K_0 boundary conditions are adopted.....	122
Figure 5-5: Accumulated horizontal displacements at 10My. Red indicates zones of largest	

horizontal movement (heave).	123
Figure 5-6: Geometry of 3D model at 10 My showing contours of effective plastic strain in the polygonally faulted interval.	124
Figure 5-7: Silica diagenetic transformation zone, offshore Norway modified after Ireland (2011). Only a selection of the total number of interpreted polygonal faults are shown. The blue boundary represents the inferred Opal A/CT transformation boundary (see density log). The purple boundary marks the inferred base of the tier which is seen to coincide with the transformation of Opal CT to Chert.	125
Figure 5-8: Modelled porosity evolution for a point near the base of the tier. In reality the porosity would be further reduced as Opal CT is transformed to Chert, in addition to other reactions such as the transformation of smectite to illite which takes place at elevated temperatures.	126
Figure 5-9: Geometry, loading and boundary conditions for 2D evolutionary models. The green section denotes the initial geometry. The red lines indicate the deposition horizons for the chemically affected layers. The blue line indicates the deposition horizon for the overlying non-chemically affected layer. Thermal gradient and approximate sedimentation rates also shown.	128
Figure 5-10: Simulated 2D evolution of a polygonal fault system at (a) 3.7My (b) 5.0My (c) 7.0My. Note the layer-bound nature of the faults which terminate at specific stratigraphic levels, in this case indicating the transition from chemically to non-chemically affected layers.	131
Figure 5-11: Comparison between model results and tier geometries (a) faulting interpretation at end of simulation (b) classic platform geometry (Cartwright, 2011) (c) PFS in the Lower Congo Basin (Gay et al., 2004).	132
Figure 5-12: Influence of thermal gradient on stress path in q - p' space. (a) Stress path in q - p' space (b) Evolution of K_0 . The black line represents the high thermal gradient case and the red line represents the low thermal gradient case.	133
Figure 5-13: Accumulated displacements (in metres) in the vertical direction for (a) orthotropic chemical flow rule (b) isotropic chemical flow rule. In the orthotropic case the development of localised faults is not predicted.	134
Figure 5-14: Ratio of q/p' at $t=6.0$ My (a) orthotropic flow rule (b) isotropic flow rule. High values (red) indicate intersection of the yield surface in shear. Low values (blue) sediments are on the cap and compacting. The isotropic expression of diagenetic volume strain results in a ductile-brittle transition whereas the orthotropic expression does not.	135
Figure 5-15: Plot showing the range of stresses that may be obtained in models with orthotropic and isotropic chemical flow rules. Note that the range of stress states obtained for orthotropic flow rule is to the right of critical state.	136
Figure 5-16: Maximum fault throw versus fault height for a number of shallow polygonal fault systems, modified after (Shin et al., 2010). The faults plotted are from various locations including West Africa, North Sea and Brazil. The results of simulations featuring reductions in the residual friction are also shown (squares) and fall within the expected range.	137
Figure 5-17: Influence of residual friction on fault propagation (a) Fault throw profiles for various values of residual friction (b) Zoomed image of a single fault showing displacement within the tier for a residual friction value of 8.13°	138

Figure 5-18: Accumulated horizontal displacements for various residual friction angles. Maximum displacement contour is 12.9m. Hot contours indicate displacement to the right and correspond to the magnitudes reported in Table 5-6. Interpreted fault style is also shown. (a) 20.58° (b) 12.54° (c) 8.13° (d) 5.21°..... 139

Figure 5-19: (a) Decoupling of tiers in North Sea due to the presence of a sandstone-rich slope fan (Jackson et al., 2014). Tier structure in the Espirito Santo Basin (Carruthers, 2012). Note the coupling of tiers in the South. The presence of the sandy Facies D results in a decoupling of tiers in the North. 140

Figure 5-20: Influence of the presence of coarse-grained intervals (a) Distribution of effective plastic strain. (b) Interpretation of faulting style showing decoupling and development of a "supra-tier" and "sub-tier" (c) Contours of elastic modulus (stiffness) in MPa showing the contrast between the stiffer and more competent sand and the comparatively weak sediments hosting the polygonal faults. 141

Figure 5-21: Geometry, loading and boundary conditions for 3D evolutionary models. The green section denotes the initial geometry. The red surfaces indicate the deposition horizons for the chemically affected layers. The blue surface indicates the deposition horizon for the overlying non-chemically affected layer. Thermal gradient and approximate sedimentation rates are also shown. 143

Figure 5-22: Contours of effective plastic strain showing planform geometry of various horizons through the tier. (a) Horizon H3 (b) Horizon H2 (c) Horizon H1 (d) Horizon H0 (base of tier). See Figure 5-21 for horizon locations. Note the random orientations of faults that reflects the isotropic horizontal stress state and how fault connectivity changes at various horizons. No appreciable plastic strain is observed at the base of the tier..... 144

Figure 5-23: Isocontours of accumulated displacement in xy for (a) Horizon H3 (b) Horizon H2 (c) Horizon H1 (d) Horizon H0 (base of tier). See Figure 5-21 for horizon locations. Interpreted faults also shown. Largest heave is in the upper section of the tier and is negligible at the base of the tier as indicated by the cool contours. The largest displacement (heave) is observed close to the faults and decays away from it. 145

Figure 5-24: Model output showing material and stress state at Horizon H2 at present day, corresponding to a burial depth of ca 600m (a) Contours of preconsolidation pressure (b) Contours of effective mean stress. The contours indicate that at this depth and time the sediment is tending back towards the K_0 condition although the sediment still appears slightly overconsolidated with an OCR of between 1.1 and 1.5..... 146

Figure 5-25: (a) Inferred polygonal fault system, Lake Superior (Cartwright et al., 2004). Upper image shows small scale faults on shallow seismic of the lake bed with faults highlighted in red. (b) Inferred polygonal planform geometry at Lake Superior. (c) Suggested evolution of intraformational faults in the Boom Clay (Dehandschutter et al., 2005). 150

Figure 5-26: Shallow PFS, West Africa. Left image shows planform geometry. Red line denotes location of seismic section shown in upper right image. Depth between top of shallow tier and seabed is approximately 80m. 151

Figure 5-27: Cartoon showing idealised early evolution of sediments. The volume change arising from the 3D volumetric strain leads the specimen to a denser than critical state condition and therefore appears overconsolidated..... 152

Figure 5-28: Plot of specific volume versus effective mean stress for 1D consolidation case. 153

Figure 5-29: Plot of specific volume versus effective mean stress for 3D consolidation case. Prior to point B the 3D volume reduction takes place rapidly leading to a pseudo-overconsolidation.....	154
Figure 5-30: Contours of effective plastic strain and accumulated displacements at 1.0My and 1.5My. Burial to depth of 155m is shown. Note how faults nucleate in the lower third of the tier and have not been buried to depths exceeding between 60-90m.	156
Figure 5-31: Evolution of porosity (a) conventional consolidation (b) three-dimensional consolidation.	157
Figure 5-32: Evolution of preconsolidation pressure (a) conventional consolidation (b) three-dimensional consolidation.	158
Figure 5-33: Evolution of Yield Stress Ratio (YSR*). Note that as the three-dimensional consolidation begins the material appears to be more consolidated. As this process moves to completion the sediment tends back to the normal consolidation trend.	159
Figure 5-34: Stress evolution for shallow case. Note that the process is completed within the first 1My and after just over 2My the value of K_0 has increased to approximately 0.8.	159
Figure 5-35: Correlation between diagenetic textures and intensity of polygonal faulting in the Sanzhou Sag (Ding et al., 2013).	162
Figure 5-36: Diatomaceous sediments on the Peruvian continental margin. (a) Expected and observed consolidation styles showing apparent overconsolidation in the first 80 metres (Lee et al., 1990) (b) Images of core samples - note the shallow sample (left) exhibits decimetre scale shear fractures indicated by red arrows (Hill and Marsters, 1990).....	164
Figure 5-37: Core photographs from Lake Superior (A. Bolton - unpublished manuscript). Note the decimetre scale shear fractures (red arrows).	165

Chapter 6 Polygonal Faults and the Influence of Horizontal Stress Anisotropy

Figure 6-1: (a-b) Polygonal faults interacting with tectonic faults. Images used with permission from J. Cartwright (c-d) 3D view of Eocene horizon and seismic attribute map from the Sable Basin, offshore Nova Scotia showing interactions between polygonal faults and larger tectonic faults (Hansen et al., 2004).	172
Figure 6-2: Modification of polygonal planform geometry due to a sloping base (a) Planform geometry for a PFS in Faroe-Shetland Basin (Cartwright, 2011) (b) Planform geometry for a PFS in Nankai Trough (Heffernan et al., 2004).	172
Figure 6-3: Interactions between polygonal fault systems and salt structures (a) North Pierce salt diapir, North Sea (Carruthers, 2012) (b) Offshore West Africa (used with permission from J. Cartwright). Note how the planform geometry changes close to the salt diapirs in both examples. Fault length also appears to change in response to the anisotropic stress field, yet spacing of faults is consistent. Transition boundary is shown via the dashed red line.	173
Figure 6-4: Planform geometry polarisation in a deepwater fold and thrust belt, SE Asia, modified after (Morley et al., 2014). Faults become polarised as they enter the deformation front associated with the fold belt. A fold is present below the shown horizon with a N-S to NNW-SSE trending axis. The green triangle marks the inferred isotropic region and the yellow triangle marks the region polarised by the underlying fold. The red triangle indicates another anticline but in a region not associated with polygonal faulting. Note marked change	

in fault length.	174
Figure 6-5: Summary of polarisation of polygonal planform geometry from various forms of horizontal stress anisotropy. Red arrows indicate orientation of $s_{H,max}$ and blue arrows indicate orientation of $s_{h,min}$. Inferred horizontal stress state is shown along with boundary marking transition from isotropic to anisotropic stress states. (a) tectonic faults (b) slopes (c) salt diapirs (d) anticlines/fold belts.....	176
Figure 6-6: Plan view of model domain showing setup for conceptual investigation for stress anisotropy study. For comparison with rose diagrams the x and y directions correspond to EW and NS respectively. The z direction lies in the plane - see Section 5.2.2 for more detail regarding model setup.....	178
Figure 6-7: Horizontal stress ratio for a selection of 140 interrogation points on the H1 horizon prior to the development of the polygonal faults. The values shown for each scenario were used to calculate the average HSR as shown in Table 6-1.....	179
Figure 6-8: Variation in the degree of horizontal stress anisotropy. Note that in case (a) the contours indicate that the Horizontal Stress Ratio is very close to 1. There is only a very slight change in case (b) reflecting extremely subtle anisotropy. As the imposed displacements increase the contours indicate that the level of anisotropy grows larger, as shown in (c) and (d).....	180
Figure 6-9: Variation of intensity of faulting with horizontal stress anisotropy. Note that as the horizontal stress difference increases the number of faults observed decreases.....	181
Figure 6-10: Variation of fault spacing with level of horizontal stress anisotropy. The spacing varies widely regardless of the magnitude of the horizontal stress difference.	182
Figure 6-11: Horizontally isotropic case (a) Contours of effective plastic strain at the end of the simulation (b) Interpreted polygonal planform geometry at the end of the simulation. ..	183
Figure 6-12: Horizontal stress anisotropy scenario 1 (a) Contours of effective plastic strain at the end of the simulation (b) Interpreted polygonal planform geometry at the end of the simulation.....	184
Figure 6-13: Horizontal stress anisotropy scenario 2 (a) Contours of effective plastic strain at the end of the simulation (b) Interpreted polygonal planform geometry at the end of the simulation.....	185
Figure 6-14: Horizontal stress anisotropy scenario 3 (a) Contours of effective plastic strain at the end of the simulation (b) Interpreted polygonal planform geometry at the end of the simulation.....	186
Figure 6-15: Rose diagrams as visualisation of fault strike directions for various degrees of horizontal stress anisotropy. Note the marked reorientation of faults in (b).....	188
Figure 6-16: Rose diagrams as visualisation of fault strike directions for various degrees of horizontal stress anisotropy. Note how virtually all faults strike East-West.....	189
Figure 6-17: Data displayed in Figure 6-15 and presented in the form of histograms. For the isotropic case there is no obvious bias in fault azimuth. A progressive transition towards faults striking approximately East-West is observed.	190
Figure 6-18: Variation of approximated fault lengths for all faults in each sensitivity. Horizontal stress differences are (a) 0.01% (b) 0.19% (c) 1.83% (d) 3.05%. Note how the range of fault lengths is much wider where anisotropy is greatest.....	192

Figure 6-19: (a) Variation in minimum fault length in metres as a function of horizontal stress anisotropy (b) Variation in maximum fault length in metres as a function of horizontal stress anisotropy..... 193

Figure 6-20: Development of faults for one sensitivity (a) Initial fault development (b) developed and connected faults (c) effective plastic strain along the transect shown in (b) (d) transect taken along faults in the CNS (Carruthers and Cartwright, 2010). 195

Figure 6-21: (a-b) Coalescence of faults observed in models leading to the formation of ‘kinks’ (c) Radial fault traces around a fault diapir in the Espirito Santo Basin (Carruthers, 2012). 197

Figure 6-22: Polygonal faults developing in the hanging wall of a large tectonic fault (used and modified with permission from J. Cartwright). The solid black line indicates the location of the fault and the dashed black line indicates the inferred boundary between horizontally isotropic and anisotropic stress states. The green and purple boxes are of equal area and demonstrate the difference in fault intensity in the anisotropic and isotropic regions respectively. Note the changes in fault intensity between the two regions, and also the modification of fault length and strike direction..... 199

Figure 6-23: Fracture patterns in deeply buried sandstones created via application of (a) isotropic strain imposed at boundaries (b) moderate anisotropic strain imposed at boundaries which is larger in the x direction (c) strong anisotropic strain imposed at boundaries which is larger in the x direction (Olson et al., 2007). Note how the intensity and strike direction of the fractures changes in response to horizontal stress anisotropy..... 200

Figure 6-24: Potential approach for using planform geometry to estimate paleostress using image modified after Morley et al., (2014). In (a) the domain is broken down into cells. Azimuth, spacing and length relationships are established for each cell and by comparing to a reference region with an approximately isotropic stress state, a contour map of stress anisotropy could then be created as shown in (b). 201

Figure 6-25: Lithological influence on planform geometry, modified after Ding et al., (2013). At locations S90 and D163 the diagenetic reaction is associated with a strong dissolution and minor re-precipitation and here faulting is well developed and numerous (green box). At locations S92 and Y104 the reaction is associated with weak dissolution and stronger cementation, coinciding with a reduction in the number of faults (purple box). Locations shown correspond to images in Figure 5.34. This situation could be misinterpreted as resulting from changes in stress conditions. 203

Figure 6-26: (a) Ratio between minimum and intermediate principal stresses at a horizon pierced by a salt diapir, North Sea (Rockfield, 2012). Red colours indicate isotropy, blue indicates anisotropy (b) Interpretation of (a) using similar contour bands to Figure 6-24(b). Note how there is very high horizontal stress anisotropy near the diapir but that within approximately 1-2 diapir radii this has decayed almost exponentially to a value of less than 2%. 205

Chapter 7 Conclusions and Suggestions for Future Investigation

Figure 7-1: Results from Chapter 4 (a) Stress path and state boundary surface evolution for a chemical porosity change of 10% (b) Corresponding evolution of K_0 and comparison with experimental data. Note data is normalised to allow for qualitative comparison..... 213

Figure 7-2: Results from Chapter 5 (a) Successful recovery of the polygonal planform geometry from 3D sensitivity study (b) coherence slice showing polygonal fault system in North Sea (used with permission from J. Cartwright). Note the strong resemblance between model output and an actual polygonal fault system.....215

Figure 7-3: Results from Chapter 6 (a) Planform geometry and rose diagram for horizontally isotropic case (b) Planform geometry and rose diagram for horizontally anisotropic case (c-d) relationships between anisotropy and fault intensity and length respectively. The results indicate that even small differences in the magnitude of the horizontal stresses is sufficient to cause dramatic changes to the planform geometry, as displayed in the two rose diagrams. Note also the changes in the number and length of the faults.217

Figure 7-4: Inferred polygonal fault system in the exposed Khoman Chalk, Egypt (a) Detailed interpretation of planform geometry (Tewksbury et al., 2014), (b) Calcite fins indicate that at some point the faults were transmitting fluids and help to define the locations of faults. It is uncertain as to whether this indicates early dewatering or fluid migration after the faults had formed (Tewksbury et al., 2011).223

Figure 7-5: Concepts of a proposed future coupled study (a) Dependency of mudstone and claystone permeability on clay fraction, modified after Yang and Aplin, (2010) (b) Strong algorithmic coupling between mechanical and seepage fields (c, d) Previous utilisation of chemical compaction laws to investigate chemically induced overpressures in Jurassic sandstones, North Sea (Crook, 2010).226

Figure 7-6: Potential stress paths and faulting style for (a) diagenetically induced shear failure with hydrostatic pore pressure (b) diagenetically induced shear failure with development of overpressure.228

LIST OF TABLES

Chapter 2 Modification of Structure in Soils and Soft Rocks

Table 2-1: Summary of characteristics of PFS from around the globe, Part 1 (Cartwright and Dewhurst, 1998). Note sediments are exclusively claystones or biogenic mudstones/chalks. 42

Table 2-2: Summary of characteristics of PFS from around the globe, Part 2 (Cartwright and Dewhurst, 1998). Note the tiers are within the first kilometre of burial and were very slowly deposited.43

Chapter 4 Incorporating the Influence of Burial Diagenesis at Shallow Depths

Table 4-1: Selected poroelastic properties.94

Table 4-2: Plastic properties for definition of SR3 yield surface and plastic potential. Note negative values indicate tension.....95

Table 4-3: Chemical properties for Empirical Diagenetic Law.95

Table 4-4: Structure properties.....96

Chapter 5 Field Scale Analysis of the Formation and Evolution of Polygonal Fault Systems

Table 5-1: Comparison between model output and criteria for PFS identification as outlined by Cartwright and Dewhurst (1998). 124

Table 5-2: Poroelastic properties for evolutionary models. 127

Table 5-3: Plastic properties for evolutionary models. 128

Table 5-4: Chemical compaction properties for evolutionary models. 129

Table 5-5: Deconstructing properties for evolutionary models. 129

Table 5-6: Summary of residual friction simulations. Note the relationship between residual friction and both maximum throw and maximum horizontal displacement. 137

Table 5-7: Comparison between evolutionary model output and criteria for PFS identification as outlined by Cartwright and Dewhurst (1998). 147

Table 5-8: Poro-elastic properties for weak clay. Note the steeper slope of the unloading-reloading line which reflects a weak and compressible material. 152

Table 5-9: Plastic properties for weak clay. 152

Chapter 6 Polygonal Faults and the Influence of Horizontal Stress Anisotropy

Table 6-1: Summary of imposed horizontally anisotropy stress states. In case 1, no displacements are applied to the model boundary and hence the averaged horizontal stress ratio is close to unity. 178

Table 6-2: Number of faults observed for various levels of horizontal stress anisotropy..... 181

Table 6-3: Summary of fault strike relationships. As the horizontal stress difference becomes more pronounced an increasing percentage of faults begin to strike in the direction of the intermediate principal stress. 187

Dedicated to my son George and also to Alwyn and Mavis Roberts

‘For nature is a cunning nurse. She gives us lollipops all the way, and when the lollipop of hope and the lollipop of achievement are done, she gently inserts in our toothless gums the lollipop of remembrance. And with that pleasant vanity we are soothed to sleep.’

A. G. Gardiner

The Vanity of Old Age

Chapter 1

AN INTRODUCTION TO POLYGONAL FAULT SYSTEMS

Polygonal Fault Systems (PFS) have been studied using both 2D and 3D seismic data for over two decades (Henriet et al., 1989). Polygonal faults were first discovered in conventional 2D seismic data from the Southern North Sea and onshore Belgium (Henriet et al., 1989, 1991). The faults were unusual and interesting as they were inferred to have a non-tectonic origin, due in part to the large areas of passively subsiding continental basins over which they were observed. The term *polygonal fault* was coined shortly after to provide a distinction between these newly observed faults and other fault families (Cartwright, 1994). The term *polygonal* refers to the fact that the faults commonly intersect bedding planes with a variety of azimuths that define random polygons when observed in plan. The more recent availability of high quality 3D seismic data has allowed for the identification of a large number of PFS, and has permitted advances in our understanding of the nature and characteristics of PFS; these are discussed in Section 1.2.

1.1 Rationale

Despite these developments in our knowledge of the nature of PFS a critical question remains unsolved: *what caused them?* A universally accepted mechanism for the formation of polygonal faults has to date not been found. A number of hypotheses for PFS genesis have been presented but each struggles to find application to all known instances of polygonal fault formation. The enormous lateral extent and an observed confinement to specific, fine-grained stratigraphic intervals are strong arguments for a *constitutive* trigger that suggests the faults are present due to a particular characteristic of the host material. The search for this trigger is an area of on-going scientific research, of which this thesis is a contribution. The mechanisms suggested for PFS are discussed further in Section 1.3. PFS are observed in an increasing number of sedimentary basins with a truly global distribution and their economic and environmental significance has been realised for some time. An understanding of their genesis in particular has implications across a number of industrial activities.

1.1.1 Seal Integrity

Perhaps most importantly are the consequences of PFS genesis on the sealing integrity of fine-grained sedimentary stratigraphies. Low permeability sequences frequently form the areal seal (caprock) in many petroleum systems. These layers act as effective barriers to fluid migration and the layers below them are associated with the accumulation of these fluids. Thus, they become attractive targets for petroleum exploration (Hantschel and Kauerhau, 2009). The integrity of the caprock is therefore of great importance. In the context of the influence of PFS on petroleum systems a good example is the exploration of the Qiongdongnan Basin, South China Sea. Workers investigating the exploration prospectivity of this region have identified an extensive PFS overlying the regional reservoir unit (Sun et al., 2009, 2010). The presence of the PFS leads to some initial ambiguity regarding the likely location of accumulated hydrocarbons as shown in Figure 1-1.

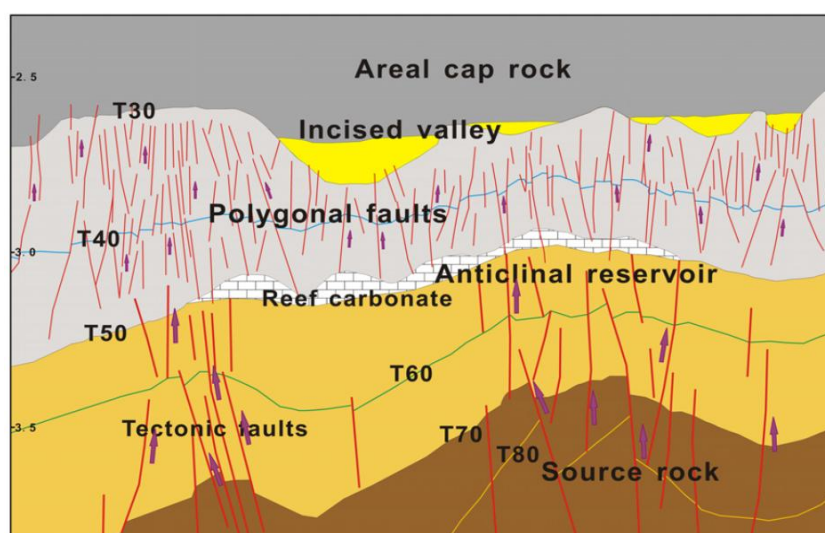


Figure 1-1: Petroleum system, Qiongdongnan Basin (Sun et al., 2010). The presence of polygonal faults overlying the anticlinal reservoir means that their potential influence as a seal-bypass system should be carefully considered.

The authors suggest that the polygonally faulted interval may act as a seal-bypass system (Cartwright et al., 2007) and permit fluid migration from the anticlinal reservoir to the overlying incised valley units. A similar scenario is reported in the Hammerfest Basin, Southwest Barents Sea, where the presence of a PFS has implications for fluid migration and gas leakage dynamics (Ostanin et al., 2012). The high cost of drilling virgin and/or exploratory wells means that the impact of potential seal-bypass mechanisms should be considered carefully.

1.1.2 Waste Repositories and Sequestration

Fine-grained sequences are also targets for carbon sequestration and High Level Waste storage repositories (Dehandschutter et al., 2004, 2005) and once again the prediction of the mechanical response and bulk flow properties of these layers is crucial (Miyazawa et al., 2011). The impact of PFS in compromising the integrity of such sequences needs to be considered, and the mechanism by which they form may have fundamental consequences even for layers that are not observed to contain polygonal faults. The increasing interest in using fine-grained sequences for processes such as CO₂ storage underlines the environmental importance of understanding PFS genesis in terms of offsetting emissions.

1.1.3 Reservoir Compartmentalisation and Reservoir Quality

In many cases PFS form in multiple tiers and can be separated by comparatively porous sand bodies that may themselves be attractive exploration targets. The coarser-grained sands do not appear to be affected by the same processes that trigger PFS formation in the layers above and below it. However, in the right conditions the faults can propagate and eventually pervasively fault the sand body (Möller et al., 2004). The result in this scenario would be the effective compartmentalisation of the reservoir unit. This will have consequences for the interpretation of fluid migration and the strategy of developing a field of this kind (Jolley et al., 2010). In rare cases the polygonally faulted interval might represent the targeted reservoir formation. Such an instance is reported in the Niobrara formation, Colorado. This thin tier consists of a mix of shales, marls and limestones and the play is only economically viable because the dense fracture network allows for sufficient connected porosity (Sonnenberg and Underwood, 2012), and the presence of the polygonal fault system could be a key consideration in determining reservoir quality.

1.1.4 Hydraulic Stimulation

Another important implication relates to the process of artificial hydraulic fracture. The mechanism by which the polygonal faults develop is currently disputed. An appraisal of the means by which fine grained sediments can become naturally fractured could provide useful insights into approaches for the artificial fracture of shale gas units by injection of water at high pressures, commonly known as *hydraulic fracturing* or *fracking*. Unconventional resources are widely regarded as a key future energy resource and understanding how to maximise production from shale gas reservoirs is therefore paramount, and much of this hinges on the effective exploitation of discrete fracture networks.

1.1.5 Summary

The importance of identifying PFS on interpreting hydrocarbon plays, storage of CO₂ and High Level Waste has been highlighted, and in-doing so has demonstrated that definitively concluding the mechanism, or mechanisms, by which they form would be of great interest to industry.

1.2 Characteristics of Polygonal Fault Systems

1.2.1 Global Distribution and Extent

Since the early studies of the early nineties, a great deal has been learned about the nature of PFS. The discovery of PFS in over 100 basins worldwide reveals how frequently they are encountered in the subsurface. The vast majority of these cases relate to divergent continental margin basins, although some PFS are developed in abyssal, foreland and intracratonic basins (Cartwright, 2011). Figure 1-2 shows the global distribution of PFS and they have been found to be laterally extensive and cover vast areas that make them truly unique as geological structures. For example, an identified PFS in the Australian Eromanaga Basin extends over an area in excess of 2,000,000 km². Assessment of typical values for the lateral extent is difficult due to limitations on the coverage of 2D/3D seismic surveys, however a minimum lateral extent would be approximately 150,000 km² (Cartwright and Dewhurst, 1998). In most cases PFS form in passively subsiding sedimentary basins, hence the early inference that tectonic influences are not a controlling factor in PFS formation.

1.2.2 Geometry and Lithology

PFS typically have a complicated and truly three-dimensional geometry. Figure 1-3 shows a range of classic PFS planform (map-view) geometries. The pattern and spacing of faulting varies between different locations, although recent evidence suggests crude scaling relationships between fault spacing and the thickness of the hosting layer (Carruthers, 2012).

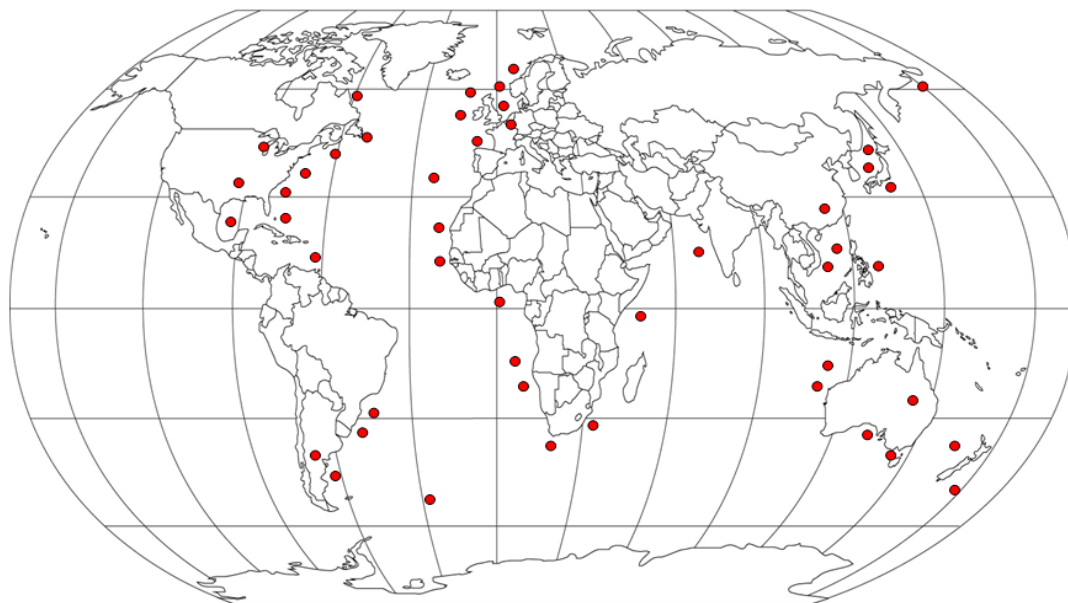


Figure 1-2: Global Distribution of known Polygonal Fault Systems. As clearly demonstrated, the vast majority of the systems are observed on passive continental margin slopes.

As will be discussed in greater detail later in Chapter 6, this pattern can be strongly influenced by regional stress anisotropy that can arise, for example, due to the presence of a salt diapir. This is shown in Figure 1-4.

Examination of Figure 1-4 indicates a more typical PFS geometry further away from the diapir, with the random distribution of strike reflecting an inferred horizontally isotropic stress state. Closer to the diapir the PFS is aligned in a strong radial pattern (Carruthers, 2012). This influence is due to the modification of the regional stress field from the presence of the salt diapir. Other factors influencing geometry can include slopes, pockmarks, tectonic faults, or facies variation due to the presence of a slump or mass-transport deposit (MTD).

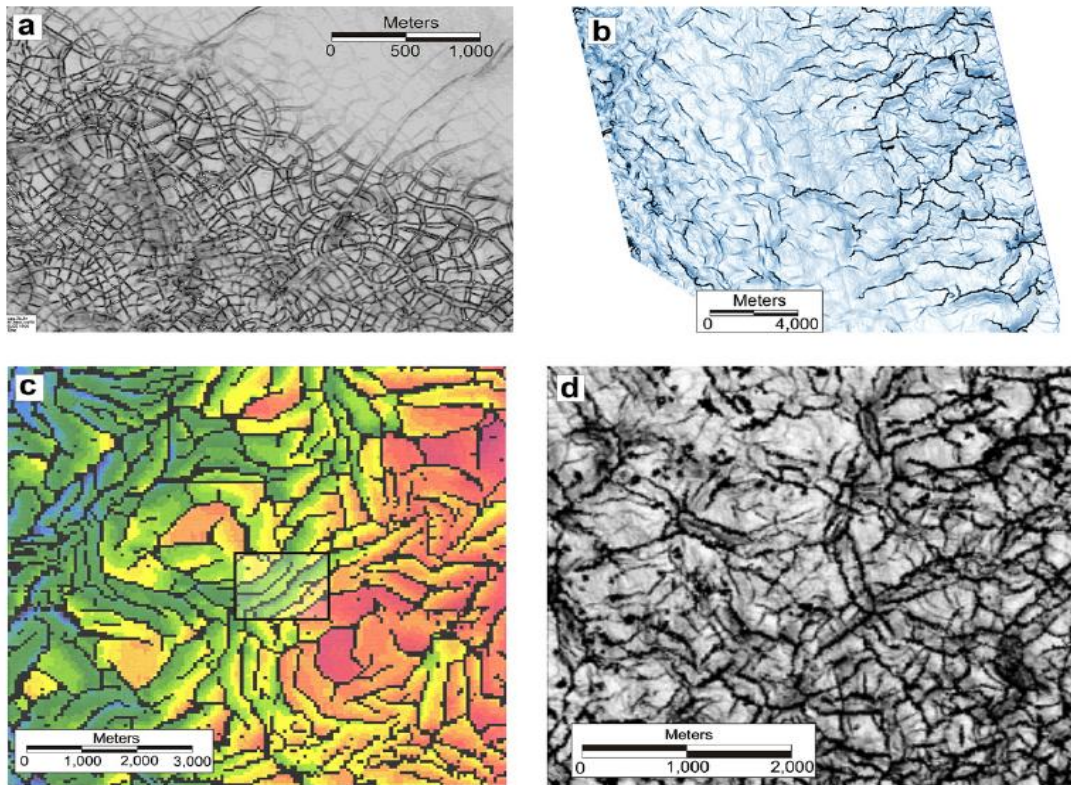


Figure 1-3: Examples of Polygonal Fault System planform geometries (Cartwright, 2011). Note the random fault orientation in all examples.

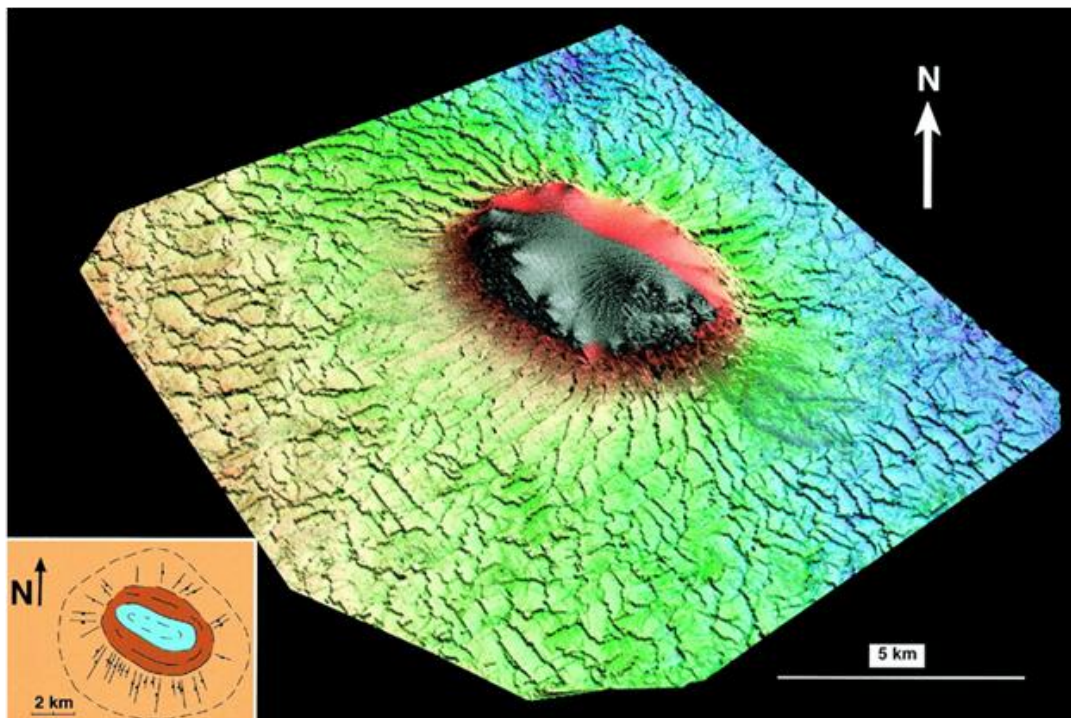


Figure 1-4: Change in PFS planform geometry in the Central North Sea (CNS) due to the presence of a salt diapir (Davison et al., 2000).

PFS have also been observed to conform to specific stratigraphic intervals or tiers. Tiers can range from tens of metres to over a kilometre in thickness. The geometry and thickness variation of the tier is thought to exert some control on PFS geometry as demonstrated in Figure 1-5. Figure 1-5(a) shows the classic tier arrangement in which the normal faults define a series of grabens in cross-section. Figure 1-5(b) shows a wedge tier, where fault dip is often found to be towards the basin centre. Strain and throw are also assumed to increase towards the basin centre. Figure 1-5(c) shows a complex tier geometry, with some faults being restricted by other more dominant faults. This indicates the possibility that PFS formation is a transient process. Confinement to tiers potentially indicates a strong constitutive control on the formation of PFS and this is further reinforced by the observation that PFS tend to favour fine-grained hemipelagic sediments such as mudstones, claystones and shales (Cartwright and Dewhurst, 1998).

PFS have additionally been observed in fine-grained carbonates, such as the Wyandot Chalk in the Sable Basin, offshore Nova Scotia (Hansen et al., 2004). PFS are not known to form in sand rich sediments and are seen to die out where there is a variation from clay-rich to coarser grained sand-rich facies (Carruthers, 2012). PFS are observed to contain exclusively normal faults. Fault dip and polarity vary depending on the geological setting. In the case of the Wyandot chalk faults dips are in the range 50-70° with an average dip of 61°. However, examples from Oligocene-Miocene and middle Eocene mudstones of the Central North Sea have average dips of 45° and 37° respectively. These differences are attributed to (Hansen et al., 2004);

- 1 Different burial depths and hence exposure to different amounts of vertical compaction.
- 2 Variations in shear strength, τ , and as a consequence the angle of internal friction, ϕ' .
- 3 A degree of uncertainty in the internal velocity when measuring dips using seismic data.

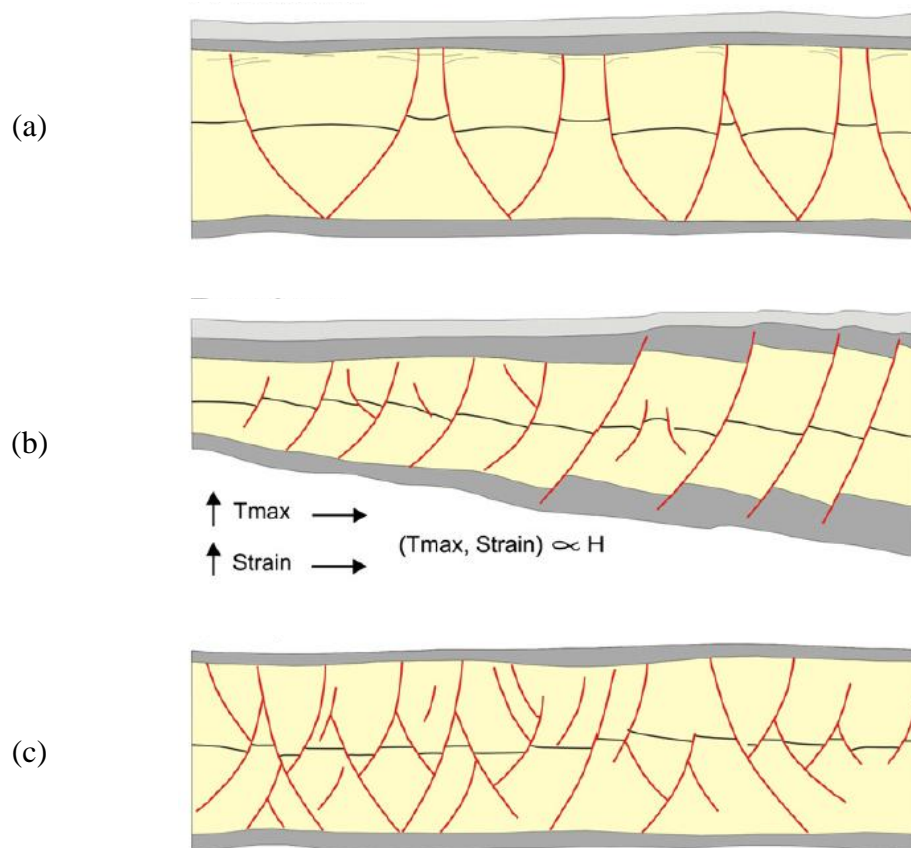


Figure 1-5: Cross-sections through typical Polygonal Fault Systems (a) Ideal Tier (b) Wedge Tier (c) Complex Tier (Cartwright, 2011).

1.2.3 Timing of Polygonal Fault Formation

There is some ambiguity regarding the propagation of the faults and the duration over which this takes place. The complex polygonal fault tier shown in Figure 1-5(c) suggests that the faulting is a transient process, as some faults appear to be restricted in propagation by other more dominant, fully-formed faults. Additionally, polygonal faults are also in some instances inferred to 'fill-the-space' between larger existing polygonal faults, suggestive that the process responsible for their formation could be transient or reactivated (Cartwright and Lonergan, 1996).

PFS are in general believed to form shortly after deposition in shallow marine environments. This conclusion is supported by inferred young polygonal fault systems in offshore Angolan sediments (approx. 5My old) and a clay layer below Lake Superior (deposited ca 8ka) (Wattrus et al., 2003). In both cases the faults are in close proximity to the sediment-water

interface. However, increasing evidence for coincidence of PFS and diagenetic fronts indicates a potential thermal trigger which might allow for the faults to develop at slightly greater depths (Davies and Ireland, 2011). It is widely accepted that PFS form within the first kilometre of burial.

1.2.4 Identification of a Polygonal Fault System

The seven criterion for identification of a PFS are outlined below in order of their respective diagnostic value (Cartwright and Dewhurst, 1998);

- 1 Map geometry: polygonal planform fault patterns.
- 2 Vertical extent: the fault system is layer-bound, and delimited by regionally correlatable stratigraphic surfaces.
- 3 Areal extent: the fault system is distributed over a large part of the basin (>150,000 km²).
- 4 Fault type and throw: the faults are all normal in type, with throws ranging from 5 to 100m.
- 5 Fault spacing: the faults are closely spaced (100-1000m).
- 6 Tiers: the deformed interval may be subdivided into two or more tiers, typically because of facies changes, though this is an area of ongoing research.
- 7 Fault polarity: faults may switch from apparently *synthetic* to *antithetic* series, or in wedges they may dip consistently upslope.

The criterion are mainly concerned with geometric and spatial relationships as these can be relatively easily obtained from good quality seismic data.

1.3 Suggested Mechanisms for the Genesis of Polygonal Fault Systems

As noted in previous sections the cause of PFS formation is still a topic of ongoing research and debate. Numerous mechanisms have been proposed, but each struggles to find compatibility with all known PFS instances. The major mechanisms proposed are discussed in more detail below. The reader is advised to review publications by Cartwright (2011) and Gouly (2008) which provide comprehensive and contrasting analysis on the subject of PFS genesis, the relevant details of which are included herein.

As highlighted in Section 1.1, an important first concept to understand, and one commonly proposed causal mechanism, is that due to the apparent confinement of PFS to particular

stratigraphic units coupled with the enormous length scale that is often observed, the trigger will likely be a constitutive property as opposed to some imposed stress condition.

Another important concept that was alluded to in Section 1.2 is that PFS commonly form in regions where tectonic influence from regional compression/extension or slopes is negligible. Hence, PFS present a scenario whereby shear failures with reasonably large offsets are observed in regions where the sediment has been predominantly consolidated in one-dimension (often referred to as the K_0 condition). This is potentially suggestive of a departure from "*Terzaghi consolidation*" which is a cornerstone of traditional soil mechanics theory (Terzaghi and Peck, 1996) and some of the suggested mechanisms favour this line of enquiry.

1.3.1 Downslope Gravity Sliding

In this scenario, PFS are suggested to have formed due to the influence of gravitational forces on a sloped surface. Goult (2008) discounts this as a controlling mechanism on PFS development due to the fact that polygonal faults are often observed on basin floors where dips are very close to zero. Furthermore, a slope at the base of the tier would produce a preferential alignment towards the depocentre whereas observation suggests only a slight bias. Analysis of a gently sloping PFS system near the Khop structure, offshore Mauritania, suggests stronger alignment away from the depocentre (Ireland et al., 2011).

1.3.2 Overpressure Development

During the natural consolidation of sediments the progressive loss of porosity (a measure of the volume of pore space) is attributed to the time-dependent expulsion of pore fluids. This is proportional to the permeability of the sediment, which is a measure of how easily fluids drain through the rock matrix, the length of drainage paths, and the rate of sedimentation. In the fine-grained sediments that typically host PFS the permeability is expected to be fairly low even at shallow burial depths. Permeability can be particularly low in mudstones with a high proportion of clay size particles (Yang and Aplin, 2010). Hence, given sufficiently rapid sedimentation, the pore fluid may find it considerably more difficult to escape and lead to the development of fluid pressures greater than hydrostatic. This is commonly referred to as *overpressure*, and in this situation a larger proportion of the overburden is supported by the pore fluid and less by the soil skeleton. If the overpressure becomes sufficiently high and is eventually larger than the smallest principal stress it is expected that the formation will become *hydrofractured* (Cartwright, 1994). This concept has been suggested as the genetic trigger for PFS formation. It is reinforced in part by a coincidence of inferred PFS and fluid

escape features such as pockmarks (Cartwright et al., 2004; Gay et al., 2004).

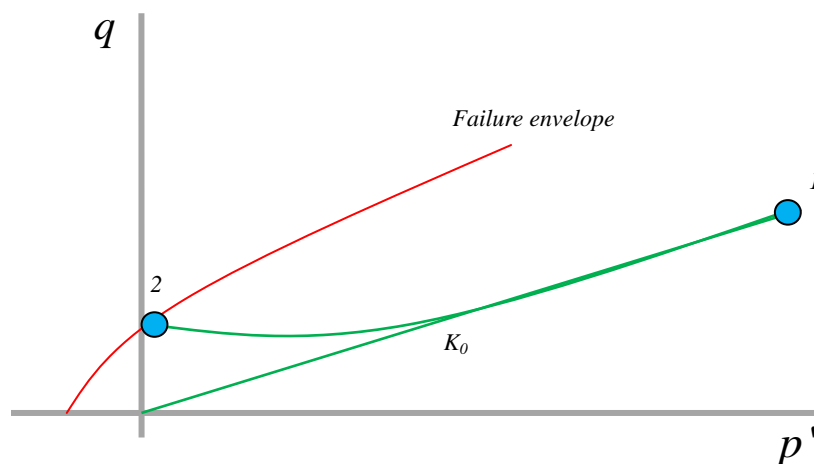


Figure 1-6: Overpressure model for PFS genesis. Sediment is consolidated to Point 1 along the K_0 stress path, thereafter the inability for the sediment to dewater leads to reduction in effective mean stress and eventual failure at Point 2.

The theory is however disputed by Gouly (2001, 2008) who states that *"a constant ratio between the horizontal and vertical effective stresses is maintained during uniaxial compaction, so the stress state does not move towards brittle failure Therefore, overpressure may be discounted as a generic cause for the development of layer-bound polygonal fault systems."* Whilst this is essentially correct, it should be noted that overpressure might still play an important role and compliment mechanisms that are associated with reduction in the smallest compressive principal stress. Figure 1-6 shows the basic principles of the overpressure model and a potential stress path.

Remarks 1 Note that in this thesis stresses are plotted in the Cambridge stress space, with the effective mean stress (p') as the abscissa and the deviatoric stress (q) as the ordinate. This stress space is preferred over the more familiar $\tau - \sigma'_n$ space that is often adopted for pressure dependent, quasi-brittle constitutive models. This decision is driven by how the selected material models are formulated, and is common for critical state models. See Chapter 3 for more detail.

1.3.3 Density Inversion

Gravitational instabilities arising from density inversion have also been attributed as the cause of PFS formation (Henriet et al., 1991; Watterson et al., 2000). In this model, the

gravitational instability arises from normally compacted layers overlying highly overpressured layers. This theory suffers from the fact the resolution of gravitational instabilities is often difficult to achieve even with the inclusion of strong tectonic forces e.g. in salt tectonics (Goult, 2008).

1.3.4 Residual Friction on Fault Planes

The residual friction approach was first proposed by Goult (2001). If subjected to sufficiently large strains, soils and soft-rocks tend towards a condition of perfect plasticity, referred to as the critical state. In this stress state plastic shearing occurs without change in volume or effective stresses. Physically, the material is in a turbulent condition whereby the soil is continuously remoulded and the structure remains random (Wood, 1990). This is often considered to be a lower bound in terms of soil/rock strength. Laboratory experiments involving ring shear apparatus have revealed that in clays subjected to sufficiently large strains the particles become preferentially orientated in the direction of the failure plane. As a consequence the friction generated on this "polished" surface is much lower than the friction mobilised at the critical state, resulting in a reduction in the angle of the critical state line.

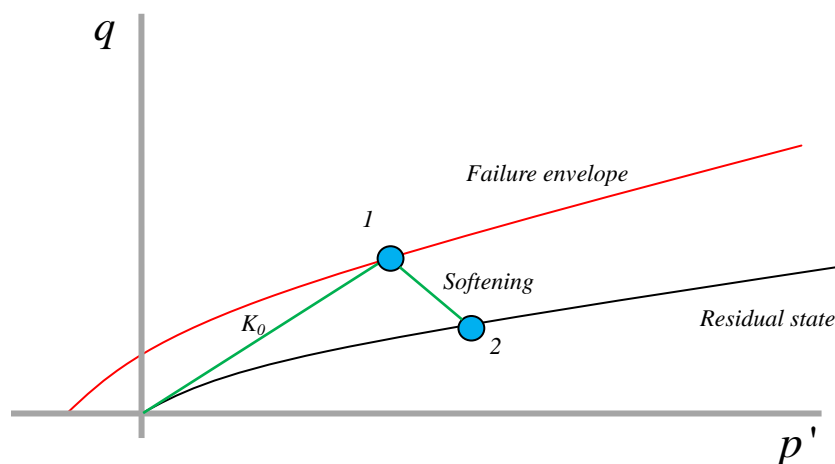


Figure 1-7: Proposed model for the residual strength mechanism, modified after (Goult, 2001). Sediment is consolidated to Point 1 along the K_0 stress path which intersects the peak strength failure envelope and then softens to the residual state at Point 2.

Goult (2001) suggests that due to the fact that PFS are commonly found in sediments featuring high content of clay size particles that this may be a valid causal mechanism. It would additionally explain the absence of PFS in sediments that have larger grain sizes such

as sandstones.

Gouly (2008) proposes that validation of this mechanism would be reinforced if for a cohesion of zero the ratio of horizontal and vertical effective stresses for failure on optimally dipping faults is given by Equation 1-1 (Jaeger and Cook, 2007).

$$\sigma'_h / \sigma'_v = \left(\sqrt{1 + \mu^2} - \mu \right)^2 \quad \mathbf{1-1}$$

For low values of residual friction, μ , such as in the range 0.11 to 0.14 the ratio of effective stresses is between 0.76 and 0.8. This is in agreement with well data from layers known to host PFS in the Central North Sea identified by Gouly and Swarbrick (2005).

An issue with this model is that it is not obvious how the sediment would originally reach a state of failure. Gouly (2001) suggests a model whereby the stress path followed in K_0 conditions could meet the initial failure envelope and then tend toward the residual state as shown in Figure 1-7, but this concept is not supported by any known laboratory testing. Gouly (2008) proposes repeated, short-term transient affects from earthquakes might be sufficient to advance the material to a state of initial failure.

Furthermore, as pointed out by Cartwright (2011), the extrapolation of the laboratory scale ring shear experiments cited by Gouly to the highly complex architecture of fault planes in the field is questionable. Despite the issues concerning residual friction on fault planes as a genetic mechanism for PFS development, it is plausible that this theory might play an important role in the ease of subsequent fault displacement and propagation.

1.3.5 Syneresis

Syneresis is a process known to occur in substances comprising of a continuous fine-grained solid network that is immersed in a continuous liquid phase, commonly referred to as a *gel*. Specifically, the process involves the spontaneous volumetric contraction of the solid network and subsequent expulsion of the fluid. Syneresis will occur when the internal forces of attraction are greater than the internal forces of repulsion. Syneresis cracks are documented in laboratory tests in clays that flocculated before settling. The degree of flocculation, and hence randomness of particle orientations on sedimentation, generally increases with the concentration and valency of the cations in the solution. After settling, the flocs contract and lose water under their own weight, until clay islands develop with cracks on all sides.

This argument for PFS genesis was first presented by Cartwright and Dewhurst (1998) and is the favoured causal mechanism for PFS discovered in several other locations e.g. Cartwright et al., 2004; Hansen et al., 2004. There is criticism for syneresis as a universal genetic mechanism due to the fact that syneresis is only observed at exceedingly high porosities. Additionally, the requirements for experimental investigations of syneresis in terms of changing of pore fluid chemistry (Di Maio, 1996) do not make it applicable to all known instances of PFS genesis, with Lake Superior being perhaps the most significant exclusion. Finally, PFS are found in other sedimentary rocks besides mudstones and claystones (Goult, 2008) and it is also uncertain as to what depth the internal forces of attraction exert a more significant influence than forces generated due to the load of the overburden (J. Cartwright - personal communication).

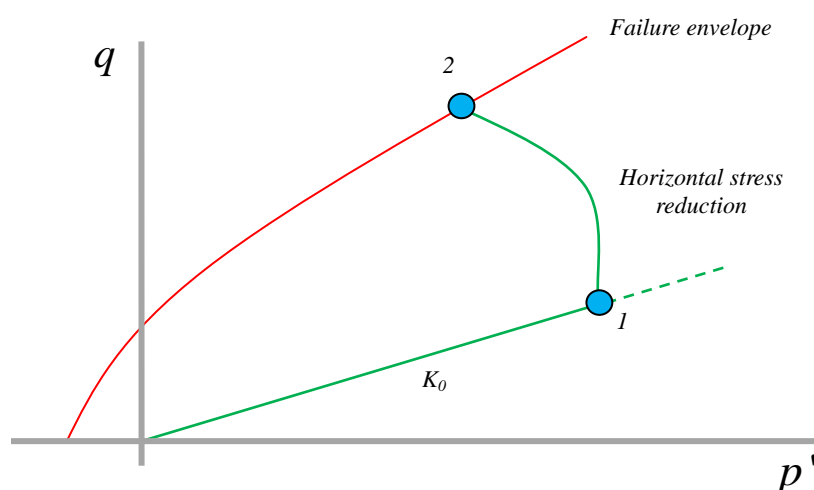


Figure 1-8: Proposed consolidation behaviour in the syneresis and chemical compaction models. Sediment is consolidated to Point 1 along the K_0 stress path, thereafter a reduction in the horizontal stress leads to a deviated stress path which intersects the failure envelope.

1.3.6 Chemical Compaction

Chemical compaction has been proposed as a potential mechanism for PFS genesis. This has been driven by a noted coincidence of PFS and diagenetic fronts, such as the Opal A/CT transformation boundary (Praeger, 2009; Neagu et al., 2010; Cartwright, 2011; Davies and Ireland, 2011). It has been thought for some time that diagenetic reactions exert some control on PFS genesis (Hansen et al., 2004) but more recently the discovery of the proximity of diagenetic fronts to polygonally faulted intervals is thought to indicate a closer relationship.

Laboratory experimentation and simple numerical modelling of dissolution type processes has shown a change in the gradient of the K_0 line due to a reduction of the horizontal effective stress (Shin et al., 2008). This is considered a novel mechanism in advancing sediments toward a state of shear failure. The relationship between chemical compaction, material behaviour and polygonal faults is discussed in greater detail in Chapter 2. Figure 1-8 provides a diagrammatical representation of the stress evolution for chemical compaction (specifically dissolution) and syneresis.

1.4 Summary

Networks of polygonal faults are located in many basins around the world and it is almost certain that the number currently observed on 2D and 3D seismic data is only representative of a fraction of the total number that exist. The importance of establishing the genetic mechanism for PFS development has been outlined and advancing our knowledge of polygonal fault genesis has important implications for hydrocarbon/unconventional exploration and CO₂ sequestration. These are areas with ever increasing relevance to global economics and the environment. A brief overview of the principal theories that have been ventured to explain PFS genesis has been included with a focus on the merits and weaknesses of each in their application to PFS genesis.

The important point that the driver for PFS formation is likely to be constitutive has been stressed, and this is reflected by the fact that the most favoured mechanisms for PFS genesis, namely syneresis and chemical compaction, share this common theme. Theories that deviate from this concept, such as density inversion and gravity sliding have been shown to have significant drawbacks in terms of their applicability to all known instances of polygonal fault genesis. The residual friction and overpressure arguments are perhaps less likely candidates for explaining PFS formation, but it is plausible that they might have a significant contribution as supplementary mechanisms.

1.5 Objective and Scope of the Thesis

This thesis aims to provide an in-depth computational geomechanics based analysis of the compaction behaviour of fine-grained sediments such as mudstones with specific consideration of PFS formation. In particular the analysis of the processes affecting soil/rock structure is targeted and links between these processes and suggested mechanisms for PFS formation are to be investigated. The most important goal is to use these links to provide a

rigorous geomechanical argument to explain the genesis by recasting existing models in the soil-structure framework, and then developing existing constitutive models that have been built on the critical state concept. A key question to address is whether the genesis of PFS is really that uncommon, or whether they just appear because of a poor understanding of the mechanics and processes involved in the early consolidation of sediments. The observation of PFS in numerous locations around the globe perhaps suggests the later. These arguments are to be tested in simple uniaxial consolidation simulations with a principal goal being the demonstration of shear failure. This will be carried out using the state-of-the-art Finite/Discrete Element software *ELFEN*. Extension of the simple models to field scale application and identification of the criteria outlined by Cartwright and Dewhurst (1998) is considered critical in providing evidence of modelled polygonal fault networks. The main objective is the recovery of PFS from the models that arise solely due to the imposed physics. To the authors knowledge the recovery of a polygonal fault network with forward modelling technology has to date not been attempted or published.

Extension of these cases to examine the interaction of PFS and forms of stress anisotropy is another key objective. Primary focus is given to studies involving slopes, tectonic forces, pockmarks and salt diapirs, all of which are known to cause geometry modification to PFS (Carruthers, 2012). The objective of this element of the study is to quantify the level of anisotropy required to cause reorganisation of the planform geometry. Again this contribution would be useful to academia and industry, potentially allowing for an approximate quantification of (paleo)stress anisotropy solely by inspection of seismic data.

There are also more general themes/objectives that run through this work. The first is developing a better appreciation of the evolution of sediments over geological time and how this may lead to natural deviations from the standard theory of sediment compaction. Consequences of this are that models based on simple relationships between porosity and depth or effective stress (such as those routinely adopted in basin modelling software) may miss key aspects of the sediment evolution. This is particularly important if the sedimentary layers in question have important roles in a petroleum system, as is the case with the development of PFS. Another of these more general themes relates to the use of advanced computational modelling as an investigative tool. In the case of PFS, the suggested formation mechanisms involve the influence of not just mechanical behaviour, but also thermal and/or chemical effects and high overpressures, necessitating the coupling of various key physical

processes. As such it would appear that physical modelling at the bench scale and laboratory investigations might deliver limited insight. Numerical forward modelling could fill a gap here and find significant use as an analysis tool in studying PFS as well as other unusual and poorly understood phenomena occurring in the subsurface.

1.5.1 Primary Study Objectives

- 1 Detailed investigation of modifications to soil/rock structure and ties to PFS genesis, and construction of a solid geomechanical argument for PFS formation.
- 2 Testing of the main argument using geomechanical forward modelling software. Recovery of a PFS and validation against the Cartwright and Dewhurst criteria.
- 3 Use of geomechanical modelling to investigate stress anisotropy conditions.

1.5.2 Secondary Study Objectives

- 1 Developing a deeper understanding of sediment evolution over geological time.
- 2 Demonstration of sophisticated geomechanical forward modelling as a useful analysis tool.

1.6 Layout of Thesis

This thesis consists of seven chapters. The introduction is considered in the present chapter and a brief synopsis of the remaining chapters is provided in the following;

Chapter 2 presents a discussion of the principal sources of structure in soils and soft rocks. A thorough examination of the relevant literature is provided including laboratory analysis, well data and numerical models. Connections to the PFS genesis mechanisms discussed in Chapter 1 are identified with focus on the influence of diagenesis on soil structure. The approach adopted for the remainder of the study is outlined and justified.

Chapter 3 discusses the computational approach that is adopted in this research. The material model that is used is introduced, and the advantage of critical-state based approaches over more familiar constitutive models is outlined.

Chapter 4 presents geomechanical arguments for PFS development are developed and discussed. An in-depth discussion on how the material modelled is developed to incorporate the macro-scale influence of kinetically driven supplementary compaction processes (diagenesis), most importantly capturing the modification of sediment strength. outlines the process followed in the creation of a generic material characterisation. The results of single

element tests of the generic characterisation are summarised. Specifically, it is shown how consideration of the influence of supplementary compaction processes might lead to shear failure and localised faulting in the K_0 scenario. The development of the stress path, ratio of horizontal/vertical stress and the evolution of the state boundary surface are shown.

Chapter 5 extends the work in the previous chapter by modelling the development of polygonal faulting in field scale simulations. Characterisations developed in Chapter 4 are tested before a sensitivity study is undertaken to establish what might be the key implications for a diagenetic model of PFS development. The argument is extended to consider processes that are not strictly diagenetic but that may have similar implications for the constitutive response.

Chapter 6 focuses on adapting the field scale simulations so that they may be used to investigate the response of polygonal faults to scenarios of horizontal stress anisotropy. Sources of horizontal stress anisotropy known to influence the polygonal planform geometry are described. A simple conceptual modelling strategy is outlined, and relationships between the magnitude of horizontal stress anisotropy and the structural style of the tier are presented and discussed. A potential workflow for establishing paleostress is discussed along with some obvious constraints regarding its application.

Chapter 7 presents a concise summary of the work contained within this thesis. Discussions of novel contributions to the understanding of polygonal faults made within the thesis are provided. Detailed discussion on potential shortcomings or assumptions is also presented together with ideas for future study directions.

1.7 References

- Carruthers, T. D., 2012, Interaction of polygonal fault systems with salt diapirs: Unpublished PhD Thesis - Cardiff University, p. 526.
- Cartwright, J. A., 2011, Diagenetically induced shear failure of fine-grained sediments and the development of polygonal fault systems, *in* *Marine and Petroleum Geology*: Elsevier Ltd, p. 1593–1610.
- Cartwright, J. A., 1994, Episodic basin-wide hydrofracturing of overpressured Early Cenozoic mudrock sequences in the North Sea Basin: *Marine and Petroleum Geology*, v. 11, no. 5, p. 587–607.
- Cartwright, J. A., and D. N. Dewhurst, 1998, Layer-bound compaction faults in fine-grained sediments: *Geological Society of America Bulletin*, v. 110, no. 10, p. 1242–1257.
- Cartwright, J. A., M. Huuse, and A. C. Aplin, 2007, Seal bypass systems: *AAPG Bulletin*, v. 91, no. 8, p. 1141–1166.
- Cartwright, J. A., and L. Lonergan, 1996, Volumetric contraction during the compaction of mudrocks: a mechanism for the development of regional-scale polygonal fault systems: *Basin Research*, v. 8, no. 2, p. 183–193.
- Cartwright, J. A., N. J. Watrus, D. E. Rausch, and A. Bolton, 2004, Recognition of an early Holocene polygonal fault system in Lake Superior: Implications for the compaction of fine-grained sediments: *Geology*, v. 32, no. 3, p. 253–256.
- Davies, R. J., and M. T. Ireland, 2011, Initiation and propagation of polygonal fault arrays by thermally triggered volume reduction reactions in siliceous sediment: *Marine Geology*, v. 289, no. 1-4, p. 150–158.
- Davison, I., I. Alsop, P. Birch, C. Elders, N. Evans, H. Nicholson, P. Rorison, D. Wade, J. Woodward, and M. Young, 2000, Geometry and late-stage structural evolution of Central Graben salt diapirs, North Sea: *Marine and Petroleum Geology*, v. 17, no. 4, p. 499–522.
- Dehandschutter, B., S. Vandycke, M. Sintubin, N. Vandenberghe, P. Gaviglio, J.-P. Sizun, and L. Wouters, 2004, Microfabric of fractured Boom Clay at depth: a case study of brittle–ductile transitional clay behaviour: *Applied Clay Science*, v. 26, no. 1-4, p. 389–401.
- Dehandschutter, B., S. Vandycke, M. Sintubin, N. Vandenberghe, and L. Wouters, 2005, Brittle fractures and ductile shear bands in argillaceous sediments: inferences from Oligocene Boom Clay (Belgium): *Journal of Structural Geology*, v. 27, no. 6, p. 1095–1112, doi:10.1016/j.jsg.2004.08.014.

-
- Gay, A., M. Lopez, P. Cochonat, and G. Sermondadaz, 2004, Polygonal faults-furrows system related to early stages of compaction - upper Miocene to recent sediments of the Lower Congo Basin: *Basin Research*, v. 16, no. 1, p. 101–116.
- Goultly, N. R., 2008, Geomechanics of polygonal fault systems: a review: *Petroleum Geoscience*, v. 14, no. 4, p. 389–397.
- Goultly, N. R., 2001, Mechanics of layer-bound polygonal faulting in fine-grained sediments: *Journal of the Geological Society*, v. 159, no. 1991, p. 239–246.
- Goultly, N. R., and R. E. Swarbrick, 2005, Development of polygonal fault systems: a test of hypotheses: *Journal of the Geological Society*, v. 162, no. 4, p. 587–590.
- Hansen, D. M., J. W. Shimeld, M. A. Williamson, and H. Lykke-Andersen, 2004, Development of a major polygonal fault system in Upper Cretaceous chalk and Cenozoic mudrocks of the Sable Subbasin, Canadian Atlantic margin: *Marine and Petroleum Geology*, v. 21, no. 9, p. 1205–1219.
- Hantschel, T., and A. I. Kauerhauf, 2009, *Fundamentals of Basin and Petroleum Systems Modeling*: Springer, p. 476.
- Henriet, J. P., M. De Batist, W. Van Vaerenbergh, and M. Verschuren, 1989, Seismic facies and clay tectonic features in the southern North Sea: *Bulletin of the Belgian Geological Society*, v. 97, p. 457–472.
- Henriet, J. P., M. De Batist, and M. Verschuren, 1991, Early fracturing of Paleogene clays, southernmost North Sea: relevance to mechanisms of primary hydrocarbon migration, *in* Spenser, A.M. (Ed.), *Generation, Accumulation and Production of Europe's Hydrocarbons*. Special Publications of the European Association of Petroleum Geologists: p. 217–227.
- Ireland, M. T., N. R. Goultly, and R. J. Davies, 2011, Influence of stratigraphic setting and simple shear on layer-bound compaction faults offshore Mauritania: *Journal of Structural Geology*, v. 33, no. 4, p. 487–499.
- Jaeger, J., and N. G. Cook, 2007, *Fundamentals of Rock Mechanics*: Wiley-Blackwell, p. 488.
- Jolley, S. J., Q. J. Fisher, and R. B. Ainsworth, 2010, Reservoir compartmentalization: an introduction: *Geological Society, London, Special Publications*, v. 347, no. 1, p. 1–8.
- Di Maio, C., 1996, Exposure of bentonite to salt solution : osmotic and mechanical effects: *Géotechnique*, v. 46, no. 4, p. 697–707.
- Miyazawa, D., H. Sanada, T. Kiyama, Y. Sugita, and Y. Ishijima, 2011, Poroelastic Coefficients for Siliceous Rocks Distributed in the Horonobe Area , Hokkaido , Japan: *Journal of the Mining and Materials Processing Institute of Japan*, v. 127, no. 3, p. 132–138.

-
- Möller, N. K., J. G. Gjelberg, O. Martinsen, M. A. Charnock, B. Færseth, S. Sperrevik, and J. A. Cartwright, 2004, A geological model for the Ormen Lange hydrocarbon reservoir: Norwegian Journal of Geology, v. 84, p. 169–190.
- Neagu, R. C., J. A. Cartwright, and R. J. Davies, 2010, Measurement of diagenetic compaction strain from quantitative analysis of fault plane dip: Journal of Structural Geology, v. 32, no. 5, p. 641–655.
- Ostanin, I., Z. Anka, R. di Primio, and A. Bernal, 2012, Identification of a large Upper Cretaceous polygonal fault network in the Hammerfest basin: Implications on the reactivation of regional faulting and gas leakage dynamics, SW Barents Sea: Marine Geology, v. 332-334, p. 109–125.
- Praeger, T., 2009, Heterogeneities in fine-grained sediments and their impact on seal quality: Unpublished PhD Thesis - Cardiff University, p. 242.
- Shin, H., J. C. Santamarina, and J. A. Cartwright, 2008, Contraction-driven shear failure in compacting uncemented sediments: Geology, v. 36, no. 12, p. 931.
- Sonnenberg, S. A., and D. Underwood, 2012, Polygonal fault systems: A new structural style for the Niobrara formation, Denver Basin, Colorado, *in* AAPG Annual Convention and Exhibition, Long Beach, California.
- Sun, Q., S. Wu, F. Lü, and S. Yuan, 2010, Polygonal faults and their implications for hydrocarbon reservoirs in the southern Qiongdongnan Basin, South China Sea: Journal of Asian Earth Sciences, v. 39, no. 5, p. 470–479.
- Sun, Q., S. Wu, G. Yao, and F. Lü, 2009, Characteristics and formation mechanism of polygonal faults in Qiongdongnan Basin, northern South China Sea: Journal of Earth Science, v. 20, no. 1, p. 180–192.
- Terzaghi, K., and R. B. Peck, 1996, Soil Mechanics in Engineering Practice: John Wiley & Sons, p. 549.
- Watterson, J., J. Walsh, A. Nicol, P. A. R. Nell, and P. G. Bretan, 2000, Geometry and origin of a polygonal fault system: Journal of the Geological Society, v. 157, no. 1995, p. 151–162.
- Wattrus, N. J., D. E. Rausch, and J. A. Cartwright, 2003, Soft-sediment deformation in Lake Superior: Evidence for an immature Polygonal Fault System?, *in* P. Van Rensberger, R. R. Hillis, A. J. Maltman, and C. K. Morley, eds., Subsurface Sediment Mobilization: Geological Society, London, Special Publications, p. 323–334.
- Wood, D. M., 1990, Soil Behaviour and Critical State Soil Mechanics: Cambridge University Press, p. 488.
- Yang, Y., and A. C. Aplin, 2010, A permeability–porosity relationship for mudstones: Marine and Petroleum Geology, v. 27, no. 8, p. 1692–1697.

Chapter 2

MODIFICATION OF STRUCTURE IN SOILS AND SOFT ROCKS

Depositional porosity and subsequent volume reduction due to increasing burial stresses are cornerstones of traditional soil and rock mechanics theory. Much time and effort has been devoted to attempting to better understand how sediments behave over geological time. Attention has been given to developing compaction trends for various rock types, with particular focus on shales and mudstones as these are often the dominant lithology in many sedimentary basins. Figure 2-1 shows a representative sample of published compaction curves for shales and mudstones (Athy, 1930; Baldwin and Butler, 1985; Hudec et al., 2006).

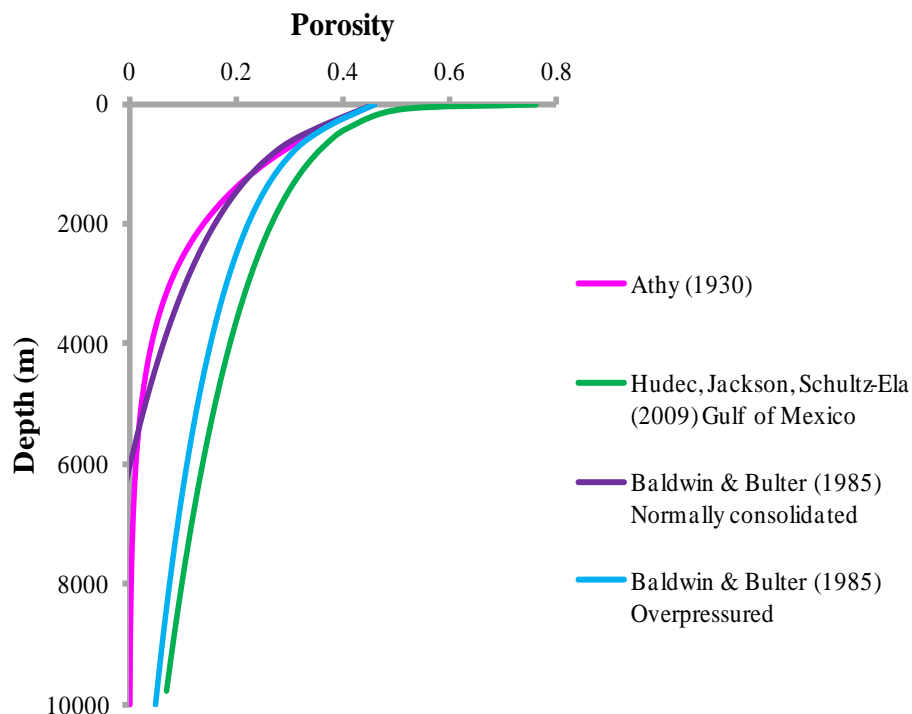


Figure 2-1: Typical compaction curves for Shales (Athy, 1930; Baldwin and Butler, 1985; Hudec et al., 2006).

Frequently it is observed that sediments in the subsurface do not conform to these trends,

which are often empirically based. In some instances this difference can be attributed to the inability of the sediment to consolidate due to rapid sedimentation and low permeability, as in the case of the normally and overpressured examples in Figure 2-1. The development of overpressure explains the higher porosity of the sequence relative to the normally consolidated model, as compaction is inhibited. However, other processes may also contribute to deviations from the curves. As an illustration, Figure 2-2 shows compaction trends plotted against published data from a North Sea well (Nordgård Bolås et al., 2008). In this well, which is dominated by shales and muds, the uppermost section of the column appears to be well represented by the green curve. It is assumed that only effective stress driven mechanical compaction is taking place in this section. However, there is a noticeable change in the deeper sections of the well and this is attributed to additional chemical processes.

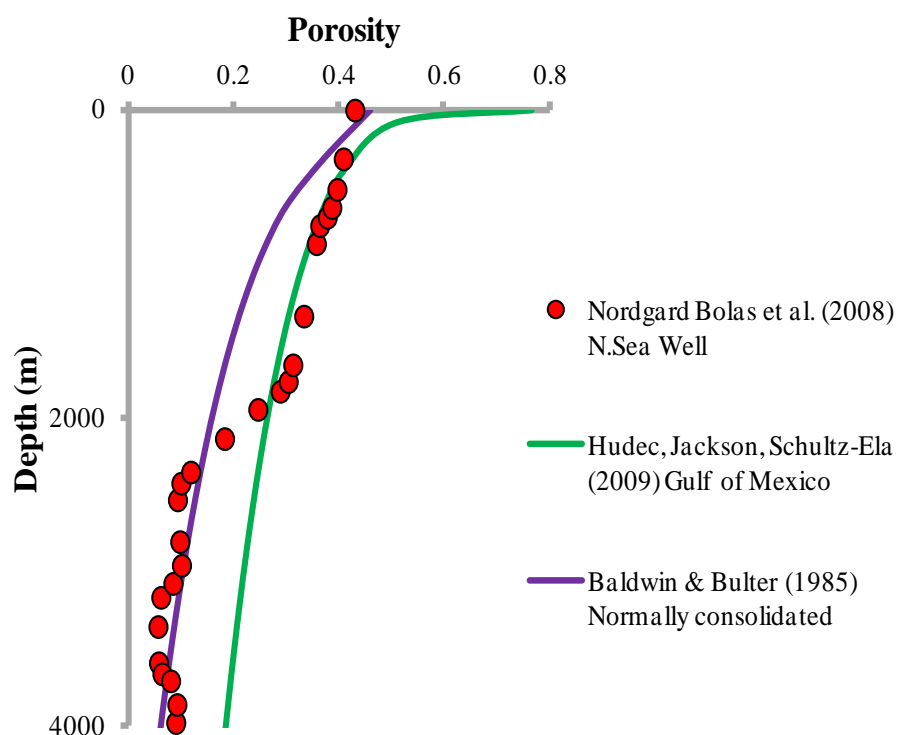


Figure 2-2: Comparison between compaction curves and trend observed in North Sea Wells (Baldwin and Butler, 1985; Hudec et al., 2006; Nordgård Bolås et al., 2008).

Diagenetic reactions will be discussed in greater detail later in this chapter. These chemical reactions have the effect of modifying the consolidation behaviour primarily through their effect on sediment *structure*. This particular case is clearly operating at rather substantial depth, however similar mechanisms may operate at various times during the burial of a

sedimentary layer, and many are prominent near surface. Figure 2-2 has been included to stress that in many cases, consideration of the mechanical behaviour alone is often insufficient to explain the observed behaviour of sedimentary layers.

Over the past two to three decades, an increasing number of researchers have studied the influence of soil structure on sediment deformation (Burland, 1990; Cotecchia and Chandler, 2000; Cafaro and Cotecchia, 2001). It is suggested that structure should be accorded equal importance as porosity and stress history (Leroueil and Vaughan, 1990), such is its influence on the compressive and shearing behaviour of sediments. Consequently, the processes that govern the state of structure and hence the geomechanical response of the sediment merit inclusion in this thesis. Therefore, this Chapter aims to provide a concise overview of these processes and explore the possible links to PFS genesis. The fact that structure is often not considered in the assessment of the mechanical behaviour of soft rocks despite its clear influence is interesting in the context of polygonal faults, where a seemingly non-conventional consolidation behaviour is sought to reconcile their curious presence in the subsurface. Furthermore, the confinement of PFS to predominantly fine grained clays and porous chinks, which are often found to be highly sensitive to structural changes, is further indication that an investigation of the various processes that control the development and removal of structure is potentially significant in understanding the genesis and evolution of polygonal faults.

2.1 Introduction to Structured Sediments

In essence, structure refers to how the *fabric* and *bonding* of the sample effect its behaviour. Fabric concerns the arrangement of particles that make up the soil, whilst bonding describes inter-particle forces that are not of a purely frictional nature. All natural samples are found to have some level of structure and consequently exhibit different behaviour from remoulded and artificially sedimented laboratory samples. Sources of structure are classified as either being *sedimentation* or *post-sedimentation*. *Sedimentation structure* develops during and after deposition and results solely from one dimensional consolidation. This type of structure is present only in normally consolidated clays and can encompass many different fabrics and degrees of bonding. *Post-sedimentation structure* describes any level of structure that develops due to processes other than one dimensional consolidation or subsequent to deposition e.g. creep. These generally occur over geological time frames. It can be difficult to definitively classify sources of structure.

The seminal paper by Burland (1990) introduced a methodology for assessing the degree of structure in clays and mudstones. With regards to the compressive behaviour, results from oedometer (uniaxial consolidation) experiments are often plotted as shown in Figure 2-3. A measure of volume change, normally either volumetric strain, porosity, void ratio or specific volume, is plotted against the range of effective vertical stresses to which the specimen is exposed. For a number of different clays Figure 2-3 shows typical profiles which indicate approximately linear trends of decreasing volume with increasing logarithm of effective vertical stress. When these values are normalised with respect to the initial porosity, it is found that they coalesce to form a single curve in $e - \log \sigma'_v$ space (Burland, 1990).

By standardising this procedure the concept of the *Intrinsic Compression Line* (ICL) is introduced that represents the behaviour of completely destructured sediments (Burland, 1990), see Figure 2-4. The ICL provides a reference state for the intrinsic behaviour of a sediment and allows for the level of structure in the natural specimen to be assessed. The level of structure can be inferred from the distance of the compression line for the natural (in-situ) specimen to the ICL. Structured samples have an ability to maintain higher porosities for a given vertical effective stress, which is attributed to the more stable, structured framework of the solid matrix. As such they will lie on the sedimentation compression line (SCL), some distance to the right of the ICL, with the magnitude of this distance reflecting the level of structure. The SCL and ICL are shown in Figure 2-5.

The level of structure is sometimes referred to as the *sensitivity* of the sediment. As the effective vertical stresses get larger, the compression line of the structured specimen is found to tend to the ICL and this reflects the progressive mechanical breakdown of structure until it is completely removed and the two lines are coincident.

It has been suggested that structure may be thought of as a form of *pseudo-overconsolidation* (Leroueil and Vaughan, 1990). Overconsolidation refers to the maximum stress that the sample has been exposed to relative to the current stress state. It is common for sediments to become unloaded (via erosion of overlying layers) or uplifted, so that in their current state they are exposed to lower stresses than they have been historically. The ratio of the pre-consolidation pressure to the current stress state (measured as the vertical effective stress or effective mean stress) is referred to as the *overconsolidation ratio*, or OCR. A normally consolidated specimen i.e. one whose current stress state is identical to the maximum past

stress state, has an OCR of 1. It is not unusual for some sediments to have very large overconsolidation ratios, such as the stiff Todi Clay which has an OCR of 12.6 (Burland et al., 1996). More simply, overconsolidation refers to the size of the region in stress-space in which the material behaves elastically and thus deformations are recoverable on removal of the load. Therefore, a more structured specimen might be regarded as having a larger state boundary surface (a region in stress space defining the limit of elastic behaviour). This is shown conceptually in Figure 2-6, along with the K_0 stress path. The lower compressibility and increased strength of the structured sample is reflected in the larger State Boundary Surface. Should destructuring take place the SSBS would tend toward the ISBS.

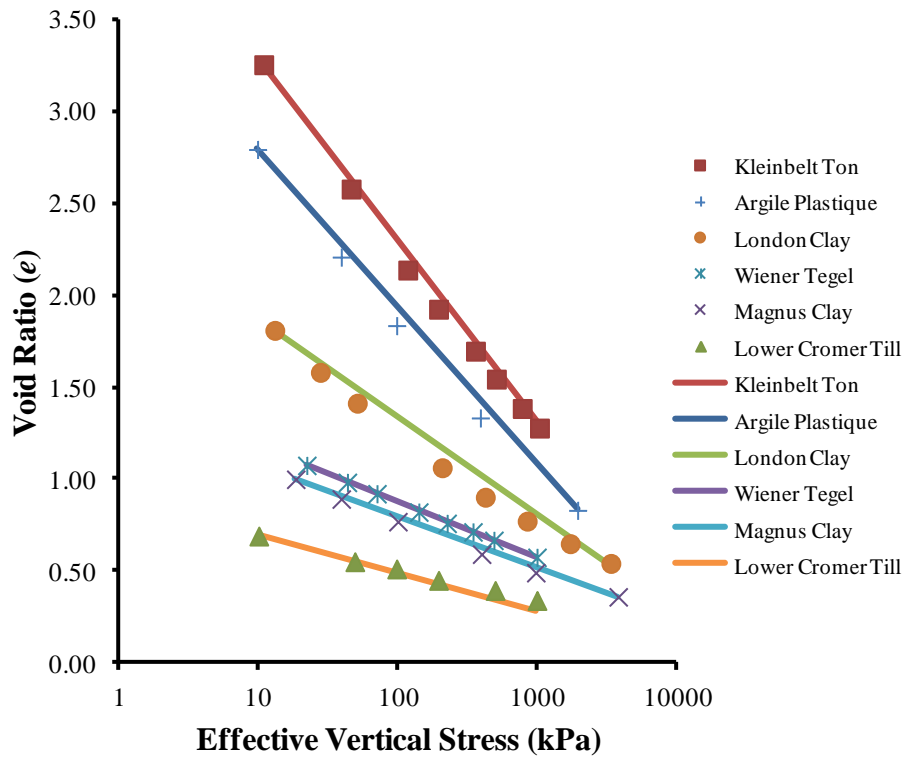


Figure 2-3: 1-D Compression curves for six different clays (cf Burland, 1990).

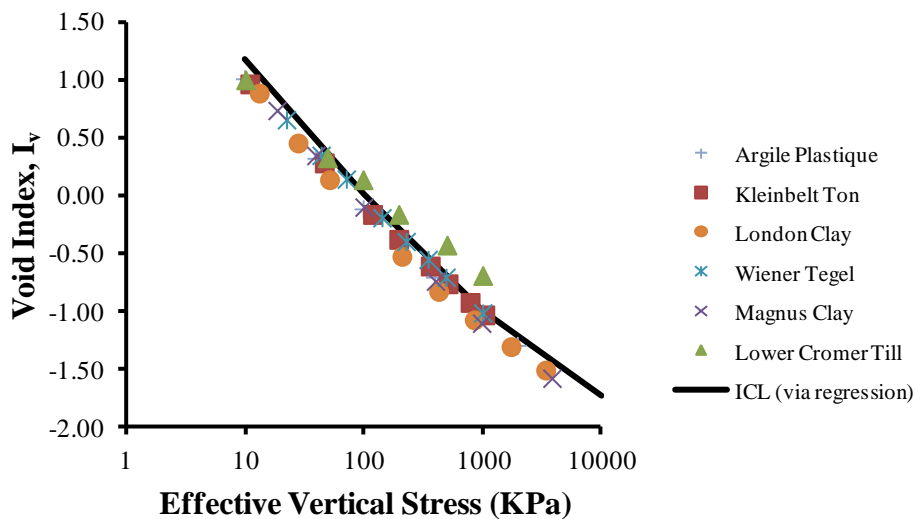


Figure 2-4: Compression curves for the clays in Figure 2.1 normalised to obtain the Intrinsic Compression Line, or ICL (cf Burland, 1990).

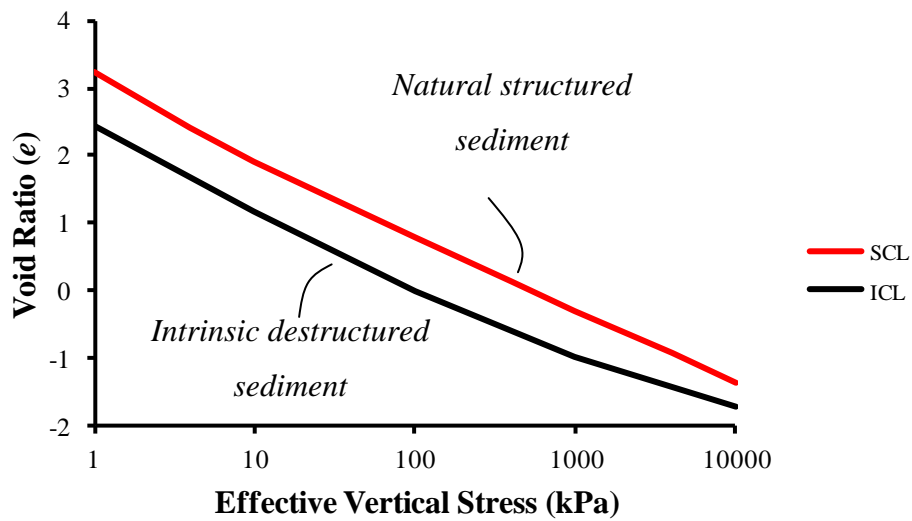


Figure 2-5: Typical compression lines for a natural and destructured specimen. Note that the natural sample can sustain a higher void ratio for a given effective vertical stress.

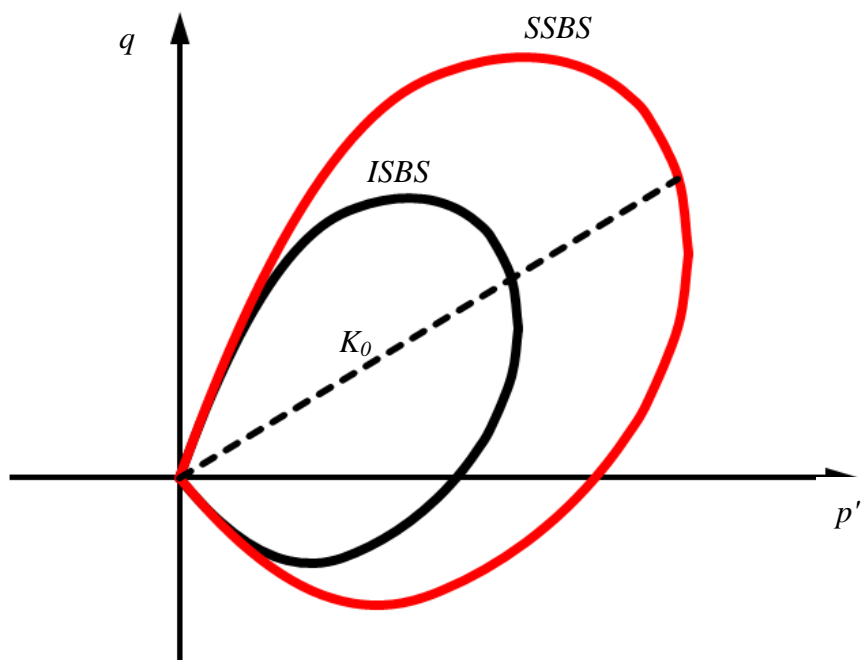


Figure 2-6: Conceptual model of Intrinsic State Boundary Surface (ISBS) and Structured State Boundary Surface (SSBS). The state boundary surface for the structured material is larger than the equivalent destructured specimen, reflecting the influence of sedimentation and post sedimentation processes.

2.2 Processes that Influence the Level of Structure

A great deal is now known about the nature of structure in sediments, how it affects the behaviour of the sediment, and also factors which encourage development of structure. Some of the principal processes affecting structure are discussed in this Section.

2.2.1 Depositional Environment

A common form of sedimentation structure is that which is formed due to the nature of the depositional environment. For example, flocculation or an inefficient packing of particles can lead to an open and *metastable* fabric. Quick clays are an example of sediments that feature this type of structure. Quick clays can be highly sensitive and the fabric can be very unstable. This behaviour has been shown experimentally using structure-sensitive kaolinite (Mitchell and Soga, 2005). In these studies samples were prepared following one of two methods. The first method was sedimented using a static compaction method in which the sample retained an open, flocculated structure. The second method involved kneading the sample; the high shear strains associated with this process allowed for the removal of any structure. On testing of the two samples, the behavioural response exhibited in stress-strain curves was remarkably different as shown in Figure 2-7. Comparison of the response of the samples shows that:

- 1 The peak strength for the sample with a flocculated structure is over five times greater than that of the kneaded sample.
- 2 The residual strength of the samples is almost identical i.e. the flocculated structure of the static compaction sample is completely destroyed via shearing.
- 3 The recoverable deformation, i.e. elastic deformation, of the flocculated structure sample at small strains is high, ranging between 60 and 90 percent. Conversely, the elastic response of the kneaded samples is confined to only 15 to 30 percent of the total deformation at peak load.
- 4 The samples illustrate the much greater ability of the braced-box type of fabric that remains after static compaction to withstand stress without permanent deformation than is possible with the destructured fabric associated with kneading.
- 5 Failure of the structured samples is brittle compared to the ductile response of the non-structured samples. The loss of strength in the structured case is dramatic post yield.
- 6 Macro-fabric also influences the strength of clays (Mitchell and Soga, 2005). Experiments

on the Bothkennar clay show that samples with mottled facies, in which the bedding features have been disrupted and mixed by burrowing molluscs and worms (bioturbation), are stronger and stiffer than samples with distinct bedding or laminated features. Laminated samples show the softest response, though typically the strength of laminated specimens is highly dependent on the direction of loading relative to the laminations. This is shown in Figure 2-8.

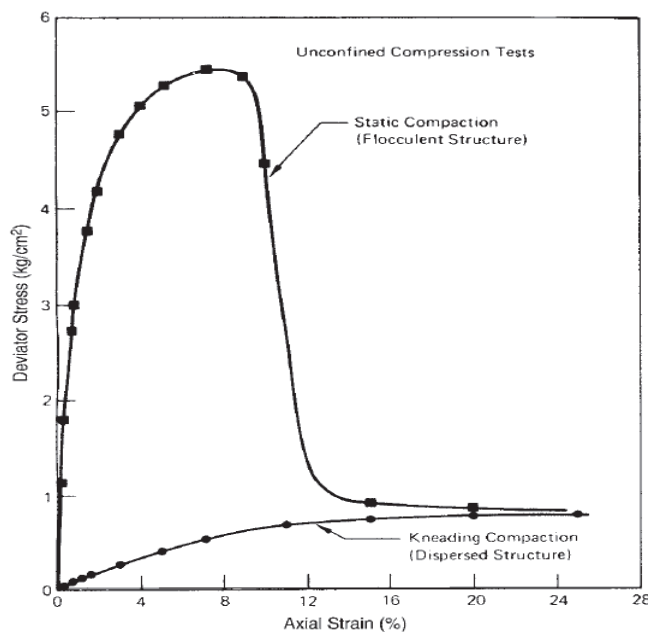


Figure 2-7: Stress-strain behaviour of kaolinite compacted by static and kneading methods (Mitchell and Soga, 2005). Note that when subject to sufficiently large axial strains the samples tend to the same residual strength, reflecting the intrinsic state.

Prior to this the strengths and result deformation styles are markedly different.

2.2.2 Weathering

Weathering processes change the types and relative proportions of ions in solution, which, in turn, can alter the flocculation–deflocculation tendencies of the soil after disturbance. Some change in the undisturbed strength is also probable; however, the major effect on sensitivity is usually through change in the remoulded strength. Strengths and sensitivities may be increased or decreased, depending on the nature of the changes in ionic distributions (Chandler and Apted, 1988; Cafaro and Cotecchia, 2001).

Nova et al., (2003) has incorporated sediment degradation due to weathering into various constitutive models. In this work the influence of weathering on bonded geomaterials is explored under K_0 conditions for normally consolidated and overconsolidated materials. The

authors note the complexity and variable nature of weathering processes e.g. time of exposure, temperature, intensity of chemical attack. As such in the formulation these factors are assumed to be approximated by a single scalar variable (X_d) in the range 0 to 1 whose value represents the transition between a fully bonded and cohesionless material. Though this is a fairly straightforward approach and the complicated processes are approximated by a time dependent scalar variable, comparison between numerical simulations and experimental data presented by the authors is generally favourable. Similar approaches have been taken by other researchers when considering the water-weakening characteristics of chalks (Hickman, 2004).

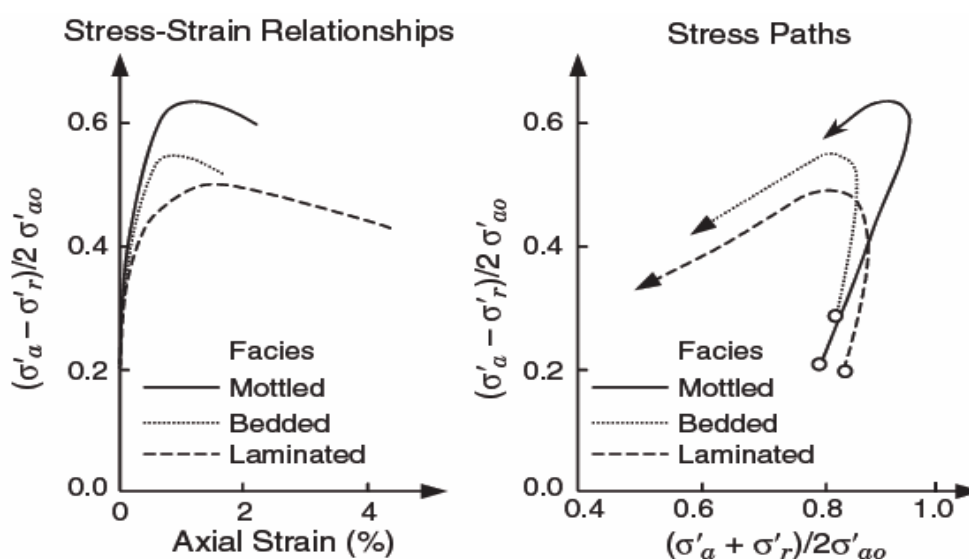


Figure 2-8: Effect of macro-fabric on undrained response of Bothkennar Clay (Mitchell and Soga, 2005). Note the strength variation in the different samples depending on whether they exhibited mottled, bedded or laminated facies.

2.2.3 Thixotropic Hardening

Thixotropy is an isothermal, reversible, time-dependent process occurring under conditions of constant composition and volume whereby at rest a material stiffens but softens or liquefies upon remoulding, as displayed in Figure 2-9. Thixotropic hardening may account for low to medium sensitivity and for a part of the sensitivity of quick clays.

Thixotropic hardening occurs when remoulding results in a lack of equilibrium of the inter-particle forces. If the inter-particle force balance results in attraction that is in excess of repulsion, there will be a tendency toward flocculation of particles and particle groups and for reorganization of the water-cation structure to a lower energy state. Both effects, which have

been demonstrated experimentally, take time because of the viscous resistance to particle and ion movement. The effect of time after disturbance on the pore water pressure has been shown to be particularly significant. The importance of thixotropic hardening in contributing to the sensitivity of clay in the field is impossible to determine as the initial state of a clay deposit in nature is usually far different than at the present time, and the history of an undisturbed clay bears little resemblance to that of a remoulded sample. The results of studies on samples allowed to harden starting from present composition, however, suggest that sensitivities up to approximately 8 may be possible due to thixotropy.

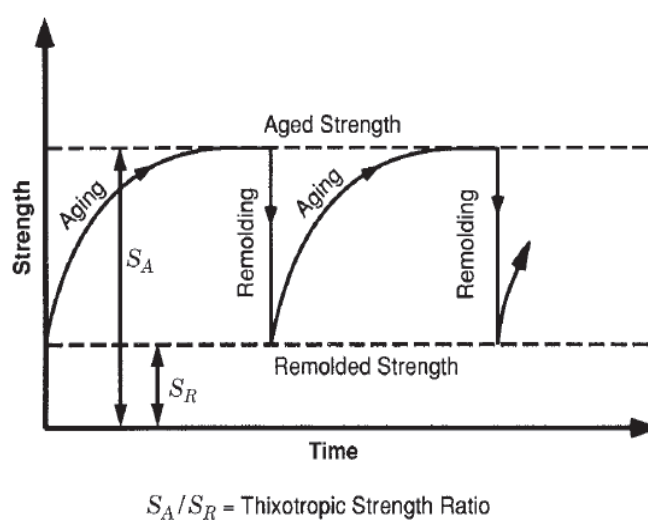


Figure 2-9: Modification of material strength due to thixotropy, (Mitchell and Soga, 2005).

2.2.4 Creep

Creep is a time-dependent mechanism that occurs in many soils and soft-rocks and is not ascribed to changes in effective stress resulting from dissipation of pore fluid i.e. conventional consolidation. Creep is related to volume change over time due to particle-readjustment at nearly constant effective stresses (Wood, 1990). Defining specific creep mechanisms can be difficult, and depending on the lithology creep may be related to various sub-processes such as sub-critical crack growth, pressure-solution creep etc.

In general, creep in soft rocks is dependent on a number of factors;

- 1 The nature of the sediment - mineral composition (clay content), microstructural characteristics, and state of lithification all influence creeping behaviour.

-
- 2 Material state and stress conditions - the stress state relative to the state boundary surface will govern whether creep in shear or compactional creep are observed, and creep is known to be highly sensitive to the rate of loading e.g. in chalks (Omdal, 2010).
 - 3 Environmental conditions - Pore fluid chemistry and temperature can control creep behaviour.

Figure 2-10 and Figure 2-11 show the influence of a *creep stage* in a hydrostatic compaction test at various loading rates on Lixhe chalk (De Gennaro et al., 2003), and an oedometer test on a remoulded clay (Burland, 1990) respectively. If the stresses are held constant, volume loss is still observed to be taking place and this is attributed to creep. Once the specimens are reloaded it is clear that they do not follow the same path as the standard tests. Instead, the newly derived structure from the creeping phase means that the specimens are able to withstand larger imposed stresses for the same porosity/void ratio. Eventually, at a critical value of imposed vertical effective stress the structure is broken down and tends back to the same curve as the standard test. It should be noted that the curve post-yield is far steeper than for the standard test reflecting more dramatic volume loss with increasing stress (higher compression index, λ). It is also important to also stress that like many of the other processes discussed, creep over geological time remains poorly understood. Typically creep experiments run for periods of several months and in some cases may run in excess of a year (Gasc-Barbier et al., 2004). Targeting claystones and mudstones for use as host strata for HLW disposal, e.g. Opalinus Clay and Boom Clay in Belgium and Switzerland (Dehandschutter et al., 2004, 2005; Corkum and Martin, 2007; François et al., 2009), has necessitated the use of extended creep testing. This is driven by the need to isolate the waste material for prolonged periods of time, often of the order of hundreds of thousands of years, and hence develop predictive modelling tools that can describe the long term behaviour of the sediment. However, clearly some extrapolation will be necessary in order to bridge the divide between the behaviour of the sediment as observed over several decades and behaviour over geological time, with obvious uncertainty in the relationship between these two end members.

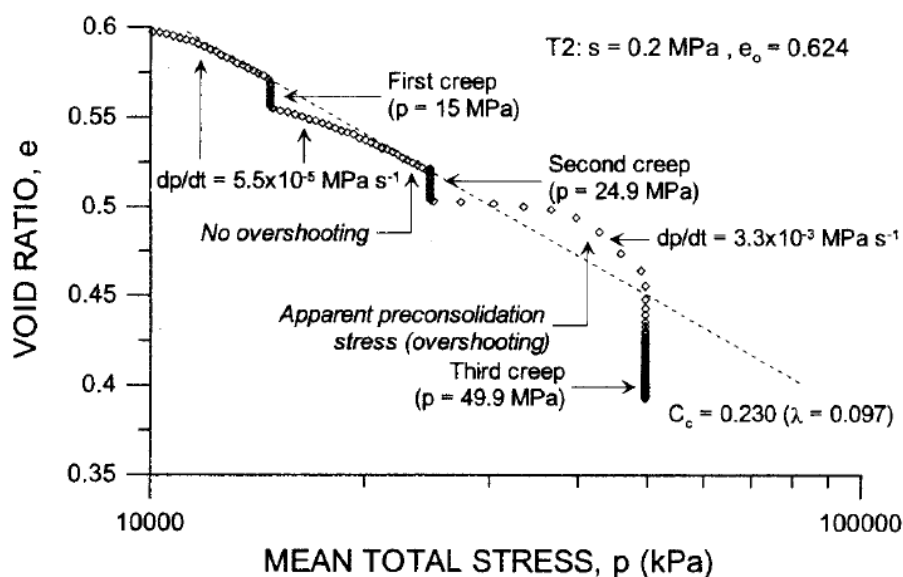


Figure 2-10: Hydrostatic Compaction of a chalk with creep stages (De Gennaro et al., 2003). Note that volume change continues to take place at constant mean stress during the creep stages.

2.2.5 Cementation

Many soils and rocks contain carbonates, iron oxide, alumina, and/or organic matter that may precipitate at interparticle contacts. This acts to reinforce the solid matrix and cement the material (or particles). On disturbance, the cemented bonds may be destroyed and lead to a loss in material strength. The loss in material strength is typically realised through a marked reduction in the cohesion, attributed to the rupture of cemented interparticle bonds. Whereas uncemented specimens might display diffuse compactive behaviour, high levels of cementation are associated with very brittle failure, as demonstrated in testing on sands in Figure 2-12 (Leroueil and Vaughan, 1990). In this example the elastic behaviour is seen to also vary as a function of cementation level, with the 4% cementation sample exhibiting stiffer behaviour in the elastic regime.

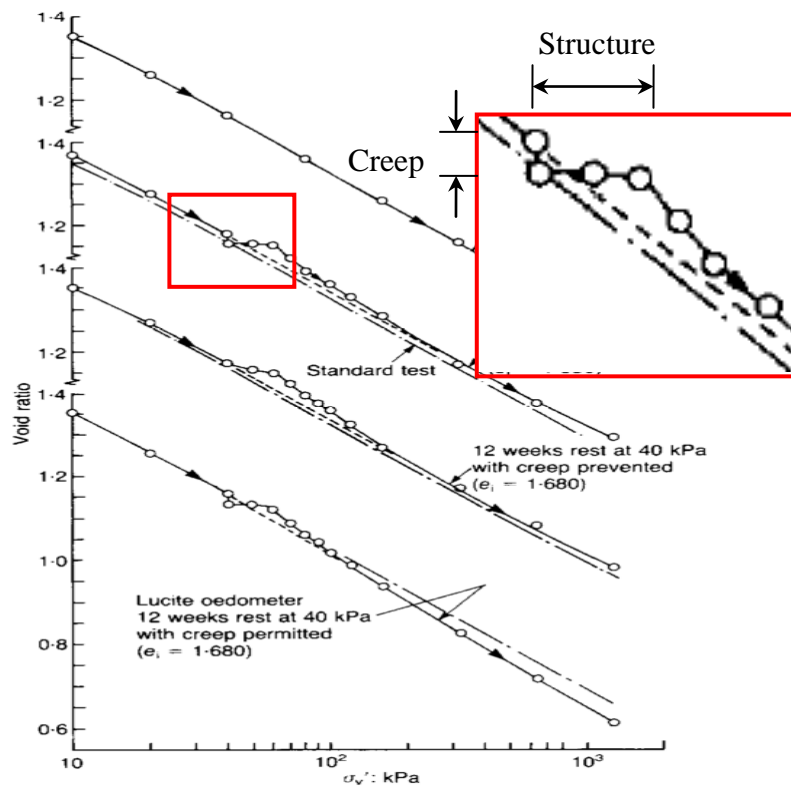


Figure 2-11: Effect of creeping phases on soil structure (cf, Burland, 1990). Note that volume change continues when the stresses are held constant due to grain slippage and rotation. The material fabric is different after the creep stage which is reflected in the higher yield stress attained before resumed consolidation.

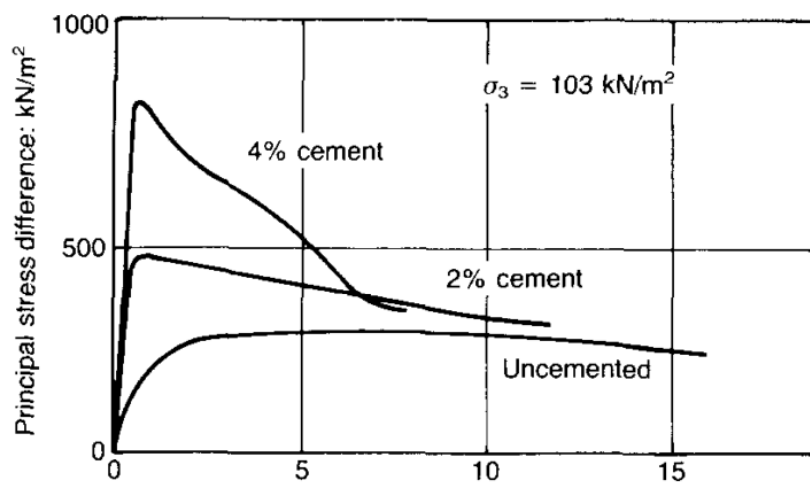


Figure 2-12: Behaviour of cemented and uncemented sands (Leroueil and Vaughan, 1990).

Horpibulsuk et al., (2010) investigated the behaviour of cemented clays during the development and testing of a Structured Modified Cam Clay (SMCC) material model. The following observations were made:

- 1 Due to the effect of the cementation structure, the voids ratio of the clay with the same mineralogy in a cemented state is generally much higher than that of natural clay. During yielding, breakdown of the cementation takes place, and the ability of the sample to maintain the higher voids ratio changes as cementation structure decreases. However, quantitatively speaking, for high-water-content clay, the additional voids ratio sustained by the cementation structure is much higher than that sustained by the natural soil structure. The breakup rate of the cementation in cemented clay is generally higher than that of naturally structured clay, which is indicated by the larger compression index, λ .
- 2 The size of the initial yield surface and the tensile strength of cemented clay increases with cementation bond strength. Due to the effect of cementation, the cemented clay mainly exhibits the elastic behaviour when the stress state is inside the state boundary surface.
- 3 The resistance to elastic deformation and the yield stress increase with cementation bond strength, which is shown by the lower swelling index, κ . In other words, the greater the degree of cementation, the higher the virgin yield compression index, λ . This is due to the sudden breakdown of the cementation bonds for high cementation bonding.
- 4 Strain softening behaviour is seen for cemented clay that is loaded at various positions both inside and on the yield surface. This is attributed to the crushing of the soil-cementation structure. This feature of strain softening behaviour of cemented clay occurs when loaded inside the yield surface and is caused by interlocking, which is due to the dismembering of clay clusters.
- 5 A comparison of the shear behaviour of cemented clay to that of natural clay shows that the final strength of cemented clay, both in terms of the shear stress and the shear stress ratio, is generally higher than that of natural clay.
- 6 It appears the variation in mechanical properties of cemented clay is basically isotropic.

These observations are typical of the response of cement derived structure. The key points are the higher compression index on yielding, increased resistance to permanent deformation and

strain softening response post-yield. It would seem that some clays and mudstones can have a substantial sensitivity that is attributed to cementation. For example, Sangrey (1972) investigated four naturally cemented Canadian clays which have sensitivities of between 45 and 780. Additionally, studies of a late glacial plastic clay revealed a sensitivity of between 70 and 80 (Bjerrum and Wu, 1967). As such very large differences may exist in the relative strengths of the natural material and the remoulded material (intrinsic state) due to the presence of cementation structure.

2.2.6 Diagenesis

Diagenetic processes can be complicated and may occur at a variety of depths. Diagenetic reactions are sensitive to factors such as pore fluid chemistry and the composition of the sediment, however many diagenetic processes are found to be principally kinetically driven and very strongly dependent on temperature gradients. These processes can be closely linked to cementation, particularly if a phase of the diagenetic reaction is concerned with the precipitation of minerals at grain contacts.

2.2.6.1 Sandstones (Diagenetic)

Sandstones that are well sorted do not compact much under static loading and consequently may have similar properties at depths of 2500-3000m. At higher temperatures (>120°C) corresponding to depths exceeding 3500m Quartz cementation may occur. In this process dissolution and precipitation may occur at Quartz-Quartz grain contacts or at Stylolites (Bjørkum et al., 1998). Diagenetic factors do not usually affect sandstones strongly until they are buried to quite substantial depths (in excess of 2km) although carbonate cementation can have an influence on behaviour and is quite common at shallow depths.

2.2.6.2 Carbonates (Diagenetic)

Behaviour of carbonates is known to be strongly dependent on the nature of near surface processes (Tucker and Wright, 1990). The wide variety of early diagenetic processes that effect carbonate sediments has made modelling them in a quantitative sense difficult. Some of the early processes can include;

- 1 Dissolution of aragonite and magnesian calcite.
- 2 Precipitation of low-Mg calcite.
- 3 Dolomitization.

The large volumes of material that can be added or removed in these processes can exert a strong influence on the mechanical behaviour of the sediment during early burial. For example, a recent study performed by Croizé et al., (2010) has revealed the impact of early carbonate diagenesis. The study focuses on the testing of eleven limestones and five dolostones cored at shallow depths of between 39 and 365 mbsf. The sediments are inferred to have been deposited as loose bioclastic grains and mud in shallow paleo-water depths estimated to have been less than 100m deep. K_0 testing of the samples was performed to applied vertical stresses of 50MPa and the results are shown in Figure 2-13. Of note is that the majority of samples remain elastic for the duration of the test which is attributed to a stable structure developed by the early diagenetic processes, with an associated high level of overconsolidation and low compressibility. An important point here is that mechanical compaction will not be the main process of porosity reduction until the samples reach vertical stresses as high as 50MPa. This would equate to at least 4km burial depth.

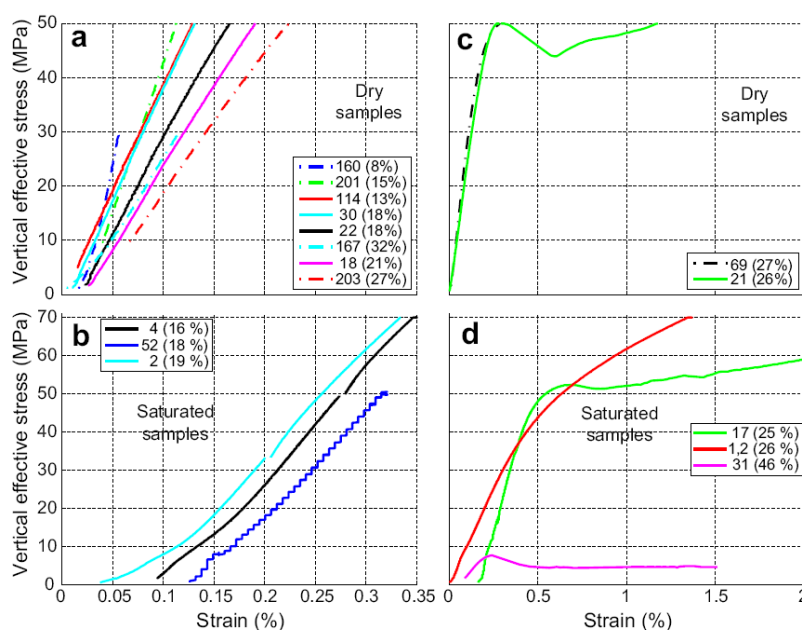


Figure 2-13: Response of Carbonate samples in K_0 testing (Croizé et al., 2010). Note how samples do not yield and respond elastically to very high vertical stresses.

2.2.6.3 Mudstones, Claystones and Shales (Diagenetic)

The diagenetic processes relating to the lithification and structure modification of mudstones is of specific interest to this study, particularly those occurring at relatively shallow depths. It is suggested that the compaction behaviour of mudrocks may be described adequately using traditional soil mechanics theory for burial up to depths between 2000m and 3000m (Pouya et

al., 1998). However, it is also noted that this assumption can only realistically be made for mudstones that do not have high carbonate and silica contents. In general, mudstone diagenesis is divided into early and late stage processes. Late stage processes generally occur at substantial depth and are related to clay minerals becoming unstable. The abundance of clay minerals is dependent on factors such as depositional environment, climate and the contribution of early diagenetic processes.

Some of the principal late stage diagenetic reactions are;

- 1 The smectite-illite transformation which normally takes place at temperatures greater than 65°C (Worden et al., 2005). This reaction is dependent on the supply of K⁺ ions as well as other factors and can consequently occur over a wide temperature range.
- 2 Kaolinite transforms to illite or chlorite when K-feldspar is present at depths of between 3 and 4km, corresponding to temperatures between 130 and 140°C.
- 3 Chlorite occurs mostly as a minor part of the present clay minerals and may be authigenically formed from kaolinite or smectite in deeply buried sediments.

Assessment of shallow diagenetic processes affecting clays and mudstones are arguably more important to study due to the fact that much evidence points firmly to PFS formation within the first kilometre of burial. Shallow diagenetic processes affecting mudstones include;

- 1 Opal A/CT transformation (Williams and Crerar, 1985) where dissolution of amorphous Opal (A) takes place and is re-precipitated as cristobalite and tridymite (CT) or Chert. This reaction is known to take place in depths of only a few hundred metres and can be activated at temperatures of 17°C or lower (Matheney and Knauth, 1993). This reaction is enhanced in carbonate-rich sediments.
- 2 Quartz cementation can occur at depths of around 1000m. Sources of quartz cement precipitation include reactions between clay minerals and dissolution of Opal A.
- 3 Carbonate dissolution and cementation can take place at low burial depths and create a stiff matrix prior to any significant mechanical compaction. Carbonates may have a clastic origin but may also be biologically derived.

An example of the influence of early diagenetic influences is seen in the difference between Kimmeridge Westbury Clay (KWC) and Kimmeridge Bay Clay (KBC). These two clays are thought to have essentially the same origin but have very different properties (Nygård et al.,

2004). KWC is a fossil rich clay with a porosity of 0.5, an estimated maximum burial depth of 0.5km, and a low strength (no discernible pre-consolidation strength). Conversely, KBC is a laminated shale buried to somewhere between 1.7 and 3.0km (so likely exposed to temperatures in excess of 80°C) with a porosity of around 0.2. KBC displays very stiff behaviour as shown in Figure 2-14. Exposing KWC to stresses similar to those experienced by KBC in K_0 testing reveals that KWC has a significantly higher porosity, see Figure 2-14. At a depth of approximately 2000m burial, KWC has porosity nearly 13.5% higher. This difference is attributed to the modification of KBC during burial diagenesis.

2.2.6.4 Microbial Activity

It is also worth noting that a host of diagenetic reactions are controlled by microbial activity (Parkes et al., 2000). These processes include denitrification, methanogenesis, iron reduction and sulphate reduction. Many of these processes are commonly identified in sediments on continental slope and shelf settings. Sulphate reduction in particular may lead to carbonate precipitation and dolomitization. The carbonate is derived from the microbial mineralisation of organic matter (Raiswell and Fisher, 2004). Sulphate reduction is thought to be sensitive to sedimentation rate, with sediments deposited rapidly exhibiting faster removal rates of Ca^{2+} and hence more rapid precipitation of cements. The study by Raiswell and Fisher (2004) however does indicate that in some wells there is an inconsistency between the expected weights of calcite and dolomite in samples and the presence of carbonate concretions.

Therefore, in some cases, alternative factors may influence the rate of the sulphate reduction, or a depositional hiatus may allow more time for the formation of cements. The cementing effect of the carbonate may lead to an apparent overconsolidated initial state and influence the behaviour of the sediment both before and after yield.

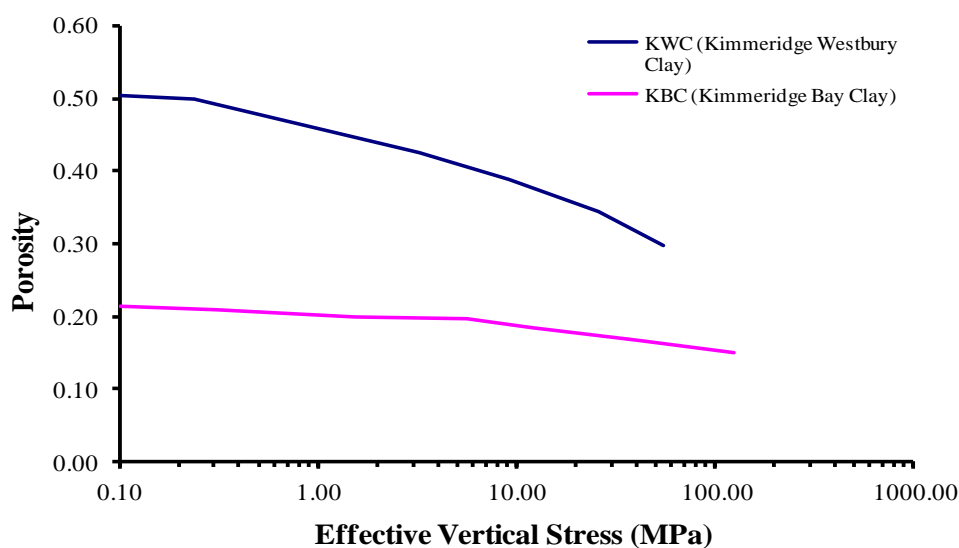


Figure 2-14: Comparison of K_0 testing on Kimmeridge Bay and Kimmeridge Westbury Clays. Note that for the same vertical stress there is a large difference in porosity of the two samples.

2.3 Summary

This chapter has aimed to discuss briefly the influence of structure and post-sedimentation processes on the evolutionary behaviour of geomaterials. Understanding the complex behaviour of these materials is critical for the appraisal of possible scenarios that might lead to the genesis of polygonal faults. This is due to the fact that there is a likely constitutive control on the formation of PFS, and this point was emphasised in Chapter 1.

2.3.1 Key Points

Some of the key discussion points of the chapter are highlighted below;

- 1 The behaviour of soils and soft rocks in compaction and shear can in many cases not be satisfactorily described when only the mechanical behaviour is considered.
- 2 Traditionally only depositional porosity and subsequent modification during burial are considered. The use of empirical relationships used to constrain porosity-depth trends can be useful in identifying instances where other processes may be significant.
- 3 Processes that affect the structure of the soil are thought to be as important as stress history and depositional porosity. These processes have been shown to be diverse and may

operate over a wide range of depths and physio-chemical conditions.

- 4 The process of assessing the level of structure has been discussed.
- 5 A selection of individual structure modifying mechanisms have been reviewed. These have included the nature of the depositional environment, creep and diagenesis. All were shown to result in marked differences in sediment behaviour via their influence on sediment stiffness and the failure characteristics.

2.3.2 Relevance to PFS Genesis

It is interesting to seek some connections between PFS genesis, as discussed in Chapter 1, and the structure modifying mechanisms discussed in this chapter. Table 2-1 and Table 2-2 provide a concise summary of some of the PFS features observed globally, and are modified after Cartwright and Dewhurst (1998).

Location	Age	Tier Type	Dominant mineralogy
St Georges Bank	Middle/upper Miocene	Claystone	Smectite
New Jersey	Middle Eocene to Pliocene	Claystone	Illite/Kaolinite
West of Shetland	Middle Eocene/lower Pliocene	Claystone	Illite-Smectite
Carpentaria Basin	Cretaceous and Tertiary	Claystone	Undifferentiated Clay
Mount Isa Basin	Tertiary	Claystone	Undifferentiated Clay
Bass Basin	Oligocene to Miocene	Claystone	Undifferentiated Clay
Namibia	Tertiary	Claystone	Undifferentiated Clay
Orange Basin	Turonian to Paleocene	Claystone	Undifferentiated Clay
Venture Basin	Tertiary	Claystone	Undifferentiated Clay
Southeast Africa	Late Senonian	Claystone	Smectite
Eromanga Basin	Cretaceous	Claystone	Smectite
North Sea Basin	Eocene to Oligocene	Claystone	Smectite
Voring Basin	Mid Oligocene to Pliocene	Biogenic	Biogenic Silica
Goban Spur	Mid to late Eocene	Biogenic	CaCO ₃ (30% clay at base)
Hatteras Basin	Mid to late Eocene	Biogenic	CaCO ₃ /silica
New Jersey	Eocene	Biogenic	CaCO ₃ /silica
Challenger Plateau	Eocene to middle Miocene	Biogenic	CaCO ₃
Rockall Trough	Lower Miocene to Pliocene	Biogenic	CaCO ₃ /clay
Hatton-Rockall Basin	Upper Eocene to mid Pliocene	Biogenic	CaCO ₃
Exmouth Plateau	Paleocene to lower Eocene	Biogenic	CaCO ₃
Chatham Rise	Miocene to Pliocene	Biogenic	CaCO ₃
Deep Ivorian Basin	Lower Oligocene/lower Miocene	Biogenic	CaCO ₃ /Opal CT

Table 2-1: Summary of characteristics of PFS from around the globe, Part 1 (Cartwright and Dewhurst, 1998). Note sediments are exclusively claystones or biogenic mudstones/chalks.

Modification of Structure in Soils and Soft Rocks

As was discussed in Chapter 1, the tiers almost exclusively contain very fine-grained claystones, biogenic mudstones and nano-fossil chalks. There are some important observations to be made from this data set. The depositional environments are predominantly hemipelagic or pelagic and associated with low sedimentation rates. To the authors knowledge there are no known PFS observed in fine grained sequences from seismic data sets in the shallow Gulf of Mexico, where deposition of mudstones is thought to have proceeded at a much higher rate than those listed in Table 2-2 (Rowan and Weimer, 1998) and there is wide discussion regarding the extent of non-mechanical alteration of such sediments.

Location	Min depth (mbsf)	Max depth (mbsf)	Depositional Environment	Min sed. rate (m/My)	Min sed. rate (m/My)	Min porosity	Max porosity
St Georges Bank	100	940	Hemipelagic	2	200	45	60
New Jersey	200	1500	Hemipelagic	12	109	50	
West of Shetland	113	413	Hemipelagic	6.3	56	50	70
Carpentaria Basin	400	800	Hemipelagic		Low		
Mount Isa Basin	400	1000	Hemipelagic		Low		
Bass Basin	700	1000	Restricted Marine		Low		
Namibia	0	1000	Marine slope		50		
Orange Basin	200	800	Open Marine	N.D.	N.D.		
Venture Basin	400	600	Pelagic	N.D.	N.D.		
Southeast Africa	500	600	Hemipelagic	11	54		
Eromanga Basin	50	1500	Pelagic		20		
North Sea Basin	500	1500	Slope/basin floor	5	100	30	50
Voring Basin	100	1000	Hemipelagic		100	50	60
Goban Spur	27	278	Pelagic	2	15	40	60
Hatteras Basin	590	950	Pelagic		51	40	60
New Jersey	1000	1500	Hemipelagic	30	109	47	60
Challenger Plateau	250	650	Pelagic	5	110	51	57
Rockall Trough	100	800	Pelagic	46	51	58	70
Hatton-Rockall Basin	70	700	Pelagic		40	40	
Exmouth Plateau	317	811	Pelagic	2	20	35	62
Chatham Rise	200	500	Pelagic	26	120	55	
Deep Ivorian Basin	208	350	Pelagic		25	60	70

Table 2-2: Summary of characteristics of PFS from around the globe, Part 2 (Cartwright and Dewhurst, 1998). Note the tiers are within the first kilometre of burial and were very slowly deposited.

Specifically, laboratory testing appears to suggest that the influence of post-sedimentation processes is not as profound in some Gulf of Mexico sediments. This highlights the possibility that the nature of the depositional environment, and hence the early development of structure could be a control on PFS genesis. Equally this observation could be suggestive

of a diagenetic trigger for PFS genesis, as it was noted that the depositional fabric could exert a control on early and burial diagenesis. This might be reinforced by the fact that the review of diagenesis highlighted the broad range of early processes that effect mudstones and carbonates in particular. On the other hand coarser grained facies such as sandstones, which are not known to host PFS, are typically less susceptible to shallow diagenetic processes. The discussion on the possibility of microbial influence is also interesting as this also suggests that these are sensitive to lower rates and or depositional hiatuses, and therefore compatible with conditions reported in many PFS.

2.3.3 Suggested Approach

The mechanisms known to influence structure are summarised in Figure 2-15. Also displayed are the suggested mechanisms for PFS development. It is clear that diagenesis is known to both modify the structure and behaviour of sediments, and is also a suggested candidate for triggering PFS genesis.

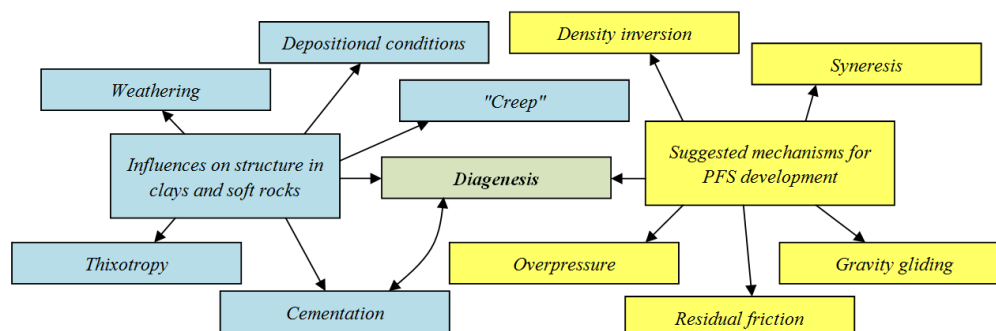


Figure 2-15: Assessment of criterion for structure development and PFS formation.

Given this link, and growing evidence suggesting a more intimate relationship between PFS and shallow diagenesis, it is suggested that the triggering of polygonal fault genesis via these reactions is investigated in this thesis. The following chapter will be therefore concerned with describing the methodology that will be adopted in testing the diagenetic hypothesis, via introducing the key components of computational forward modelling and geomaterial characterisation.

2.4 References

- Athy, L. F., 1930, Density, porosity, and compaction of sedimentary rocks: AAPG Bulletin, v. 14, p. 1–24.
- Baldwin, B., and C. O. Butler, 1985, Compaction Curves: AAPG Bulletin, v. 69, no. 4, p. 622–626.
- Bjerrum, L., and T. H. Wu, 1967, Fundamental Shear-Strength Properties of the Lilla Edet Clay: *Géotechnique*, v. 10, p. 101–109.
- Bjørkum, P. A., E. H. Oelkers, P. H. Nadeau, O. Walderhaug, and W. M. Murphy, 1998, Porosity Prediction in Quartzose Sandstones as a Function of Time, Temperature, Depth, Stylolite Frequency, and Hydrocarbon Saturation 1: AAPG Bulletin, v. 82, no. 4, p. 637–648.
- Burland, J. B., 1990, On the compressibility and shear strength of natural clays: *Géotechnique*, v. 40, no. 3, p. 329–378.
- Burland, J. B., S. Rampello, V. N. Georgiannou, and G. Calabresi, 1996, A laboratory study of the strength of four stiff clays: *Géotechnique*, v. 46, no. 3, p. 491–514.
- Cafaro, F., and F. Cotecchia, 2001, Structure degradation and changes in the mechanical behaviour of a stiff clay due to weathering: *Géotechnique*, v. 51, no. 5, p. 441–453.
- Cartwright, J. A., and D. N. Dewhurst, 1998, Layer-bound compaction faults in fine-grained sediments: *Geological Society of America Bulletin*, v. 110, no. 10, p. 1242–1257.
- Chandler, R. J., and J. P. Apter, 1988, The effect of weathering on the strength of London Clay: *Quarterly Journal of Engineering Geology*, v. 21, p. 59–68.
- Corkum, A. G., and C. D. Martin, 2007, The mechanical behaviour of weak mudstone (Opalinus Clay) at low stresses: *International Journal of Rock Mechanics and Mining Sciences*, v. 44, no. 2, p. 196–209.
- Cotecchia, F., and R. J. Chandler, 2000, A general framework for the mechanical behaviour of clays: *Géotechnique*, v. 1, no. 4, p. 431–447.
- Croizé, D., S. N. Ehrenberg, K. Bjørlykke, F. Renard, and J. Jahren, 2010, Petrophysical properties of bioclastic platform carbonates: implications for porosity controls during burial: *Marine and Petroleum Geology*, v. 27, no. 8, p. 1765–1774.
- Dehandschutter, B., S. Vandycke, M. Sintubin, N. Vandenberghe, P. Gaviglio, J.-P. Sizun, and L. Wouters, 2004, Microfabric of fractured Boom Clay at depth: a case study of brittle–ductile transitional clay behaviour: *Applied Clay Science*, v. 26, no. 1-4, p. 389–401.

-
- Dehandschutter, B., S. Vanduycke, M. Sintubin, N. Vandenberghe, and L. Wouters, 2005, Brittle fractures and ductile shear bands in argillaceous sediments: inferences from Oligocene Boom Clay (Belgium): *Journal of Structural Geology*, v. 27, no. 6, p. 1095–1112.
- François, B., L. Laloui, and C. Laurent, 2009, Thermo-hydro-mechanical simulation of ATLAS in situ large scale test in Boom Clay: *Computers and Geotechnics*, v. 36, no. 4, p. 626–640.
- Gasc-Barbier, M., S. Chanchole, and P. Bérest, 2004, Creep behavior of Bure clayey rock: *Applied Clay Science*, v. 26, no. 1-4, p. 449–458, doi:10.1016/j.clay.2003.12.030.
- De Gennaro, V., P. Delage, Y. J. Cui, C. Schroeder, and F. Collin, 2003, Time-dependent behaviour of oil reservoir chalk: A multiphase approach: *Soils and Foundations*, v. 43, no. 4, p. 131–147.
- Hickman, R. J., 2004, Formulation and Implementation of a Constitutive Model for Soft Rock: Virginia Polytechnic Institute and State University, p. 424.
- Horpibulsuk, S., M. D. Liu, D. S. Liyanapathirana, and J. Suebsuk, 2010, Behaviour of cemented clay simulated via the theoretical framework of the Structured Cam Clay model: *Computers and Geotechnics*, v. 37, no. 1-2, p. 1–9.
- Hudec, M. R., M. P. A. Jackson, and D. D. Schultz-Ela, 2006, The paradox of minibasin subsidence into salt: Clues to the evolution of crustal basins: *Geological Society of America Bulletin*, v. 121, no. 1, p. 201–221.
- Leroueil, S., and P. R. Vaughan, 1990, The general and congruent effects of structure in natural soils and weak rocks: *Géotechnique*, v. 40, no. 3, p. 467–488.
- Matheney, R. K., and L. P. Knauth, 1993, New isotopic temperature estimates for early silica diagenesis cherts: Geological Society, London, Special Publications, v. 21, no. 6, p. 519–522.
- Mitchell, J. K., and K. Soga, 2005, *Fundamentals of Soil Behavior*: John Wiley & Sons, p. 592.
- Nordgård Bolås, H. M., C. Hermanrud, T. A. Schutter, and G. M. Grimsmo Teige, 2008, Is stress-insensitive chemical compaction responsible for high overpressures in deeply buried North Sea chalks?: *Marine and Petroleum Geology*, v. 25, no. 7, p. 565–587.
- Nova, R., R. Castellanza, and C. Tamagnini, 2003, A constitutive model for bonded geomaterials subject to mechanical and/or chemical degradation: *International Journal for Numerical and Analytical Methods in Geomechanics*, v. 27, no. 9, p. 705–732.
- Nygård, R., M. Gutierrez, R. Gautam, and K. Høeg, 2004, Compaction behavior of argillaceous sediments as function of diagenesis: *Marine and Petroleum Geology*, v. 21, no. 3, p. 349–362.

-
- Omdal, E., 2010, The Mechanical Behavior of Chalk under Laboratory Conditions Simulating Reservoir Operations: Unpublished PhD Thesis - University of Stavanger, p. 88.
- Parkes, R. J., B. A. Cragg, and P. Wellsbury, 2000, Recent studies on bacterial populations and processes in subseafloor sediments : A review: *Hydrogeology Journal*, no. 8, p. 11–28.
- Pouya, A., I. Djeran-Maigre, V. Lamoureux-Var, and D. Grunberger, 1998, Mechanical behaviour of fine grained sediments : experimental and three-dimensional constitutive model: *Marine and Petroleum Geology*, v. 15, p. 129–143.
- Raiswell, R., and Q. J. Fisher, 2004, Rates of carbonate cementation associated with sulphate reduction in DSDP/ODP sediments: implications for the formation of concretions: *Chemical Geology*, v. 211, no. 1-2, p. 71–85.
- Rowan, M. G., and P. Weimer, 1998, Salt-Sediment Interaction, Northern Green Canyon and Ewing Bank (Offshore Louisiana), Northern Gulf of Mexico: *AAPG Bulletin*, v. 82 (1998), no. 5, p. 1055–1082.
- Sangrey, D. A., 1972, Naturally cemented sensitive soils: *Géotechnique*, v. 22, no. 1, p. 139–152.
- Tucker, M. E., and V. P. Wright, 1990, *Carbonate Sedimentology*: Wiley, p. 482.
- Williams, L. A., and A. D. Crerar, 1985, Silica Diagenesis, II. General Mechanisms: *Journal of Sedimentary Petrology*, v. 55, no. 3, p. 312–321.
- Wood, D. M., 1990, *Soil Behaviour and Critical State Soil Mechanics*: Cambridge University Press, p. 488.
- Worden, R. H., D. Charpentier, Q. J. Fisher, and a. C. Aplin, 2005, Fabric development and the smectite to illite transition in Upper Cretaceous mudstones from the North Sea: an image Analysis Approach: *Geological Society, London, Special Publications*, v. 249, no. 1, p. 103–114.

Chapter 3

COMPUTATIONAL STRATEGY AND CONSTITUTIVE MODELLING

A key objective identified in the opening chapter was the use of forward numerical modelling as a tool for investigating the genesis and development of polygonal fault systems. This chapter is concerned with providing context to the application of computational modelling via a brief discussion of some of the principal techniques that are commonly adopted in analysing the evolution of geological structures. The key aspects and challenges of using computational modelling technology in the analysis of the formation of geological structures is covered. The computational strategy adopted in this study is reviewed in addition to a discussion of alternative approaches. The constitutive model that is adopted in the study is introduced.

3.1 Methods for Investigating the Formation of Geological Structures

3.1.1 Conventional Approaches

The formation of geological structures reflects extremes of both spatial and temporal scales. This is due to the fact the structures evolve over geological time meaning that typically structures may develop over tens or hundreds of millions of years. Additionally, a single thrust fault may develop over several kilometres, whilst the formation of a passive margin requires examination of the evolution of hundreds of kilometres of the upper crust. Two conventional approaches used to study the evolution of geological structures are now introduced, and their effectiveness at capturing realistic rock deformation is discussed.

3.1.1.1 Bench Scale and Centrifuge Modelling

Bench scale experiments allow for the kinematic, dynamic, and geometric characteristics of the problem to be represented at a reduced scale via the principles of physical similarity. In effect an entire passive margin may be represented by a model approximately one metre in length. Typically brittle materials such as overburden sediments are represented using layers of graded sand. Décollements or layers that exhibit viscous behaviour, such as evaporites or

overpressured muds, are commonly represented by silicone polymer gum (SGM-36). Bench scale modelling has been applied to a large number of scenarios including; salt tectonics (Vendeville and Jackson, 1992a; Schultz-Ela et al., 1993; Guglielmo Jr et al., 1999), extensional regimes (McClay, 1990), and compressional regimes (Dooley et al., 2009; Duerto and McClay, 2009). Conceptual bench-scale modelling is useful as it allows for the real-life scenario to be constrained and uses simple analogue materials. These are advantageous when trying to interpret complex geological scenarios. In some cases the use of physical modelling has served as validation of revolutionary explanations for the presence of some structures, as is the case with reactive salt diapirism (Vendeville and Jackson, 1992a). This is shown in Figure 3-1 where extension of the side walls of a physical modelling allow for the formation of grabens in the brittle sand overburden. This serves to promote so-called reactive diapirism which is driven by the thinning, rotation and subsidence of the overburden, which serves to permit salt movement up-section.

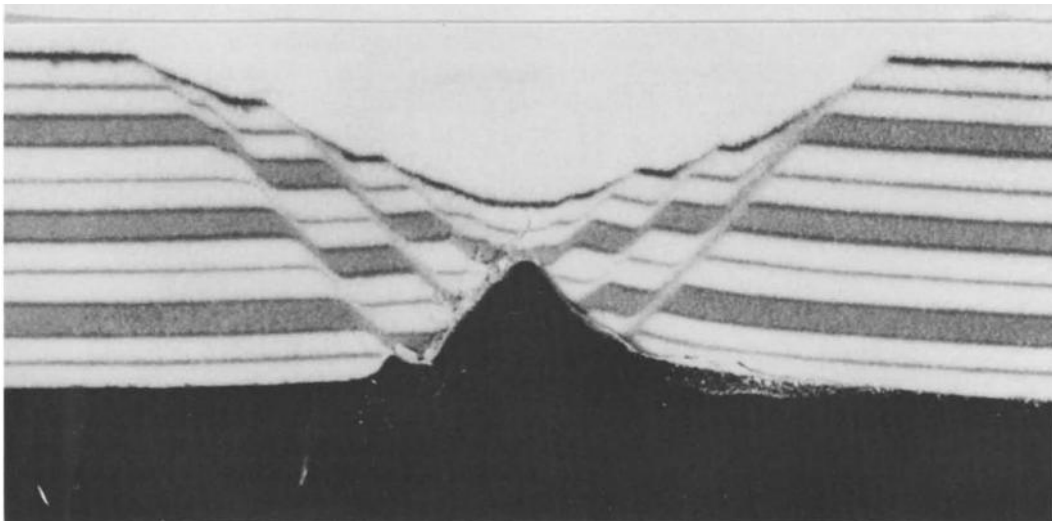


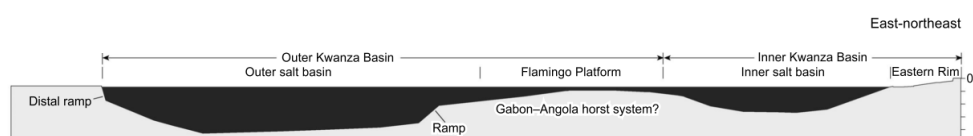
Figure 3-1: Bench scale modelling of reactive diapirism. Taken from (Vendeville and Jackson, 1992b).

Whilst this demonstrates some of the advantages of physical modelling, it is important to note the limitations of this approach. The most significant drawback is that the materials selected to represent the various sediments are very basic and only consider a rudimentary mechanical response. As Chapter 2 noted the deformation of sediments is very complicated and may be influenced by the generation of overpressures, and elevated temperatures may trigger chemical processes which affect the sediment behaviour and hence exerts a control on the formation of structures. Bench scale models are, however, useful in providing boundary

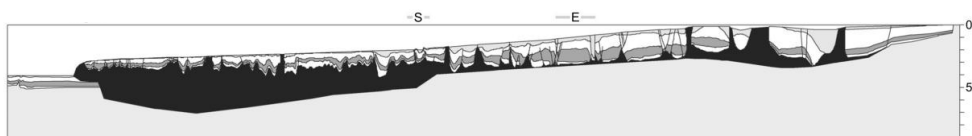
conditions for numerical models to be benchmarked (Crook, Owen, et al., 2006).

3.1.1.2 Kinematic Modelling

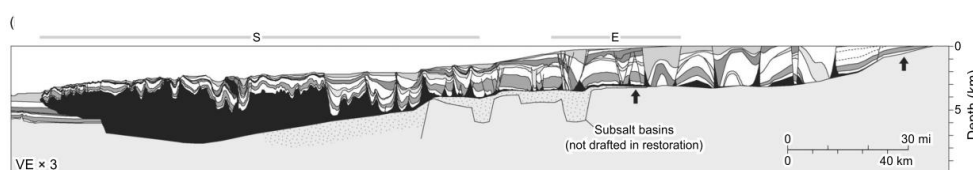
Kinematic techniques are often used to analyse the evolution of geological structures. These approaches attempt to reverse a deformed configuration into its original un-deformed state and have been used at both the local (Erslev, 1991) and regional scales (Hudec and Jackson, 2004), finding application in a range of tectonic regimes. An example of a kinematic restoration can be found in Figure 3-2, where the evolution of a 2D section of the Kwanza Basin, offshore Angola is shown. The simplicity of kinematic techniques has led to them being considered as an invaluable structural analysis tool, particularly in the petroleum industry.



(a) Aptian (120Ma)



(b) End Oligocene (24Ma)



(c) Present Day (0Ma)

Figure 3-2: Regional scale kinematic restoration showing various stages in the evolution of the Kwanza Basin, offshore Angola. Restoration performed using the Geosec restoration software, modified after (Hudec and Jackson, 2004).

Kinematic restorations however are limited by a number of underlying assumptions. The technique relies on the assumption of conserving cross-sectional area (in 2D restorations),

linear elastic constitutive descriptions, and conservation of the line length of folded strata. This leads to a number of undesirable consequences. For example, the cross-sectional area conservation implies that rocks are incompressible, thus ignoring the development of volumetric strains which are pervasive in the subsurface in the form of compaction bands, joints, faults etc (Lovely et al., 2012). The evolution of such features is becoming an area of increasing interest as conventional exploration seeks to recover from more difficult regions, and unconventional resources receive more interest. The consequence of these assumptions is that the description of the constitutive behaviour of rocks in these models is at best crude and ignores their true mechanical response (Gray et al., 2014). Additionally, the methodology of working from present day backwards to a specific point in geological time means that little explanation can be provided of the causative mechanisms that led to development of particular structures.

3.1.2 Suggested Approach for Investigating Polygonal Fault Evolution

The approaches detailed in Sections 3.1.1.1 and 3.1.1.2 have found frequent application in studies of the formation of geological structures. However, as noted these techniques make assumptions about the constitutive behaviour of the sedimentary sequences they seek to model. Chapters 1 and 2 have highlighted that capturing the constitutive behaviour of the sediments within polygonally faulted intervals is likely to be crucial to studying their development.

It is therefore unsurprising that these techniques have not been extensively used in the study of PFS. A study by Victor and Moretti (2006) is an example of a limited number of publications that do use these techniques. The authors focus on bench scale modelling of polygonal fault genesis. Figure 3-3 show the model setup in which a layer of silicone gum is placed on slopes of between 0° and 5° . Graded sand is slowly added to represent the layers within a polygonally faulted sequence. As the ductile silicone begins to spread down-slope a network of polygonal "rafts" begins to develop that closely resembles the polygonal platform geometry noted in many PFS. However, it was noted in Chapter 1 that gravitational spreading is not favoured as a primary mechanism for PFS formation due to the fact that in many cases the faults have formed where regional dips are much less than 1° . As such it is mainly identified as a complementary mechanism that serves to bias polygonal fault orientation.

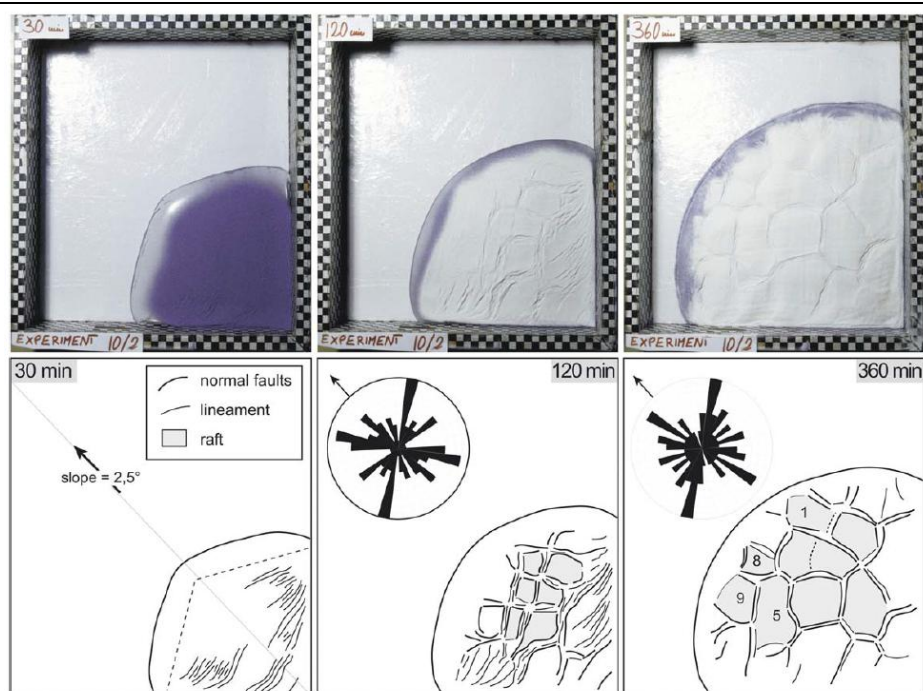


Figure 3-3: Bench scale modelling of polygonal fault genesis. Taken from (Victor and Moretti, 2006).

Given the constraints in some of the conventional modelling approaches, which are reflected in their limited use in the literature relevant to polygonal faults, it is suggested that computational modelling offers an attractive alternative approach. The use of computational modelling to study polygonal faults is explored in the remainder of the thesis.

3.2 Computational Modelling

As computational power has increased there has been an increasing reliance on the use of numerical modelling in the engineering and earth sciences disciplines. The advantage of these techniques is that they can be applied to complicated problems where solutions that do not have trivial or simplistic boundary conditions can be obtained. For example, these problems frequently take the form of Partial Differential Equations (PDE's), where exact solutions are only given in restricted circumstances. Using the methods described below, through a process of spatial and temporal discretisation these equations can often be reduced to a simpler form and may be approximated for a wide variety of boundary or loading conditions, including complex nonlinear behaviour. An in depth discussion of all aspects of this constantly expanding field are well beyond the scope of this thesis, and consequently a concise, uncomplicated discussion that captures some of the key points is offered here.

3.2.1 Potential Frameworks

Computational modelling is a large field of research which offers many possible approaches. Some important aspects to consider are the scale of the problem (resolution), material models that will be included to represent the relevant rock masses, and magnitude and nature of the expected deformation. A more complete review of this subject may be found in various publications (Peric and Crook, 2004; Crook, Willson, et al., 2006; Massimi et al., 2007; Scrofani, 2007) and a complete discussion is beyond the scope of this chapter.

3.2.1.1 The Continuum Approach

The methodology for addressing the problem of geological structure evolution may adopt two approaches. The continuum approach assumes that the processes and properties being modelled may be represented as smoothly varying fields e.g. density, stress. The strategy for employing continuum methods involves firstly dividing the domain (Ω) into smaller subdomains to form a mesh of connecting nodes on which calculations are made. This process is known as spatial discretisation, or meshing. The problem is also discretised in a temporal sense, such that calculations are made at certain intervals, or timesteps, as the problem progresses. The calculations require the addition of boundary conditions and loads imposed on the boundary of the domain ($\partial\Omega$), as well as body forces applied to the entire domain e.g. gravitational forces, in order to evaluate displacements, velocities and accelerations. The basics of the continuum modelling approach are shown in Figure 3-4.

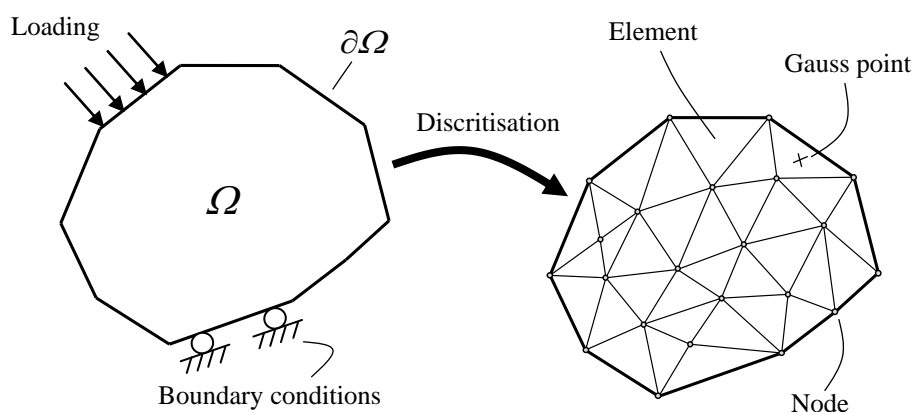


Figure 3-4: Continuum modelling approach.

The two most popular continuum methods are the Finite Element Method (FEM) and the Finite Difference Method (FDM), although other methods such as the Finite Volume Method (FVM) and Boundary Element Method (BEM) also exist. The principal difference between

FEM and FDM is that the former approximates the governing equations once they have been re-cast into their weak (or integral) form. Conversely the FDM approximates the governing equations in their strong form (as finite difference approximations to the partial differential equations). The FDM has found some application in geological forward modelling (Fuchs et al., 2011) but suffers from an inability to handle complex domain geometries and free surfaces. It consequently finds application in the field of Computational Fluid Dynamics and the forward modelling publications which utilise Finite Difference schemes tend to focus on diapirism related to density inversion (Zaleski and Julien, 1992). The FEM (Zienkiewicz and Taylor, 2005; Zienkiewicz et al., 2005) is generally better suited to problems that feature non-linearity, irregular geometries and complicated boundary conditions. As such FEM is well established in the forward modelling literature and has found application in studying a wide variety of geological structures.

3.2.1.2 The Discrete Approach

The alternative to the continuum approach is to treat the domain as an assembly of discrete particles. The interactions between the discrete particles are governed by Newtonian Law's of motion. Normal and shear contact is a function of penetration and the motion of particles is evaluated at particle centroids taking into account contributions from adjacent particles. These approaches do not require a constitutive law as model input and deformation arises purely from particle interactions. These techniques are often successful in replicating the discrete behaviour of geomaterials e.g. brittle faulting and fracturing.

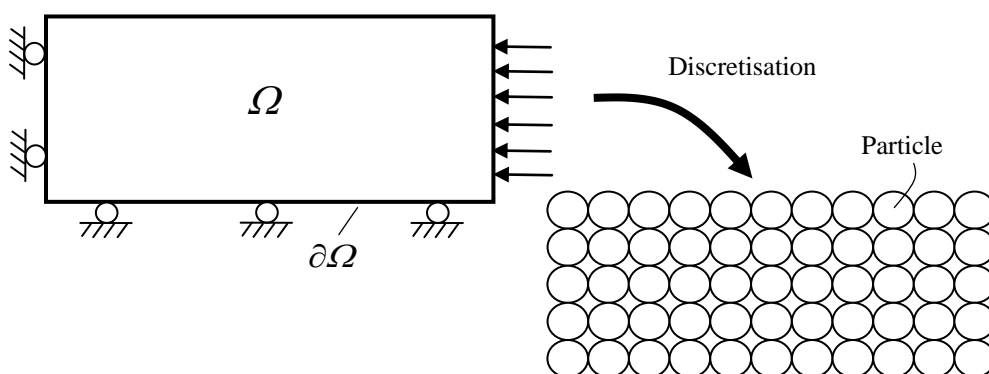


Figure 3-5: Discrete modelling approach with particle method.

An issue with these approaches however is an excessively long solution time arising from

cumbersome searches that are needed to evaluate particle interactions. This introduces issues regarding model resolution (Yin et al., 2009). As such the scope of the model may be limited. There are additional issues relating to how these models are initialised, and complications when the behaviour of other processes need to be included.

3.2.1.3 Discussion of Approaches

The continuum and discrete approaches both have advantages and disadvantages for modelling of geological structures. However, qualitatively the approaches may exhibit similar deformation styles, as shown in Figure 3-6. It is important to consider computational efficiency, and any modelling approach seeking to investigate polygonal faulting should be flexible enough to address the problem.

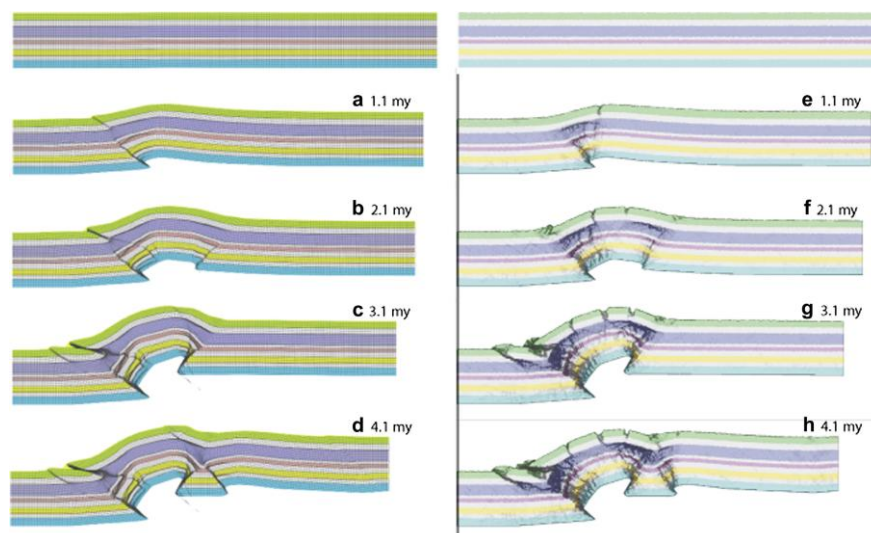


Figure 3-6: Comparison of continuum (left) and discrete (right) approaches for modelling the evolution of contractional geological structures (Gray et al., 2014).

3.2.2 Description of the Kinematics

A further complication now arises regarding the treatment of excessive deformation and gross topology changes encountered in geological problems and more specifically the frame of reference that is adopted to describe the kinematics. There are three principal formulations.

3.2.2.1 Eulerian

The Eulerian description is frequently utilised in simulations involving fluids and finds application in scenarios where the various rock layers and assumed to behave as viscous Newtonian or Non-Newtonian fluids (Woidt, 1978; Zaleski and Julien, 1992). This is a very

crude approximation to the nature of materials which may exhibit brittle, plastic deformation. The Eulerian approach has the disadvantages that the replication of faulting is often not possible or inaccurate and that tracking the interface between different materials can become problematic (Crook, Willson, et al., 2006).

3.2.2.2 Arbitrary Lagrangian Eulerian

In this approach, often abbreviated to ALE, an attempt is made to extract the desirable components of both the Lagrangian and Eulerian approaches (Fullsack, 1995; Gemmer et al., 2004, 2005; Gradmann et al., 2009). However, depending on the precise formulation this method may still inherit issues from both the Lagrangian and Eulerian descriptions. An example of this is the reduced but not eliminated requirement for remeshing of the problem. The explicit treatment of discontinuous displacement fields is also not trivial.

3.2.2.3 Lagrangian

The Lagrangian description, commonly referred to as the material description, has the advantages of straightforward treatment of interfaces between materials and the direct modelling of the material state evolution. As such the complex constitutive behaviour of various rock types can be easily represented, as can the initiation and subsequent propagation of faults. These attractive features mean that this strategy is the most frequently employed. However, the large deformations encountered can cause distortion of the finite element mesh, which if left untreated can lead to poor accuracy and early termination of the analysis. This can be mitigated by employing adaptive finite element approaches (Peric et al., 1996) which allow for remeshing of the problem.

3.3 ELFEN

3.3.1 Introduction

The above indicates that there are a variety of potential options in terms of the framework adopted for analysing problems in structural geology. Consideration should be given to the range of geological processes involved and the strategy adopted should be assessed in its ability to treat these processes.

In this study, analysis of the sediment evolution is carried out using ELFEN, a flexible Finite/Discrete Element package that can be utilised to solve a large number of physical problems. ELFEN is particularly well adapted to studying geological problems.

3.3.2 Finite Element Framework

For the current application, a Quasi-Static Explicit Lagrangian Finite Element formulation is used which is complemented by robust and efficient automated adaptive remeshing techniques. Concisely, the software solves a reduced form of the discretised momentum equation in an explicit fashion, i.e. equilibrium is not enforced at each step, and the loading is deemed to occur sufficiently slowly in order for inertial terms to be neglected. The method followed in the software is discussed in depth in Peric and Crook (2004) and in outlining their framework the authors consider many of the possible issues and requirements, such as finite deformation, deposition, erosion and coupled-processes. As such one can argue this is a robust platform on which to undertake the modelling tasks. Advanced constitutive models are also available in ELFEN which are detailed in the following sections (Refer to Appendix for more detail). These are able to successfully replicate many aspects of soil/rock behaviour. The continuum approach adopted here raises questions regarding the treatment of localised failure zones (faults). Inclusion of advanced algorithms for identifying localisations, as well as concepts from Nonlinear Fracture Mechanics (NLFM), allows for faults to be represented and for the mesh independent dissipation of energy post failure (Kato, 2010).

3.4 Constitutive Models for Geomaterials

A recurring point in the discussion of PFS has been that there is strong evidence for a constitutive trigger for their formation. As such it is critical that any modelling approach adopts suitable constitutive models for the application. The following sections are concerned with describing the constitutive model that will be used as the foundation for the modelling tasks.

3.4.1 Background

Constitutive laws are used to represent the physical response of a geomaterial, and define the relationship between deformation (strains) and stress state by choosing a selection of appropriate internal variables. Over the past few decades there has been an increased interest in incorporating more sophisticated material models into geomechanical modelling. Traditionally, models such as Mohr-Coulomb and Drucker-Prager have been used to describe soil behaviour. However, these models are limited in their ability to model all aspects of soil deformation, most notably in their most basic forms they are concerned solely with shear strength and unable to account for strengthening of the material via compaction. This can be incorporated by including an additional surface (cap). However, there may be issues with

such an implementation, and it is convenient if the function defining the limit of the elastic domain is continuous and differentiable. Regardless of the shortcomings in accuracy and applicability of these models, they regularly find application in numerical forward models, notably in the simulation of problems relating to salt tectonics (Schultz-Ela, 2003; Gemmer et al., 2005; Gradmann et al., 2009).

More recently there has been a marked increase in the use of more sophisticated material models that use a critical state framework. These are often adopted in salt tectonics based research (Luo et al., 2011; Nikolinakou, 2011) although they also find use in applications relating to thrusting and folding (Albertz and Lingrey, 2012; Albertz and Sanz, 2012). These models are key in capturing both the shear and compressive behaviour of soils and rocks and are essential if the study intends to examine the coupled processes of mechanical deformation and flow in porous media. With consideration to the current application and in particular the geomechanical arguments proposed in Chapter 2, it is important that the material model adopted is able to represent both compactive, strain-hardening behaviour as well as strain-softening behaviour in shear.

3.4.2 Requirements for Elastoplastic Soil and Rock Models

The general requirements for the formulation of an elastoplastic material model for soils and soft rocks are detailed below (Wood, 1990). With these components the basic mechanical behaviour of a soil or rock can effectively be described for a variety of imposed stress states. For capturing the response due to more sophisticated phenomena, such as liquefaction, water-weakening or creep, other components may be required.

3.4.2.1 Elastic Law

The elastic law describes the nature of deformations within the state boundary surface and is a function of poisson's ratio, ν and Young's Modulus, E . Elastic deformations are recovered when loads are removed. Commonly, this is adjusted to incorporate a poroelastic law such as Cam Clay so that the volume of voids can be incorporated and the material is able to consider porous flow. Many materials exhibit more complex elastic behaviour. This additional complexity may result from anisotropy i.e. elastic properties in laminated materials may vary in horizontal and vertical directions, or the elastic behaviour might be sensitive to temperature (thermally induced elastic strains).

3.4.2.2 State Boundary Surface

The state boundary defines the region of allowable stresses in stress-space and separates elastic from plastic deformations. For a material to reach inaccessible stress states i.e. lying outside of the current state boundary surface, changes to the material state are required.

3.4.2.3 Plastic Potential

The plastic potential is concerned with describing the various modes of plastic deformation, specifically the quantities of plastic shear strain and plastic volumetric strain. Models may be used with the function defining the plastic potential described in an identical way to the function for the state boundary surface (or yield surface). This is referred to as associated plasticity and is less complex than cases where the two functions differ, or non-associated plasticity. However, depending on the application the associated case may incorrectly predict the contributions of the shear and volumetric plastic strain components.

3.4.2.4 Hardening Law

The hardening law describes the relationship between plastic strain increments and the size of the state boundary surface. Positive increments will be associated with volumetric expansion and hence a reduction in the size of the yield surface. Conversely, negative increments are indicative of compaction and enlarging of the yield surface. This relationship is dictated by the hardening curve.

3.5 Constitutive Model: Soft Rock 3 (SR3)

3.5.1 An Introduction to Critical State Soil Mechanics

The requirement to capture both the shear and compacting response of soft rocks that was outlined previously leads naturally to the adoption of constitutive models based on the critical state framework. Concisely, critical state models are based on the premise that when deformed soils and soft rocks will tend towards a condition of isochoric flow (constant volume) at which unlimited plastic shearing will take place with no further changes in effective stress. This is known as the critical state and physically the structure of the soil is being continuously broken down and remoulded (Wood, 1990).

The critical state separates two domains that are associated with non-isochoric volume changes in the material. On the 'dry side' of the critical state line failure is in shear, localised, and associated with softening and volumetric expansion (dilation). On the 'wet side' the compaction will be more diffuse and associated with volumetric contraction (compaction). In

reality the response may be more complicated. For example, the formation of compaction bands, shear-enhanced compaction and tensile fracture might be observed and need to be accounted for within the constitutive model.

3.5.1.1 State Boundary Surface

The SR3 model is a single surface, rate independent, non-associated plasticity model based on critical state concepts. It can be thought of as a significantly enhanced Modified Cam Clay variant. The SR3 model is the base model in a hierarchical family of models that are specifically formulated for the analysis of material evolution over geological timeframes (Crook, Owen, et al., 2006; Crook, Willson, et al., 2006). The details of the SR3 constitutive model are given below with reference to the ingredients for formulating an elastoplastic soil model listed in the previous section. The state boundary surface is expressed in scaled-stress space which is common for soil and rock models. For the formulation of measures to assess the material state it is useful to use invariants. These are scalar values (tensors of rank 0) that are constant, or invariant, regardless of the basis or coordinate system adopted.

Remarks 1 In the following sections matrix notation is adopted in the description of various aspects of the constitutive models. Bold face characters e.g. \mathbf{A} denote non-scalar variables i.e. vectors or tensors.

The equation defining the state boundary surface, denoted Φ , is a function of three stress invariants

$$\Phi(p', q, r) = 0 \quad \mathbf{3-1}$$

where p is scaled from the first principal invariant of the Cauchy stress tensor I_1 , q is a scaled value of the second principal invariant of the deviatoric stress tensor J_2 , and r is a function of J_2 and the third principal invariant of the deviatoric stress tensor J_3 . Alternatively p' and q are referred to as the mean stress and the deviatoric stress, respectively. The relationships between them are as follows

$$p' = \frac{1}{3}I_1, \quad q = \sqrt{3J_2}, \quad r = \left(\frac{27}{2}J_3\right)^{1/3} \quad \mathbf{3-2}$$

The first invariant of the Cauchy stress tensor is given below, together with the second and third invariants of the deviatoric part

$$I_1 = \text{tr}[\boldsymbol{\sigma}], \quad J_2 = \frac{1}{2} \boldsymbol{s} : \boldsymbol{s}, \quad J_3 = \det(\boldsymbol{s}) \quad \mathbf{3-3}$$

where \boldsymbol{s} is the deviatoric part of Cauchy stress tensor i.e. $\boldsymbol{s} = \boldsymbol{\sigma} - p\mathbf{I}$ with \mathbf{I} being the second-order identity tensor (equivalent to the Kronecker delta, δ_{ij}). In addition, the corresponding infinitesimal strain invariants are

$$\varepsilon_v^e = \text{tr}[\boldsymbol{\varepsilon}^e], \quad \varepsilon_q^e = \sqrt{\frac{2}{3} \boldsymbol{e}^e : \boldsymbol{e}^e}. \quad \mathbf{3-4}$$

where ε_v^e and ε_q^e are the volumetric and deviatoric (effective) components of infinitesimal elastic strain tensor, respectively. The deviatoric strain tensor may be written as $\boldsymbol{e}^e = \boldsymbol{\varepsilon}^e - (1/3)\varepsilon_v^e \mathbf{I}$. The function defining the state boundary surface is a smooth three-invariant surface that intersects the hydrostatic axis in both tension and compression. The state boundary surface is shown in principal stress space and p - q space in Figure 3-7(a) and (c) respectively, and is defined as

$$\Phi(\boldsymbol{\sigma}, \varepsilon_v^p) = g(\theta, p')q + (p' - p_t') \tan \beta \left(\frac{p' - p_c'}{p_t' - p_c'} \right)^{1/n} \quad \mathbf{3-5}$$

where p' is the effective mean stress, q is the deviatoric stress, θ is the Lode angle, p_t' is the tensile intercept of the yield surface with the hydrostatic axis, p_c' is the pre-consolidation pressure or compressive tensile intercept of the yield surface with the hydrostatic axis, β and n are material constants that define the shape of the yield surface in the p' - q plane and $g(\theta, p)$ is a function that controls the shape of the yield function in the deviatoric plane. Many expressions for the deviatoric plane correction plane $g(\theta, p)$ have been proposed and a useful general expression is defined as

$$g(\theta, p') = \left[\frac{1}{1 - \beta^\pi(p')} \left(1 + \beta^\pi(p') \frac{r^3}{q^3} \right) \right]^{N^\pi} \quad \mathbf{3-6}$$

where N^π is material constant and β^π is defined in a similar manner to (Desai and Salami, 1987) as

$$\beta^\pi(p') = \beta_0^\pi \exp\left(\beta_1^\pi p' \frac{p_{c0}'}{p_c'}\right) \quad 3-7$$

and β_0^π and β_1^π are material constants and p_{c0} and p_c are the initial and current pre-consolidation pressure respectively. Equation 3-6 defines the dependency of the yield surface aspect ratio in the deviatoric plane and can represent the experimentally observed behaviours of many types of rocks. Figure 3-7(b) depicts the transition of the yield surface in the deviatoric plane, which can change from a rounded triangular at low confining pressure to a more circular profile as the confining pressure becomes higher. Equation 3-6 is scaled so that the strength in triaxial compression directly corresponds to strength calibrated using compressive triaxial (CTC) tests and the strength is reduced in reduced triaxial extension (RTE) tests; i.e.

$$\begin{aligned} \text{RTE} \quad \theta = -30^\circ \quad \sin 3\theta = -1 \quad g &= \left[\frac{1 + \beta^\pi}{1 - \beta^\pi} \right]^{N^\pi} \\ \theta = 0^\circ \quad \sin 3\theta = 0 \quad g &= \left[\frac{1}{1 - \beta^\pi} \right]^{N^\pi} \\ \text{CTC} \quad \theta = 30^\circ \quad \sin 3\theta = 1 \quad g &= 1 \end{aligned} \quad 3-8$$

The dependence of β^π on the effective mean stress enables the observed transition from the rounded-triangular yield surface at low mean stress to a circular yield surface at high mean stress, see Figure 3-7(b). In Equation 3-7 the correction term p_c^0 / p_c is introduced so that the original yield surface transitional effect along the pressure evolution can be kept with the current yield surface status.

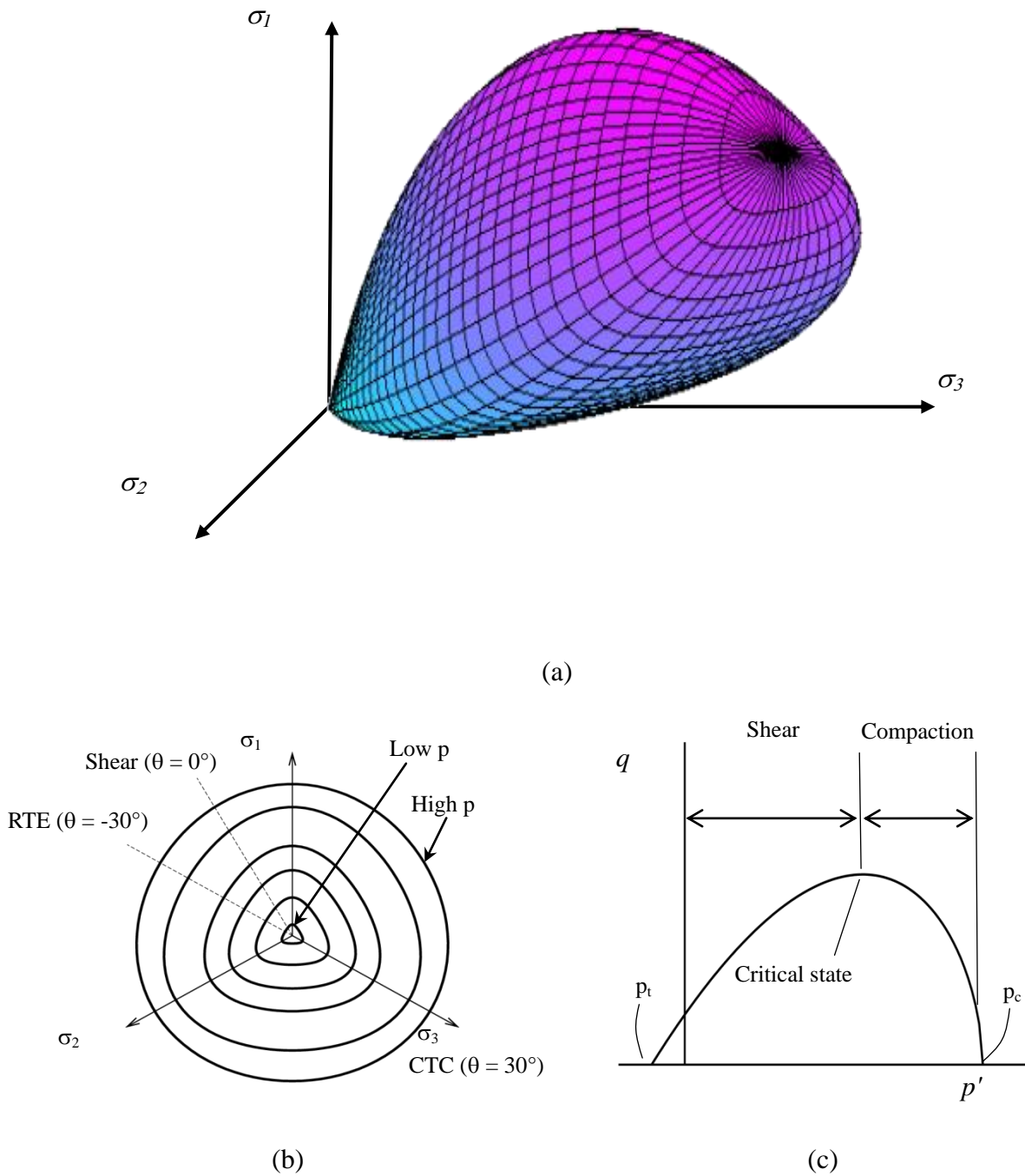


Figure 3-7: The SR3 state boundary surface. (a) Principal stress space (b) Deviatoric (π) plane (c) Meridian plane (p' - q space).

3.5.2 Flow Rule Definition

The evolution of the plastic flow is defined by a non-associated flow rule so that the plastic strain rate is defined as;

$$\dot{\boldsymbol{\varepsilon}}^p = \dot{\lambda} \frac{\partial \Psi}{\partial \boldsymbol{\sigma}} \quad 3-9$$

where $\dot{\lambda}$ is the plastic multiplier and $\Psi(\boldsymbol{\sigma}, \varepsilon_v^p)$ is the plastic potential defined as

$$\Psi(\boldsymbol{\sigma}, \varepsilon_v^p) = g(\theta, p')q + (p' - p_t') \tan \psi \left(\frac{p' - p_c'}{p_t' - p_c'} \right)^{1/n} \quad 3-10$$

From inspection it is clear that the plastic potential has an identical form to the state boundary surface but with defined with angle ψ instead of β (Figure 3-8). The plastic multiplier $\dot{\lambda}$ defines the magnitude of the plastic strain and is consistent with the Kuhn-Tucker loading/unloading criterion:

$$\Phi(\boldsymbol{\sigma}, q) \leq 0 \quad \dot{\lambda} \geq 0 \quad \dot{\lambda} \Phi(\boldsymbol{\sigma}, q) = 0 \quad 3-11$$

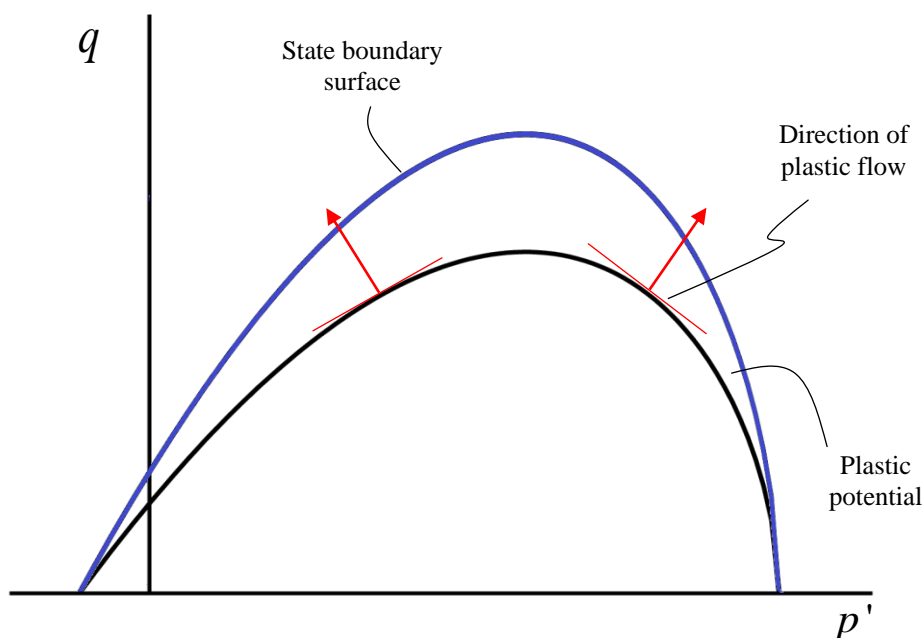


Figure 3-8: Plastic potential in meridian plane.

3.5.3 Volume Change

The plastic potential surface of the SR3 model defines a surface to which the direction of

plastic strain increment is orthogonal. The location of the stress point on the plastic potential surface therefore defines the ratio between the incremental shear plastic strain $\delta\varepsilon_q^p$ and the incremental volumetric plastic strain $\delta\varepsilon_v^p$, i.e., whether the material is dilating or compacting. An alternative useful measure for visualisation of dilatancy is the angle β^d between the strain increment vector and the p axis where

$$\beta^d = \tan^{-1} \left[\frac{\delta\varepsilon_q^p}{\delta\varepsilon_v^p} \right] \quad 3-12$$

Note that from the flow rule $\delta\varepsilon_q^p = \delta\lambda (\partial\Psi / \partial q)$ and $\delta\varepsilon_v^p = \delta\lambda (\partial\Psi / \partial p)$, hence

$$\beta^d = \tan^{-1} \left[\frac{\partial\Psi / \partial q}{\partial\Psi / \partial p} \right] \quad 3-13$$

When $g=1$, i.e. CTC case, the following derivatives are obtained

$$\frac{\partial\Psi}{\partial q} = 1 \quad \text{and} \quad \frac{\partial\Psi}{\partial p} = \tan\psi \left[1 + \frac{p - p_t}{n(p - p_c)} \right] \left(\frac{p - p_c}{p_t - p_c} \right)^{1/n} \quad 3-14$$

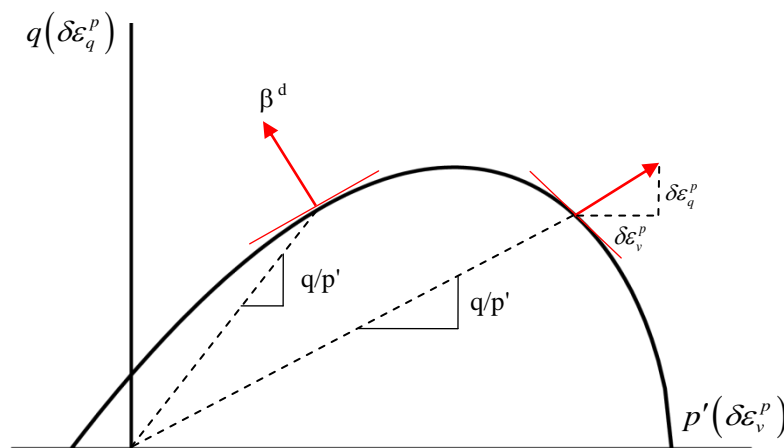


Figure 3-9: Definition of dilation parameter, β^d .

From this definition of dilation it is clear that the evolution of localised shear zones will be dependent on the configuration of deviatoric and mean stresses. Where the ratio q/p' is very high we might expect highly extensional plastic flow and the formation of shear bands. Where the ratio of q/p' is lower we expect compactive and diffuse deformation. This ratio therefore serves as a good measure of the anticipated deformation style.

3.5.4 Hardening Law and Poro-Elasticity

The evolution of the state boundary surface is defined by the relationship of the pre-consolidation pressure p_c and tensile intercept p_t to the volumetric plastic strain ε_v^p i.e.

$$p_c = p_c(\varepsilon_v^p) \text{ and } p_t = p_t(\varepsilon_v^p) \quad \mathbf{3-15}$$

Several different hardening/softening laws are available. The curve may be evaluated explicitly, however the most commonly used variation is piecewise linear. The hardening data is determined using Cam Clay hardening constants κ and λ (Figure 3-10) as follows:

$$p_c = p_{c0} \left[\exp \left(\frac{v \varepsilon_v^p}{(\lambda - \kappa)} \right) \right] \quad \mathbf{3-16}$$

$$p_t = p_{t0} \left[\exp \left(\frac{v(\varepsilon_v^p)_{\max}}{(\lambda - \kappa)} \right) \right]$$

where v is the specific volume and $(\varepsilon_v^p)_{\max}$ is the maximum dilational volumetric plastic strain.

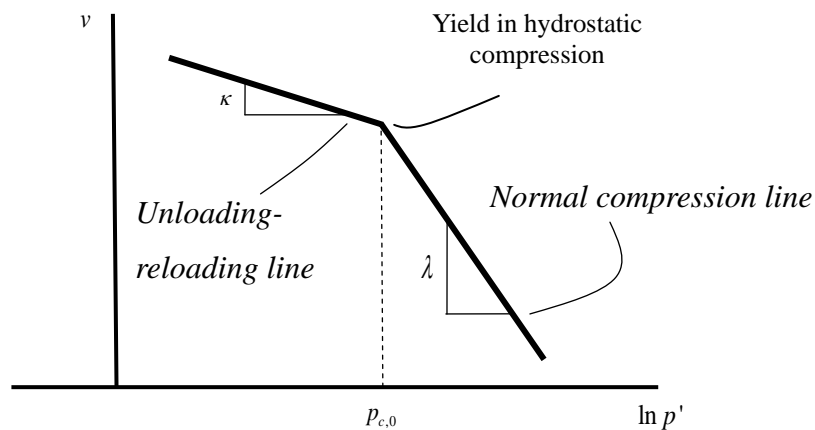


Figure 3-10: Hardening model.

The adopted poro-elastic law is the so-called Cam Clay model. The stiffness or elastic modulus, E , is evaluated as;

$$E = 3(1 - 2\nu)K \quad \mathbf{3-17}$$

Where, ν is Poisson's ratio, and the bulk modulus K is a function of the porosity, slope of the

unloading-reloading line, κ , and the effective mean stress, i.e;

$$K = K_0 + \frac{1}{\kappa} \left(\frac{1}{1-\phi} \right) p' \quad 3-18$$

3.5.5 Elastoplastic Stress Update

Following the explicit solution of the discretised momentum balance equation (see Appendix), the incremental displacements at the new timestep are known. From the incremental displacements, incremental strains can be obtained. We may then calculate the updated components of the Cauchy stress tensor by defining a constitutive relationship between the strains and stresses, as given below;

$$\boldsymbol{\sigma}^{Trial} = {}^t \boldsymbol{\sigma} + \mathbf{D}_{ne} \Delta \boldsymbol{\varepsilon} \quad 3-19$$

where \mathbf{D}_{ne} is the matrix form of nonlinear elastic modulus, $\Delta \boldsymbol{\varepsilon}$ is the incremental strain and superscript t denotes values at time t . In elastoplastic models this temporary calculated stress is commonly known as the trial stress, $\boldsymbol{\sigma}^{Trial}$. If the trial stress corresponds to a location in stress space that lies within the state boundary surface i.e. $\Phi(\boldsymbol{\sigma}^{Trial}, \boldsymbol{\varepsilon}_v^p) \leq 0$ then the step is elastic and therefore $\boldsymbol{\sigma}^{Trial} = \boldsymbol{\sigma}$. If the function defining the state boundary surface is violated then a stress update must be applied and is defined by

$${}^{t+\Delta t} \boldsymbol{\sigma} = \boldsymbol{\sigma}^{Trial} - \mathbf{D}_{ne} \Delta \boldsymbol{\varepsilon}^p \quad 3-20$$

Where, by employing a fully implicit backward Euler integration scheme, the incremental flow rule $\Delta \boldsymbol{\varepsilon}^p$ is defined as

$$\Delta \boldsymbol{\varepsilon}^p = \Delta \lambda \frac{\partial \Psi}{\partial {}^{t+\Delta t} \boldsymbol{\sigma}} = \Delta \lambda {}^{t+\Delta t} \boldsymbol{\phi} \quad 3-21$$

The state boundary function after completion of the stress update is defined as

$$\begin{aligned} \Phi\left({}^{t+\Delta t} \boldsymbol{\sigma}, {}^{t+\Delta t} \boldsymbol{\varepsilon}_v^p\right) &= g\left(\theta, {}^{t+\Delta t} p\right) {}^{t+\Delta t} q + \left({}^{t+\Delta t} p - {}^{t+\Delta t} p_t\right) \tan \beta \left(\frac{{}^{t+\Delta t} p - {}^{t+\Delta t} p_c}{{}^{t+\Delta t} p_t - {}^{t+\Delta t} p_c} \right)^{1/n} \\ &= 0 \end{aligned} \quad 3-22$$

The plastic corrector may then be formulated using the requirement that Equations 3-20, 3-21,

and 3-22 must be satisfied at $t+\Delta t$. Therefore an eight equation system is formed and is defined as;

$$\begin{aligned}
 Y_1 &= {}^{t+\Delta t}\boldsymbol{\sigma} - \boldsymbol{\sigma}^{trial} + \Delta\lambda \mathbf{D}_{ne} {}^{t+\Delta t}\boldsymbol{\varphi} \\
 Y_2 &= g\left(\theta, {}^{t+\Delta t}p\right) {}^{t+\Delta t}q + ({}^{t+\Delta t}p - {}^{t+\Delta t}p_t) \tan\beta \left(\frac{{}^{t+\Delta t}p - {}^{t+\Delta t}p_c}{{}^{t+\Delta t}p_t - {}^{t+\Delta t}p_c}\right)^{1/n} \\
 Y_3 &= \Delta\varepsilon_v^p - \Delta\lambda \text{tr}({}^{t+\Delta t}\boldsymbol{\varphi})
 \end{aligned} \tag{3-23}$$

where \mathbf{Y}_1 is a vector of length 6, and the primary unknowns are the six stress components ${}^{t+\Delta t}\boldsymbol{\sigma}$, the plastic multiplier $\Delta\lambda$, and the incremental volumetric strain $\Delta\varepsilon_v^p$. This system may be solved using Newton-Raphson iteration; i.e.

$$\begin{bmatrix} \frac{\partial Y_1}{\partial \boldsymbol{\sigma}} & \frac{\partial Y_1}{\partial(\Delta\lambda)} & \frac{\partial Y_1}{\partial(\Delta\varepsilon_v^p)} \\ \frac{\partial Y_2}{\partial \boldsymbol{\sigma}} & \frac{\partial Y_2}{\partial(\Delta\lambda)} & \frac{\partial Y_2}{\partial(\Delta\varepsilon_v^p)} \\ \frac{\partial Y_3}{\partial \boldsymbol{\sigma}} & \frac{\partial Y_3}{\partial(\Delta\lambda)} & \frac{\partial Y_3}{\partial(\Delta\varepsilon_v^p)} \end{bmatrix} \begin{Bmatrix} d\boldsymbol{\sigma} \\ d(\Delta\lambda) \\ d(\Delta\varepsilon_v^p) \end{Bmatrix} = (-1) \begin{Bmatrix} Y_1 \\ Y_2 \\ Y_3 \end{Bmatrix} \tag{3-24}$$

3.6 Regularisation of the Material Softening

The adoption of the continuum approach for the class of problems that are to be studied means that issues arise regarding the treatment of localisations, and specifically the sensitivity of the global response to the fineness of the finite element mesh. To demonstrate this concept consider the axial loading of a 1D brittle bar of unit width as shown in Figure 3-11.

The setup for the models is identical, save for the discretisation. In Model A a single finite element of length L is used to represent the bar, whereas in model B is modelled with 3 finite elements of length $L/3$. Numerical perturbations will always cause the fracture to localise to one finite element, even with constant tensile strength. Once the element has failed the adjacent elements will unload. The two models will return force-displacement relationships shown in Figure 3-12.

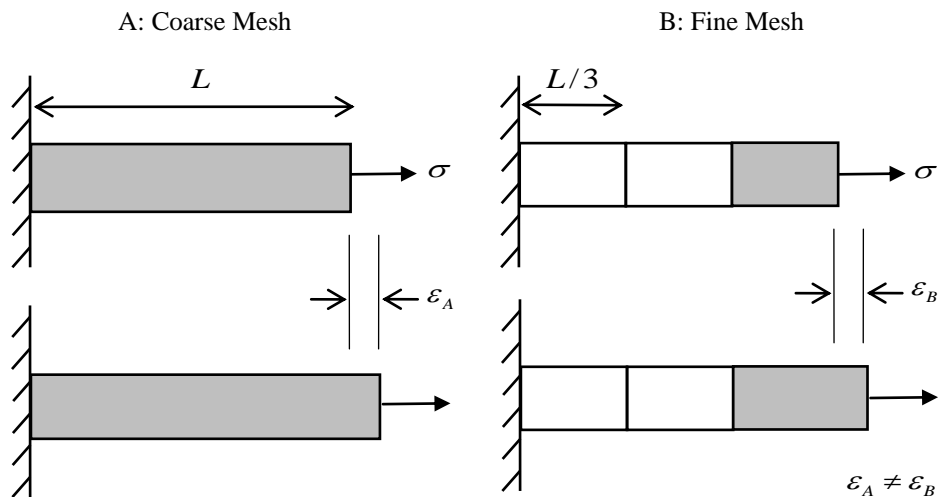


Figure 3-11: Demonstration of energy dissipation for a 1D brittle bar loaded axially.

The region region designates the failed element.

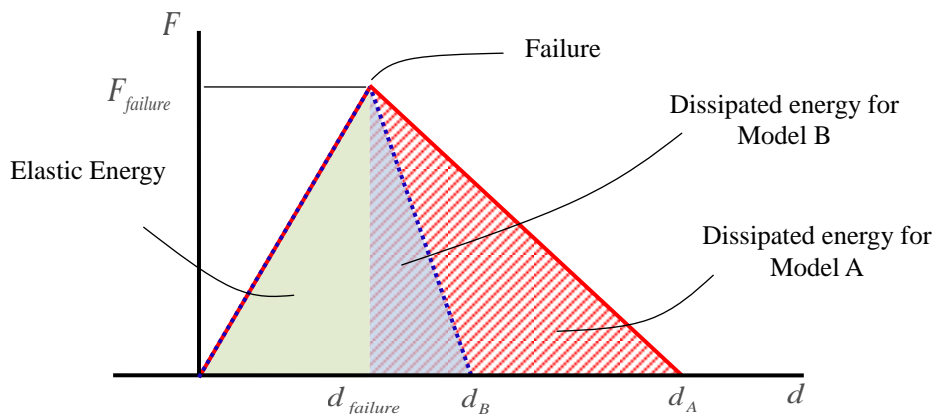


Figure 3-12: Force-displacement relationships for axial bar problem with differing mesh sizes.

It is clear that the dissipated energy due to plasticity is not consistent for the two different finite element meshes. There are a number of strategies available to maintain consistent energy dissipation for arbitrary finite element meshes in continuum models e.g. gradient plasticity methods, Cosserat continuum methods (Kato, 2010). For the current application a method of fracture energy regularisation is introduced that effectively scales the softening based on the element size (Crook et al., 2003) and may be expressed as;

$$\left(\bar{\varepsilon}^p\right)^{(e)} = \left(\bar{\varepsilon}^p\right)^{(m)} \left[\frac{l_c^{(m)}}{l_c^{(e)}} \right]^n \quad \text{3-25}$$

where $\bar{\varepsilon}^p$ is an appropriate scalar measure of plastic strain that determines the material softening, n is a material constant, and $l_c^{(m)}$ and $l_c^{(e)}$ are the material and element characteristic lengths. Both $l_c^{(m)}$ and $l_c^{(e)}$ are shown in Figure 3-13. The material characteristic width would typically be evaluated via laboratory testing. Note that Equation 3-25 is strictly valid for the condition where $l_c^{(e)} \geq l_c^{(m)}$ i.e. the localisation is confined to a single finite element. The advantage of the above implementation is that it is independent of the constitutive model and therefore maybe implemented for a range of constitutive models, such as the SR3 and Mohr-Coulomb models that form part of this study.

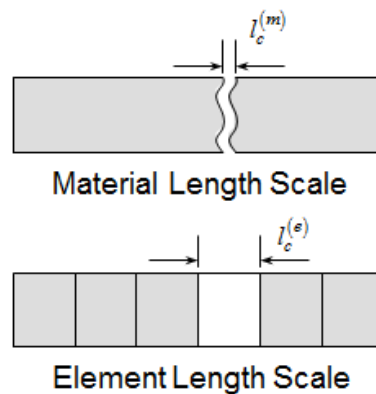


Figure 3-13: Definition of material and element length scales for regularisation of fracture energy dissipation.

3.7 Conclusions

This chapter has been concerned with describing the key concepts of geomechanical forward modelling and has covered three important topics which are summarised below.

3.7.1 Studying Polygonal Faults

Conventional techniques such as kinematic restoration or bench scale modelling are widely adopted in analysing the evolution of geological structures at various scales. However, the discussion of these techniques highlighted significant issues, most notably crude or over-simplified representations of the constitutive behaviour of soft rocks. Much evidence points to polygonal fault genesis being controlled by the constitutive nature of sediments within the

tier. For this reason these techniques find infrequent use in studying polygonal. Adoption of geomechanical modelling techniques appears to potentially be both a novel and useful tool for exploring the genesis and development of PFS.

3.7.2 Computational Framework

The important elements of computational modelling tools have been outlined. Some key considerations are the methodology of discretising the domain and solving the relevant set of equations. The description of the kinematics is also crucial and the adoption of a particular reference frame may have implications for the types of problems that can effectively be studied. For this reason it is important to adopt a flexible modelling framework in which the key processes that govern the evolution of a geological structure can be incorporated. For this reason the explicit finite element code ELFEN is adopted as it allows for;

- Direct representation of the material state
- Intrinsic representation of free surfaces
- Handling of gross deformation and topology changes e.g. deposition associated with geological structure evolution
- Frictional contact between layers and/or faults if required
- Identification of emerging localisations.

3.7.3 Constitutive Modelling

The important aspects of constitutive modelling of geomaterials have been covered in detail. The four main components of elastoplastic soil models have been described, and a suitable material model has been introduced with reference to these components. The constitutive model is denoted SR3 and is based on critical state concepts. It may be used to describe both the shear and compactive behaviour of a range of soils and soft rocks. Other constitutive models, such as Mohr-Coulomb, are more familiar to most engineers and geoscientists and find frequent application to a range of materials. It is stressed however that in their traditional form their ability to capture all aspects of the behaviour of geomaterials is limited, particularly treatment of compaction. The addition of a compaction cap can allow for compaction to be more effectively treated.

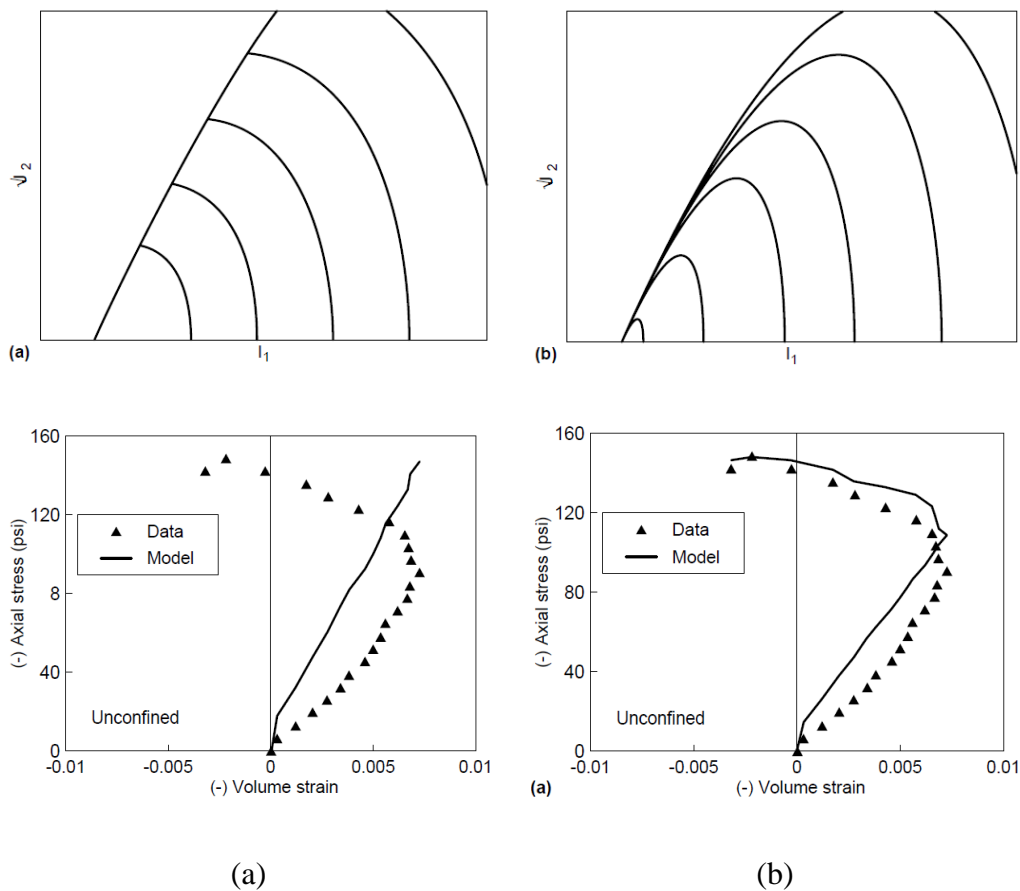


Figure 3-14: Observed and modelled stress strain responses using (a) two surface cap plasticity model (b) continuous surface model (Fredrich and Fossum, 2002).

The ability of the constitutive model to capture the transition between dilation and compaction is crucial for this study. As noted, the less sophisticated models such as Mohr-Coulomb or Drucker-Prager can be furnished with an additional cap-surface in so called "two-surface" models. However, these also struggle to deal with dilative-compactive transitions as shown in Figure 3-14, where the model featuring a continuous surface like the SR3 is able to successfully capture the experimental response of a unconfined triaxial test (Fredrich and Fossum, 2002). The two-surface model is unable to capture the experimental data adequately.

An additional important concept has also been discussed relating to energy dissipation in plasticity and how this may be sensitive to the finite element mesh. The solution to this problem has been described in the form of fracture energy regularisation and this approach is implemented for the presented constitutive models.

3.8 References

- Albertz, M., and S. Lingrey, 2012, Critical state finite element models of contractional fault-related folding: Part 1. Structural analysis: *Tectonophysics*, v. 576-577, p. 133–149.
- Albertz, M., and P. F. Sanz, 2012, Critical state finite element models of contractional fault-related folding: Part 2. Mechanical analysis: *Tectonophysics*, v. 576-577, p. 150–170.
- Crook, A. J. L., D. R. J. Owen, S. Willson, and J. Yu, 2006, Benchmarks for the evolution of shear localisation with large relative sliding in frictional materials: *Computer Methods in Applied Mechanics and Engineering*, v. 195, no. 37-40, p. 4991–5010.
- Crook, A. J. L., S. Willson, J. G. Yu, and D. R. J. Owen, 2003, Computational modelling of the localized deformation associated with borehole breakout in quasi-brittle materials: *Journal of Petroleum Science and Engineering*, v. 38, no. 3-4, p. 177–186.
- Crook, A. J. L., S. Willson, J. Yu, and D. Owen, 2006, Predictive modelling of structure evolution in sandbox experiments: *Journal of Structural Geology*, v. 28, no. 5, p. 729–744.
- Desai, C. S., and M. R. Salami, 1987, A constitutive model and associated testing for soft rock: *International Journal of Rock Mechanics and Mining Sciences & Geomechanics Abstracts*, v. 24, no. 5, p. 299–307.
- Dooley, T. P., M. P. a. Jackson, and M. R. Hudec, 2009, Inflation and deflation of deeply buried salt stocks during lateral shortening: *Journal of Structural Geology*, v. 31, no. 6, p. 582–600.
- Duerto, L., and K. McClay, 2009, The role of syntectonic sedimentation in the evolution of doubly vergent thrust wedges and foreland folds: *Marine and Petroleum Geology*, v. 26, no. 7, p. 1051–1069.
- Erslev, E., 1991, Trishear Fault-Propagation Folding: *Geology*, v. 19, no. 6, p. 617–620.
- Fredrich, J. T., and A. F. Fossum, 2002, Large-Scale Three-Dimensional Geomechanical Modeling of Reservoirs: Examples from California and the Deepwater Gulf of Mexico: *Oil & Gas Science and Technology*, v. 57, no. 5, p. 423–431.
- Fuchs, L., H. Schmeling, and H. Koyi, 2011, Numerical models of salt diapir formation by down-building: the role of sedimentation rate, viscosity contrast, initial amplitude and wavelength: *Geophysical Journal International*, p. no–no.
- Fullsack, P., 1995, An arbitrary Lagrangian-Eulerian formulation for creeping flows and its application in tectonic models: *Geophysical Journal International*, v. 120, no. 1, p. 1–23.
- Gemmer, L., C. Beaumont, and S. J. Ings, 2005, Dynamic modelling of passive margin salt tectonics: effects of water loading, sediment properties and sedimentation patterns: *Basin Research*, v. 17, no. 3, p. 383–402.

-
- Gemmer, L., S. J. Ings, S. Medvedev, and C. Beaumont, 2004, Salt tectonics driven by differential sediment loading: stability analysis and finite-element experiments: *Basin Research*, v. 16, no. 2, p. 199–218.
- Gradmann, S., C. Beaumont, and M. Albertz, 2009, Factors controlling the evolution of the Perdido Fold Belt, northwestern Gulf of Mexico, determined from numerical models: *Tectonics*, v. 28, no. 2, p. 1–28.
- Gray, G. G., J. K. Morgan, and P. F. Sanz, 2014, Overview of continuum and particle dynamics methods for mechanical modeling of contractional geologic structures: *Journal of Structural Geology*, v. 59, p. 19–36.
- Guglielmo Jr, G., B. C. Vendeville, and M. P. A. Jackson, 1999, Isochores and 3-D visualization of rising and falling salt diapirs: *Marine and Petroleum Geology*, v. 16, no. July, p. 849–861.
- Hudec, M. R., and M. P. A. Jackson, 2004, Regional restoration across the Kwanza Basin, Angola: Salt tectonics triggered by repeated uplift of a metastable passive margin: *AAPG Bulletin*, v. 88, no. 7, p. 971–990.
- Kato, J., 2010, Computational Strategies for Predicting Localisations in Forward Modelling of Geological Structures: Unpublished PhD Thesis - Swansea University.
- Lovely, P., E. Flodin, C. Guzowski, F. Maerten, and D. D. Pollard, 2012, Pitfalls among the promises of mechanics-based restoration: Addressing implications of unphysical boundary conditions: *Journal of Structural Geology*, v. 41, p. 47–63.
- Luo, G., M. A. Nikolinakou, P. B. Flemings, and M. R. Hudec, 2011, Geomechanical modeling of stresses adjacent to salt bodies : 1 . Uncoupled models.
- Massimi, P., A. Quarteroni, F. Saleri, and G. Scrofani, 2007, Modeling of salt tectonics: *Computer Methods in Applied Mechanics and Engineering*, v. 197, no. 1-4, p. 281–293.
- McClay, K., 1990, Extensional fault systems in sedimentary basins: a review of analogue model studies*: *Marine and Petroleum Geology*, v. 7, no. August, p. 206–233.
- Nikolinakou, M. A., 2011, Geomechanical Modeling of Stresses Adjacent to Salt Bodies : 2 . Poro-Elasto-Plasticity and Coupled Overpressures: *AAPG Bulletin*.
- Peric, D., and A. J. L. Crook, 2004, Computational strategies for predictive geology with reference to salt tectonics: *Computer Methods in Applied Mechanics and Engineering*, v. 193, no. 48-51, p. 5195–5222.
- Peric, D., C. Hochard, M. Dutko, and D. R. J. Owen, 1996, Transfer operators for evolving meshes in small strain elasto-plasticity: *Computer Methods in Applied Mechanics and Engineering*, v. 137, no. 3-4, p. 331–344.

-
- Schultz-Ela, D., 2003, Origin of drag folds bordering salt diapirs: AAPG Bulletin, v. 87, no. 5, p. 757–780.
- Schultz-Ela, D., M. Jackson, and B. Vendeville, 1993, Mechanics of active salt diapirism: Tectonophysics, v. 228, no. 3-4, p. 275–312.
- Scrofani, G., 2007, Numerical basin modeling and tectonics: Unpublished PhD Thesis - Politecnico di Milano, p. 155.
- Vendeville, B., and M. Jackson, 1992a, The fall of diapirs during thin-skinned extension*: Marine and Petroleum Geology, v. 9, no. 4, p. 354–371.
- Vendeville, B., and M. Jackson, 1992b, The rise of diapirs during thin-skinned extension*: Marine and Petroleum Geology, v. 9, no. 4, p. 331–354.
- Victor, P., and I. Moretti, 2006, Polygonal fault systems and channel boudinage: 3D analysis of multidirectional extension in analogue sandbox experiments: Marine and Petroleum Geology, v. 23, no. 7, p. 777–789.
- Woidt, W.-D., 1978, Finite element calculations applied to salt dome analysis: Tectonophysics, v. 50, p. 369–386.
- Wood, D. M., 1990, Soil Behaviour and Critical State Soil Mechanics: Cambridge University Press, p. 488.
- Yin, H., J. Zhang, L. Meng, Y. Liu, and S. Xu, 2009, Discrete element modeling of the faulting in the sedimentary cover above an active salt diapir: Journal of Structural Geology, v. 31, no. 9, p. 989–995.
- Zaleski, S., and P. Julien, 1992, Numerical simulation of Rayleigh-Taylor instability for single and multiple salt diapirs: Tectonophysics, v. 206, no. 1-2, p. 55–69.
- Zienkiewicz, O. C., and R. L. Taylor, 2005, The Finite Element Method For Solid and Structural Mechanics: Elsevier, p. 631.
- Zienkiewicz, O. C., R. L. Taylor, and J. Z. Zhu, 2005, The Finite Element Method: It's Basis and Fundamentals: Elsevier, p. 733.

Chapter 4

INCORPORATING THE INFLUENCE OF BURIAL DIAGENESIS AT SHALLOW DEPTHS

Chapter 1 presents the principal mechanisms that have been previously suggested to explain polygonal fault genesis, highlighting the advantages and disadvantages of each in the context of its ability to explain polygonal fault genesis. The key observation is that evidence suggests that PFS formation is often driven by the constitutive response as a consequence of structure (fabric) development that results in a departure from the “normal consolidation behaviour” of the sediment. The experimental data reviewed in Chapter 2 shows that the response of the material can vary widely with the level of sediment structure (fabric). Processes that fall under the umbrella term *diagenesis* e.g. dissolution and precipitation/cementation provide a means for structure development. In many circumstances, these reactions are predominantly stress-insensitive and driven principally by temperature changes. Some of these processes are active even at depths of a few tens of metres; e.g. early dolomitization of carbonates (Croizé et al., 2010).

Chapter 3 introduced the important elements of the computational modelling approach adopted in this thesis to investigate the mechanics of polygonal fault development. Two crucial components are; (1) a robust, adaptive finite element framework that is able to deal with the large deformation (finite-strain) typically associated with problems encountered in structural geology; (2) a material model that is able to represent both the compaction and shear failure of sediments and the transition between these states i.e. a material model founded on critical state concepts.

This chapter investigates how various diagenetic mechanisms modify structure and outlines how this may lead to conditions of shear failure even during uniaxial consolidation; i.e. in the absence of imposed tectonic deformation. Structure modification due to diagenetic processes are studied and geomechanical models are constructed and tested via simulations. The Opal A/CT transformation is studied in detail but the applicability of the proposed model(s) to other reactions whose characteristics may differ are also discussed.

4.1 PFS Formation Due to Early Silica Diagenesis

4.1.1 Rationale

Examination of evidence discussed in Chapter 2 indicates that diagenetic structure changes affect porosity, material strength, and failure modes. Furthermore, in the post-yield configuration the rupturing of diagenetically sourced bonding, also known as destructuring, means that these meta-stable structured sediments tend to exhibit localised strain-softening behaviour. These characteristics are advantageous for promoting fault initiation at shallow depth.

4.1.2 Mechanical Response to Silica Diagenesis

Silica diagenesis involves the progressive dissolution of amorphous Opal (Opal A) and precipitation as cristobalite and tridymite, or Opal CT. Deeper burial and exposure to higher temperatures eventually results in Opal CT transforming to Quartz (Isaacs, 1982). The Opal A/CT transformation is generally associated with an approximate 20% drop in porosity, attributed primarily to the dissolution of Opal A (Spinelli et al., 2007; Neagu et al., 2010; Davies and Ireland, 2011). The reaction is principally driven by temperature, although mineralogy is also an important component. Presence of smectite is thought to inhibit the reaction, whilst it is accelerated by the presence of carbonates. The Opal A/CT diagenetic transformation is targeted for initial investigations related to structure development and breakdown. This is influenced by the following considerations;

1. There is a noted coincidence of Opal A/CT diagenetic boundaries and PFS, potentially suggestive of some causal relationship (Davies et al., 2009; Praeger, 2009; Neagu et al., 2010; Cartwright, 2011; Davies and Ireland, 2011).
2. The Opal A/CT reaction is known to occur at relatively shallow depths, certainly less than 1km in depth, and so coincides with the range of depths over which PFS are believed to form.
3. The reaction takes place on a regional scale, with the strong seismic reflection event (increase of acoustic impedance) corresponding to the transition typically observed over large areas of the basin.
4. Diatomaceous sediments that may become altered during the Opal A/CT transformation are known to be structured and resist consolidation, owing to the presence of nanofossils such as diatoms which provide a strong, stiff rock matrix. These sediments,

therefore, already exist in a "meta-stable" condition and further alteration of the structure through dissolution and precipitation followed by mechanical breakdown may result in post-peak softening.

5. Experimental studies of early diagenesis, diatomaceous oozes and siliceous rocks (mainly in ODP cruise reports) provide sufficient data to populate the mechanical and chemical material parameters.

The affect that the Opal A/CT diagenetic transformation has on the mechanical properties of mudstones is generally poorly understood, however two relevant case studies which have focused on this topic are discussed below.

4.1.2.1 Horonobe Case Study

Recent work at the site of the Horonobe Underground Research Laboratory (URL) in Hokkaido, Japan has provided the motivation to establish the mechanical strength and porous flow characteristics of massive siliceous mudstones (Ishii et al., 2011). The URL is located on the eastern margin of a Neogene-Quaternary sedimentary basin on the western side of northern Hokkaido. The basin fill consists of the Wakkanai, Koetoi, Yuchi and Sarabetsu formations (from bottom to top). The two layers of interest are the Wakkanai and Koetoi formations. The Wakkanai formation is composed mainly of massive and homogeneous siliceous mudstone rich in Opal CT (40-50 wt.%). The overlying Koetoi formation is a massive and homogenous diatomaceous mudstone rich in Opal A (40-50 wt.%). Detailed study of the Wakkanai and Koetoi formations has shed light on how diagenetic processes affect the mechanical strength of siliceous rocks.

Figure 4-1 displays the variation in physical properties within the diatomaceous and siliceous mudstones. The authors highlight some interesting trends in the data. There are spikes in the strength data at the transition zone between the Koetoi and Wakkanai formation. These trends correspond to an approximate 20% reduction in porosity over a fairly small interval. This porosity reduction is attributed to the Opal A to Opal CT diagenetic transformation.

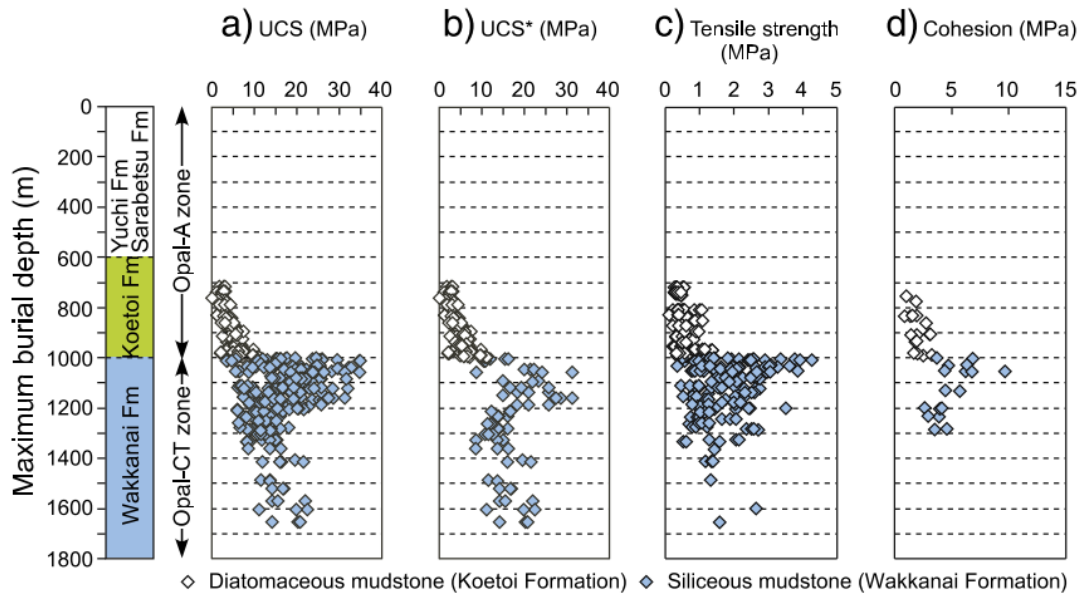


Figure 4-1: Strength profiles across Opal A/CT transition zone (Ishii et al., 2011). The transition zone that straddles the interface between the Koetoi and Wakkanai Formations is observed to coincide with large variations in unconfined compressive strength (UCS), tensile strength and cohesion.

The evolution of porosity and material state across the Opal A/CT boundary is summarised in Figure 4-2. Mechanical compaction dominates above and below the transition zone. Within the transition zone, additional volume change takes place due to the dissolution of the siliceous tests, as well as cementation due to Opal CT precipitation.

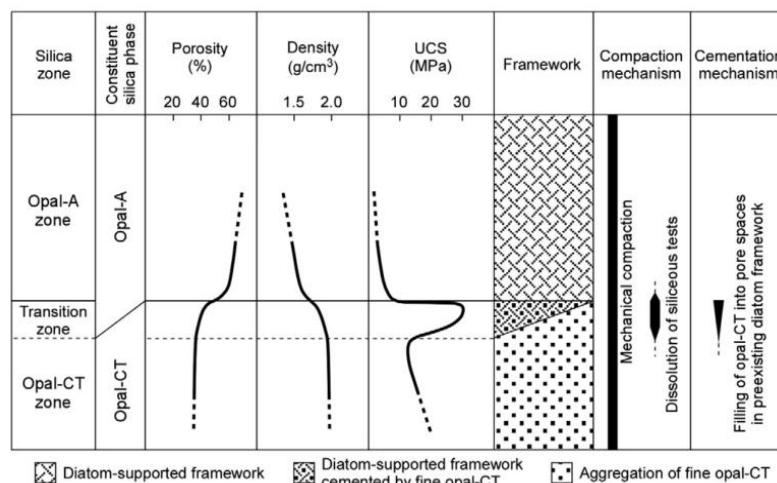


Figure 4-2: Evolution of material state across Opal A/CT transition zone (Ishii et al., 2011).

The effect of the diagenetic transformation on specimens above and below the transition zone

Incorporating the Influence of Burial Diagenesis at Shallow Depths

is also covered in a complementary paper which features triaxial testing of samples at various confining pressures (Sanada et al., 2009), see Figure 4-3. The tests at confining pressures of $1.5\sigma'$ for the diatomaceous mudstone and $0.25\sigma'$ for the siliceous mudstone are roughly comparable in terms of magnitude. The response for the diatomaceous mudstone is diffuse with perhaps the presence of some compaction bands. Conversely, the siliceous mudstone shows very brittle failure with high angle shear bands. Similar trends have been observed in analysis of the Opal A/CT transition in the Monterey formation, California (Ireland, 2011).

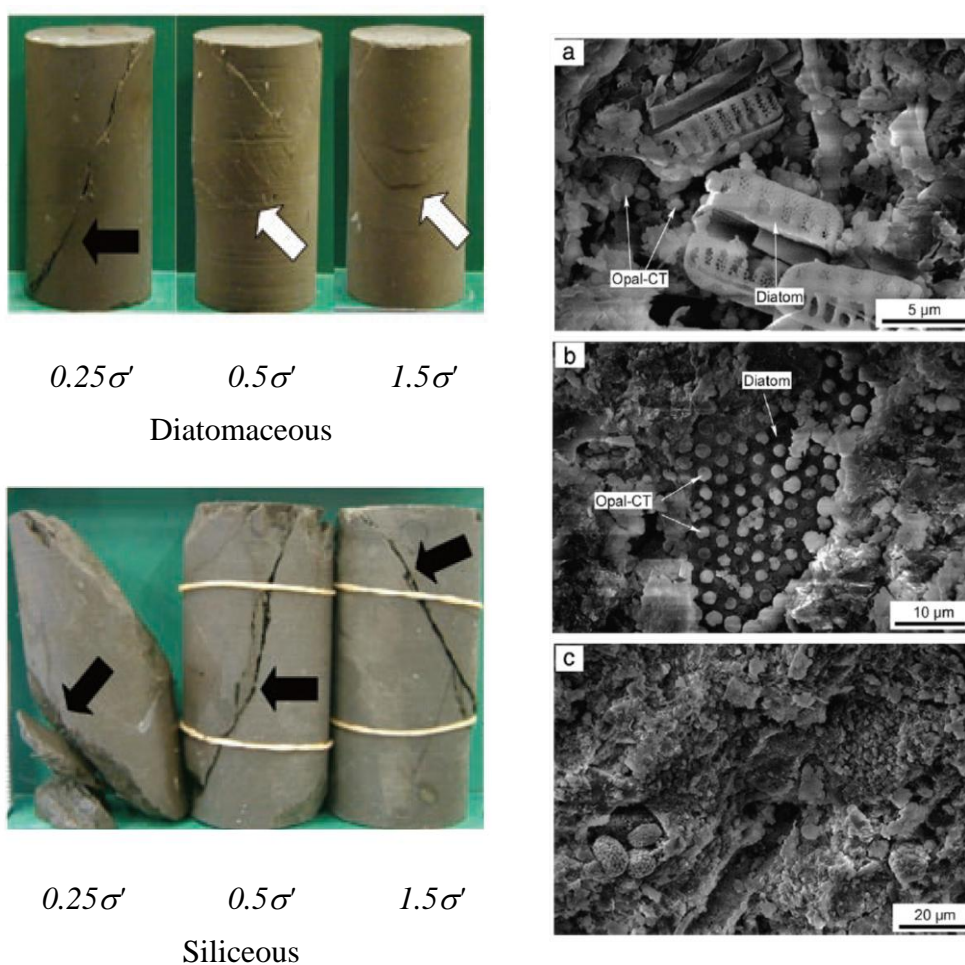


Figure 4-3: Triaxial tests above and below the transition zone at the site of the URL at Horonobe. SEM images showing microstructure for (a) Diatomaceous mudstone just above transition zone (b) Transition zone (c) Siliceous mudstone just below the transition zone.

The siliceous samples exhibit strain softening behaviour regardless of the level of confining pressure, indicative of *overconsolidation*. The source of the disparity in the response of material samples is inferred to be *diagenetically influenced structural changes*. Scanning

Electron Microscope (SEM) images display the variation in microstructure and are shown in Figure 4-3 (Ishii et al., 2011). Image Figure 4-3(a) shows an SEM image of a sample just above the transition zone in the diatomaceous mudstone where an intricate network of diatoms with some Opal CT filling the spaces between them is observed. Image Figure 4-3(b) is of a sample taken from the siliceous Wakkanai formation. There is some noticeable dissolution of the Opal A rich diatoms, but they remain structurally intact. Opal CT is precipitated in the pore space and acts to significantly strengthen the rock matrix. This is proposed as an explanation of the anomalous strength profile. In Figure 4-3(c) taken from the Wakkanai formation some distance below the transition zone it is obvious that the diatom supported framework has been completely destroyed and replaced by aggregates of relatively fine and equigranular Opal CT. This study indicates that the reaction probably involves the following main sequence; (a) small volume changes at the beginning of the reaction with the material becoming significantly stronger as Opal CT is precipitated, (b) larger volume changes as Opal A dissolution increases but not to the extent where the diatoms are completely destroyed, and (c) complete destructuration due to more severe dissolution of Opal A and increasing mechanical load.

4.1.2.2 Nankai Trough Case Study

Further study of this reaction front was performed as part of the Ocean Drilling Project. ODP investigations and seismic data from the Nankai Trough make it very useful as a case study. The site has been extensively studied and has provided a wealth of data related to the diagenetic processes that effect hemipelagic sediments (Heffernan et al., 2004; Ienaga et al., 2006; Spinelli et al., 2007). (Spinelli et al., 2007) investigate diagenesis and sediment strength relationships using data from ODP wells 1173, 1174 and 1177. Wells 1173 and 1177 lie approximately 10km away from the deformation front, with 1174 sited much closer. The study provides a large amount of important data relating to thermal gradients, sediment age and strength profiles. From top to bottom the stratigraphic units of note are the Nankai trench wedge facies, Upper Shikoku Basin facies and Lower Shikoku Basin facies. Below these units is a basement of volcanoclastics and basalt. The Nankai trench wedge facies occupies approximately the first 90 to 100mbsf and is composed of a mix of hemipelagic mud and sandy/silty turbidite sequences. The Upper Shikoku Basin facies occupies the interval between 100 and 350mbsf. It is predominantly composed of hemipelagic mud and contains an abundance of ash layers in various stages of alteration.

Incorporating the Influence of Burial Diagenesis at Shallow Depths

The Lower Shikoku Basin facies is also mainly hemipelagic mudstone but does contain a smaller number of ash layers which are noticeably altered. The base of the Lower Shikoku Basin facies is young and was deposited within the last 5My. The temperature gradient is particularly steep with temperatures in excess of 50°C being reached within the first 250m. The focus here is given to well 1173, but similar trends are observed across all data sets. Figure 4-4 displays the porosity depth trend for well 1173. There is a noticeable deviation from the assumed compaction trend at approximately 100m. This corresponds to the boundary between the Upper Shikoku Basin facies and the Nankai trench wedge facies. Below this depth there is very little porosity change with depth and the porosity remains constant at around a value of 0.6. At the transition between the Upper and Lower Shikoku Basin Facies, ca. 350m depth, there is a sharp change in the porosity, with an approximate reduction to a value of 0.4. Backscattered electron images of sediments within the Upper Shikoku Basin facies at a depth of 219mbsf are shown in Figure 4-5A. Black regions indicate regions of porosity and light grey indicates areas of greatest density. The dark grey material is Opal, although it is not obvious from a petrographic analysis whether this material is Opal A or Opal CT. The Opal is more clearly imaged in Figure 4-5B where it appears in yellow, and it is clear that the Opal is present as a coating around grain contacts.

The authors venture a conceptual model to explain the anomalous porosity profile and suggest that Opal diagenesis is the cause. More specifically, precipitation of small amounts of Opal CT coats the grains and cements the rock matrix to an extent that porosity loss is inhibited and the trend deviates from the expected progressive loss of volume with depth (as followed in traditional stress driven soil mechanics theory). The sudden loss of porosity is attributed to breakdown by mechanical loading with additional dissolution of Opal A.

It should be noted that the exact diagenetic processes that are taking place within these sediments is still not fully understood and may involve other reactions, such as the diagenesis of water-lain volcanic ash deposits (Cartwright, 2011), which are thought to be distributed throughout the apparently cemented section (White et al., 2011).

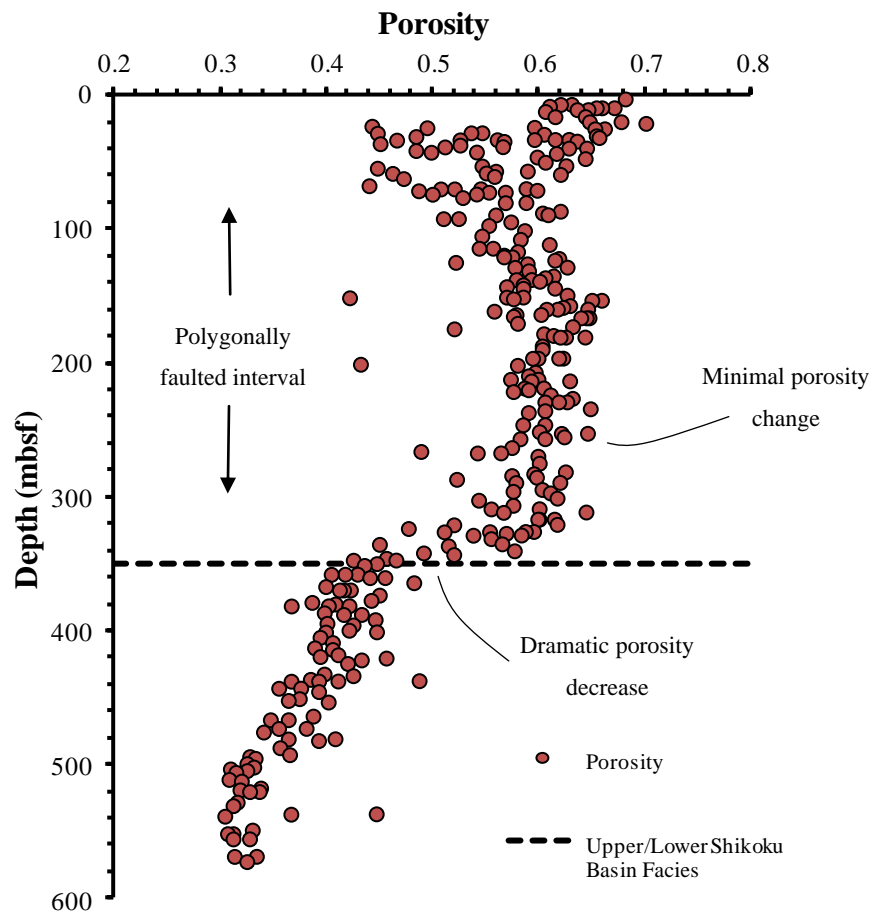


Figure 4-4: Porosity profile for well 1173 (Spinelli et al., 2007).

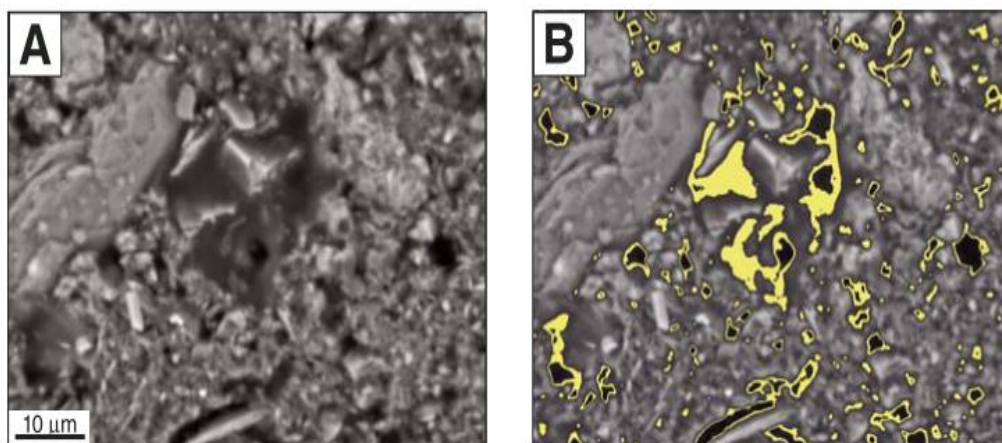


Figure 4-5: Opal acting to cement pore-space (Spinelli et al., 2007). A shows an SEM image from a sample taken from the Upper Shikoku Basin facies. B indicates regions of inferred Opal cement.

4.1.2.3 Summary of Case Studies

From these two cases it appears that during the Opal A-CT reaction there is a substantial modification of the material state. This is attributed to both the dissolution of Opal A, which serves to provide a dramatic porosity reduction, and precipitation of Opal CT which acts to cement the rock matrix. Increase in cohesion and tensile and compressive strength are observed. Triaxial testing also indicates that the post-yield material response of Opal A and Opal CT rich sediments is very different and is attributed to the pseudo-overconsolidation provided by Opal CT precipitation.

4.2 Geomechanical Argument

The typical mechanical response of a mudstone loaded in the vertical direction from a zero initial stress state is shown in Figure 4-6. The stress path intersects the yield surface to the right of the critical state line on the compression cap. The sediment loses volume and the yield surface increases in size, reflecting the increased domain in which the sediment may behave elastically. The argument presented here is that volume change due the dissolution of Opal A will modify the stress path. In effect a strain is imposed due to dissolution and the likely outcome is deviation from the K_0 line (Figure 4-7). A change in stress state due to diagenesis is not unprecedented and it has been acknowledged for some time that a horizontal stress drop might be expected as a result of diagenesis (Bjorlykke and Hoeg, 1997). This has been expanded on in experimental studies of the effect of dissolution processes (Shin et al., 2008). In the study by (Shin et al., 2008), mixtures of glass beads and soluble salt (NaCl) were vertically loaded in an experimental apparatus that was able to monitor the horizontal stress evolution whilst maintaining K_0 conditions. The salt was then gradually dissolved and the change of horizontal stress was monitored. The grain rearrangement, forced by the dissolution of the salt grains, results in a macro-scale drop in horizontal stress, which in turn equates to the value of K_0 reducing from ca 0.67 to ca. 0.43. As the vertical stress is constant, this corresponds to an increase in deviatoric stress and a reduction in effective mean stress, increasing the likelihood that shear failure could be triggered due to the dissolution process. For localisations to occur the authors note that the material would have to exhibit post-peak strain softening characteristics.

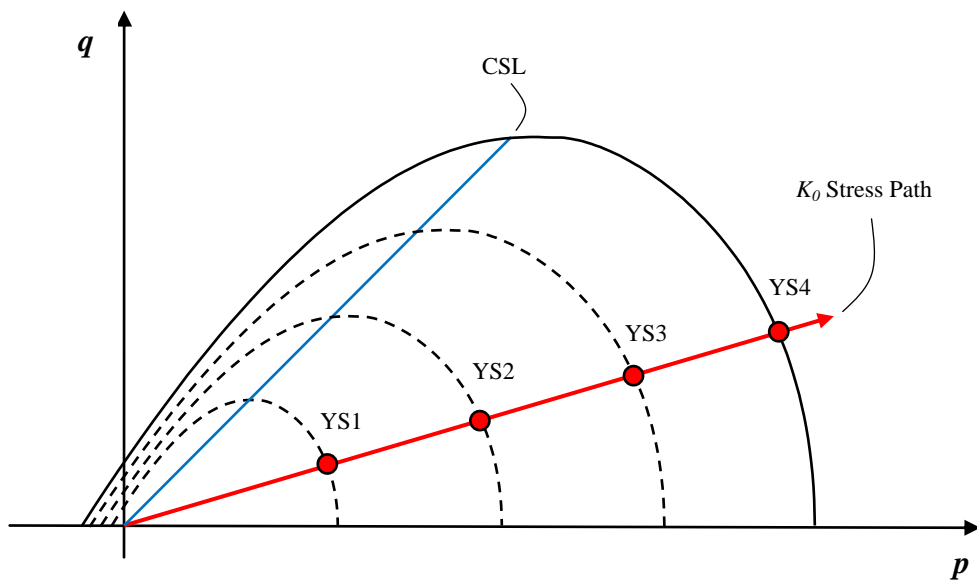


Figure 4-6: Mechanical only response (normal consolidation behaviour). Final state boundary surface is shown with the solid line. Red line represents the stress path and the blue line represents the critical state line that separates shear and compaction.

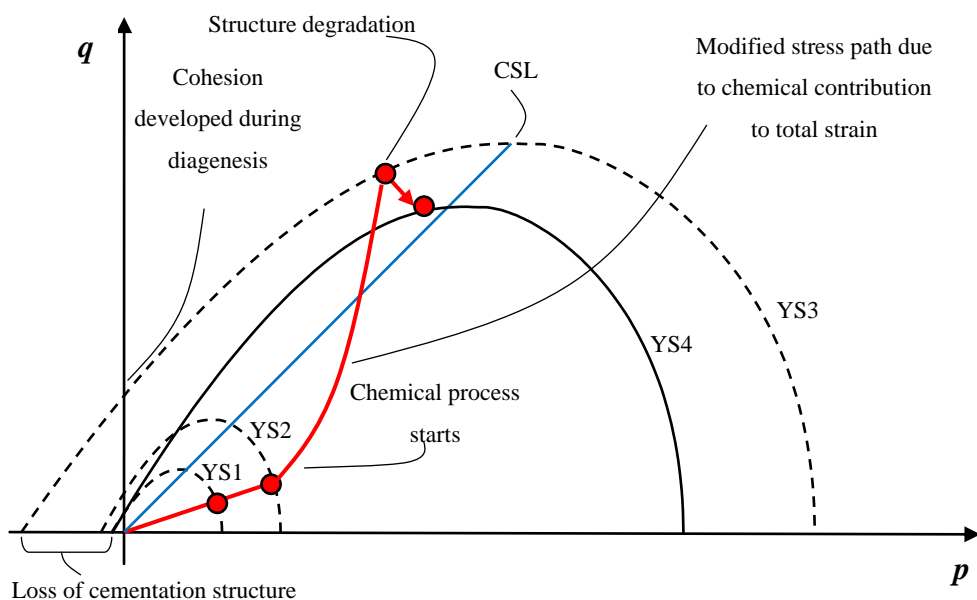


Figure 4-7: Conceptual model of the effect of chemical compaction on material response. Final state boundary surface is shown with the solid line. Red line represents the stress path and the blue line represents the critical state line that separates shear and compaction.

It is obviously difficult to precisely calibrate and capture the deformation processes that occur within the transformation zone. However, here we follow the evolutionary process described in the Horonobe case study (Ishii et al., 2011) and assume that once the activation temperature is reached then the volume reducing mechanisms will be due to both mechanical and chemical processes. Dissolution and precipitation will cause volume changes and deviations from the K_0 line. Additionally, precipitation of small amounts of Opal CT will start to cement the rock matrix resulting in a pseudo-overconsolidation and principally an increase in cohesion/tensile strength. As the reaction moves to completion the stress state may then be favourable for failure in shear and the developed cement will be broken down during destructuration. As such, the primary focus is on the pseudo-overconsolidation of the material and the chemical contribution to total strain. Given a large enough increase in cementation, the response may become governed by the elastic response and the material stress path will deviate from the K_0 line. Once the reaction moves to completion the formation may not be able to sustain the increasing mechanical load and will reach a failure state. Additionally, if dissolution processes become more dominant, the formation will become weaker and this will assist in triggering shear failure, as discussed by (Shin et al., 2008).

The Nankai Trough data shows similar volume change due to the Opal A/CT transformation as well as some cementing above the transition zone. However, it is once again stressed that the exact sequence of reactions in this section is unclear (Praeger, 2009; Cartwright, 2011). The transformation of volcanic ash to smectite, Opal CT and zeolites could have additional, unexpected impacts on the modelled reaction. Examination of the experimental test data for these sediments indicates a degree of pseudo-overconsolidation that is tentatively attributed to cementation structure, as shown in Figure 4-8.

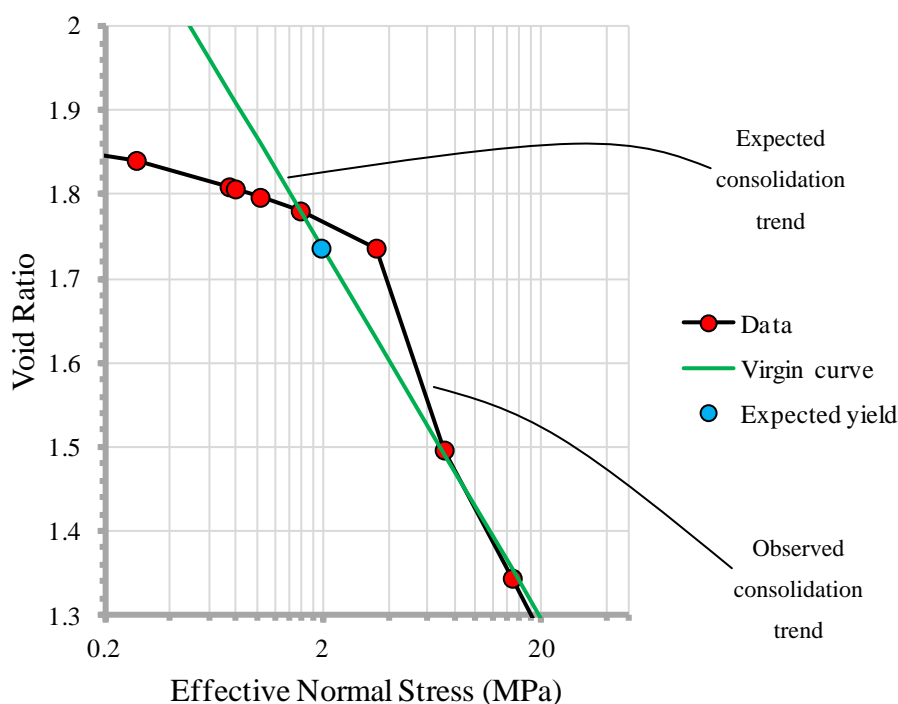


Figure 4-8: Consolidation data from Nankai Trough (Spinelli et al., 2007).

It also seems likely that the transformation of volcanic ash is associated with a change in volume, although this is potentially more subtle than the reduction associated with Opal A/CT. There are also arguments that the diagenesis of volcanic ash is isovolumetric, i.e. there is no net volume reduction during the transformation (Cartwright, 2011). In order to maintain a level of simplicity and make the results easier to interpret we assume that the argument presented above will suffice for also treating this reaction and this is covered in more detail in Chapter 5. Unfortunately, the variable nature of both the reactions and the response of the sediment at different localities is a fundamental and unavoidable consequence of the complexity of mudstone diagenesis.

To provide additional context, a model for PFS genesis founded on the critical state framework has recently been suggested to explain PFS genesis in the Vøring Basin (Laurent et al., 2012). In this model, which is not explained in great detail, the authors suggest a theory where 'strain hardening occurs' and this leads to deviation from the stress path (Figure 4-9). The source of the strain hardening is from an increasing horizontal contraction, the source of which is not stated explicitly. The authors propose that the horizontal contraction may lead to a deviation from the K_0 line, deformation along which is associated with diffuse compaction,

Incorporating the Influence of Burial Diagenesis at Shallow Depths

and eventually prompts yield at a stress state favouring shear-enhanced compaction. In this domain both shearing and compaction may be observed.

It is also suggested that any localised deformation would be in the form of high angle shear bands. This is a slightly confusing conclusion to draw, as whilst it is essentially correct that high angle shear bands will develop, this angle is relative to the maximum compressive stress (Klimczak and Schultz, 2013). As such the fault dip would actually be lower in this range. High fault dips would therefore be associated with elevated pore pressures or volumetric reduction at very shallow depths (Tewksbury et al., 2014) i.e. very low effective mean stresses. It is however acknowledged that observed angles for shear-enhanced compaction bands may vary widely. Nevertheless, there are parallels with this model and the geomechanical argument proposed here in that both require a deviation from the K_0 line in order to reach stress states that favour increasing amounts of shear deformation.

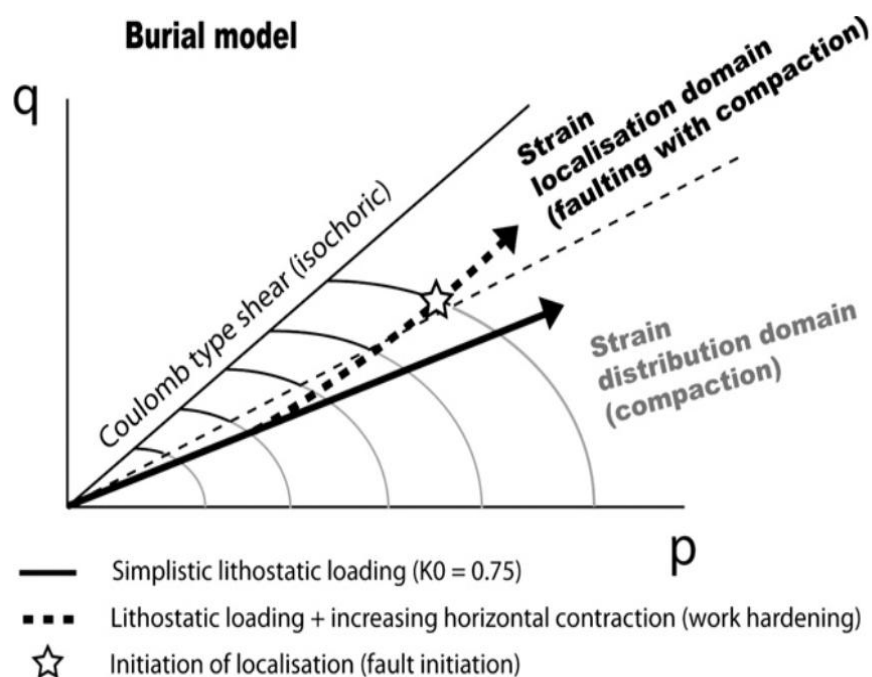


Figure 4-9: Conceptual model for PFS formation (Laurent et al., 2012). A horizontal contraction causes a deviation from the K_0 line and leads to shear-enhanced compaction.

4.3 Methodology and Implementation

4.3.1 Modelling Burial Diagenesis

The macro-scale material response must reflect the influence of both the mechanical and chemical behaviour of the sediment. The framework for considering both these processes is already in place in *ELFEN*. Owing to the small time steps associated with an explicit numerical analysis, the favoured implementation for the constitutive update is a sequential algorithm; i.e. the mechanical update is performed first with the converged stresses being corrected to account for the chemical process in a subsequent step. There is a small loss in accuracy in adopting a sequential rather than a monolithic approach; i.e. where the mechanical and chemical equations are solved simultaneously. A major advantage, however, is that additional aspects such as orthotropy or additional viscoplastic (time dependent) behaviour can be readily included if required.

The principal assumptions for the chemical compaction model are:

1. The change in porosity is the sum of the mechanical and chemically induced porosity change.
2. The chemical reaction is not initiated until an activation temperature threshold T_{low} is met.
3. A residual porosity ϕ_r is set to ensure the porosity does not become too small. Physically, this would equate to the level of porosity at which the pore space becomes completely disconnected. Given the shallow depths and modest porosity reductions this value has little influence in this study.
4. A total porosity change can be assigned to the reaction.
5. Precipitation results in a change in the tensile intercept of the yield surface.

The total change in porosity ($\Delta\phi$) is expressed as the addition of the mechanical ($\Delta\phi_m$) (elastoplastic) and chemical ($\Delta\phi_c$) (viscoplastic) contributions:

$$\Delta\phi = \Delta\phi_m + \Delta\phi_c \quad 4-1$$

The chemical compaction law is simply defined as;

$$\begin{aligned} \text{for } T < T_{low} \text{ or } \phi \leq \phi_r & \quad \Delta\phi_c = 0 \\ \text{for } T > T_{low} \text{ and } \phi > \phi_r & \quad \Delta\phi_c = \max\left({}^{t+\Delta t}\phi_c - {}^t\phi_c, 0\right) \end{aligned} \quad 4-2$$

Remarks 1 Diagenetic reactions are complex and dependent on a large number of factors e.g. composition, texture, mineralogy and pore-fluid chemistry, which may vary significantly depending on location. Here, the modelled reaction is assumed to be controlled by only temperature and time. The reaction is additionally assumed to be 'closed form' or locally sourced so that mass transfer is not considered. These assumptions appear valid as the Opal A/CT reaction is thought to operate on the grain scale without mass transfer over distances of more than a few millimetres.

The reaction is assumed to be controlled by two linear functions $f(T)$ and $g(t)$; i.e.

$$\phi_c = \phi_c^{\max} f(T)g(t) \quad 4-3$$

These functions are defined as;

$$f(T) = \min \left[\frac{T - T_{low}}{T_{upp} - T_{low}}, 1 \right] \quad g(t) = \min \left[\frac{t_c^{dur}}{t_c^{ref}}, 1 \right] \quad 4-4$$

The chemical volume strain increment may now be written as;

$$\Delta \varepsilon_v^c = -\ln \left[\frac{1 - {}^{t+\Delta t} \phi}{1 - {}^t \phi + \Delta \phi_c} \right] \quad \Delta \phi_c = {}^{t+\Delta t} \phi_c - {}^t \phi_c \quad 4-5$$

In Equation 4-5 $t+\Delta t$ and t refer to porosities at the current and previous time steps respectively. Due to the sequential implementation, an update to the converged stresses from the **SR3** material model will need to be applied. The relationship between stresses and strains may be written as:

$$\boldsymbol{\sigma} = \mathbf{D}^{ie} \boldsymbol{\varepsilon} \quad 4-6$$

Where; $\boldsymbol{\sigma}$ and $\boldsymbol{\varepsilon}$ represent the vector of six stresses and total strains respectively and \mathbf{D}^{ie} is the constitutive matrix for an isotropic elastic medium. The total strain vector may be additively decomposed into a number of separate terms linked to specific physical processes. For example this might include elastic strains, plastic strains, creep strains, and importantly for this context, strains induced by chemical processes such as mineral dissolution.

The terms of the constitutive matrix for an isotropic elastic medium are shown in Equation 4-7.

$$\mathbf{D}^{ie} = \frac{E}{(1+\nu)(1-2\nu)} \begin{bmatrix} 1-\nu & \nu & \nu & 0 & 0 & 0 \\ \nu & 1-\nu & \nu & 0 & 0 & 0 \\ \nu & \nu & 1-\nu & 0 & 0 & 0 \\ 0 & 0 & 0 & 1-2\nu & 0 & 0 \\ 0 & 0 & 0 & 0 & 1-2\nu & 0 \\ 0 & 0 & 0 & 0 & 0 & 1-2\nu \end{bmatrix} \quad 4-7$$

Or in principal stress space;

$$\begin{Bmatrix} \sigma_1 \\ \sigma_2 \\ \sigma_3 \end{Bmatrix} = \mathbf{D}^{ps} \begin{Bmatrix} \varepsilon_1 \\ \varepsilon_2 \\ \varepsilon_3 \end{Bmatrix} \quad \text{where } \mathbf{D}^{ps} = \begin{bmatrix} D_1 & D_2 & D_2 \\ D_2 & D_1 & D_2 \\ D_2 & D_2 & D_1 \end{bmatrix} \quad 4-8$$

And;

$$D_1 = \frac{E(1-\nu)}{(1+\nu)(1-2\nu)} \quad D_2 = \frac{E\nu}{(1+\nu)(1-2\nu)} \quad 4-9$$

Thus, if in equation 4-5 $\Delta\varepsilon_v^c \neq 0$ a stress update is applied to account for the change in strain due to chemical processes; i.e.

$$\begin{aligned} {}^{t+\Delta t}\sigma_1 &= {}^{Trial}\sigma_1 - (D_1\Delta\varepsilon_1^c + D_2\Delta\varepsilon_2^c + D_2\Delta\varepsilon_3^c) \\ {}^{t+\Delta t}\sigma_2 &= {}^{Trial}\sigma_2 - (D_2\Delta\varepsilon_1^c + D_1\Delta\varepsilon_2^c + D_2\Delta\varepsilon_3^c) \\ {}^{t+\Delta t}\sigma_3 &= {}^{Trial}\sigma_3 - (D_2\Delta\varepsilon_1^c + D_2\Delta\varepsilon_2^c + D_1\Delta\varepsilon_3^c) \end{aligned} \quad 4-10$$

In Equation 4-10, $t+\Delta t$ refers to the final stresses at the end of the time step and *Trial* refers to the converged stresses after the short-term elastoplastic SR3 stress update. Note that principal direction 3 corresponds to the most compressive stress and the model assumes that $\varepsilon_1 = \varepsilon_2$. The contributions of the volume strain in the various principal directions may vary between uniaxial and fully volumetric depending on how the user wishes to define the flow rule. In addition, once these changes are made other state variables must be updated such as the volumetric plastic strain, ε_v^p .

4.3.2 Considering the Influence on the Hydrostatic Intercept in Tension

Diagenetic changes influence the behaviour of the sediment, particularly the intercept on the hydrostatic axis in tension, p_t . The value of p_t changes as a function of both mechanical processes (compaction and breakdown of cementation) and chemical processes (dissolution and cementation). These processes are introduced into the model by defining a new state variable which tracks the development of structure through time. The magnitude of p_t at the new time step $t+\Delta t$ is specified as the sum of the magnitude of the mechanical p_t (${}^t p_t^{mech}$) and the incremental chemical change (Δp_t^{chem}) (calculated in previous step).

$${}^{t+\Delta t} p_t = {}^{t+\Delta t} p_t^{mech} + \Delta p_t^{chem} \quad 4-11$$

The evolution of p_t^{mech} is governed by the hardening law which is defined as;

$${}^{hard} \varepsilon_v^p < {}^t \varepsilon_v^p, {}^{hard} p_t = p_t^{chem} \quad 4-12$$

$${}^{hard} \varepsilon_v^p > {}^t \varepsilon_v^p, {}^{hard} p_t = p_t^{chem} * e^{\left(\frac{(-{}^{hard} \varepsilon_v^p) - {}^t \varepsilon_v^p}{A} \right)} \quad 4-13$$

Concisely, Equation 4-12 indicates that for a value of volumetric plastic strain less than the current volumetric plastic strain (i.e. further compression), the value of p_t is equal to the current level of p_t^{chem} . The consequence of this assumption is that any further mechanical compaction is assumed to have little influence on the level of cementation. Equation 4-13 indicates that if the next increment of volumetric plastic strain is positive (the material is dilating) then the hardening curve governing the evolution of p_t is expressed by the exponential function and the destructuring of the material can be represented. The parameter A is used to control the severity of structure removal and would need to be evaluated using sensitivity studies. The implementation is summarised in Figure 4-10.

A convenient consequence of this particular implementation is that as p_t becomes larger, the severity of destructuration increases. As noted in Chapter 2 this is consistent with observation. The implementation above follows similar methodology to other publications in which destructuring of pre-defined fabric is studied. Unlike this study, however, most previous work is focused on solely on structure degradation of structured or bonded sediments. Nevertheless, structure is often factored into the governing equations via modifications to the equations governing material hardening, as replicated here. The influence of structure on the

elastic properties, which in some cases may be significant, is not considered.

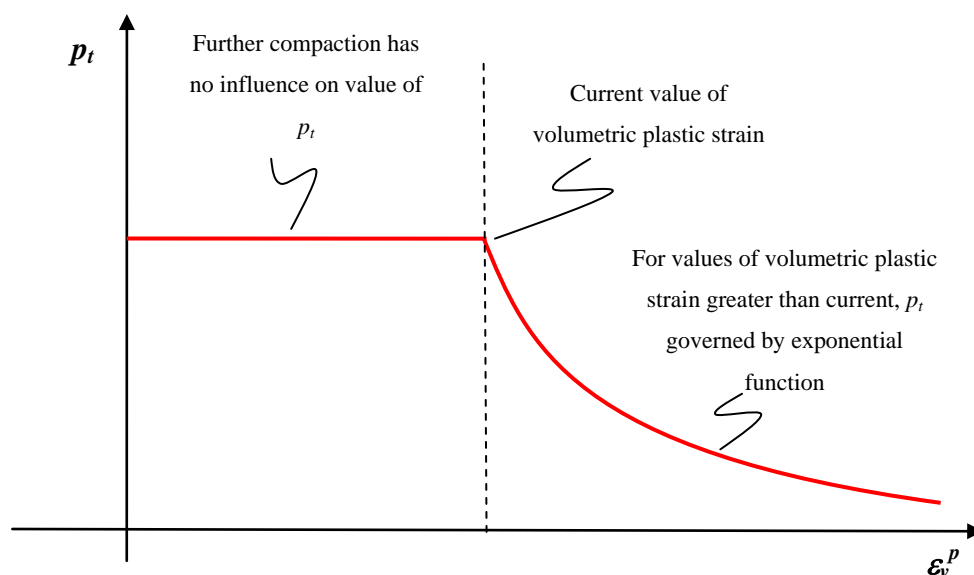


Figure 4-10: Treatment of tensile intercept on hydrostatic axis, p_t , incorporating mechanical and chemical behaviours.

4.3.3 Comments on the Modelling of Diagenesis

Naturally, despite physical justifications, the suitability of the proposed chemical compaction model for forward modelling can be questioned on the basis of the simplified assumptions. It is noted here that the methodology bears similarities to existing diagenetic models which are related to dissolution and re-precipitation processes in other lithologies (Walderhaug, 1996, 2000). The assumption is made here that the macroscopic mechanisms, in terms of the geomechanical model, for the Opal A/CT diagenetic transformation, and potentially other diagenetic processes, can be adequately represented using this simplified model. Clearly there are likely to be differences, but fundamentally all the model seeks to replicate is the volume change due to the diagenetic process and the consequences of this for the stress path and material state. As such it is judged that the existing framework, in conjunction with the modifications highlighted in the previous section, provide a suitable model to capture the evolution of sediments as they undergo this transition.

4.4 Material Characterisation

This section focuses on the characterisation of a generic diatomaceous sediment. Characterisation of a diatomaceous sediment that can be used for investigation of the Opal A/CT transition requires consideration of both the mechanical and chemical components of

the constitutive model.

4.4.1 Mechanical Behaviour

Characterisation of the mechanical response using the SR3 constitutive model requires definition of: stress-dependent poroelastic properties, yield surface shape, plastic potential shape, and hardening properties.

Parameter	Value
Poisson's Ratio (ν)	0.30
Reference Porosity (ϕ_{ref})	0.66
Reference Bulk Modulus (K_0)	10.00 MPa
Slope of URL (κ)	0.09

Table 4-1: Selected poroelastic properties.

The material model parameters for the sediment are specified in Table 4-1. The elastic response is assumed to be isotropic and consequently may be described by the Elastic Modulus and Poisson's ratio, both of which reflect values for a standard mudstone. The reference porosity is selected to reflect the average porosity observed in several publications (Volpi et al., 2003; Ishii et al., 2011), although depositional porosity for diatomaceous sediments can be significantly higher. To prevent the bulk modulus, K , from acquiring a small value at low or zero confinement a small a reference value of 10MPa is specified. The gradient of the unloading-reloading line, κ , describes the volume loss relative to increasing load when the stress state is within the yield surface. The selected value reflects a fairly stiff material. The shapes of the yield surface and plastic potential must also be described and parameters used are listed in Table 4-2. The sediment is given a low initial strength (i.e. overconsolidated to ca. 10m burial depth) to avoid instabilities, and the yield surface in principal stress space and the p - q plane is shown in Figure 4-11. Given the limited experimental data that is available values for parameters describing the yield surface shape in the meridian plane, β , ψ , and n , have been chosen that are representative of shales/mudstones. Parameter β has been calibrated so that the approximate friction angle is 30° , which is suitable for shallow diatomaceous sediments (Lee et al., 1990; Sanada et al., 2009). A similar process has been followed for describing the yield surface in the deviatoric plane.

4.4.2 Chemical Behaviour

Like the mechanical data, the chemical compaction properties are populated using data from the literature e.g. ODP cruises. Lower and upper bound temperatures for the reaction vary

Incorporating the Influence of Burial Diagenesis at Shallow Depths

widely. Temperature ranges of 25-50°C are often quoted (Neagu et al., 2010; Davies and Ireland, 2011), however it seems that temperatures as low as 17°C or indeed lower may be sufficient in some cases (Matheney and Knauth, 1993). The maximum change in porosity is reported to be around 20% (Meadows and Davies, 2009; Davies and Ireland, 2011; Ishii et al., 2011). Values of porosity reduction in the range 5% to 20% are tested in the presented simulations, which corresponds to the range reported in ODP reports (Neagu et al., 2010). The reference duration for the reaction is assumed to be quite rapid as there is evidence that the reaction occurs within a few million years given sufficiently high thermal gradients (Spinelli et al., 2007; Ishii et al., 2011; Henry et al., 2012). The value of 0.03 is applied for the residual porosity. Physically, this is the porosity at which pore space becomes disconnected, but as noted is of little consequence here. These parameters are summarised in Table 4-3.

Parameter	Value
Initial tensile intercept (p_{t0})	-0.10 MPa
Initial compressive intercept (p_{c0})	1.50 MPa
Parameter (β)	55°
Parameter (ψ)	50°
Exponent (n)	1.6
Deviatoric plane parameter (N^{π})	0.25
Deviatoric plane parameter (β_0^{π})	0.7
Deviatoric plane parameter (β_1^{π})	1.73E-01 (1/MPa)

Table 4-2: Plastic properties for definition of SR3 yield surface and plastic potential.

Note negative values indicate tension.

A new flow rule has been introduced in the chemical compaction model that allows the volume change during diagenesis to be expressed as either an orthotropic or fully volumetric strain. This change is expected to be significant in terms of modification to the stress path and both uniaxial and volumetric flow rules are investigated in the study.

Parameter	Value
Threshold temperature (T_{low})	18.0 °C
Upper reference temperature (T_{upp})	35.0 °C
Maximum porosity change ($\phi_{c,max}$)	Varies between 0.05 and 0.2
Reference duration (t_{ref})	5.0 My
Residual porosity (ϕ_{res})	0.03
Flow rule factor	Varies (either 0 or 1)

Table 4-3: Chemical properties for Empirical Diagenetic Law.

Incorporating the Influence of Burial Diagenesis at Shallow Depths

Finally, parameters are specified for the maximum allowable change in p_t over the duration of the reaction, as well as the rate at which destructuring of the material occurs should the yield surface be intersected in shear. These parameters reflect a rapid destructuring post yield - see Table 4-4.

Parameter	Value
Destructuring Parameter (A)	2E-03
Maximum p_t change (p_t^{max})	3.0 MPa

Table 4-4: Structure properties.

4.4.3 Comments on Material Characterisation

The characterisation of the mechanical and chemical response of the material necessitates the selection of a fairly large number of parameters. In total, a minimum of 21 values are required, of which 8 are needed to describe the chemical response. There is consequently potential for the difficulties in interpreting the results and the problem to become poorly constrained. Three points are raised to address these concerns:

1. The chemical compaction law is designed to be as simple as possible.
2. Introducing additional components, such as consideration of porous flow (i.e. exploring the possibility of undrained conditions and excess pore pressures), would further increase the number of parameters required.
3. Where possible parameters have been sourced from published data or using reasonable approximate values.

It is therefore stressed that despite the large number of input parameters, these are the minimum number required to address the physics of this complex problem.

4.5 K_0 Compaction - Single Element Test

Uniform K_0 Compaction can be investigated using a model for a soil sample that is represented by single finite element. A 10m by 10m element is exposed to linearly increasing vertical stresses in the range 0 - 20MPa (so depth to approximately 4km) over 20My. The element is simultaneously exposed to linearly increasing temperatures which increase from an initial temperature of approximately 10°C to an upper temperature of 100°C over the duration of the simulation. This reflects a fairly low thermal gradient of ca 25°C/km. Roller boundary conditions at the base restrict vertical movement. Rollers on the side boundaries

Incorporating the Influence of Burial Diagenesis at Shallow Depths

permit vertical movement but restrict lateral movement so that the K_0 condition is replicated. The single element test setup is shown diagrammatically in Figure 4-12 provides a visualisation of the volume reduction for cases where only mechanical compaction is operating and where both mechanical and chemical compaction are active. The geometries at 13My highlight the obvious contribution to total volume change from diagenesis.

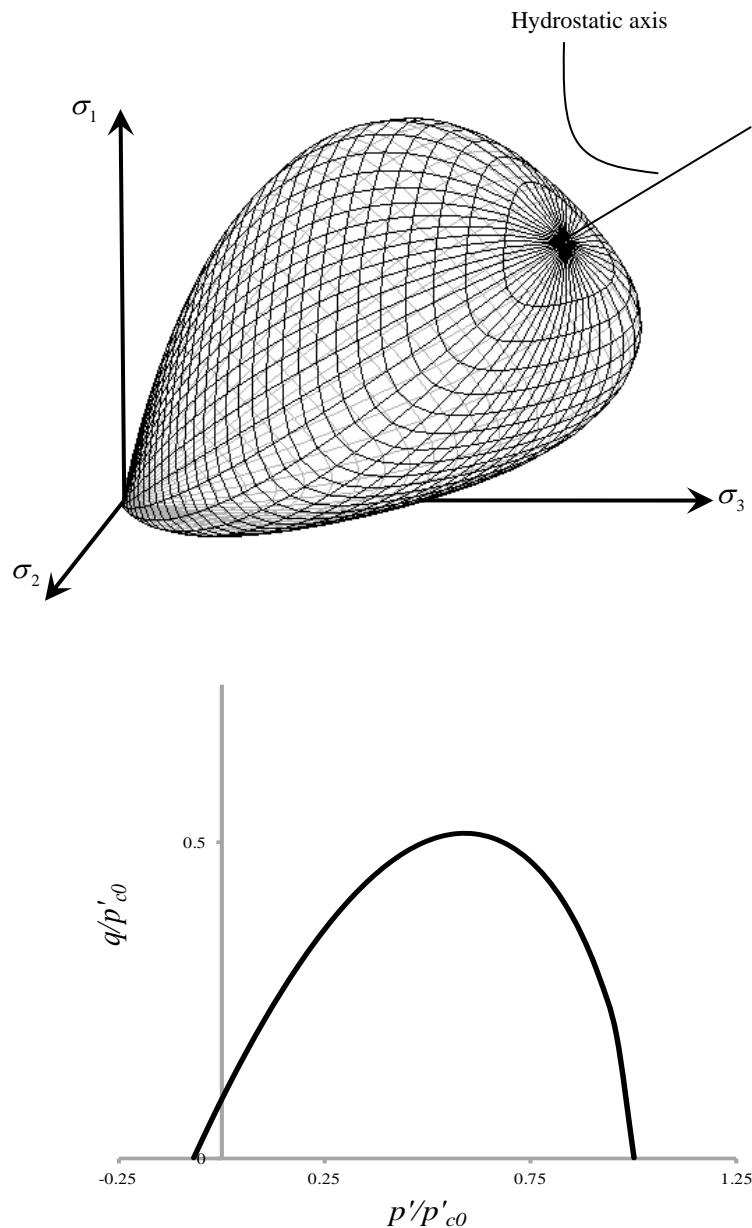


Figure 4-11: Yield surface in (a) principle stress space and (b) meridian plane (p - q space) and normalised with respect to the initial pre-consolidation pressure.

4.5.1 Mechanical Compaction Results

Initially the case where only the mechanical response is active is considered, as this provides a baseline to aid interpretation of the scenario where both mechanical and chemical compaction are active.

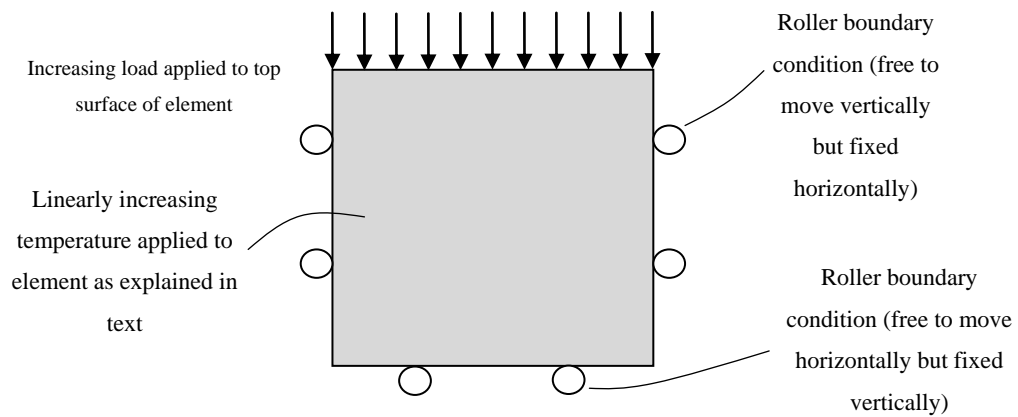


Figure 4-12: Single element simulation setup with K_0 boundary conditions.

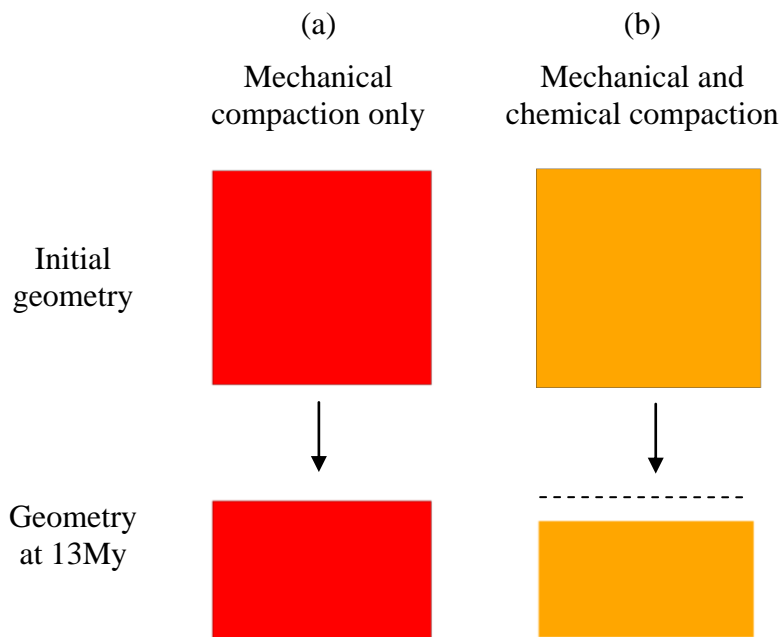
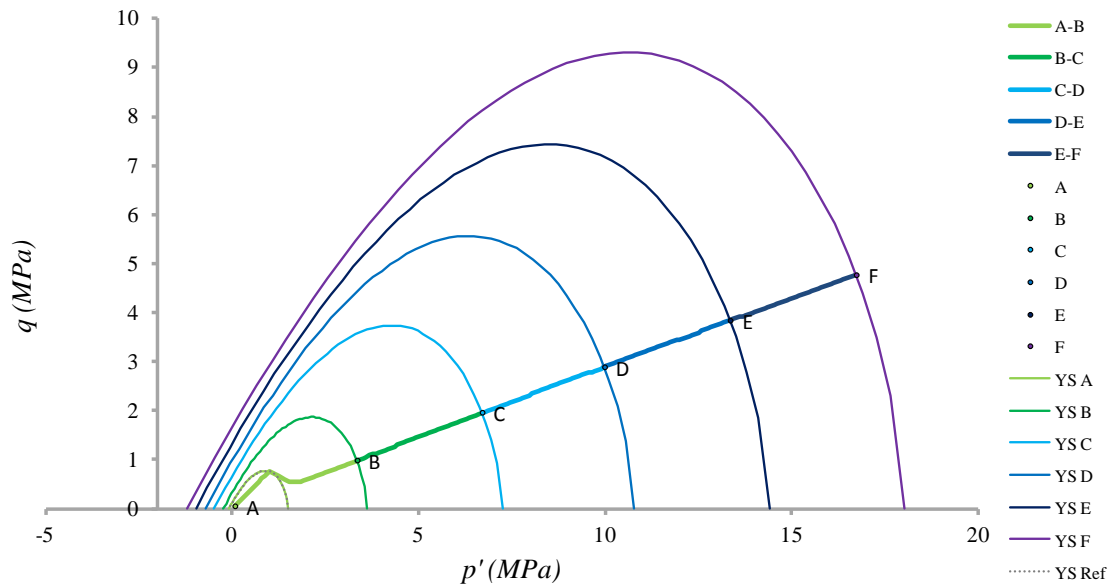


Figure 4-13: Final geometries from single element tests for cases considering (a) mechanical compaction only and (b) mechanical compaction and an additional 20% porosity loss due to diagenesis.

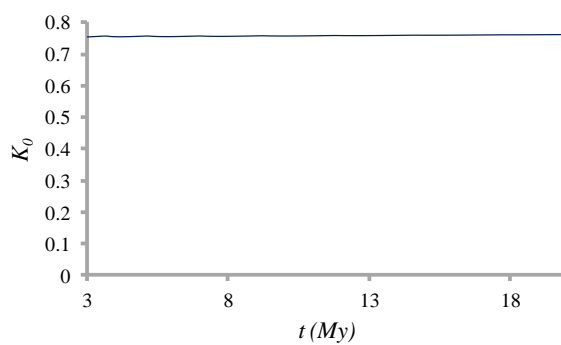
Figure 4-14(a) shows the predicted stress path and state boundary surface evolution. As expected the stress path does not deviate and maintains a constant gradient. The size of the state boundary surface increases to reflect the increasing strength of the material as it

Incorporating the Influence of Burial Diagenesis at Shallow Depths

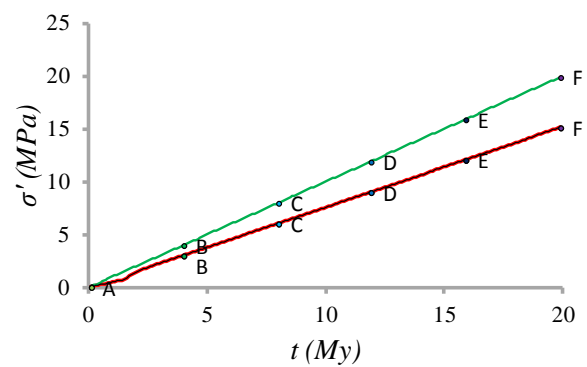
consolidates. Figure 4-14(b) and (c) show the evolution of the ratio of horizontal to vertical stress (K) and principal stress evolution respectively. These also indicate a constant ratio between the horizontal and vertical stresses.



(a)



(b)



(c)

Figure 4-14: Mechanical only response (a) stress path and state boundary surface (b) stress ratio (c) evolution of principal stresses. A constant ratio between the horizontal (red) and vertical (green) stresses is maintained throughout the simulation. The value of 0.74 is typical of mudstones and claystones (Gouly and Swarbrick, 2005).

4.5.2 Influence of Burial Diagenesis

4.5.2.1 Orthotropic Expression of Diagenetic Volume Strain

In the first case the volume change is expressed as vertical compaction, as shown diagrammatically in Figure 4-15. It is perhaps expected that due to the random orientations of the interlocking diatoms, dissolution processes might cause a volume reduction in all three directions. However, the volume strain due to other processes such as stylolite dissolution during quartz cementation in sandstones is envisaged to involve volume change but likely expressed in the vertical direction. Investigating the impact of how this change is expressed is however important as it might naturally lead to the identification of other potential mechanisms.

The evolution of the ratio of horizontal to vertical stress for various diagenetic volume changes is shown in Figure 4-16, with the flow rule defined for the orthotropic volume change scenario. In (a) a 5% change in porosity due to the chemical process is modelled.

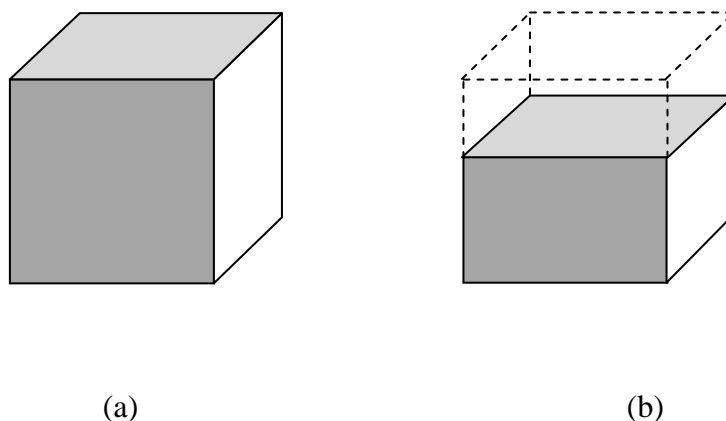


Figure 4-15: Orthotropic diagenetic volume change. (a) After mechanical compaction (b) after diagenetic volume reduction. As shown in (b), in this case the volume change attributed to the diagenetic process is expressed principally in the vertical direction.

The contribution from the chemical volume reduction is clear, and there is a noticeable drop in stress ratio. This change is fairly small however, approximately 0.12 (this is summarised for all tests in Figure 4-21). Once the chemical process moves to completion the sediment gradually returns to the K_0 condition. Cases (b) and (c) show the evolution of the stress ratio

Incorporating the Influence of Burial Diagenesis at Shallow Depths

for diagenetic volume changes of 10% and 20% respectively. It is clear that in these cases there is a more significant change in the ratio of horizontal and vertical stress, owing to the increasing increments in chemical volume change relative to sedimentation. In Figure 4-17 the evolution of the stress path and state boundary surface is shown in the meridian plane. In all cases the deviation of the stress path can be seen when compared with the stress path in Figure 4-14(a).

The chemical process is initiated between points A and B in each diagram and which also corresponds to the departure from the K_0 consolidation path. Once again, when the reaction is completed the stress path tends back towards the K_0 condition. In Figure 4-17(c) it is clear that when chemical compaction is active the stress points lie well within their corresponding state boundary surface, indicating that mechanical compaction is inhibited by the increased strength due to chemically-sourced particle dissolution and rearrangement of the matrix. Comparison between the plots in Figure 4-17 and Figure 4-14(a) also indicates that there is a significant increase in cohesion and the magnitude of the hydrostatic intercept in tension p_t , which is due to the precipitation of cements. The stress paths in the p-q plane indicate that despite deviation from the K_0 line, the sediments eventually intercept the state boundary surface on the cap (to the right of the critical state line). As such shear failure is not predicted with this material model.

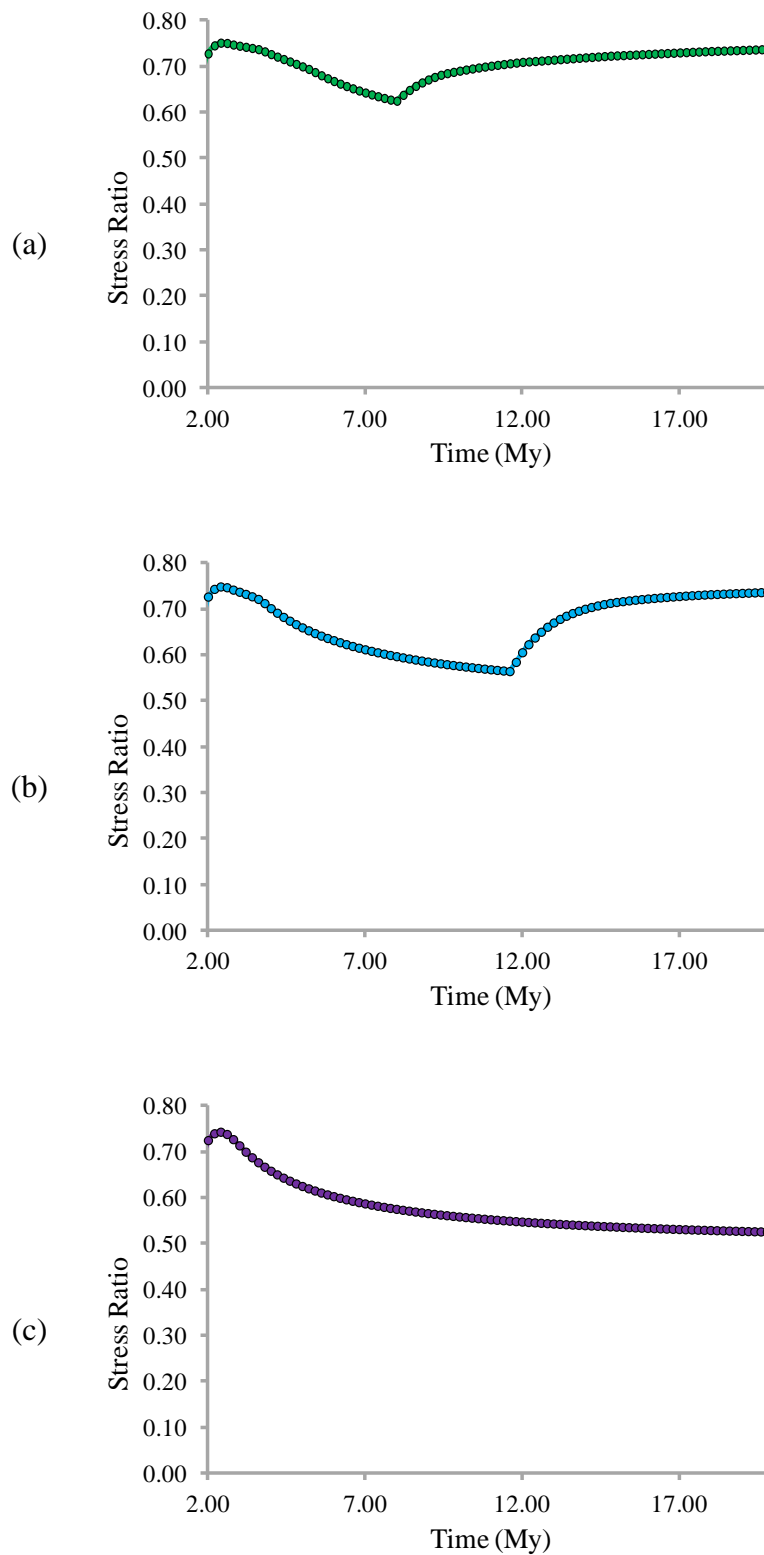


Figure 4-16: Evolution of stress ratio using the vertical compaction model for various chemical porosity changes expressed orthotropically (a) 5% (b) 10% (c) 20%.

Incorporating the Influence of Burial Diagenesis at Shallow Depths

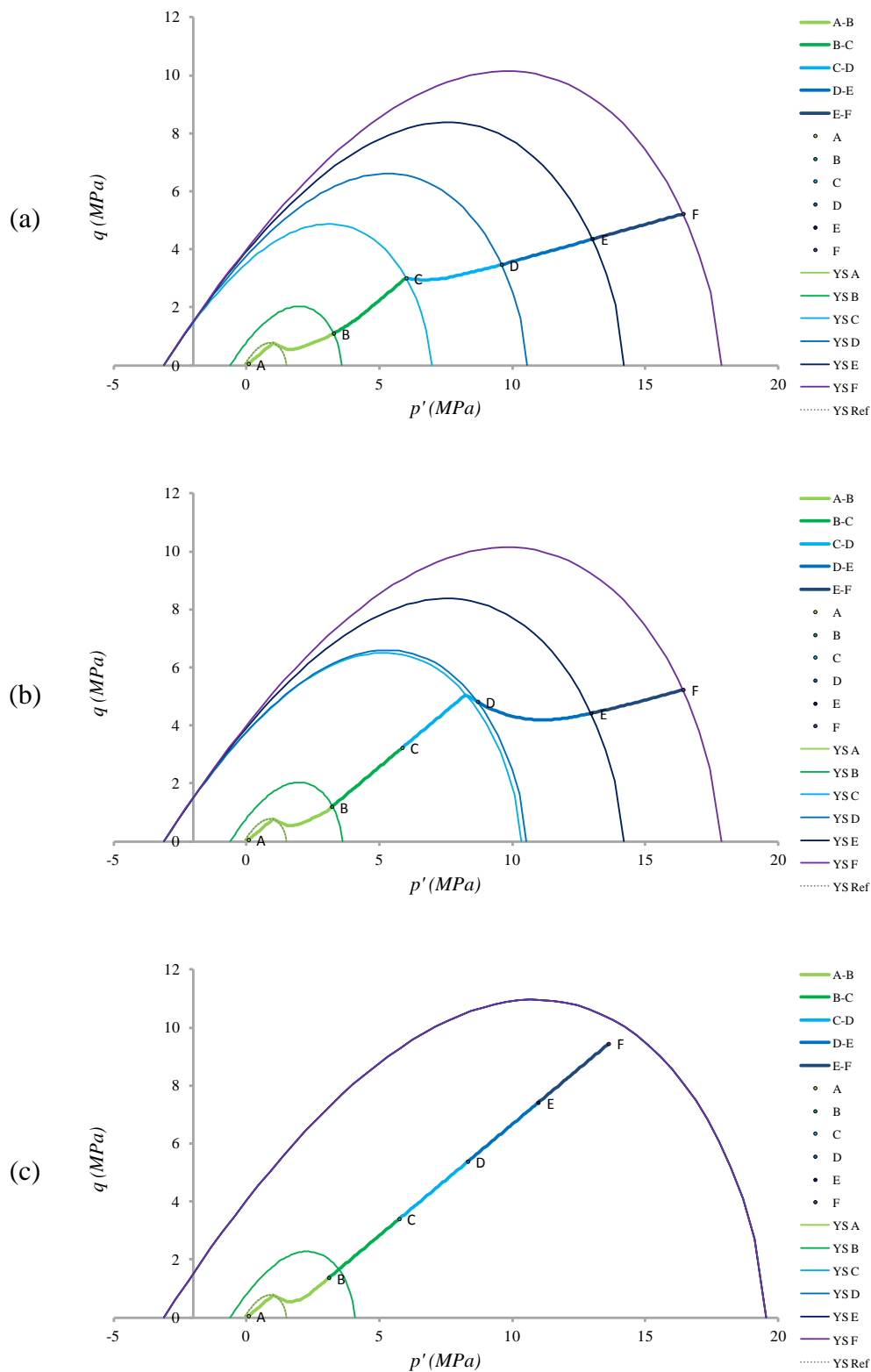


Figure 4-17: Stress path and state boundary surface evolution for various chemical porosity changes expressed orthotropically (a) 5% (b) 10% (c) 20%.

4.5.2.2 Isotropic Expression of Diagenetic Volume Strain

In this example chemical volume reduction is expressed isotropically in all three directions, as shown in Figure 4-18. Due to the fact that the reaction is now results in lateral strain in addition to vertical strain greater reduction in the K_0 stress ratio is expected.

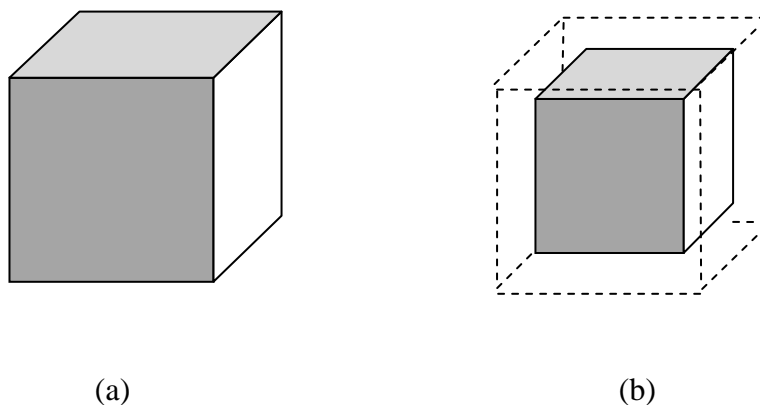


Figure 4-18: Isotropic diagenetic volume change. (a) After mechanical compaction (b) after diagenetic volume reduction. As shown in (b), in this case the volume change attributed to the diagenetic process has a component in all three axes.

Referring to Figure 4-19 the reduction in stress ratio K is clear with a larger drop in the stress ratio for all magnitudes of diagenetic volume change. This is confirmed in Figure 4-21, with the reduction in K_0 typically 0.12-0.14 less than observed in the vertical chemical compaction model. The form of the curves for the two cases are, however, similar, with the stress ratio tended back towards the K_0 condition on further burial subsequent to completion of the reaction. The stress path and state boundary surface evolution (Figure 4-20) also confirms the greater deviation of the stress path from the K_0 line. In case (a) the stress path is still intersects the yield surface to the right of the critical state line. Consequently, the additional cohesive strength due to precipitation is not lost on further mechanical yielding as the material does not fail in shear. In cases (b) and (c) however, the deviation in the stress path is sufficient to intersect the yield surface to the left of the critical state line; i.e. shear failure. For example, we observe that at point B in Figure 4-20(c) the material fails in shear and the developed cohesion from precipitation of cement is lost. However, as the reaction is still active repeated instances of structure development and breakdown are observed.

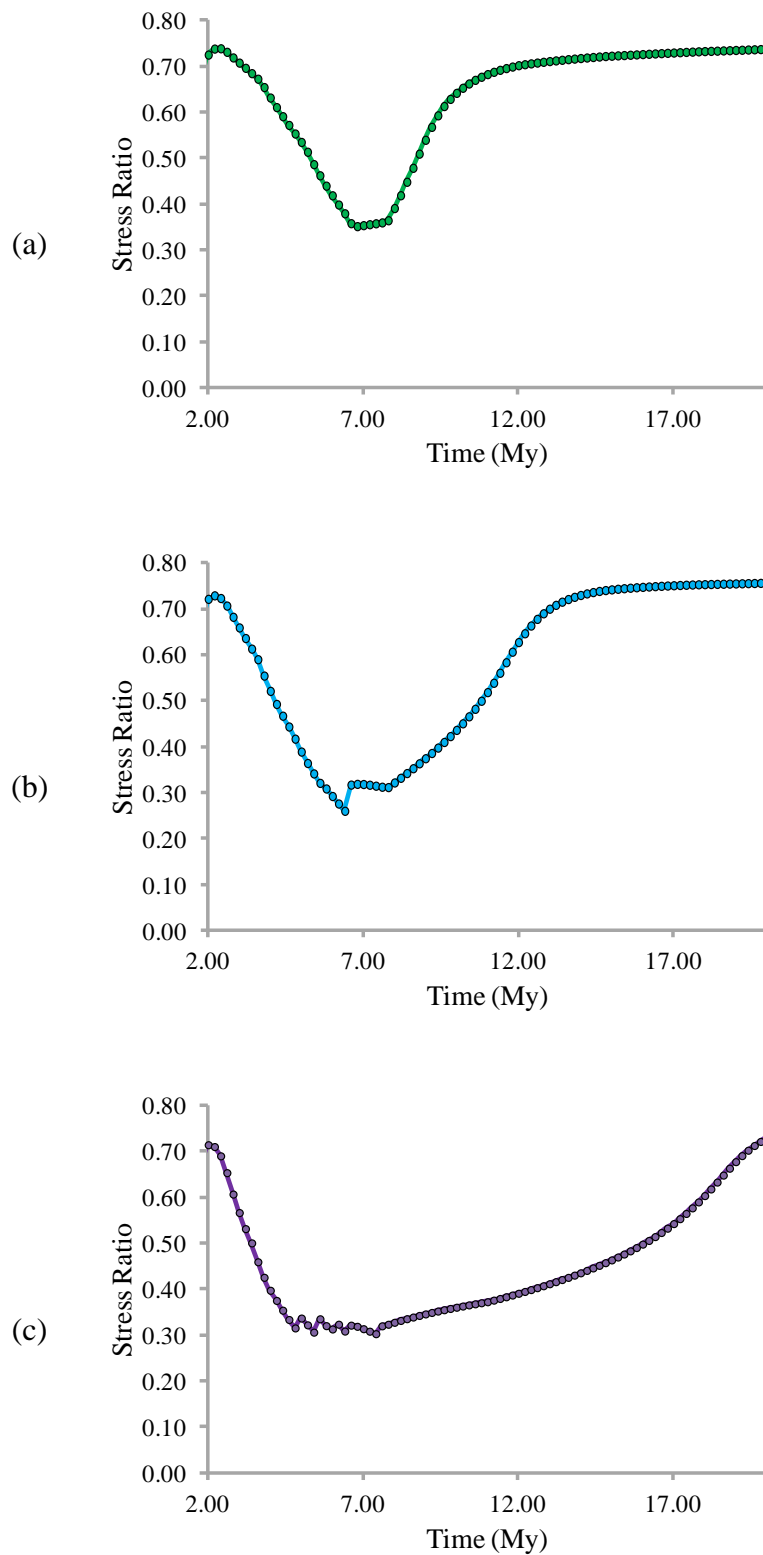


Figure 4-19: Evolution of stress ratio for various chemical porosity changes expressed isotropically (a) 5% (b) 10% (c) 20%.

Incorporating the Influence of Burial Diagenesis at Shallow Depths

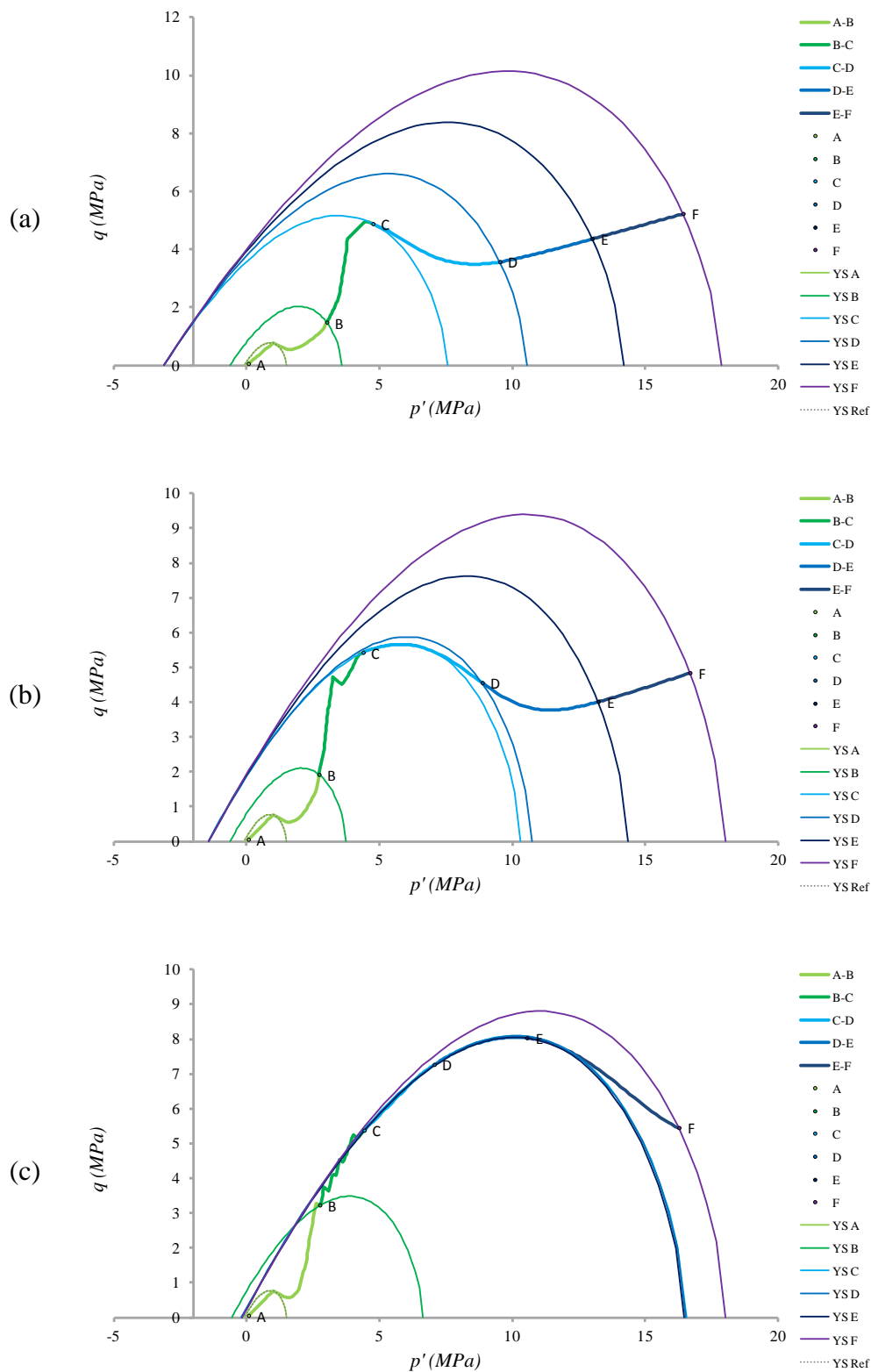


Figure 4-20: Stress path and state boundary surface evolution for various chemical porosity changes expressed isotropically (a) 5% (b) 10% (c) 20%.

Incorporating the Influence of Burial Diagenesis at Shallow Depths

As mentioned in the previous sections Figure 4-21 shows the change in stress ratio for the various changes in porosity due to the chemical process, both in the uniaxial and volumetric cases.

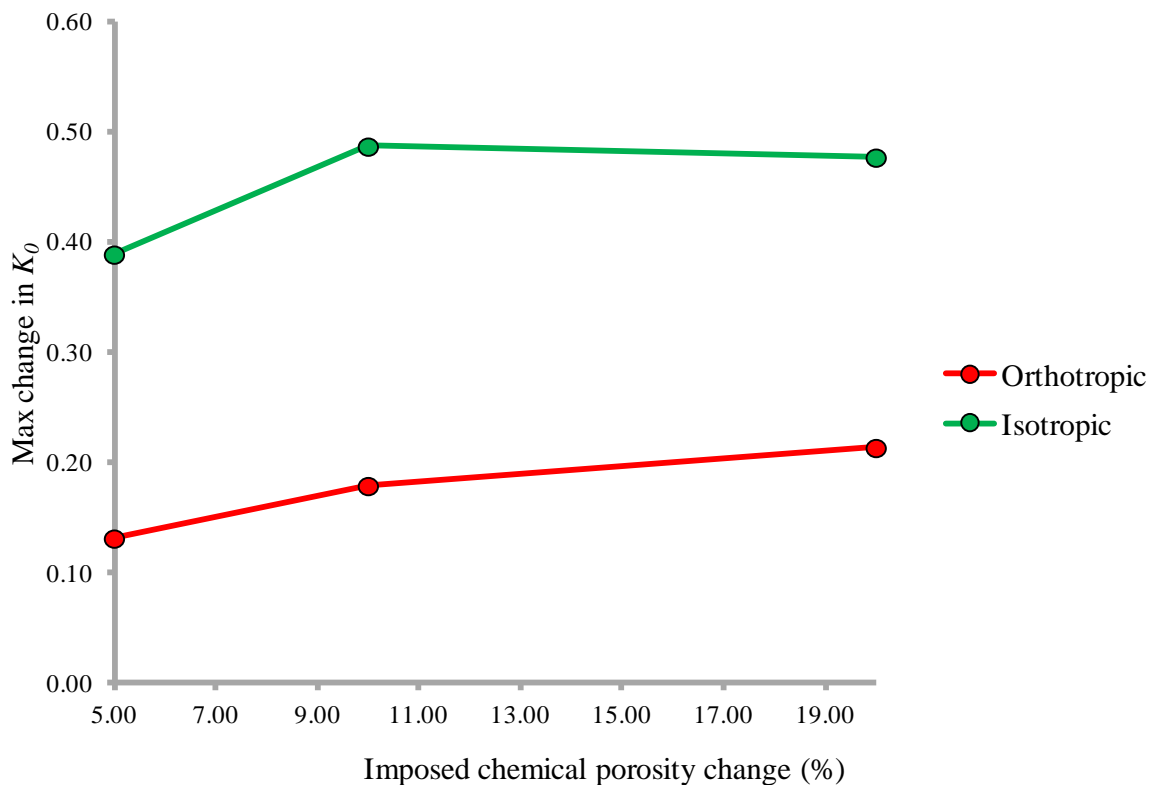


Figure 4-21: Plot summarising the reduction in K_0 for various magnitudes of chemical volume change.

Apparent trend lines are shown for both cases and it appears that the values appear to be asymptotic to a constant value at high porosity change. As such it might be expected that further increases in the value of diagenetic volume change will have diminishing influence on the change in the stress ratio.

4.5.3 Discussion of Results

The output from the single element testing is encouraging. The effect of chemical processes is realised in deviations from the expected consolidation path and changes to the state boundary surface. These observations are in line with the proposed geomechanical argument, which itself closely resembles recently ventured arguments in the literature (Laurent et al., 2012). The simulations highlight the variations in response and deformation style between the two end members of uniaxial and isotropic chemical volume reduction. The enhanced constitutive model enables definition of the flow rule for the chemical process to capture this effect. In

Incorporating the Influence of Burial Diagenesis at Shallow Depths

reality a reaction may fall in between these end members. For example it may have a chemical component of strain in all directions but predominantly in the vertical direction. Conceivably, the way in which the reaction is expressed may change with time to reflect the progressive change in sediment fabric as the reaction and mechanical compaction progress. These tests have also indicated that, providing the chemical contribution to total strain is high enough, and is expressed in all three principal directions, shear failure is predicted. This was the case for both a 10% and 20% reduction in porosity due to chemical compaction. This is a significant observation and suggests that (a) the geomechanical argument is physically reasonable, and (b) the Opal A/CT reaction could be a candidate for triggering PFS formation without the need to additionally include differential compaction due to an irregular transformation front (Davies and Ireland, 2011). Furthermore, it appears that the algorithm for assessing the development and removal of bonding performs satisfactorily. For example, for the uniaxial flow rule case with 20% porosity reduction where no shear failure is triggered there is no reduction in cement sourced strength (Figure 4-17(a)). In the equivalent case with isotropic chemical compaction, failure in shear results in repeated structure development and removal are predicted until the reaction is complete (Figure 4-20(b)).

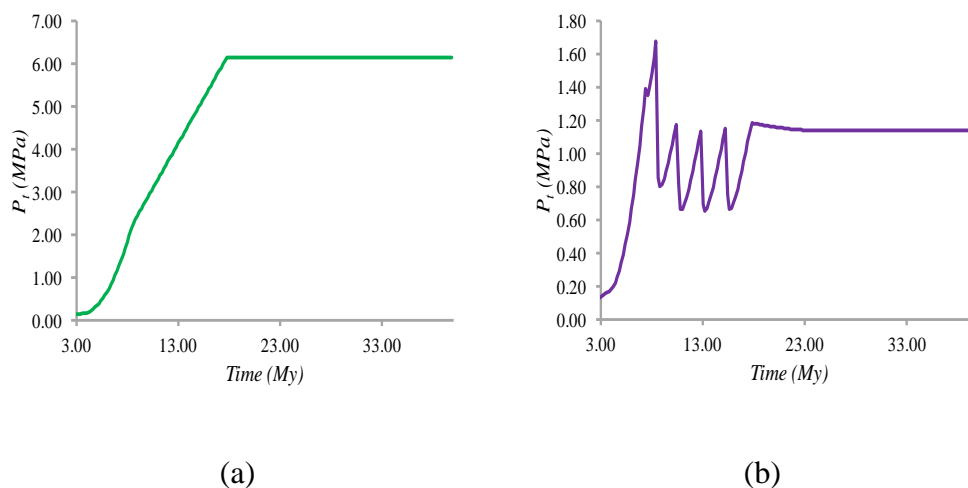


Figure 4-22: Evolution of the strength of diagenetic bonding for (a) uniaxial case with no destructuration predicted (b) volumetric case with destructuration predicted.

Whether it is entirely physically reasonable for the developed structure not to be removed due to increasing compaction as shown in case (a) is debatable, but this is a limitation of the current framework. With the adopted constitutive model, dilation due to shear deformation is only predicted for stresses which lie to the left of the critical state line in p - q space.

Consequently, as was noted, in some cases the intersection of the stress path with the yield surface was on the cap but very close to the critical state line. Interestingly, this is the zone corresponding to shear-enhanced compaction and it has been argued that this might allow for fault formation (Laurent et al., 2012). It is theoretically possible to obtain a localisation at any point on the yield surface if the material model permits this, as noted by the presence of compaction bands in some formations (Dehandschutter et al., 2004). It would be interesting to test this theory using a more sophisticated constitutive model.

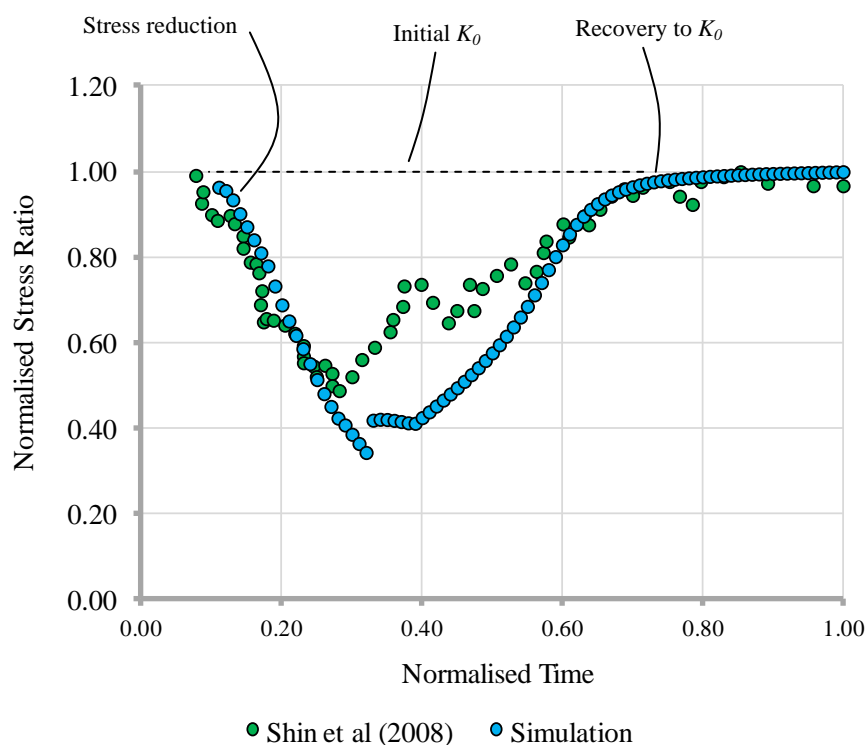


Figure 4-23: Model data for 10% porosity reduction over geological time - see Figure 4-20(b) and experiment evolution of horizontal stress ratio for an induced volume reduction of 10% (Shin et al., 2008).

Figure 4-23 shows the comparison of model results for the case shown in Figure 4-20(c) with the recently published experimental testing of chemical dissolution (Shin et al., 2008). The setup of this experiment was explained briefly in section 4.2. The results have been normalised with respect to time as the numerical and experimental tests are operating over different timescales (experiment in hours whilst numerical model is over millions of years). Additionally, the stress ratio has been normalised due to the fact the initial value of K_0 is different. The results are not strictly comparable (due to the amount of volume change

imposed). The general trend of stress ratio reduction from an initial K_0 value followed by relaxation back to K_0 , however, shows the numerical approach correlates well qualitatively with the extremely limited experimental data concerning volume change during diagenetic processes. So, in a qualitative sense, the results show promise.

4.6 Summary and Progression

The key aspects of the work presented in this chapter are summarised as:

- 1 A discussion of the constitutive response to diagenetic reactions has been provided, with the Opal A/CT reaction given particular focus. Case studies at the Horonobe URL and the Nanakai Trough allow identification of the key implications for the material response.
- 2 A geomechanical argument was outlined to explain the formation of PFS due to diagenesis. The similarities between this model and an existing model can explain the genesis of PFS in the Vøring Basin.
- 3 A procedure for incorporating the influence of chemical compaction into the elastoplastic SR3 constitutive model (introduced in Chapter 3) is explained. This model has been enhanced by introduction of a user defined chemical flow rule and a novel evolution law for tensile strength that incorporates both structure development and destructure.
- 4 A characterisation for a generic diatomaceous mudstone was developed using data from the literature, and supplemented by engineering judgement where necessary.
- 5 Single element tests reveal the behaviour of the diatomaceous mudstone when only mechanical compaction is considered. This is visualised using plots of the evolution of the stress ratio with time and the evolution of the stress path and state boundary surface.
- 6 When chemical compaction is considered the stress path deviates from the K_0 line. This observation is consistent with other genesis models and also backed up by experimental testing of chemical dissolution. Comparisons between the numerical predictions and the dissolution experiments are qualitatively good.
- 7 For the case of 20% chemical volume change, expressed in all three directions, the modification to the stress path was shown to permit failure in shear. These conditions are thought to be the most representative of the Opal A/CT transformation and this potentially identifies this transformation as a candidate for triggering PFS formation.

As noted in section 4.5.3 these results show promise. Subsequent chapters the into to bridge

the gap to field scale simulations, with the goal of observing whether localised shear failure and recovery of a system of polygonal faults is predicted.

4.7 References

- Bjorlykke, K., and K. Hoeg, 1997, Effects of burial diagenesis on stresses, compaction and fluid flow in sedimentary basins: *Marine and Petroleum Geology*, v. 14, no. 3, p. 267–276.
- Cartwright, J. A., 2011, Diagenetically induced shear failure of fine-grained sediments and the development of polygonal fault systems, *in* *Marine and Petroleum Geology*: Elsevier Ltd, p. 1593–1610.
- Croizé, D., S. N. Ehrenberg, K. Bjørlykke, F. Renard, and J. Jahren, 2010, Petrophysical properties of bioclastic platform carbonates: implications for porosity controls during burial: *Marine and Petroleum Geology*, v. 27, no. 8, p. 1765–1774.
- Davies, R. J., and M. T. Ireland, 2011, Initiation and propagation of polygonal fault arrays by thermally triggered volume reduction reactions in siliceous sediment: *Marine Geology*, v. 289, no. 1-4, p. 150–158.
- Davies, R. J., M. T. Ireland, and J. A. Cartwright, 2009, Differential compaction due to the irregular topology of a diagenetic reaction boundary: a new mechanism for the formation of polygonal faults: *Basin Research*, v. 21, no. 3, p. 354–359.
- Dehandschutter, B., S. Vandycke, M. Sintubin, N. Vandenberghe, P. Gaviglio, J.-P. Sizun, and L. Wouters, 2004, Microfabric of fractured Boom Clay at depth: a case study of brittle–ductile transitional clay behaviour: *Applied Clay Science*, v. 26, no. 1-4, p. 389–401.
- Goult, N. R., and R. E. Swarbrick, 2005, Development of polygonal fault systems: a test of hypotheses: *Journal of the Geological Society*, v. 162, no. 4, p. 587–590.
- Heffernan, A. S., J. C. Moore, N. L. Bangs, G. F. Moore, and T. H. Shipley, 2004, Initial deformation in a subduction thrust system: Polygonal normal faulting in the incoming sedimentary sequences of the Nankai subduction zone, Southwestern Japan., *in* Davies, R.J., Cartwright, J.A., Stewart, S.A., Underhill, J.R., Lappin, M. (Eds.), *3D Seismic Technology: Application to the Exploration of Sedimentary Basins*: Geological Society, London, p. 457–472.
- Henry, P., T. Kanamatsu, K. T. Moe, and M. Strasser, 2012, IODP Expedition 333: Return to Nankai Trough Subduction Inputs Sites and Coring of Mass Transport Deposits: *Scientific Drilling*, no. 14, September 2012, p. 4–17.
- Ienaga, M., L. C. McNeill, H. Mikada, S. Saito, D. Goldberg, and J. C. Moore, 2006, Borehole image analysis of the Nankai Accretionary Wedge, ODP Leg 196: Structural and stress studies: *Tectonophysics*, v. 426, no. 1-2, p. 207–220.
- Ireland, M. T., 2011, 3-D seismic investigation of the diagenesis and deformation of Cenezoic sediments on the Eastern Atlantic Margin: Unpublished PhD thesis - Durham University, p. 185.

-
- Isaacs, C. M., 1982, Geology Influence of rock composition on kinetics of silica phase changes in the Monterey Influence of rock composition on kinetics of silica phase changes in the Monterey Formation , Santa Barbara area , California: *Geology*, v. 10, p. 304–308.
- Ishii, E., H. Sanada, T. Iwatsuki, Y. Sugita, and H. Kurikami, 2011, Mechanical strength of the transition zone at the boundary between opal-A and opal-CT zones in siliceous rocks: *Engineering Geology*, v. 122, no. 3-4, p. 215–221.
- Klimczak, C., and R. A. Schultz, 2013, Shear-enhanced compaction in dilating granular materials: *International Journal of Rock Mechanics and Mining Sciences*, v. 64, p. 139–147.
- Laurent, D. et al., 2012, High-resolution architecture of a polygonal fault interval inferred from geomodel applied to 3D seismic data from the Gjallar Ridge, Vøring Basin, Offshore Norway: *Marine Geology*.
- Lee, H. J., R. E. Kayen, and W. G. McArthur, 1990, 43. Consolidation, triaxial shear-strength, and index-property characteristics of organic-rich sediment from the peru continental margin: Results from leg 112, *in* *Proceedings of the Ocean Drilling Program, Scientific Results, Vol. 112*: p. 639–651.
- Matheney, R. K., and L. P. Knauth, 1993, New isotopic temperature estimates for early silica diagenesis cherts: *Geological Society, London, Special Publications*, v. 21, no. 6, p. 519–522.
- Meadows, D., and R. J. Davies, 2009, Predicting porosity reduction due to silica diagenesis using seismic reflection data: *Marine and Petroleum Geology*, v. 26, no. 8, p. 1543–1553.
- Neagu, R. C., J. A. Cartwright, and R. J. Davies, 2010, Measurement of diagenetic compaction strain from quantitative analysis of fault plane dip: *Journal of Structural Geology*, v. 32, no. 5, p. 641–655.
- Praeger, T., 2009, Heterogeneities in fine-grained sediments and their impact on seal quality: Unpublished PhD Thesis - Cardiff University, p. 242.
- Sanada, H., S. Niunoya, H. Matsui, and Y. Fujii, 2009, Influences of Sedimentary History on the Mechanical Properties and Microscopic Structure Change of Horonobe Siliceous Rocks: *Journal of the Mining and Materials Processing Institute of Japan*, v. 125, no. 10, p. 521–529.
- Shin, H., J. C. Santamarina, and J. A. Cartwright, 2008, Contraction-driven shear failure in compacting uncemented sediments: *Geology*, v. 36, no. 12, p. 931.
- Spinelli, G. A., P. S. Mozley, H. J. Tobin, M. B. Underwood, N. W. Hoffman, and G. M. Bellew, 2007, Diagenesis, sediment strength, and pore collapse in sediment approaching

-
- the Nankai Trough subduction zone: *Geological Society of America Bulletin*, v. 119, no. 3-4, p. 377–390.
- Tewksbury, B. J., J. P. Hogan, S. a. Kattenhorn, C. J. Mehrtens, and E. a. Tarabees, 2014, Polygonal faults in chalk: Insights from extensive exposures of the Khoman Formation, Western Desert, Egypt: *Geology*, v. 42, no. 6, p. 479–482.
- Volpi, V., A. Camerlenghi, C. Hillenbrand, M. Rebesco, and R. Ivaldiz, 2003, Effects of biogenic silica on sediment compaction and slope stability on the Pacific margin of the Antarctic Peninsula: *Basin Research*, v. 15, p. 339–363.
- Walderhaug, O., 1996, Kinetic Modeling of Quartz Cementation and Porosity Loss in Deeply Buried Sandstone Reservoirs: *AAPG Bulletin*, v. 80, no. 5, p. 731–745.
- Walderhaug, O., 2000, Modeling Quartz Cementation and Porosity in Middle Jurassic Brent Group Sandstones of the Kvitebjørn Field, Northern North Sea: *AAPG Bulletin*, v. 84, no. 9, p. 1325–1339.
- White, R. J., G. A. Spinelli, P. S. Mozley, and N. W. Dunbar, 2011, Importance of volcanic glass alteration to sediment stabilization: offshore Japan: *Sedimentology*, v. 58, no. 5, p. 1138–1154.

Chapter 5

FIELD SCALE ANALYSIS OF THE FORMATION AND EVOLUTION OF POLYGONAL FAULT SYSTEMS

The previous chapter indicates that given suitable conditions, the characterised diatomaceous sediment can be advanced to a state of shear failure when the influence of diagenetically-driven volume reduction is considered. This chapter investigates the characterised material in field scale simulations, with the primary objective to establish whether the characterised materials exhibit localised shear failure. Additionally the discussion of other potential diagenetic processes is extended via assessing the sensitivity of PFS formation to various changes to model parameters. In all cases comparisons are made to tiers from seismic data in order to assess the veracity of the geomechanical argument and computational strategy in terms of modelling realistic PFS.

5.1 Field Scale Investigations Related to Opal A/CT Transformation

The single element tests in Chapter 4 indicate that for a 20% diagenetic reduction in porosity, shear failure and dilation is predicted. This condition is examined first as it provides the most likely case for the initiation of localised faults and the genesis of networks of polygonal faults.

5.1.1 Two Dimensional Models

5.1.1.1 Model Description

As an intermediate step between the single element testing, which served to validate the material response, and full 3-D modelling of polygonal faulting, two-dimensional field scale models are examined. The intention is to observe if localisations form through the chemically affected layers due to the modification of the material state and stress path. The model setup is shown in Figure 5-1. The boundary conditions replicate the K_0 condition of zero lateral strain. The diatomaceous mudstone characterised in the previous chapter is used to model elements within the upper layer whilst the base layer is represented as a generic mudstone. To reduce computational requirements, the vertical loading due to the weight of overburden is

Field Scale Analysis of the Formation and Evolution of Polygonal Fault Systems

applied as a face load on the top surface of the model. The loading rate is identical to the single element tests (see Figure 5-1), and represents a sedimentation rate of approximately 50m/My. This correlates well with the deposition rates for the vast majority of PFS as noted in Chapter 2.

The temperature distribution is applied via a spatial variation that evolves with time, so that the temperature profile applied in the single element tests can be approximated. The equivalent thermal gradient is approximately 45°C/km.

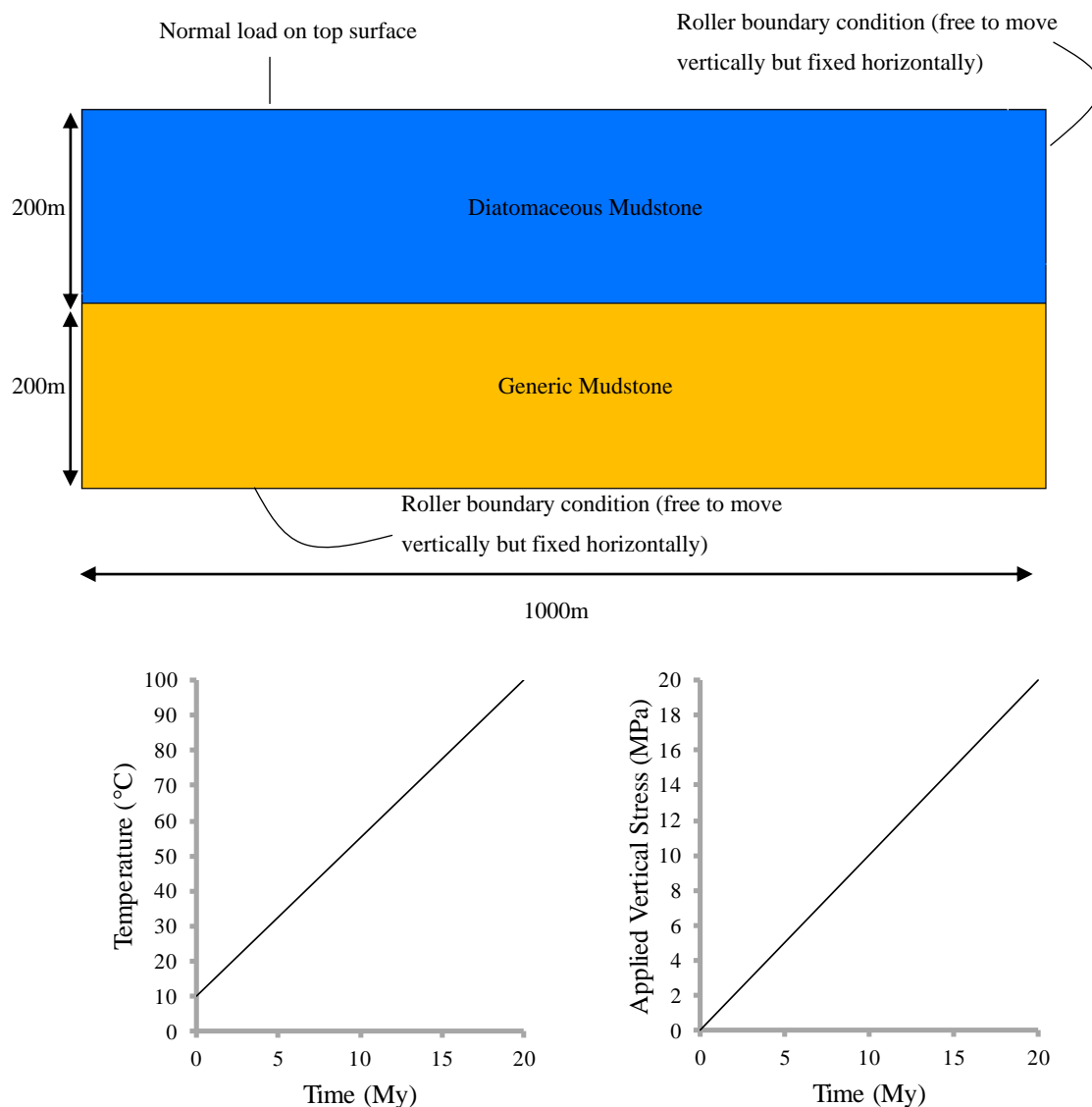


Figure 5-1: Geometry, boundary and loading conditions for 2D model. Gold layer is characterised as a generic mudstone. Overlying blue layer is characterised as diatomaceous mudstone.

Remarks 1 It is stressed that all the models presented within this chapter are not seeded with faults. That is to say that there are no geometric perturbations to model geometry in order to concentrate stress and promote localisation, which is sometimes adopted in some numerical modelling in order to drive initial failure. The deformation arises purely from the finite strain theory, boundary conditions, imposed stress path and the characterised materials.

5.1.1.2 Results

In Figure 5-2 the evolution of the accumulated effective plastic strain is shown. Figure 5-2(a) shows the model geometry at the start of the simulation. At 6My (Figure 5-2(b)) thin bands of localised effective plastic strain develop. At this time, the burial is equivalent to around 500m. This image is somewhat misleading as it suggests that fault initiation is in the upper portion of the tier. Failure is actually triggered near the base of the tier, where elements are both chemically active at earlier time, due to the increasing temperature with depth, and subjected to greater imposed stress. The kinematic freedom offered by the boundary condition on the upper surface, however, allows plastic strain to accumulate more easily.

Remarks 2 The effective plastic strain, sometimes referred to as the accumulated plastic strain or Von Mises effective plastic strain, is an invariant strain measure indicating plastic failure and is defined as (de Souza Neto et al., 2008);

$$\bar{\varepsilon}^p = \int_0^t \sqrt{\frac{2}{3} \dot{\varepsilon}^p : \dot{\varepsilon}^p} dt \quad 5-1$$

Where $\bar{\varepsilon}^p$ is the effective plastic strain and $\dot{\varepsilon}^p$ is the plastic strain rate.

At 10My, which roughly corresponds to the completion of the chemical process, it is clear that well defined and localised zones of effective plastic strain have developed in the chemically compacting sediments. There is no obvious propagation into the generic base layer. At the end of the simulation, as shown in Figure 5-2(d), the material continues to mechanically compact and the tier is substantially thinner than its initial state. The result of this increased mechanical compaction post-diagenesis is a modest flattening of the fault planes with a reduction of initial fault angle from around 46° to 42°. Shallower fault angles are often reported as tiers become more deeply buried so this result is consistent with seismic observation (Hansen et al., 2004; Cartwright, 2011).

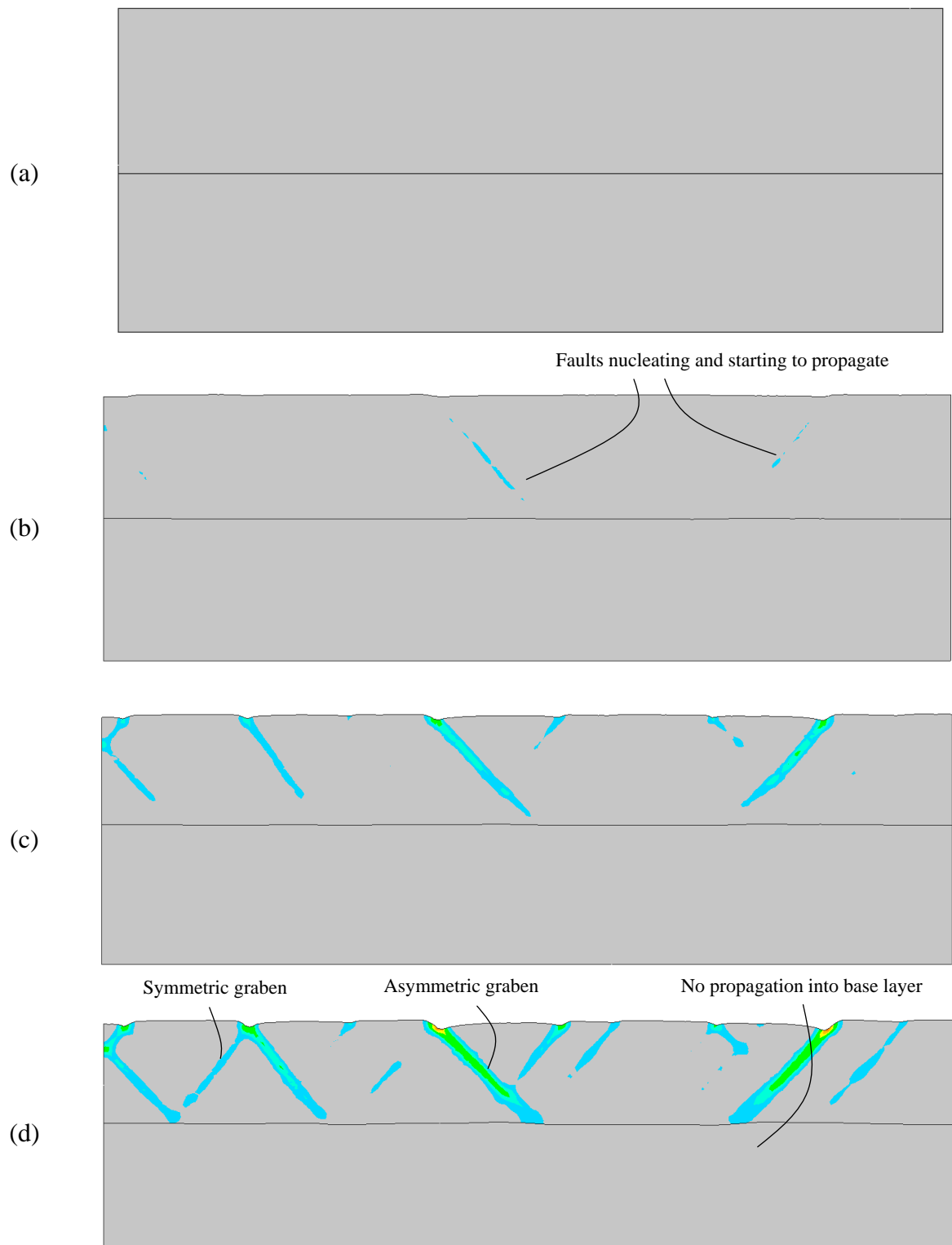


Figure 5-2: Fault evolution in 2D model. Contours of effective plastic strain at (a) 0My (b) 6My (b) 15My (c) 20My. Note how localised faults develop around 6My, are both synthetic and antithetic, and are confined to the chemically affected layer.

Field Scale Analysis of the Formation and Evolution of Polygonal Fault Systems

Figure 5-3 shows some additional useful methods for interpreting the developed faults. The material grid in (a) tracks the deformation of specified points from the reference (initial) configuration through to the final configuration. From this plot it is clear that the localised zones of deformation are both synthetic and antithetic normal faults. In the centre of the model the grid identifies an asymmetric graben. Figure 5-3(b) and (c) show the accumulated displacement in the vertical and horizontal directions respectively. The largest displacements are accumulated at the top of the tier and again it is suggested that this is the result of the additional kinematic freedom offered by the application of overburden load rather than explicitly modelling the deposition of overlying layers.

The fact that shear localisations arise naturally from the simulations provides some confidence in the ability of the computational framework. More importantly this validates the geomechanical argument proposed in Chapter 4 and confirms that the characterised material can be advanced to a state shear failure which results in the development of faults at the field scale. Chapter 1, however, indicated that a crucial validation of the modelling approach is the extension into 3D. The desire to make this step is driven by the fact that PFS are most commonly identified by their planform geometry. When viewed on a single seismic cross-section it is often not possible to discriminate between small growth faults and polygonal fault systems, and this can only be resolved by observations of the tier in map-view (Volpi et al., 2003).

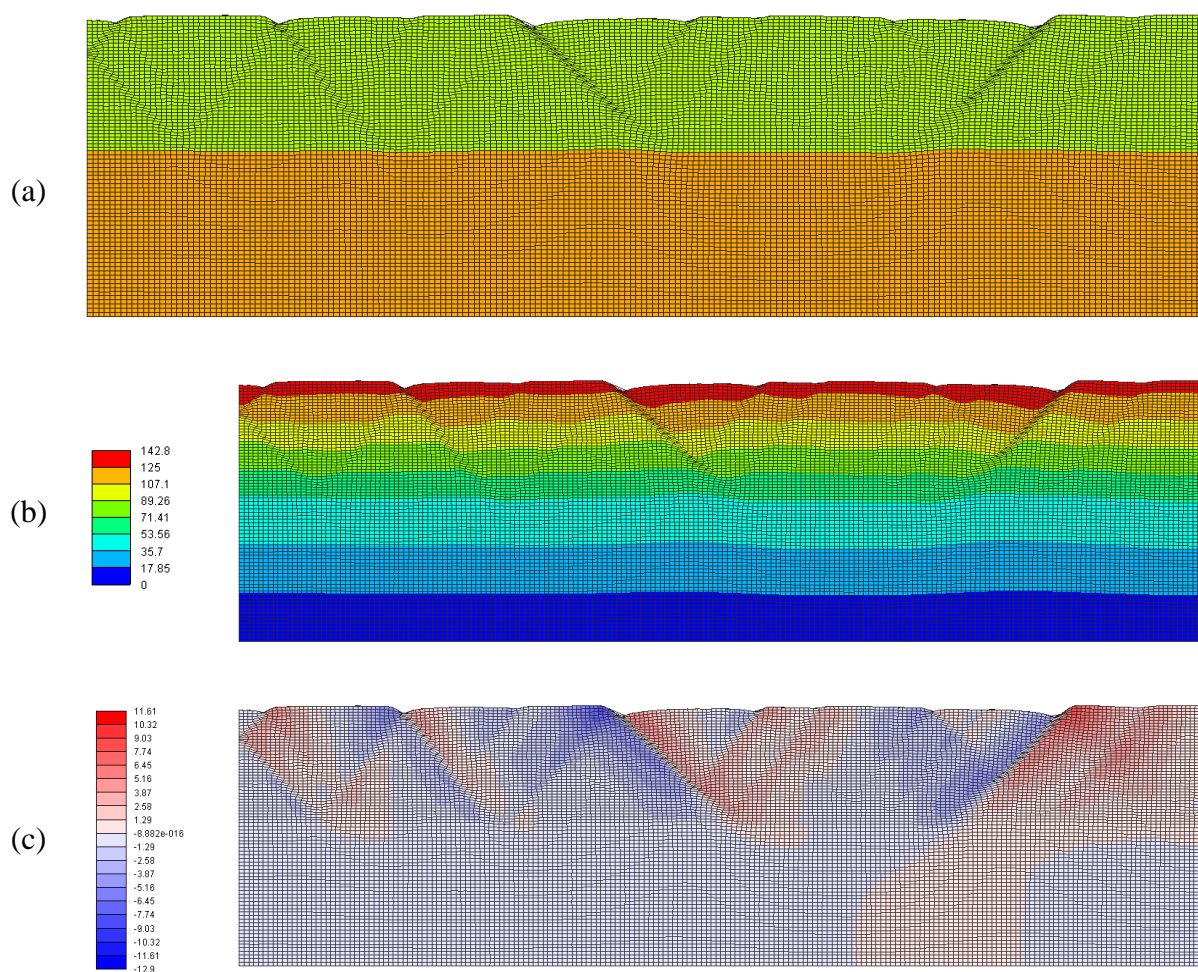


Figure 5-3: Final geometry from 2D model. (a) Material grid showing regions of intense deformation. Contours of accumulated vertical and horizontal displacement in metres are shown in (b) and (c) respectively.

5.1.2 Three Dimensional Models

5.1.2.1 Model Description

The model from the previous section is extended into 3-D but, due to computational requirements, the domain size is now halved so that the length and width are 500m, and the thickness of the diatomaceous and underlying layers are both 200m. A normal load is again applied to the top surface as a proxy for the addition of overburden load. The model setup is shown diagrammatically in Figure 5-4.

Remarks 3 The extension to 3D requires the use of a specialised element formulation. The Averaged Nodal Volumetric (ANV) strain element (Thornton and Crook, 2013) is used to overcome 'volumetric locking' which is often observed during 3D simulations with simplex

elements. Comparison of 3D pseudo-plane strain (one element through thickness) problems and 2D plane-strain simulations has demonstrated good agreement between the 2D and 3D element types (Thornton and Crook, 2014).

5.1.2.2 Results

The results of the simulations are shown in Figure 5-5 and Figure 5-6 which show contours of accumulated horizontal displacement and the effective plastic strain, $\tilde{\varepsilon}^p$, respectively. Localised regions of failure are observed that are representative of faults. In section faults have similar geometry to those observed in the 2D modelling.

Faults are exclusively normal, well connected, and display no preferred orientation, occasionally forming grabens (Figure 5-6). Furthermore, by inspection the pattern is quite uniform and reminiscent of the classic hexagonal pattern, which is rare amongst observed PFS (Cartwright, 2011). Interestingly, this pattern is only normally observed where tier thickness and base are very uniform and these are precisely the conditions modelled here. The simulation results show that within the larger faults that have accumulated more strain, there are regions of slightly more diffuse deformation and smaller faults appear to be clustered within larger ones. This is potential evidence of the fractal nature of PFS, with smaller scale faulting defining small polygonal "cells" which together often forming larger cells

5.1.3 Comments on Opal A/CT Transformation Results

5.1.3.1 Comparison with Cartwright and Dewhurst Criteria

These results appear quite promising, and this is further confirmed by assessing the model output against the criteria developed as a means of distinguishing PFS from other fault types (Cartwright and Dewhurst, 1998). The criteria are displayed in Table 5-1, in addition to an appraisal of whether the model has adequately managed to replicate each specific criterion. The criteria are listed in order of their importance in confirming the presence of a PFS.

The key criterion is the planform geometry and we can confirm that this has been replicated in Figure 5-5. and Figure 5-6 confirm that fault polarity is mixed, with both synthetic and anithetic fault dips. The faults do not propagate into the base layer, and presumably this would be the case for an overburden characterised with the same material, were it modelled. Therefore, the second criterion may be considered satisfied. Fault throw in the models appears to be low but of the order specified. The spacing criterion is also slightly lower than reported in the criteria and varies widely between ca. 65m and 120m. However, it should be

Field Scale Analysis of the Formation and Evolution of Polygonal Fault Systems

noted that at initiation of faulting the tier has compacted to about 150m thickness and so is at the lower end of reported tier thicknesses. This might therefore be explained by the observation that spacing is thought to crudely scale with tier thickness (Carruthers, 2012) and hence thinner tiers have a tighter fault spacing.

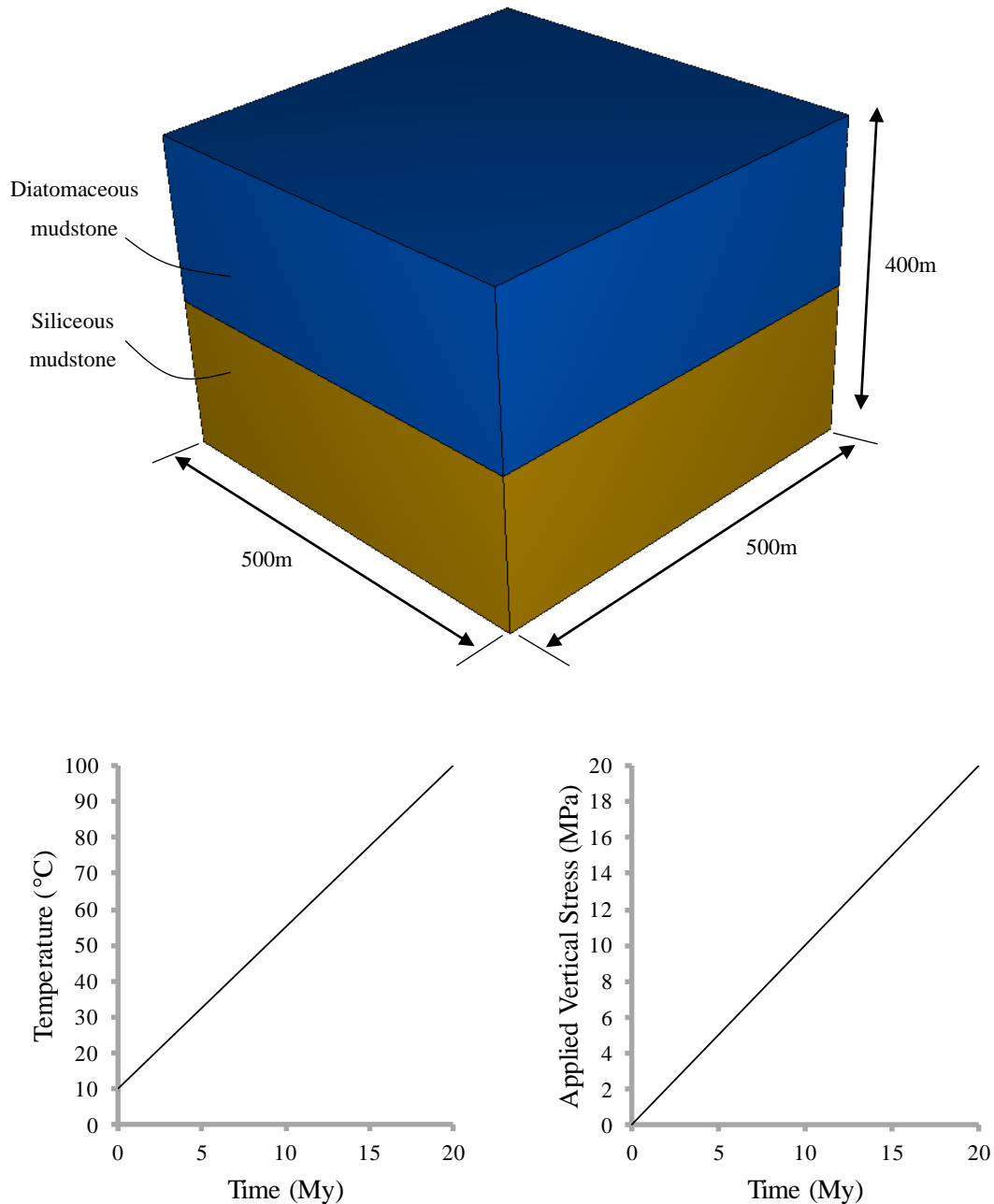


Figure 5-4: Three dimensional model loading and boundary conditions. Gold layer is characterised as a generic mudstone. Overlying blue layer is characterised as diatomaceous mudstone. K_0 boundary conditions are adopted.

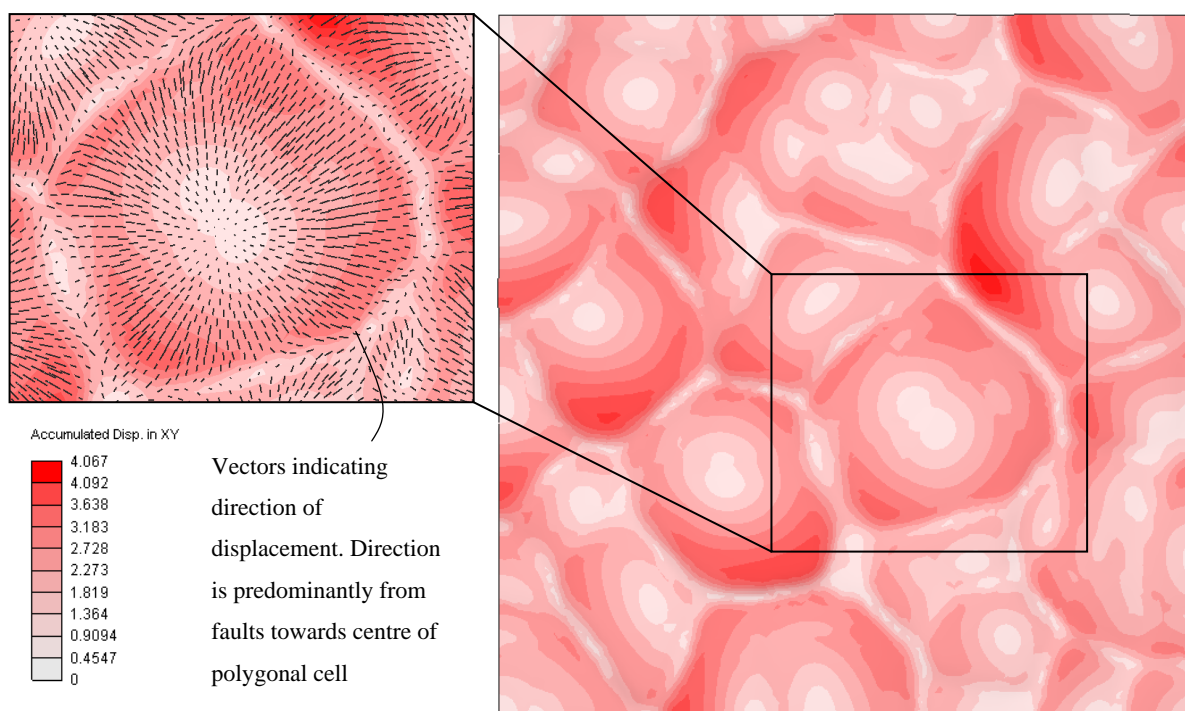


Figure 5-5: Accumulated horizontal displacements at 10My. Red indicates zones of largest horizontal movement (heave).

Due to computational constraints, it is difficult to assess the areal extent criterion. Typically faults need to be observed over vast areas which cover at least $150,000\text{km}^2$. For the current uniform cases, however, if the model boundaries were extended the faulting would continue to extend over the complete domain. The requirement for proxies for overburden loading to be applied instead of deposition of additional material means that there are limitations in the ability to assess if separate tiers would arise. This is addressed in section 5.2. It should be noted that often PFS are observed to not strictly meet the criterion listed, or only satisfy a number of these criterion (Cartwright and Dewhurst, 1998). As such, despite the fact that some of the criteria are not fully satisfied, and that due to modelling limitations some criterion cannot be fully assessed, there appears more than sufficient evidence to suggest successful modelling of the formation of a polygonal fault system. This is a key objective of the study.

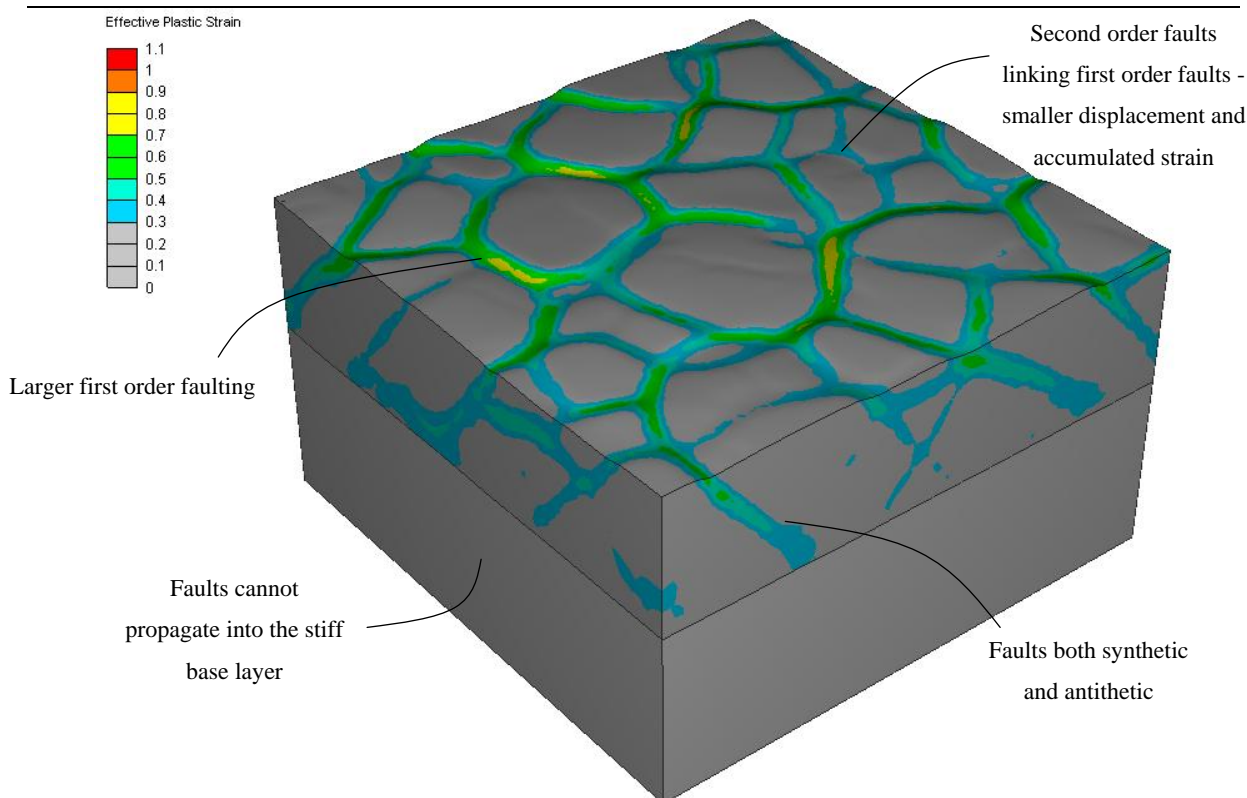


Figure 5-6: Geometry of 3D model at 10 My showing contours of effective plastic strain in the polygonally faulted interval.

Rank	Criterion	Recovered?
1	Polygonal map view patterns	Yes
2	Layer bound in the vertical direction	Yes
3	Areal extent	N/A
4	Fault type and throw 10-100m	Yes
5	Fault spacing (100-1000m)	Yes
6	Tiers	N/A
7	Mixed fault polarity	Yes

Table 5-1: Comparison between model output and criteria for PFS identification as outlined by Cartwright and Dewhurst (1998).

5.1.3.2 Comparison with Seismic Observation

Seismic data from offshore Norway (Ireland, 2011) is shown in Figure 5-7. It is clear that the interpreted polygonal faults are indeed layer-bound, and correspond to the intervals between Horizon A and Horizon B. The density log indicates that the polygonal faults, of which only a selection are interpreted, are confined to the interval that is associated with a sharp increase in density (porosity) and this inferred to be the Opal A/CT boundary. The modelling results are layer-bound and confined specifically to the interval associated with the transformation of

Opal A to Opal CT, and therefore appear to be in good agreement with the seismic interpretation. The work of Davies and Ireland (2011) suggests that an irregular spatial profile of the A/CT transformation boundary triggers faulting via differential compaction, potentially at reasonable depths. The depth range for initiation of faulting in the presented models seems to be broadly in agreement with the depths at which faults are observed on the seismic line. A seeming disparity in the model results is the interval over which the diagenetic porosity loss takes place as shown in Figure 5-8. The seismic line indicates that the interval over which the chemical volume reduction takes place is smaller, which could reflect a more rapid reaction rate than modelled due to an optimal sediment and/or pore fluid composition. The model output does however show that once the reaction has taken place the sediment framework is significantly stronger and porosity reduction is retarded until this is broken down.

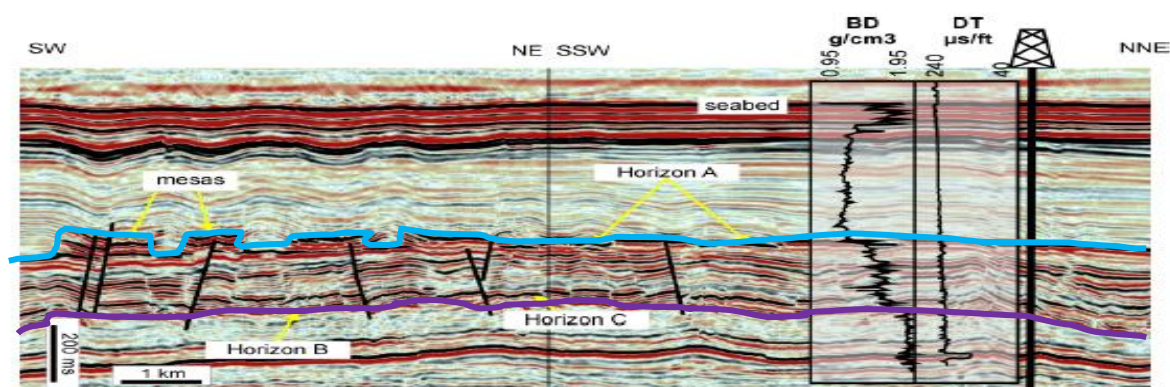


Figure 5-7: Silica diagenetic transformation zone, offshore Norway modified after Ireland (2011). Only a selection of the total number of interpreted polygonal faults are shown. The blue boundary represents the inferred Opal A/CT transformation boundary (see density log). The purple boundary marks the inferred base of the tier which is seen to coincide with the transformation of Opal CT to Chert.

The density/depth plot shows a slight reluctance to consolidate beyond the Opal A/CT transformation boundary until another step-change in porosity is observed that coincides with the transformation from Opal CT to chert. The results presented here have also suggested that the irregular boundary might not be required to initiate faulting, and that, in appropriate conditions the contribution from the chemical component to total volumetric strain is sufficient to lead to localised shear failure. It is noted however that the development of regions of subtle differential stress due to an irregular boundary would certainly serve to compliment the arguments proposed here by focusing deformation and biasing the

propagation of dominant faults. This may explain why the spacing of faults on the seismic section is somewhat larger than predicted by the model.

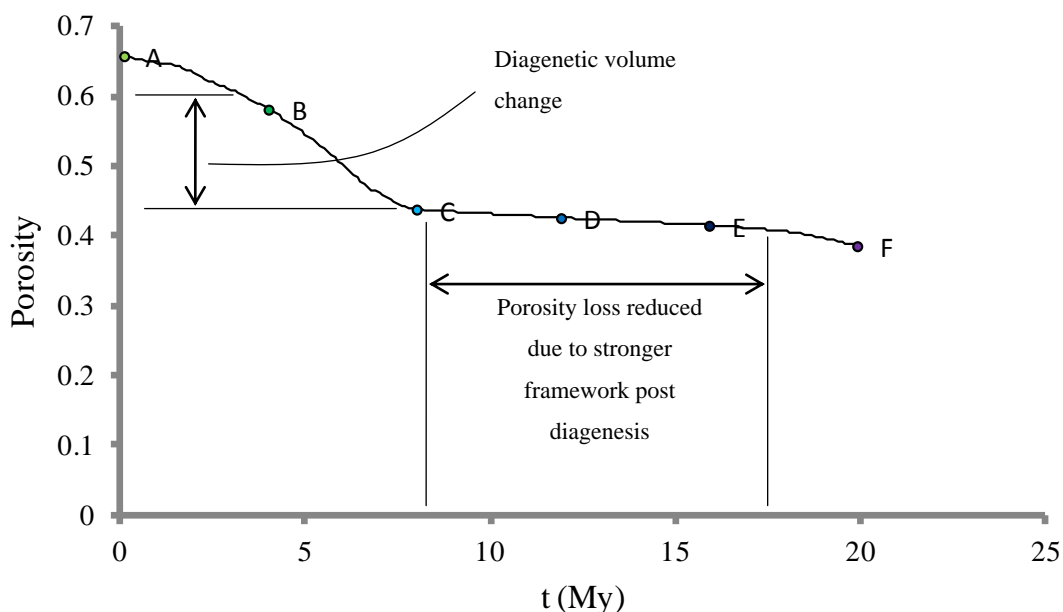


Figure 5-8: Modelled porosity evolution for a point near the base of the tier. In reality the porosity would be further reduced as Opal CT is transformed to Chert, in addition to other reactions such as the transformation of smectite to illite which takes place at elevated temperatures.

5.1.3.3 Limitations

The output from the 2D and 3D models have shown that when the influence of volume change due to chemical compaction is considered shear failure may be triggered and networks of faults are developed. These faults strongly resemble systems of polygonal faults reported from locations around the globe. Many observations of both the 2D and 3D predicted geometry satisfy criteria for PFS identification. However, the potential for further investigation using these simple models is limited. Firstly, the models assume a fixed layer thickness, and as new material is not deposited, the propagation and/or arrest of faults cannot be studied. Consequently, further examination of the transient evolution of the faults is restricted using these models.

Secondly, and most importantly, although in some cases there is strong observational evidence of coincidence of PFS and the Opal A/CT, there are many cases where tiers are observed some distance above the A/CT seismic event. It is consequently unlikely that Opal

A/CT is the only mechanism responsible for polygonal fault genesis. An investigation of some of the controls on early PFS formation due to diagenesis is therefore necessary to investigate both the principal factors governing PFS formation via diagenesis and the controls on tier structure and geometry.

5.2 Sensitivity Study - Evolutionary Models

Intentionally, the modelling within this section is conceptual but where required, modification to geometry, loading and boundary conditions and material models is justified with reference to geological observation in order to provide confidence in the modelling output.

5.2.1 Two Dimensional Model Description

The initial model comprises a generic base material that consolidates under gravitational loading over a time period of 1My (Figure 5-9). Sediment is then added incrementally at a sedimentation rate of approximately 100m/My, which corresponds to rates observed for hemipelagic sediments and approximates the upper bound of deposition rates for various PFS reported in Cartwright and Dewhurst (1998). The mechanical characterisation uses the same shape of the yield surface and plastic potential as the previous models, although the value of the initial compressive and tensile intercepts are altered to reflect a weaker material at deposition (Table 5-3). Poro-elastic properties are shown in Table 5-2.

Parameter	Value
Poisson's Ratio (ν)	0.30
Reference Porosity (ϕ_{ref})	0.66
Reference Bulk Modulus (K_0)	10.0
Slope of URL (κ)	0.02

Table 5-2: Poroelastic properties for evolutionary models.

5.2.1.1 Influence of Chemical Properties and Thermal Gradient

The first sensitivity investigated is the influence of the chemical parameters on deformation style. These parameters are shown in Table 5-4 and Table 5-5. Note that in this study the amount of porosity reduction due to the chemical reaction is reduced, and, as the thermal gradient is higher, the progresses at a faster rate.

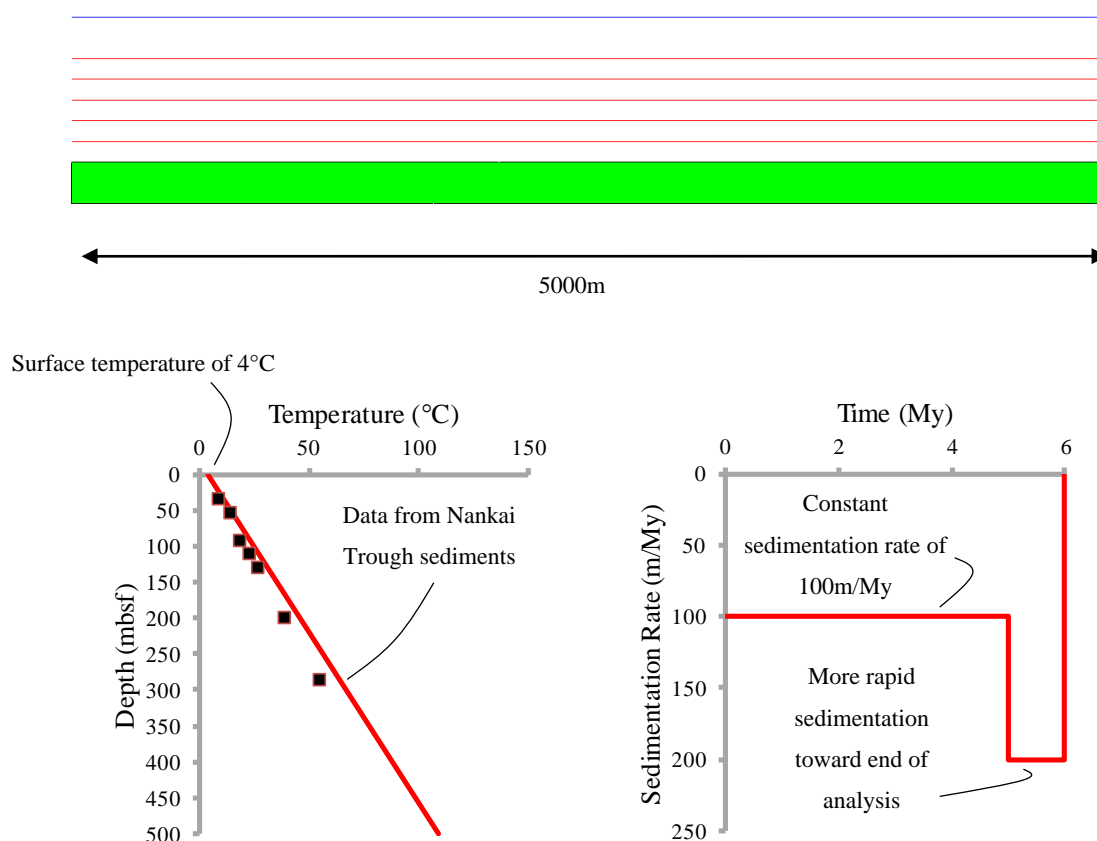


Figure 5-9: Geometry, loading and boundary conditions for 2D evolutionary models. The green section denotes the initial geometry. The red lines indicate the deposition horizons for the chemically affected layers. The blue line indicates the deposition horizon for the overlying non-chemically affected layer. Thermal gradient and approximate sedimentation rates also shown.

Parameter	Value
Initial tensile intercept (p_{t0})	-0.1 MPa
Initial compressive intercept (p_{c0})	0.2 MPa
Parameter (β)	55°
Parameter (ψ)	50°
Exponent (n)	1.6
Deviatoric plane parameter (N^z)	0.25
Deviatoric plane parameter (β_0^z)	0.7
Deviatoric plane parameter (β_1^z)	1.73×10^{-1} (1/MPa)

Table 5-3: Plastic properties for evolutionary models.

Simulation results for the sensitivity study are shown in Figure 5-10. The key observation is that despite the reduction in the total volume change due to the diagenetic process, clear, localised shear failures for boundary conditions with zero lateral strain. This opens up the

Field Scale Analysis of the Formation and Evolution of Polygonal Fault Systems

possibility that given suitable conditions, diagenetic reactions associated with smaller volume changes could be valid as triggers for PFS development.

Parameter	Value
Threshold temperature (T_{low})	18.0 °C
Upper reference temperature (T_{upp})	40.0 °C
Maximum porosity change (ϕ_c^{max})	0.05
Reference duration (t_c^{ref})	2.0 My
Residual porosity (ϕ_{res})	0.03
Flow rule factor	Varies between 0 and 1

Table 5-4: Chemical compaction properties for evolutionary models.

Parameter	Value
Destructuring Parameter (A)	5E-03
Maximum p_t change (p_t^{max})	0.25 MPa

Table 5-5: Destructuring properties for evolutionary models.

Figure 5-10(a-c) shows the evolution of the faults within the tier. In Figure 5-10(a), which captures plastic strain evolution 3.7 My after the initial deposition, a small number of faults propagate from a location near the base of the model. Failure is initiated within the first 200m but faults do not develop significant plastic strain until ca 3.2My. As highlighted previously this is an expected result for a model with deposition of layers with homogeneous chemical or material parameters (no spatial variation), as layers closer to the base will be chemically active earlier and hence fail first.

Fault propagation at shallow depth is assisted by the higher thermal gradient for this case, representative of the observed gradient in the Nankai Trough (Henry et al., 2012) where temperatures in excess of 50°C are reached within the first 200m of burial. These initial faults are designated as 1st order, i.e. adopting the terminology used in Gay et al., (2004). The loss of strength in these fault zones and the unloading of adjacent sediment means that these faults will act as preferential sites for continued deformation and fault propagation. Fault dips are both synthetic and antithetic with no obvious bias in direction. In Figure 5-10(b) the continued propagation of first order faults is seen, as well as the development of a number of second order faults which are seen to fill the space between the dominant first order faults. There is also some minor propagation towards the base on some of the first order faults, indicating that there is a component of radial fault propagation.

Field Scale Analysis of the Formation and Evolution of Polygonal Fault Systems

Figure 5-11(a) shows the final tier geometry and interpretation of the faults. Interestingly, as noted in the figure captions, faults are occasionally intercepted by other faults which become dominant, and this is a commonly observed in many tiers (Cartwright and Lonergan, 1996), and is shown conceptually in the complex tier geometry in Figure 5-11(b). This is regarded as evidence of transient growth of PFS which is confirmed by fault evolution predicted by the model. Figure 5-11(c) shows a seismic interpretation of the geometry of a PFS tier from the Lower Congo Basin with no vertical exaggeration (Gay et al., 2004). There is favourable comparison between the predicted PFS and the seismic profile although it is not suggested that the genetic mechanism for this fault system can necessarily be attributed to diagenesis.

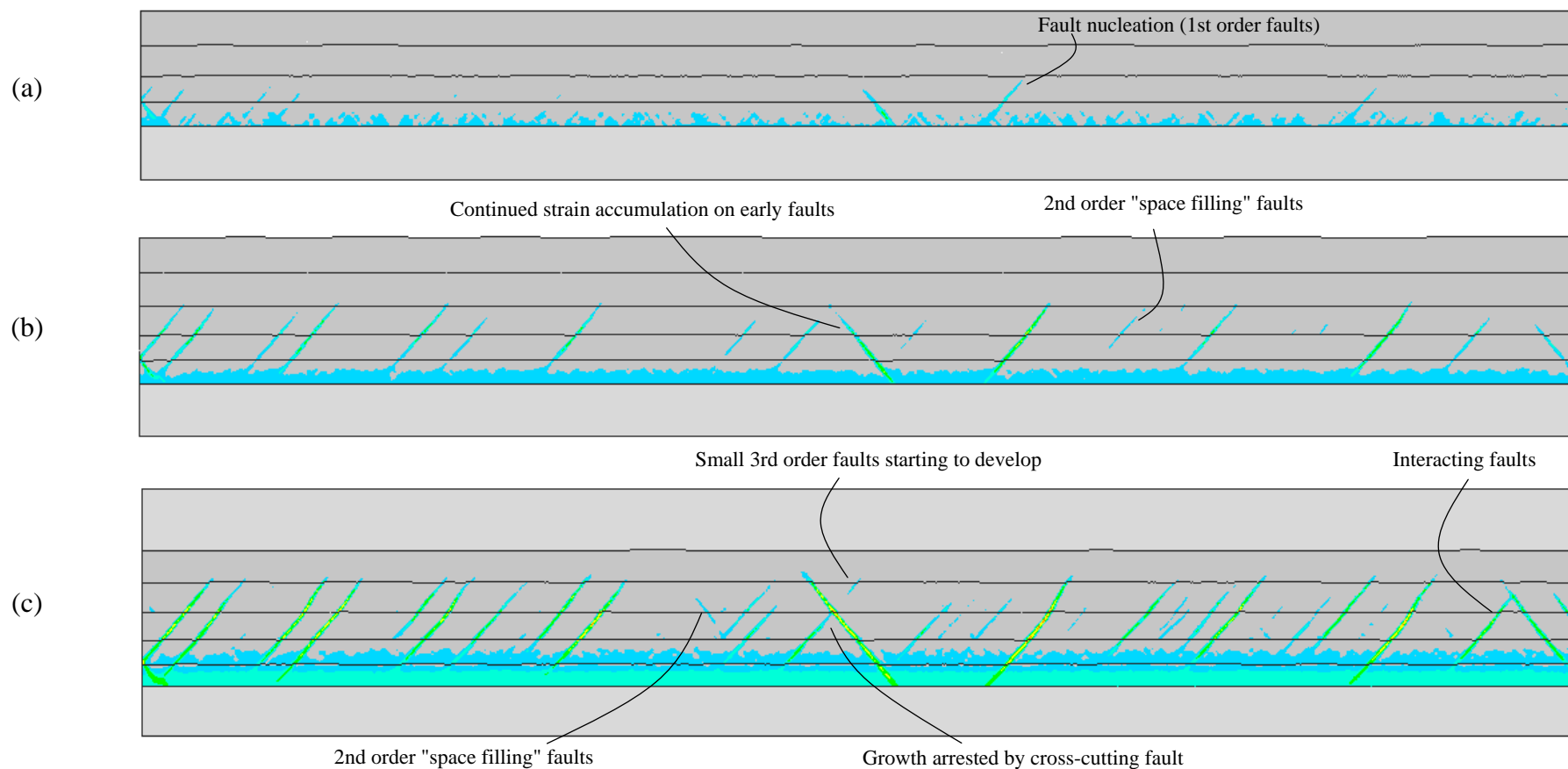


Figure 5-10: Simulated 2D evolution of a polygonal fault system at (a) 3.7My (b) 5.0My (c) 7.0My. Note the layer-bound nature of the faults which terminate at specific stratigraphic levels, in this case indicating the transition from chemically to non-chemically affected layers.

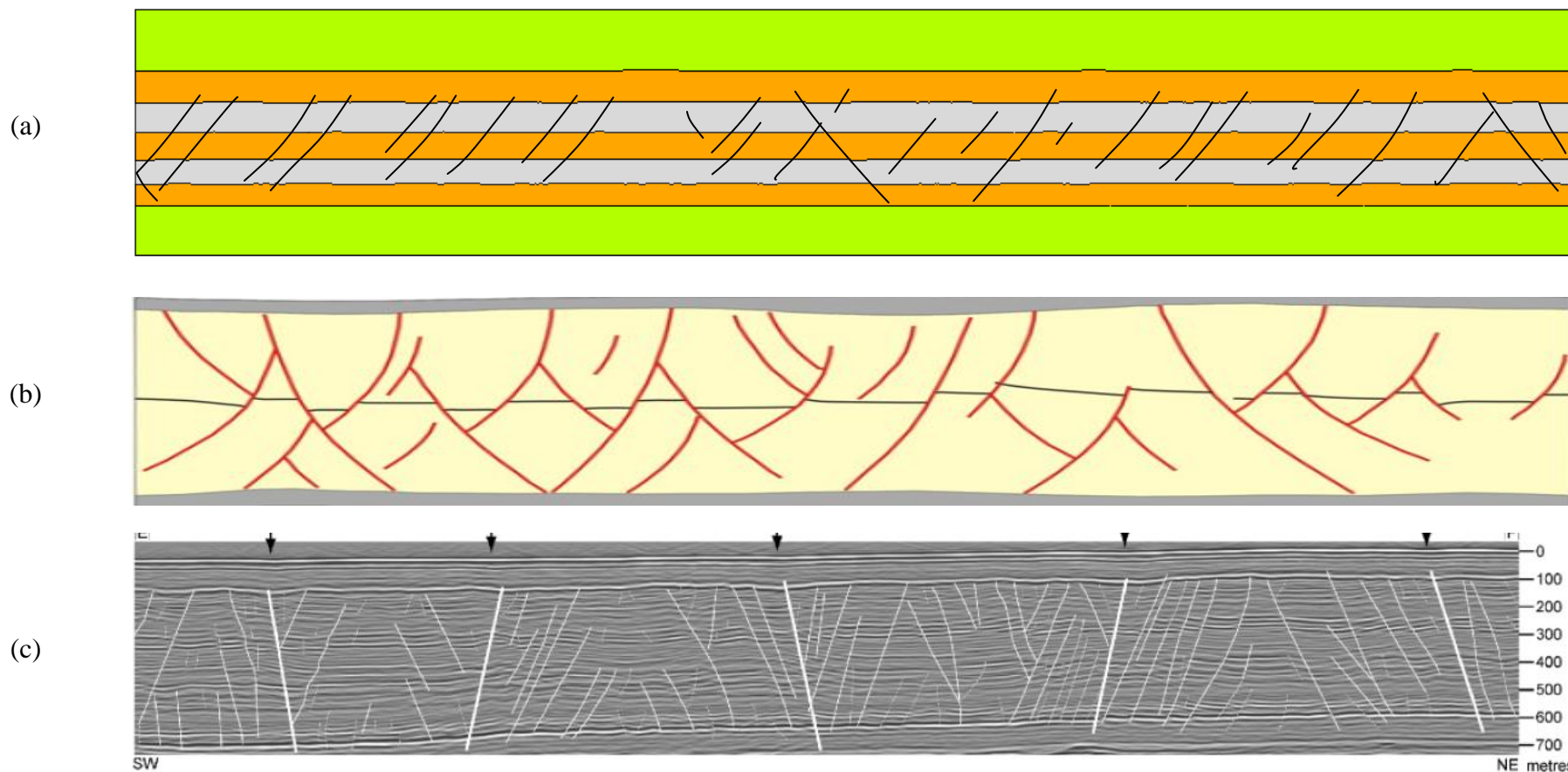


Figure 5-11: Comparison between model results and tier geometries (a) faulting interpretation at end of simulation (b) classic planform geometry (Cartwright, 2011) (c) PFS in the Lower Congo Basin (Gay et al., 2004).

The good qualitative agreement with real field-scale observations serves as additional reinforcement that the modelling approach and geomechanical argument are robust.

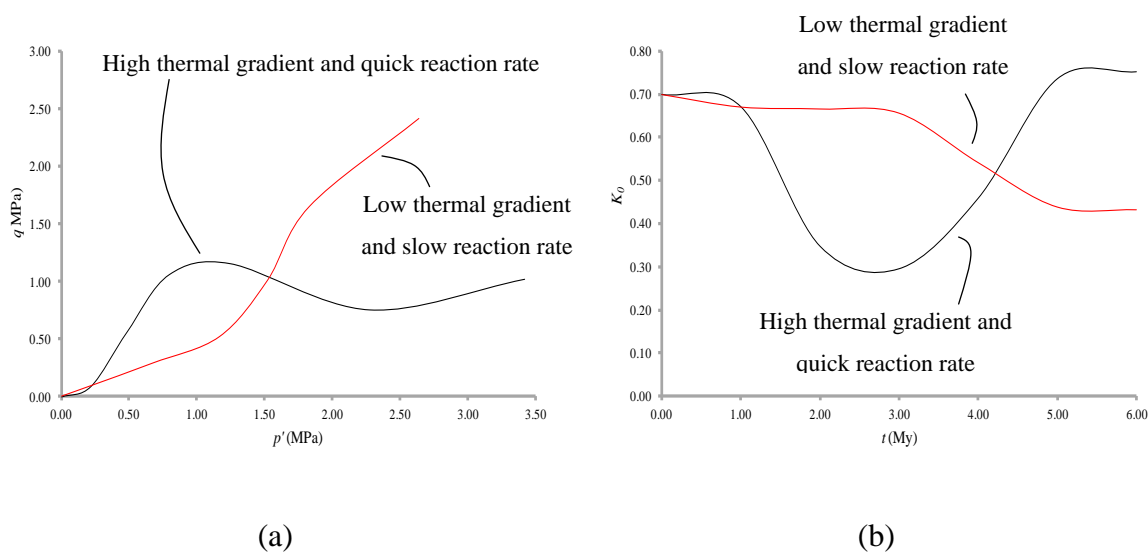


Figure 5-12: Influence of thermal gradient on stress path in q - p' space. (a) Stress path in q - p' space (b) Evolution of K_0 . The black line represents the high thermal gradient case and the red line represents the low thermal gradient case.

Altering the thermal gradient also exerts a control on deformation style. In Figure 5-12(a) the stress path with the high thermal gradient of the previous analysis is shown. It is clear that the deviation from the K_0 line is quite marked and shear failure is in this case predicted before returning to K_0 on further burial (Figure 5-12(b)). For low thermal gradient and reduced rate the initiation temperature is not reached until the sediment is buried to a greater depth and deviation from the K_0 line is less extreme.

5.2.1.2 Expression of Diagenetic Volume Change

A sensitivity study of the influence of whether the chemical reaction results in isotropic (pure volumetric) or anisotropic volume change is performed. This follows on from the single element testing in Chapter 4, which highlighted that definition of chemical volume change has a pronounced impact on the stress path. In particular this was shown to strongly influence whether the stress path in the deviatoric (q) vs. effective mean stress (p') plane reached a state favouring shear failure. Note that in the discussion of the constitutive model in Chapter 3, it was highlighted that the ratio of q/p' provides an indication of where the stress state lies relative to critical state line, and hence the subsequent deformation style.

The model developed in the preceding section is used and faults are interpreted via

Field Scale Analysis of the Formation and Evolution of Polygonal Fault Systems

examination of accumulated displacements in the vertical direction (Figure 5-13). It is clear that adoption of the orthotropic chemical flow rule does not result in the recovery of faulting. Figure 5-14 shows the ratio of q/p' at 6.0My. The ratio of q/p' varies within the tier as shown in both (a) and (b). Just below the location of the diagenetic front for the isotropic chemical flow rule scenario, the modification of the stress path is clearly seen via an increase in q/p' indicating that stress states that ultimately favour failure in shear have been reached. Below the transformation zone sediment that has undergone diagenetic alteration now tends back towards the K_0 condition and hence lower values are observed. In the orthotropic chemical flow rule case it is clear that although similar deviations from the expected stress path are taking place, these are more subtle, with the ratio of q/p' reaching values in the range approximately 0.5-0.8. These are still on the compactive side and localised shear failure is not predicted.

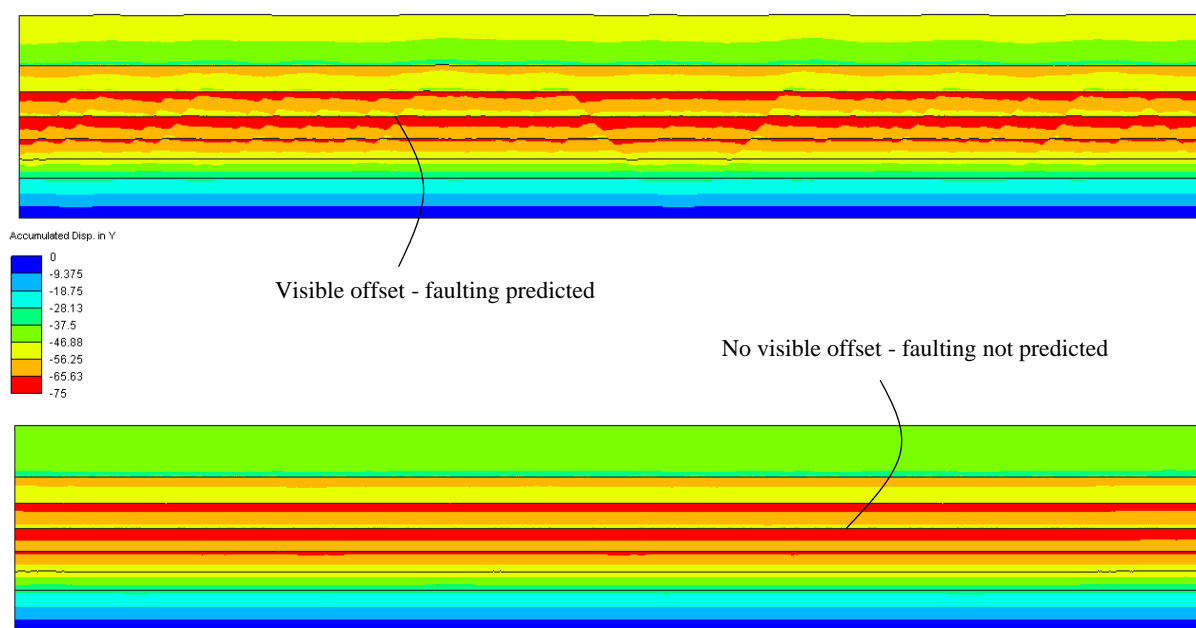


Figure 5-13: Accumulated displacements (in metres) in the vertical direction for (a) orthotropic chemical flow rule (b) isotropic chemical flow rule. In the orthotropic case the development of localised faults is not predicted.

The stress states are summarised in Figure 5-15 to reinforce the point that in the case where chemical volume change is isotropic, stresses associated with shear are obtained. The relevance of these observations is again emphasised. The nature of the reaction on the micro-structural scale is critical in determining the bulk behaviour of the sediment. As demonstrated here, this could have a pronounced influence on deformation style, which in turn would

Field Scale Analysis of the Formation and Evolution of Polygonal Fault Systems

impact the integrity of a cap-rock and dictate fluid migration pathways. If the genesis of PFS is truly as a result of diagenetic processes then this observation may provide additional constraints in identifying which sediments and reactions have the necessary characteristics. Variation of the expression and magnitude due for instance to subtle facies variation and sediment composition could further control the distribution and intensity of faulting throughout a tier.

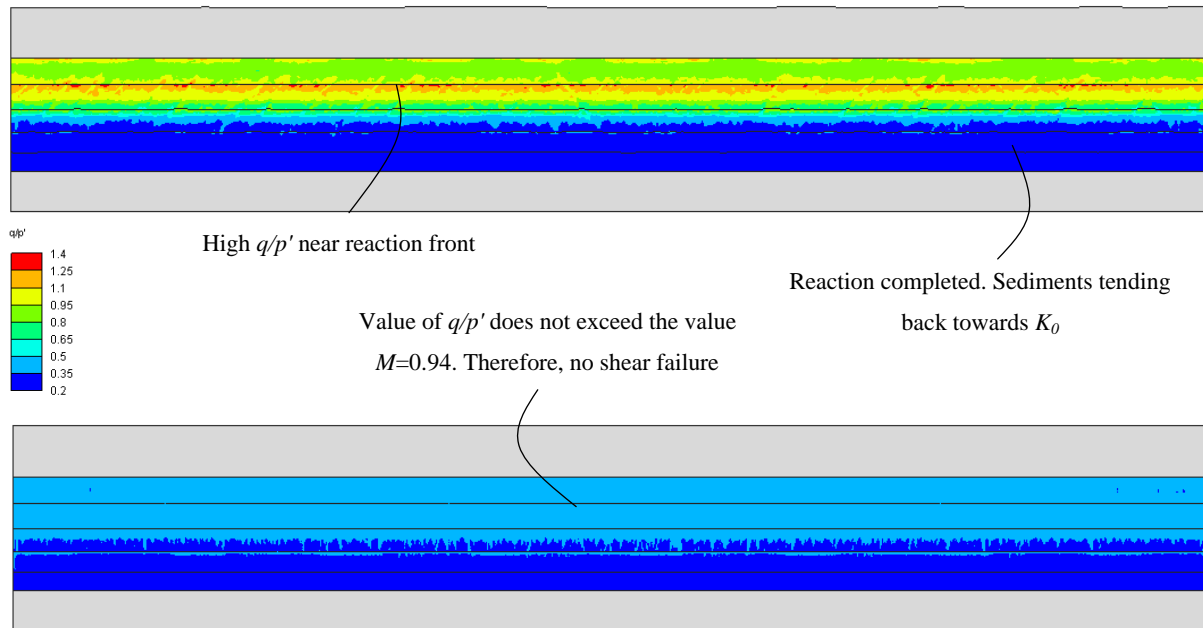


Figure 5-14: Ratio of q/p' at $t=6.0\text{My}$ (a) orthotropic flow rule (b) isotropic flow rule. High values (red) indicate intersection of the yield surface in shear. Low values (blue) sediments are on the cap and compacting. The isotropic expression of diagenetic volume strain results in a ductile-brittle transition whereas the orthotropic expression does not.

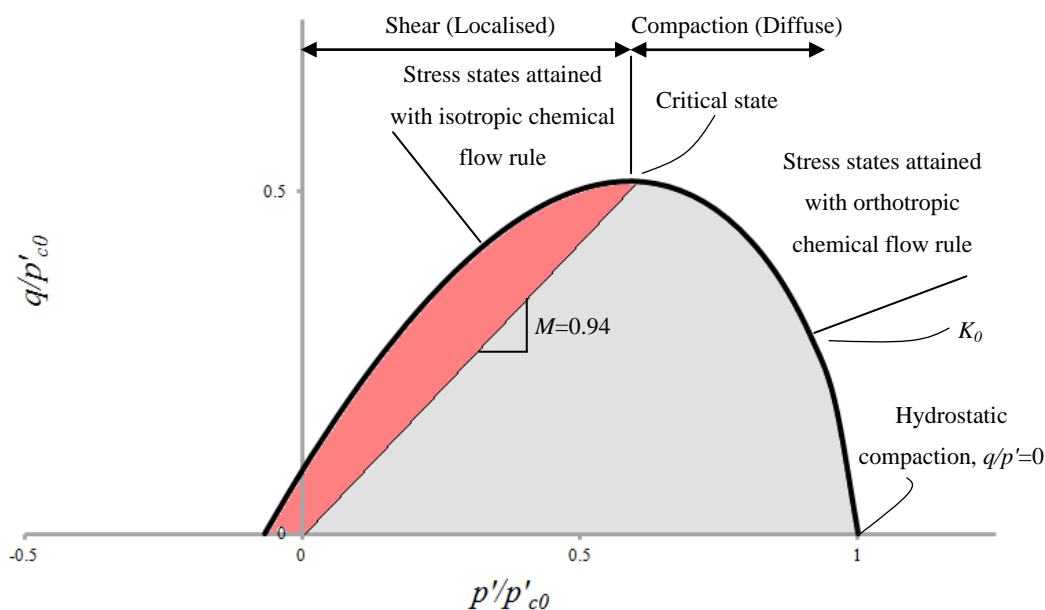


Figure 5-15: Plot showing the range of stresses that may be obtained in models with orthotropic and isotropic chemical flow rules. Note that the range of stress states obtained for orthotropic flow rule is to the right of critical state.

5.2.1.3 The Significance of Low Residual Friction

The change to the stress path and material state as the chemical reaction progresses leads the material to a state of shear failure. The throw on the faults is, however, fairly small with the maximum throw observed to be about 5m. Results reported from shallow tiers at a range of locations indicate that this value is at the lower limit for a tier of approximately 400m height (Shin et al., 2010), and the approximate relationship between fault height and throw is given in Equation 5-2.

$$\delta / H = 0.045 \pm 0.016 \quad 5-2$$

Where δ is the fault throw and H is the fault height (both in metres). This trend is also shown in Figure 5-16 for several different polygonal fault systems. Whilst several factors could contribute to this relationship, such as proximity to/interaction with adjacent faults, it is suggested that a major component is likely driven by the value of the residual friction (Shin, 2009). As noted in Chapter 1, given exposure to sufficiently high strains, fine-grained sediments often see a reduction in strength from the critical to the residual state that is associated with a preferentially aligned fabric (Wood, 1990). In order to investigate the affect of residual friction, modifications to the material model are implemented so that the user may

Field Scale Analysis of the Formation and Evolution of Polygonal Fault Systems

specify a gradual reduction of the angle of the critical state line to a lower, residual value. The threshold effective plastic strain for the start of such a reduction is set at 0.25 and is assumed to follow an exponential trend to the residual value at an effective plastic strain value of 1.0. For these sensitivities various residual friction values are used in the range $5.21^\circ \leq \phi_r \leq 20.58^\circ$.

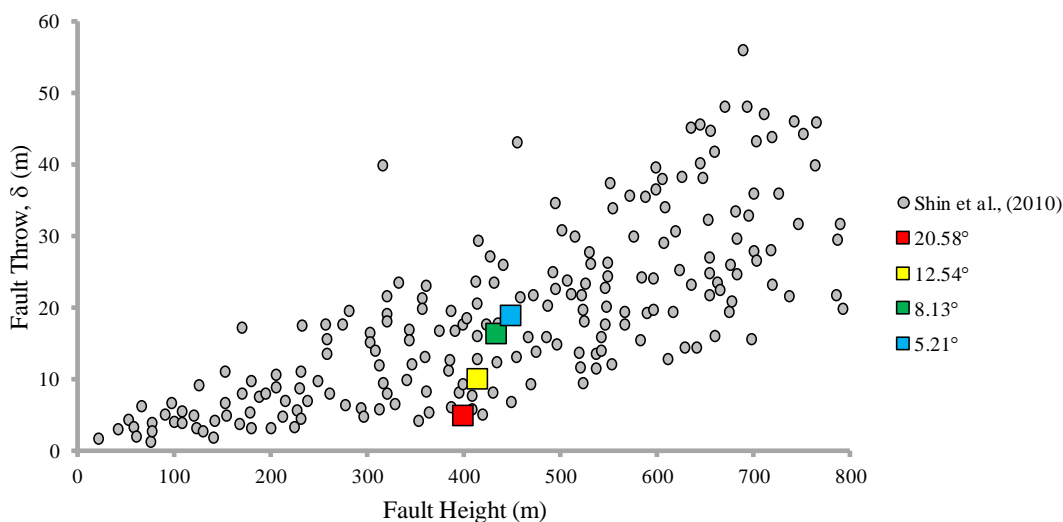


Figure 5-16: Maximum fault throw versus fault height for a number of shallow polygonal fault systems, modified after (Shin et al., 2010). The faults plotted are from various locations including West Africa, North Sea and Brazil. The results of simulations featuring reductions in the residual friction are also shown (squares) and fall within the expected range.

The results of the simulations are shown in Figure 5-17. The general throw profiles are typical of blind faults (Baudon and Cartwright, 2008) with displacement maxima located in the upper middle section, and in good agreement with profiles reported for many polygonal fault systems (Cartwright, 2011). Furthermore, there is a clear relationship between the residual friction and the observed throw as shown in Figure 5-17(a) and Table 5-6, which is in agreement with the findings of Shin et al., (2010).

Initial residual friction ($^\circ$)	Final residual friction ($^\circ$)	Maximum throw on fault (m)	Maximum observed horizontal displacement on fault (m)
20.58	20.58	5.00	2.29
20.58	12.54	10.13	5.87
20.58	8.13	16.47	7.30
20.58	5.21	19.01	8.11

Table 5-6: Summary of residual friction simulations. Note the relationship between residual friction and both maximum throw and maximum horizontal displacement.

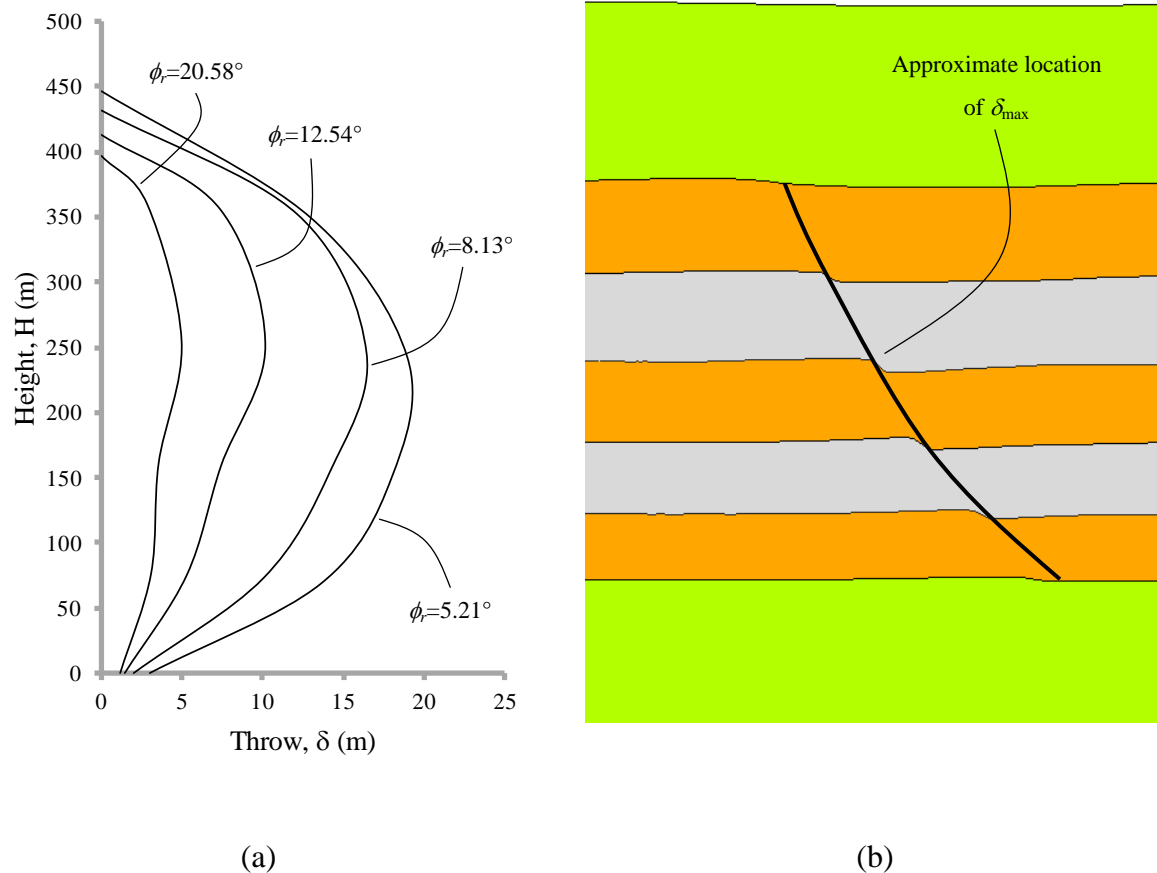


Figure 5-17: Influence of residual friction on fault propagation (a) Fault throw profiles for various values of residual friction (b) Zoomed image of a single fault showing displacement within the tier for a residual friction value of 8.13° .

When plotted against the data in Figure 5-16 the wide spread of data could be explained by variations in the frictional strength of the faults. In this scenario, sediments that grow early and accumulate large strains tend towards the residual state and develop significant larger throws. In other areas the propagation of faults may be slower, or the constitutive properties of the sediment might not correspond to extremely low residual friction values, and hence throw is more modest. It is also apparent that some faults have even larger throws than those achieved here and this difference could be due to very early initiation and propagation or that some faults are preferentially aligned with respect to the regional stress state or may be reactivated and as such accumulate larger strains and hence throws. Figure 5-18 shows the accumulated horizontal displacement for various residual friction values, showing a trend of increasing horizontal displacement with reducing residual friction angle. Also apparent is that

Field Scale Analysis of the Formation and Evolution of Polygonal Fault Systems

where the residual friction is high the faults are predicted to be planar, whereas the faults associated with low residual friction become increasingly listric as they evolve. Collectively these results indicate that whilst low residual friction may not be important for initiating early faulting, it is considered to be important in determining propagation and recovery of seismically observable throws.

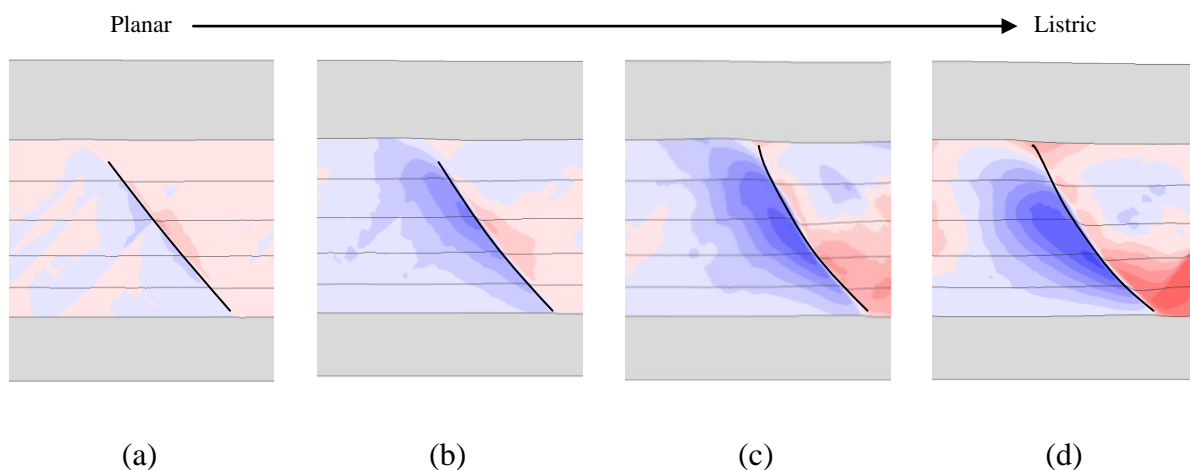


Figure 5-18: Accumulated horizontal displacements for various residual friction angles.

Maximum displacement contour is 12.9m. Hot contours indicate displacement to the right and correspond to the magnitudes reported in Table 5-6. Interpreted fault style is also shown. (a) 20.58° (b) 12.54° (c) 8.13° (d) 5.21°.

5.2.1.4 Arresting Fault Development and Changing Tier Structure

The preceding sections have highlighted an interesting and crucial characteristic of PFS; the fact that often virtually all faults seem to "die out" and cease propagating at a specific horizon. This phenomena, where previously active faults suddenly terminate, is intriguing and still debated for some field cases (Gouly and Swarbrick, 2005; Cartwright, 2011). It is often observed that this sudden termination corresponds with a change from a fine-grained material with dominantly clay size particles to coarser facies containing more silt and sand size particles (Dewhurst et al., 1999). The following model explores this behaviour by incorporating sand characterisations into the deposited materials. Specifically, two of the deposition horizons now represent sandstone intervals and the characterisations are included in the Appendix. The domain length is increased to 12.5km and sediments gently prograde over a sloping base sand sequence, to mimic conditions in Jackson et al., (2013). Figure 5-20(a) shows the predicted distribution of polygonal faults and this is interpreted in Figure

5-20(b). It is obvious that where the sands do not cross the fine grained interval faults are able to penetrate through the entire tier, and that the faults cannot traverse the entire sequence where the coarse grained interval is present. This is evidenced by the lack of any appreciable accumulated effective plastic strain within the coarse grained interval. This resistance to compartmentalisation is due to the comparatively stiffer sandstone (Figure 5-20(c)) and, importantly, the fact that it does not share the same consolidation characteristics as the chemically affected fine-grained mudstones. In some cases the propagation of faults through sand bodies is reported, typically where the sand thins below some critical thickness of less than 100m or so.

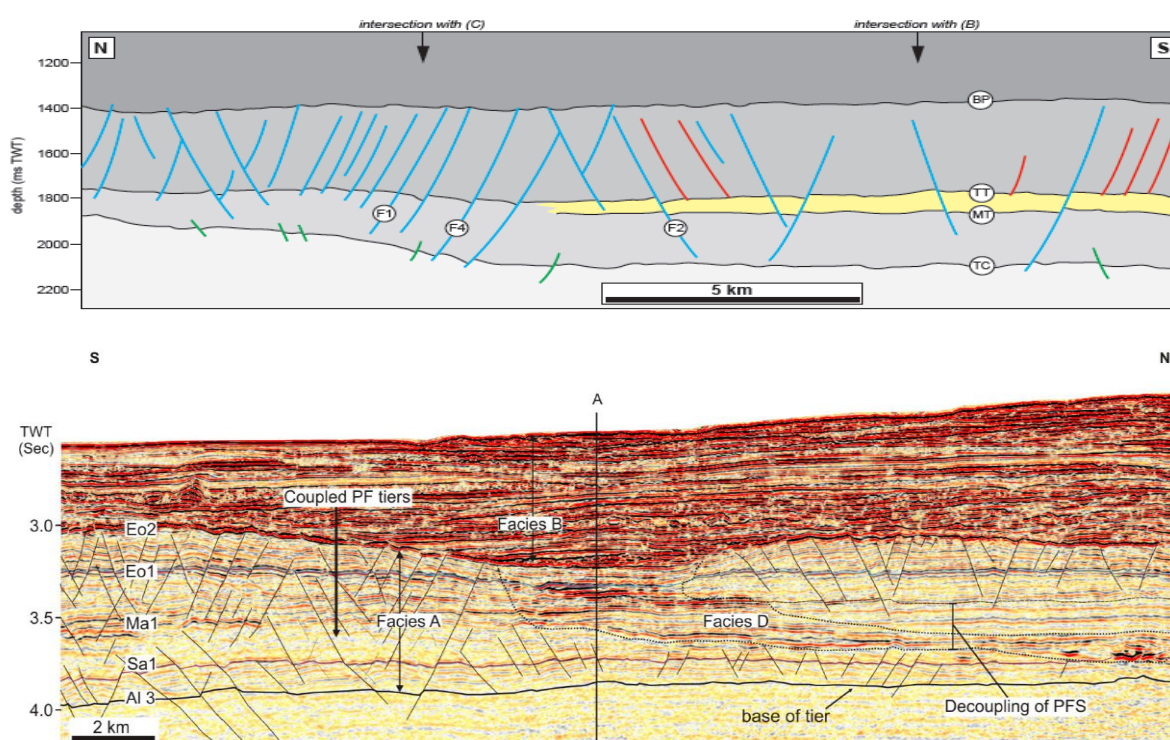


Figure 5-19: (a) Decoupling of tiers in North Sea due to the presence of a sandstone-rich slope fan (Jackson et al., 2014). Tier structure in the Espirito Santo Basin (Carruthers, 2012). Note the coupling of tiers in the South. The presence of the sandy Facies D results in a decoupling of tiers in the North.

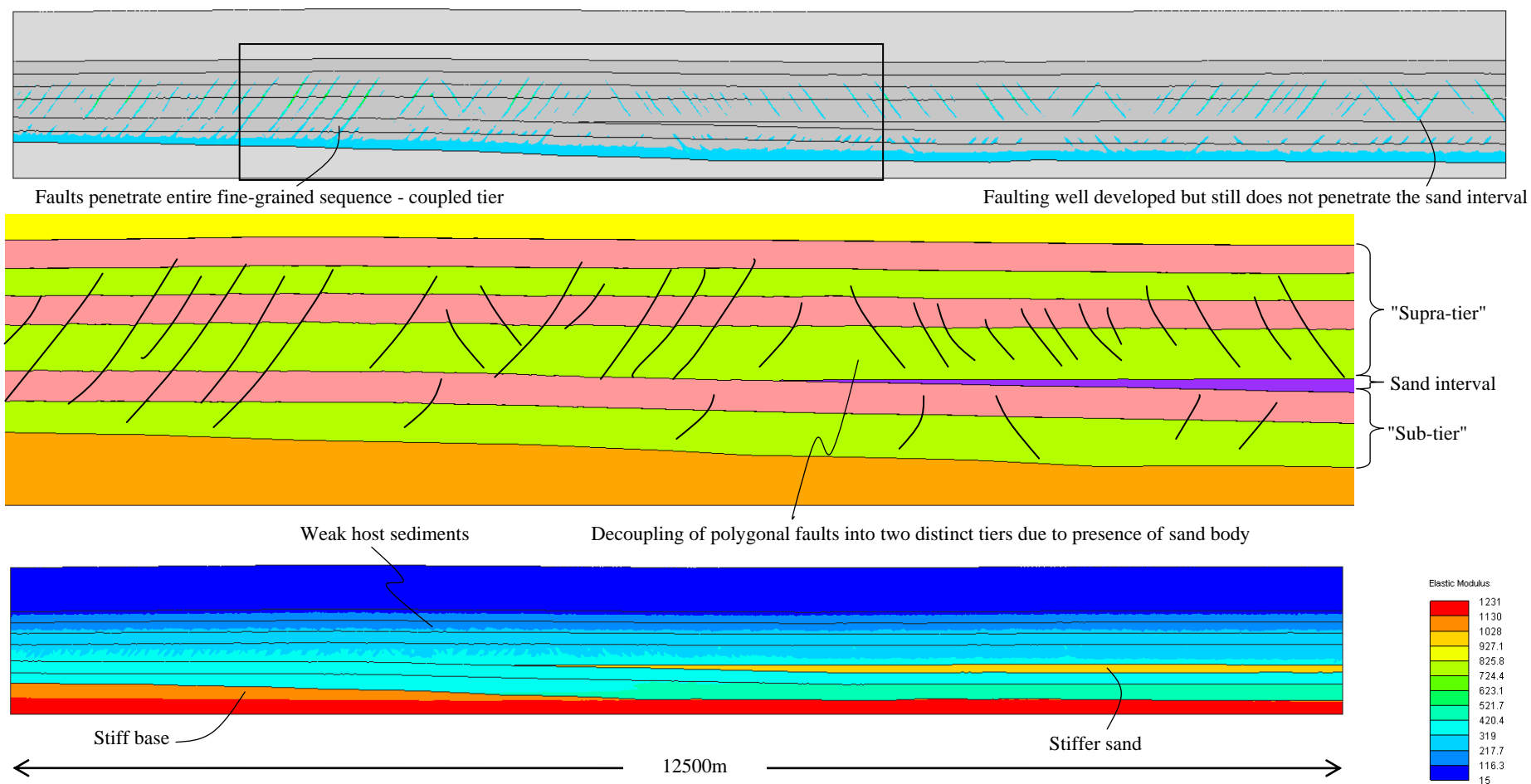


Figure 5-20: Influence of the presence of coarse-grained intervals (a) Distribution of effective plastic strain. (b) Interpretation of faulting style showing decoupling and development of a "supra-tier" and "sub-tier" (c) Contours of elastic modulus (stiffness) in MPa showing the contrast between the stiffer and more competent sand and the comparatively weak sediments hosting the polygonal faults.

The result is that the structure of the tier changes because of the presence of the sand interval. A clear decoupling of the tier is observed, ultimately resulting in two distinct tiers, whose spacing characteristics are also observed to be different. Decoupling is commonly noted in tiers where coarse grained intervals are dispersed throughout the tier in the form of sand sequences in the North Sea (Dewhurst et al., 1999; Jackson et al., 2014) or Mass-Transport Deposits/channel systems in the Espirito Santo Basin (Carruthers, 2012) - see Figure 5-19(a) and (b). The results reinforce the suggestion that polygonal faults are reluctant to form and penetrate through sandy, coarse-grained sequences, and that polygonal faults may be useful exploration tools as the decoupling of tiers can be used to constrain the spatial extents of potential thin sandstone reservoirs (Jackson et al., 2013).

5.2.2 Three Dimensional Evolutionary Model

5.2.2.1 Model Description

Extension of the results into 3-D is performed as additional validation of the modelling approach, and to gain additional insight on the structure of the system. The model setup is shown Figure 5-21. Due to computational constraints the size of the model domain is reduced (model width in 2D is 5km but is reduced to 1000m for the 3D model). It is perhaps prudent to note that although the temperature gradient applied in both 2D and 3D evolutionary cases is representative of the Nankai data (see the black dots in Figure 5-21) this is probably near the upper limit of gradients typical in the shallow crust.

5.2.2.2 Results

The complicated three dimensional geometry of a tier is demonstrated in Figure 5-22. Figure 5-22(d) shows the planform geometry at the base of tier and there are a small number of fairly diffuse faults (red indicates regions of more intense straining). Image Figure 5-22(c) shows the planform geometry a short distance further up in the tier. It is clear that the faulting is localised and more prominent at this level. Figure 5-22(b) shows that faults start to coalesce as they propagate through the tier, and some faults become dominant and arrest the growth of others. Referring to Figure 5-22(a) many of the faults are now connected, with orthogonal intersections between the majority of faults. It is also evident that there is a distinct isotropy in the planform geometry, and that despite the restricted spatial extents of the model, faults intersect bedding planes at a wide variety of azimuths.

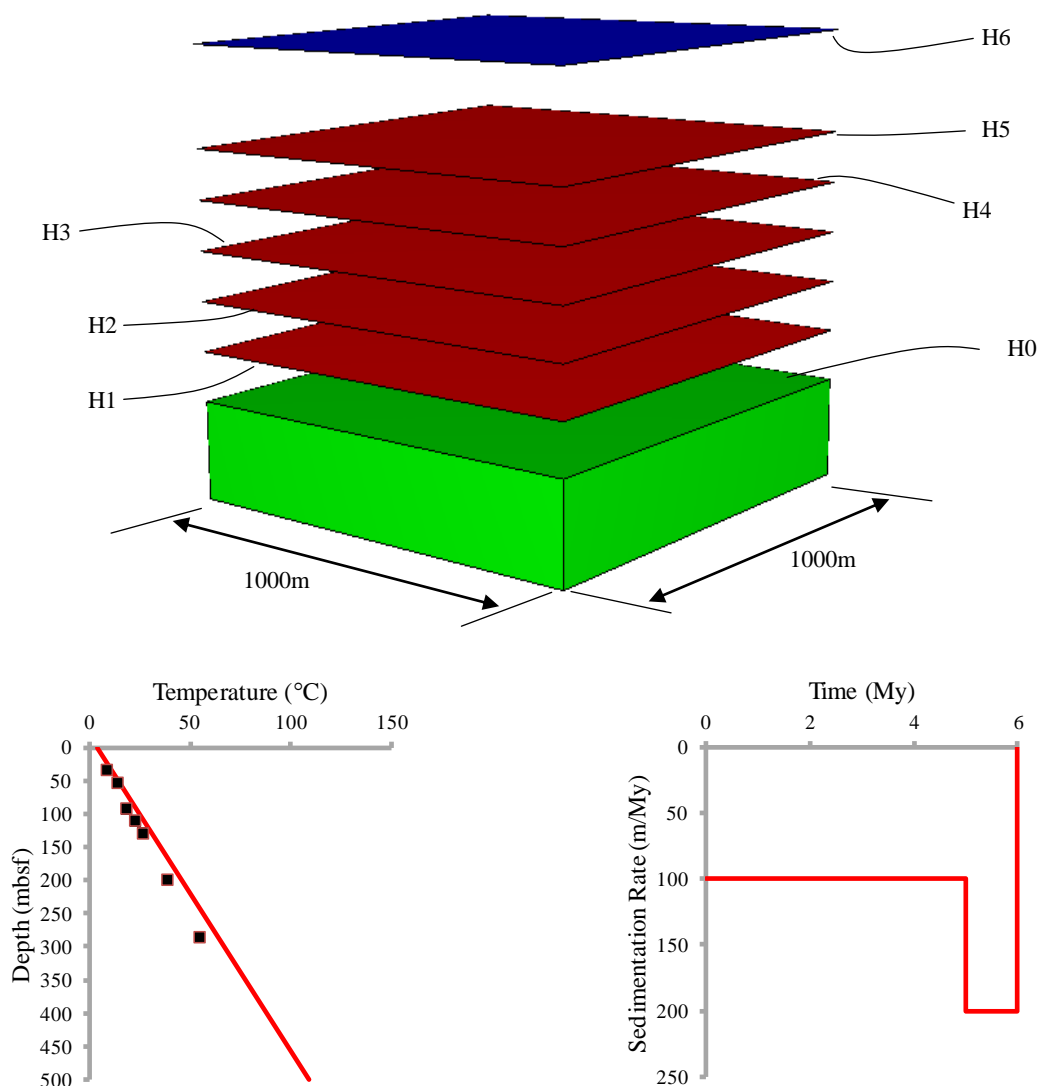


Figure 5-21: Geometry, loading and boundary conditions for 3D evolutionary models. The green section denotes the initial geometry. The red surfaces indicate the deposition horizons for the chemically affected layers. The blue surface indicates the deposition horizon for the overlying non-chemically affected layer. Thermal gradient and approximate sedimentation rates are also shown.

Figure 5-23 shows the horizontal displacements at the same horizons displayed in Figure 5-22. Warm colours indicate large accumulated horizontal displacements and cool colours indicate lower accumulated displacements. These are useful in visualising heave throughout the tier. It is obvious that the distribution is complex due to the interactions between intersecting faults. Maximum displacements are often observed in the region immediately adjacent to the faults and are seen to decay towards the centre of a polygonal cell.

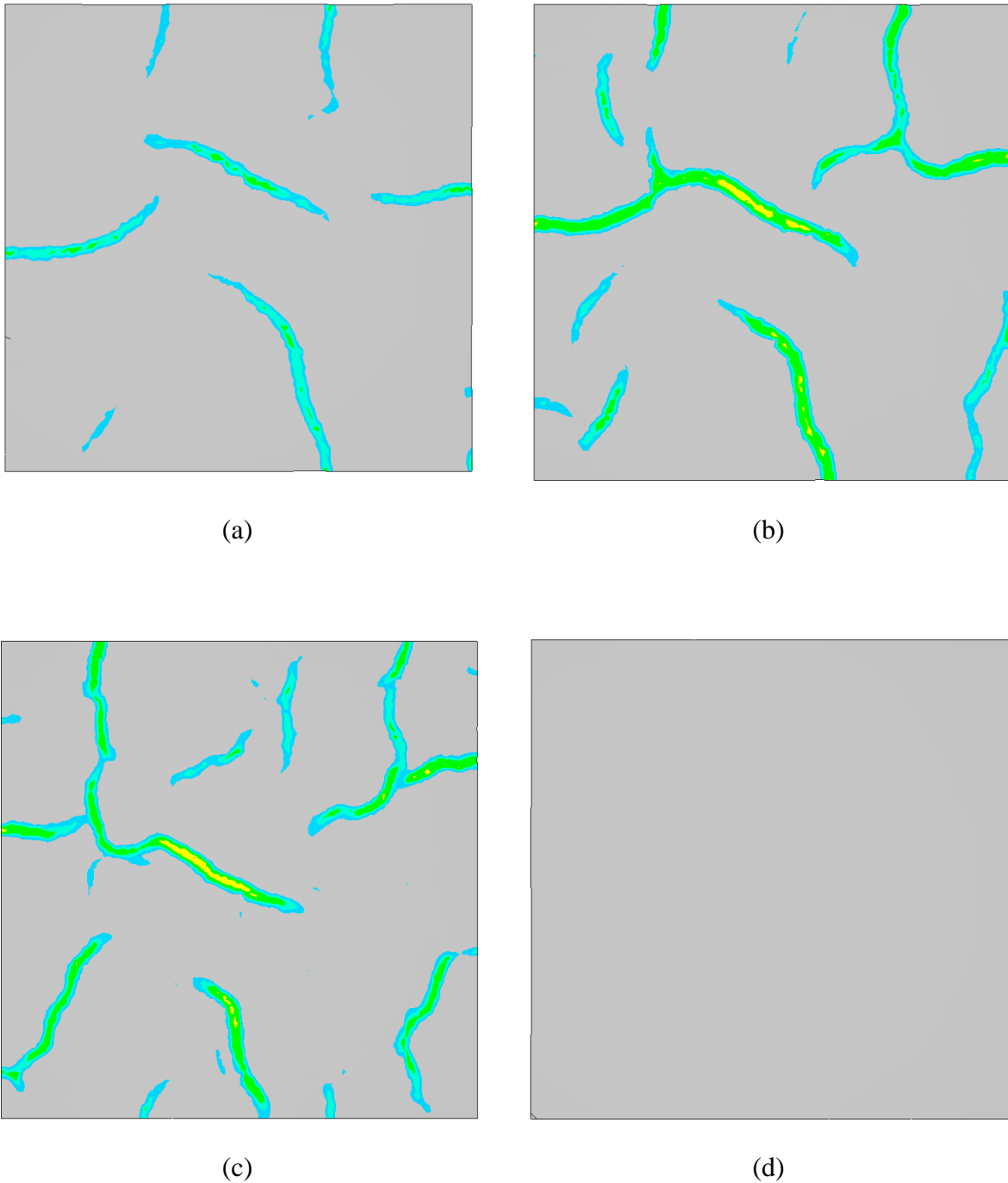


Figure 5-22: Contours of effective plastic strain showing planform geometry of various horizons through the tier. (a) Horizon H3 (b) Horizon H2 (c) Horizon H1 (d) Horizon H0 (base of tier). See Figure 5-21 for horizon locations. Note the random orientations of faults that reflects the isotropic horizontal stress state and how fault connectivity changes at various horizons. No appreciable plastic strain is observed at the base of the tier.

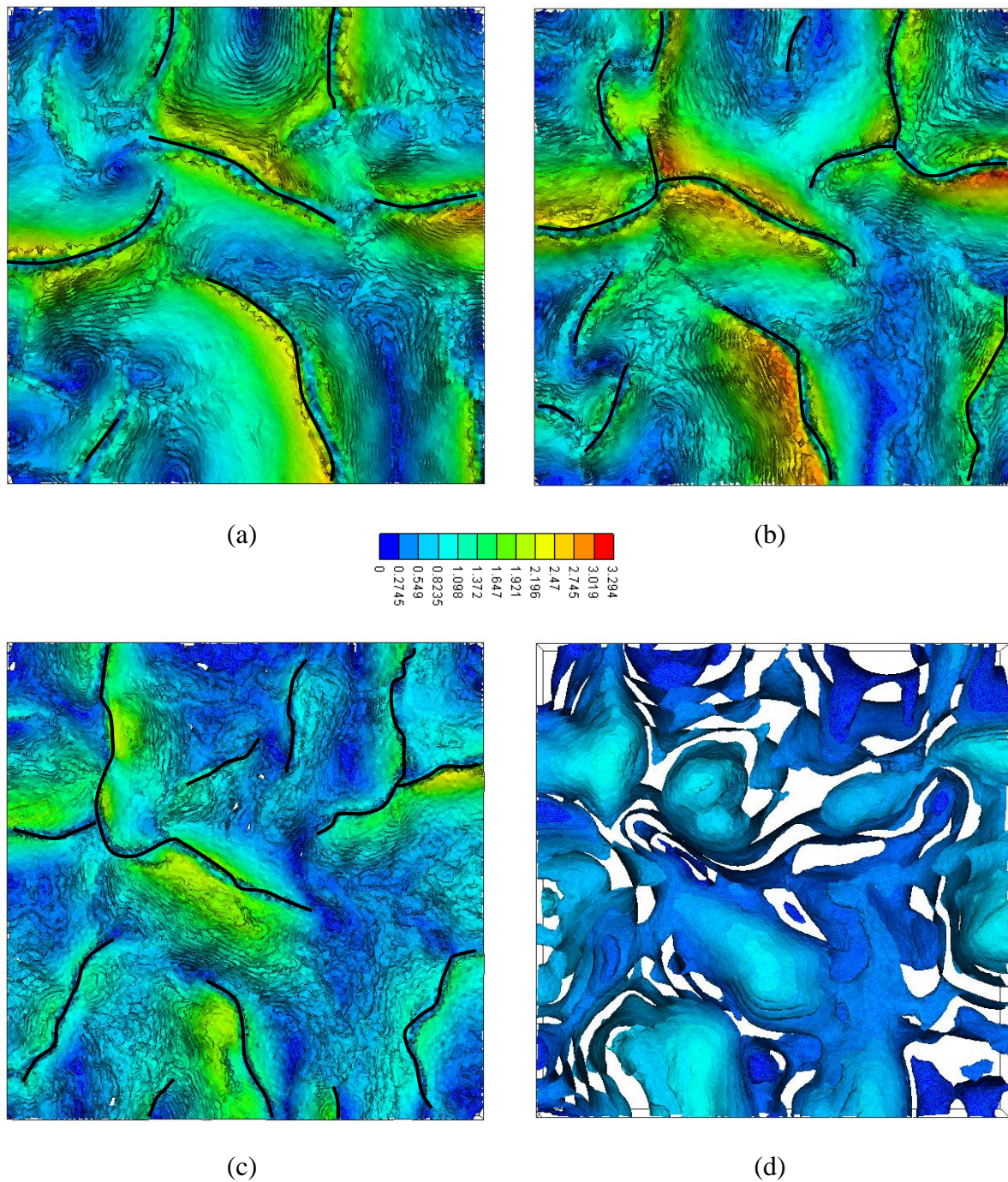


Figure 5-23: Isocontours of accumulated displacement in xy for (a) Horizon H3 (b) Horizon H2 (c) Horizon H1 (d) Horizon H0 (base of tier). See Figure 5-21 for horizon locations. Interpreted faults also shown. Largest heave is in the upper section of the tier and is negligible at the base of the tier as indicated by the cool contours. The largest displacement (heave) is observed close to the faults and decays away from it.

Field Scale Analysis of the Formation and Evolution of Polygonal Fault Systems

Figure 5-24(a) shows the present day material state (as indicated by the preconsolidation pressure) and stress state for the H3 horizon. Contours of preconsolidation pressure show significant reductions within the localisations where the material has failed in shear and softened. Contours of effective mean stress are shown in Figure 5-24(b). Note that by dividing the preconsolidation pressure by the effective mean stress we have an approximation of overconsolidation ratio. At the present day much of the sediment at this level is tending back towards the K_0 condition but it is evident that the sediment is still slightly overconsolidated ($1.1 < OCR < 1.6$). Note that in zones close to faults and particularly in regions where multiple faults intersect the stresses are noted to be slightly higher, likely attributed to increased horizontal stresses as the faults slip (Gouly, 2008).

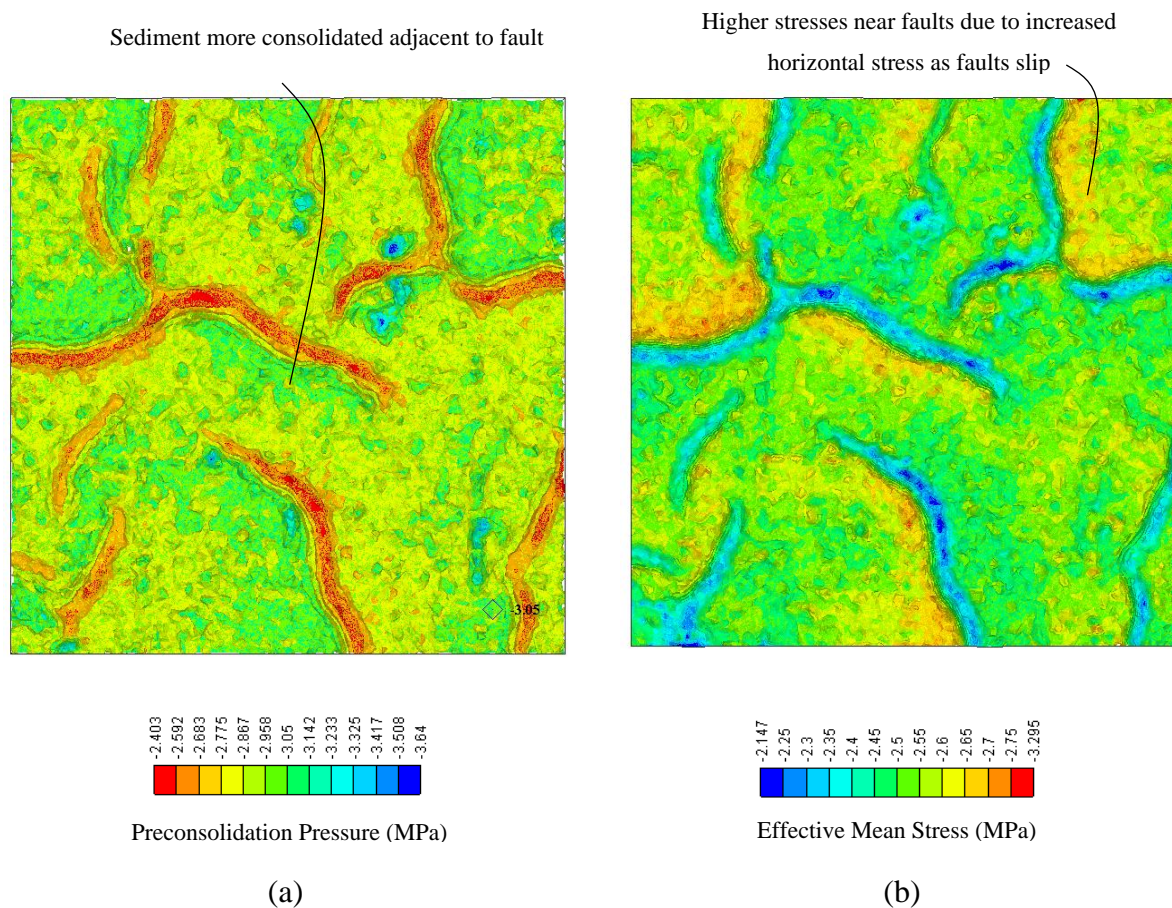


Figure 5-24: Model output showing material and stress state at Horizon H2 at present day, corresponding to a burial depth of ca 600m (a) Contours of preconsolidation pressure (b) Contours of effective mean stress. The contours indicate that at this depth and time the sediment is tending back towards the K_0 condition although the sediment still appears slightly overconsolidated with an OCR of between 1.1 and 1.5.

5.2.3 Comments

The observations made in this section reinforce the potential for diagenesis as a trigger for polygonal fault formation as well as providing detail on how this mechanism might lead to macro-scale faulting. Comparison between 2D and 3D modelling output and observation from actual fault tiers appears favourable in a qualitative sense, and comparison with the Cartwright and Dewhurst criteria again appears favourable - see Table 5-7.

Rank	Criterion	Recovered?
1	Polygonal map view patterns	Yes
2	Layer bound in the vertical direction	Yes
3	Areal extent	N/A
4	Fault type and throw 10-100m	Yes
5	Fault spacing (100-1000m)	Yes
6	Tiers	Yes (in 2D)
7	Mixed fault polarity	Yes

Table 5-7: Comparison between evolutionary model output and criteria for PFS identification as outlined by Cartwright and Dewhurst (1998).

5.3 Investigation of Intraformational Faulting at Shallow Depth

The motivation for this investigation is that in some cases polygonal faults develop in extremely shallow regions, where only mechanical compaction is expected. An example is normal faulting in chalks on the UK mainland (Hibsch et al., 2003). In this case there are indications that normal faults that were inferred to have tectonic origins may actually be polygonal faults, and that this is not widely appreciated due to the scale of the faulting relative to outcrop studies. Importantly, petrographic analysis supports genesis in the very early stages of deposition, potentially before any chemical processes were active. Further evidence comes from cases such as that reported in the Goban Spur, which is noted to be polygonally faulted in the interval between 27 and 278mbsf (Cartwright and Dewhurst, 1998) - see Chapter 2. The tier is observed to correspond to a zone where mechanical compaction is prominent but there is little evidence of diagenetic features, and evidence of combined diagenesis and mechanical compaction is only appreciable below 300mbsf (Jennings and Mazzullo, 1977). Several additional case studies are also presented in the subsequent section which feature polygonal faulting within the 'mechanical compaction domain'. Suggested potential mechanisms are discussed where appropriate.

5.3.1 Lake Superior

Recognition of a potential polygonal fault system in shallow sediments below Lake Superior indicates that polygonal fault systems might start growing in the first tens of metres of burial (Wattrus et al., 2003; Cartwright et al., 2004). The faults are hosted below the lake bed within a grey varved clay of approximately 10m thickness, as shown in Figure 5-25(a) and (b). The planform geometry is also shown and connectivity appears to be poor. The poor connectivity possibly reflects the young age of the polygonal faults, and therefore maturity of the fault network (Cartwright, 2011). This is reinforced by the fact that the sediments were deposited relatively recently, likely less than 10ka BP (Cartwright et al., 2004). The layer bound nature of the faults and the random strikes of faults in planview are convincing indicators of a potentially young polygonal fault system.

5.3.2 Boom Clay

The argillaceous Boom formation onshore Belgium has been extensively studied as it is a sequence targeted for long term storage of High Level Waste (Dehandschutter et al., 2005). Study of the formation has revealed extensive micro- and meso-scale faulting and jointing, and macro-scale faults with metre-scale offsets. The larger faults are described as intraformational as they do not extend below the Boom formation. The suggested genesis of the faults is described in Figure 5-25(c). The sediment is estimated to have been deposited during the early Oligocene (Rupelian) in shallow water depths of approximately 50m. The sequence is buried to a maximum depth of 150m before it is uplifted slightly and micro shear bands form throughout the layer. The sequence then experiences a volume reduction which facilitates the coalescence of the shear bands. Macro-scale intraformational fracturing results from continued volumetric contraction, assisted by layer parallel shortening due to regional compression during the Alpine Orogeny. It is stressed that a key aspect of the development of this intraformational fault network is the volume reduction, the source of which is not quite clear, though it is suggested that this may result from the weak nature of fine-grained argillaceous sediments in general. This endogenic behaviour is therefore not typical of coarser-grained, sandy intervals and so the faults are restricted in their ability to propagate into other layers.

5.3.3 Offshore West Africa

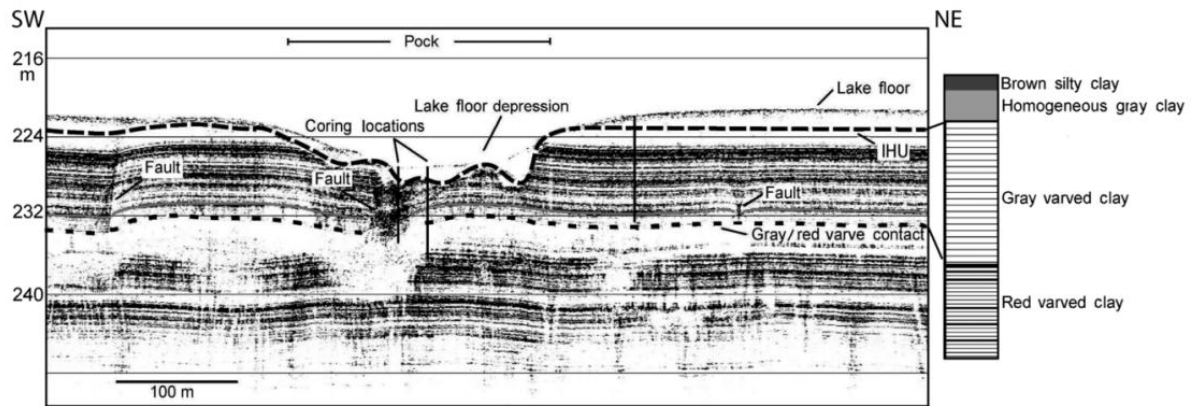
Analysis of networks of polygonal faults offshore West Africa has provided further evidence of early genesis of polygonal faults. Figure 5-26 shows an amplitude map and seismic section

of shallow sediments in the Lower Congo Basin. Interestingly the brighter reflections around some faults are interpreted to be sandy 'growth packages' and their presence is thought to indicate propagation of faults to the seabed at some stage during their evolution. In some areas of the Lower Congo Basin polygonal faults are apparent on seismic lines within the first 50m of sediment (J. Cartwright - personal communication).

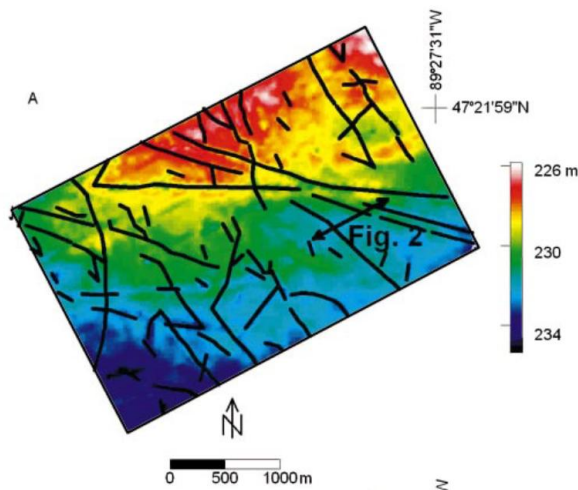
5.3.4 Approach for Conceptual Investigation

The framework of the previous diagenetic investigations may be used to impose a three-dimensional strain which mimics, for example, the volumetric "matrix strain" that is suggested in some of the discussed case studies and thought to be typical of argillaceous sediments. Specifically, we may specify a rate of volume strain due to this unspecified mechanism by carefully choosing the chemical compaction parameters and imposed thermal gradient. The anticipated differences in the two responses is shown in Figure 5-27.

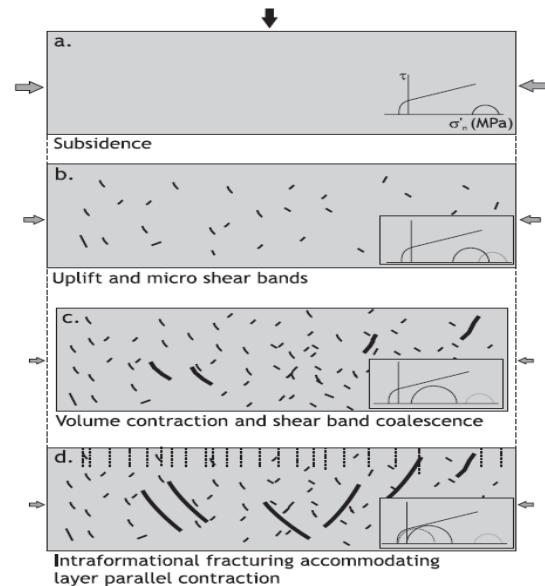
A generic near surface clay is characterised by making modifications to the previously characterised material. The parameters of Boom Clay in particular have been used to guide characterisation (BGS, 2010). Specifically, the shape of the yield surface and plastic potential in the meridian plane has been modified, and the depositional porosity has been increased to 70% which is typical for near surface and poorly consolidated specimens. The material parameters are shown in Table 5-8 and Table 5-9.



(a)



(b)



(c)

Figure 5-25: (a) Inferred polygonal fault system, Lake Superior (Cartwright et al., 2004). Upper image shows small scale faults on shallow seismic of the lake bed with faults highlighted in red. (b) Inferred polygonal planform geometry at Lake Superior. (c) Suggested evolution of intraformational faults in the Boom Clay (Dehandschutter et al., 2005).

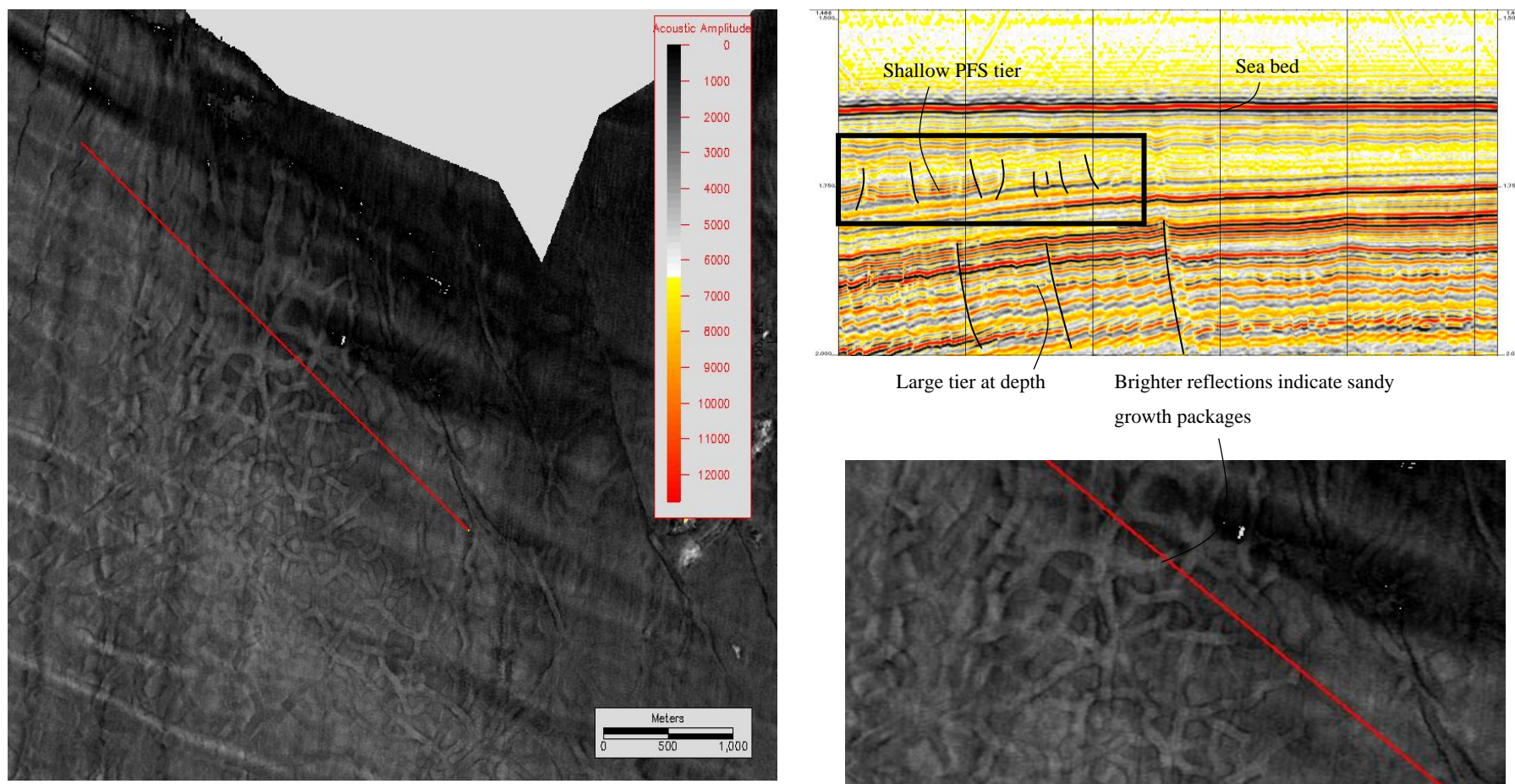


Figure 5-26: Shallow PFS, West Africa. Left image shows planform geometry. Red line denotes location of seismic section shown in upper right image. Depth between top of shallow tier and seabed is approximately 80m.

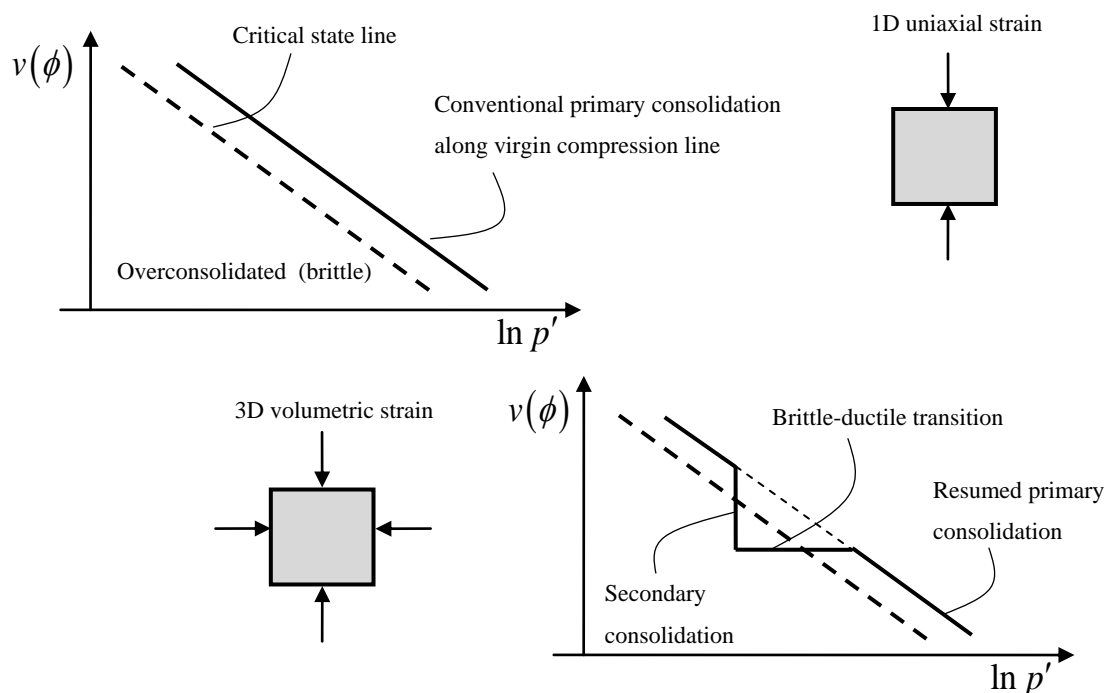


Figure 5-27: Cartoon showing idealised early evolution of sediments. The volume change arising from the 3D volumetric strain leads the specimen to a denser than critical state condition and therefore appears overconsolidated.

Parameter	Value
Poisson's Ratio (ν)	0.4
Reference Porosity (ϕ_{ref})	0.7
Reference Bulk Modulus (K_0)	10.00 MPa
Slope of URL (κ)	0.09

Table 5-8: Poro-elastic properties for weak clay. Note the steeper slope of the unloading-reloading line which reflects a weak and compressible material.

Parameter	Value
Initial tensile intercept (p_{t0})	-0.1 MPa
Initial compressive intercept (p_{c0})	0.2 MPa
Parameter (β)	45°
Parameter (ψ)	40°
Exponent (n)	1.6
Deviatoric plane parameter (N^π)	0.25
Deviatoric plane parameter (β_0^π)	0.7
Deviatoric plane parameter (β_1^π)	1.73×10^{-1} (1/MPa)

Table 5-9: Plastic properties for weak clay.

5.3.5 Results

The volume loss for the conventional consolidation case is shown in Figure 5-28. The trend exhibits a fairly typical elastic response. At approximately 200kPa, which corresponds to the characterised initial pre-consolidation pressure, the material yields and exhibits considerably more volume loss per increment of increasing stress. This marks the onset of plastic deformation and one dimensional virgin consolidation. The equivalent case for the conceptual three-dimensional consolidation scenario is shown in Figure 5-29. The initial trend is similar but there is a clear departure from the 1D case, with the additional essentially stress-insensitive volume change leading to an apparent overconsolidated state. Once the three-dimensional consolidation process is completed the sediment recovers toward the conventional consolidation trend.

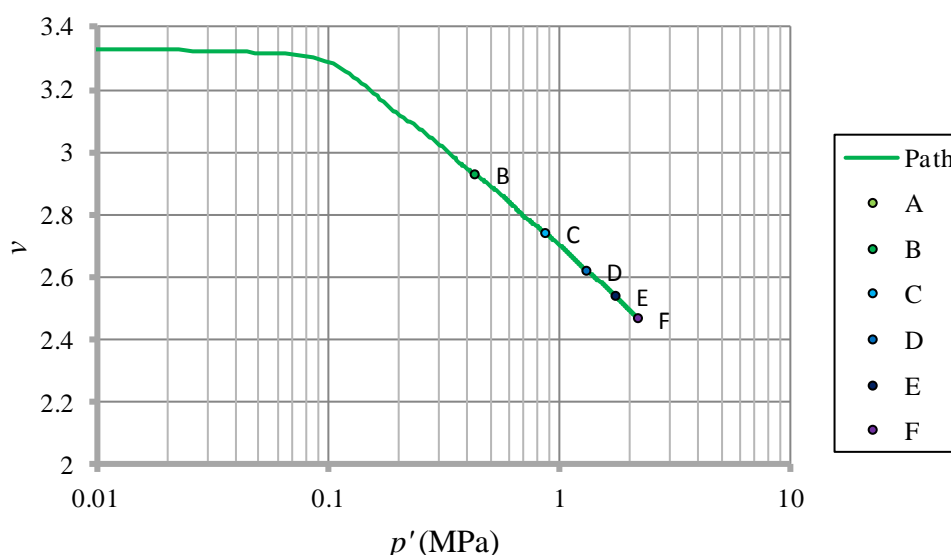


Figure 5-28: Plot of specific volume versus effective mean stress for 1D consolidation case.

At point F for both cases the total volume changes is almost identical. The second case clearly demonstrates a less conventional depositional history, which might not be easily inferred from observations of the current material state. The result of this change is once again the change in stress path and the recovery of a system of polygonal faults, as shown in Figure 5-30. Even at modest depths of less than ca 90m, the plots of effective plastic strain and accumulated horizontal displacements in (a) and (b) respectively show that localised

Field Scale Analysis of the Formation and Evolution of Polygonal Fault Systems

faulting has been initiated. With further sedimentation the faults continue to develop and are able to propagate to with 50m of the seabed. Throws on the faults are modest owing to their immaturity. Maximum throw on most faults is between 2m and 4m.

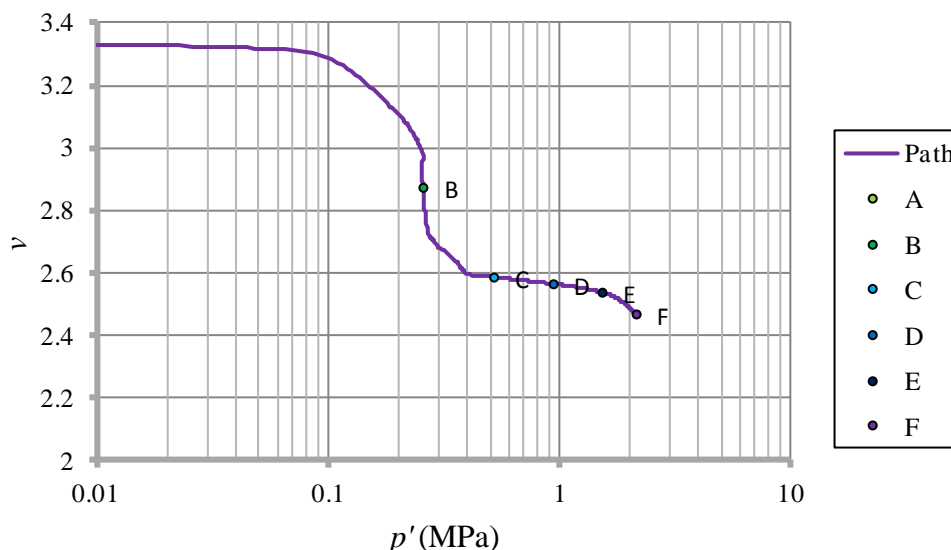


Figure 5-29: Plot of specific volume versus effective mean stress for 3D consolidation case. Prior to point B the 3D volume reduction takes place rapidly leading to a pseudo-overconsolidation.

The porosity loss during burial for the normally consolidated sample is shown in Figure 5-31(a). The sediment progressively loses volume from the depositional porosity of 0.7 to a value of 0.62 over 3My. This corresponds to burial to approximately 250m depth and is in agreement with porosity trends observed in early burial of many fine-grained sediments. Figure 5-31(b) shows the response for the case featuring an early three dimensional consolidation. From A to B the sample behaves as if it is normally consolidated. However, once the three-dimensional consolidation starts the sample loses volume more rapidly than in the previous case, yet the difference in porosity at 1My is still only around 2%. Once the three-dimensional consolidation is completed at 0.75My and the polygonal faults are starting to develop (see Figure 5-30) the porosity loss occurs at a noticeably slower rate. The reason for this retarded porosity loss is shown in Figure 5-32. Figure 5-32(a) shows the normal consolidation response and the sediment progressively loses volume and becomes more consolidated. The effect of the three-dimensional consolidation is apparent in that the value

of the pre-consolidation pressure at 1My is larger.

Similarly to the diagenetic cases in the previous sections, the three-dimensional expression of volume change has facilitated a progressive transition from ductile to brittle behaviour, and as normal consolidation behaviour resumes the stress path returns to the ductile side of the yield surface. Consequently, due to the overconsolidated state, porosity loss is inhibited between points C and E in Figure 5-32(b). Comparison between the 1D and 3D consolidation simulations also indicates that the porosities at the end of the simulation are very similar, yet the evolution and resulting deformation styles are very different. Figure 5-33 shows the evolution of the yield stress ratio (isotropic), which in this case is defined as the ratio of the preconsolidation pressure for the 3D and 1D consolidation scenarios, or;

$$YSR^* = \left(\frac{P_{c,3D}}{P_{c,1D}} \right) \quad \mathbf{5-3}$$

The change in the size of the state boundary surface arising from the different consolidation styles is clear, but note that by 3My there is no discernible difference in the inferred level of consolidation, again corresponding to ca 250m burial. This is a significant observation as it indicates that early processes may have a major impact on deformation style during early burial but that with further deposition the indicators for such processes may not be obvious. The only indicators for such an unusual consolidation style might then be the observation of unusual structures such as polygonal faults. The evolution of the principal stresses is shown in Figure 5-34 and the familiar trend of reduction of smallest principal stress (horizontal) leading to failure followed by return to K_0 is observed.

Field Scale Analysis of the Formation and Evolution of Polygonal Fault Systems

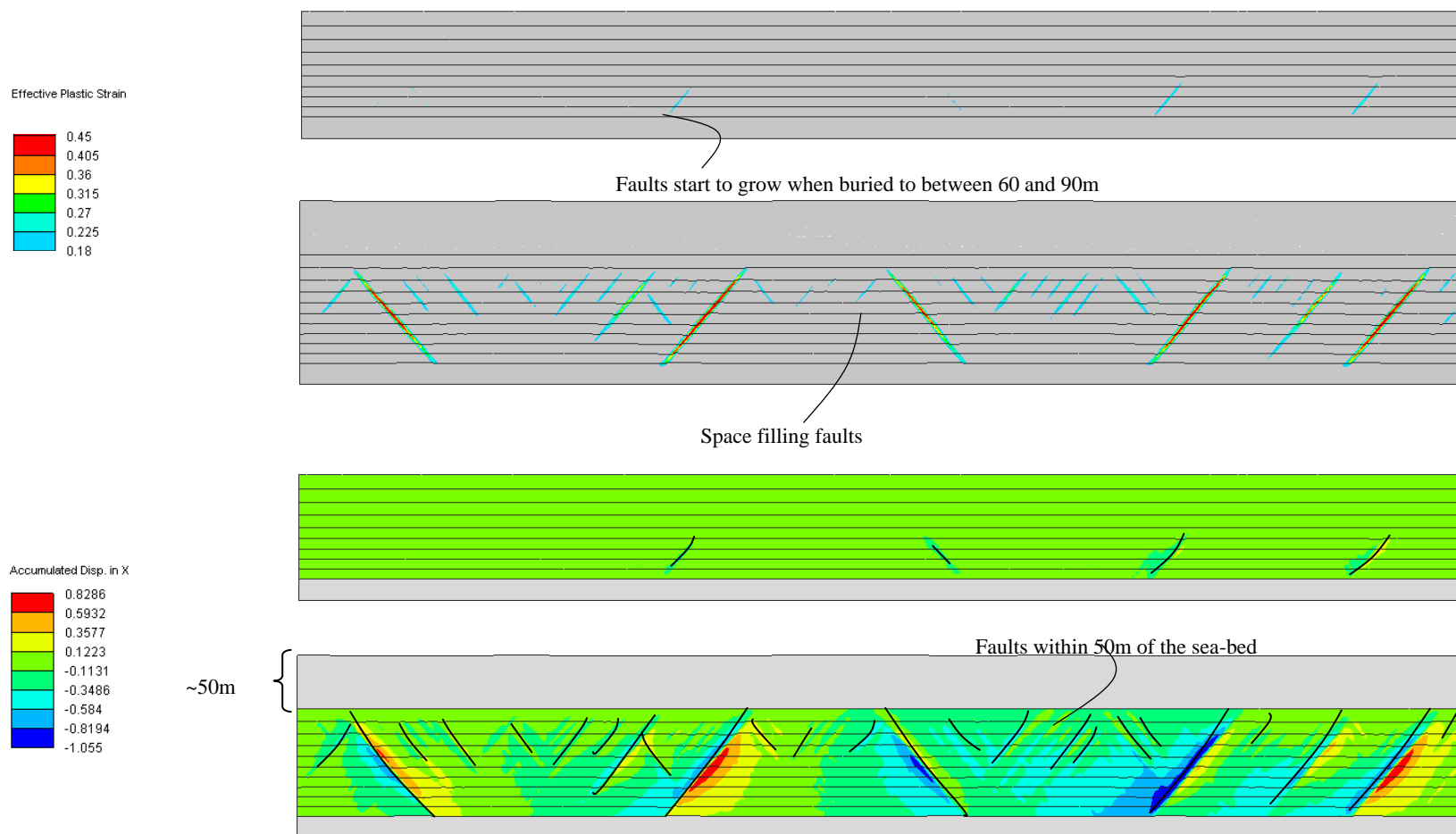


Figure 5-30: Contours of effective plastic strain and accumulated displacements at 1.0My and 1.5My. Burial to depth of 155m is shown. Note how faults nucleate in the lower third of the tier and have not been buried to depths exceeding between 60-90m.

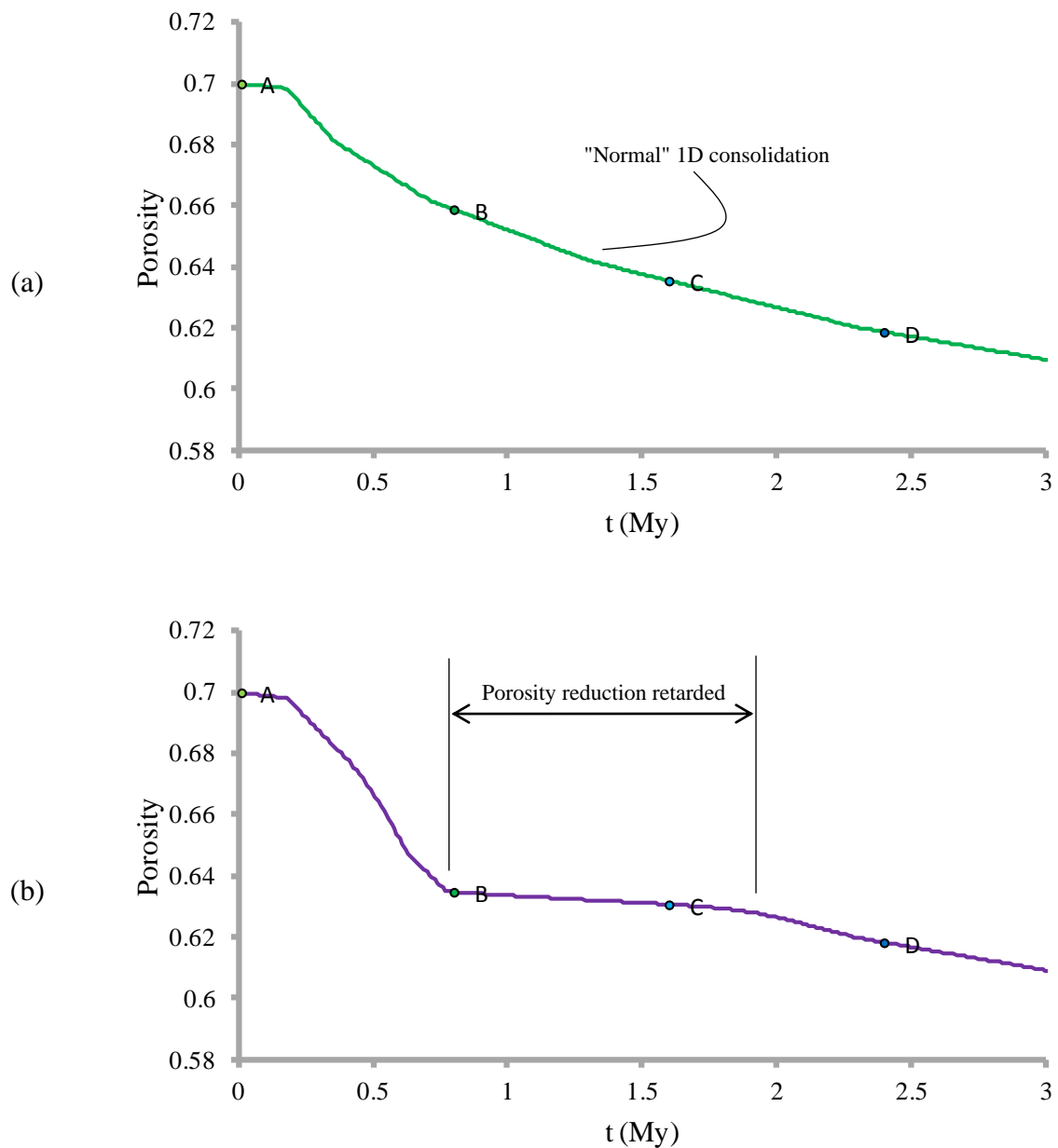


Figure 5-31: Evolution of porosity (a) conventional consolidation (b) three-dimensional consolidation.

5.3.6 Comments

The results in this section have shown that the geomechanical argument may potentially be extended beyond the diagenetic mechanism. The expression of subtle additional volume change and/or increase in strength during early burial may have similar implications as the discussed diagenetic processes. The modelling approach has made the assumption that such processes can be treated in a similar fashion to the diagenetic processes. The additional

Field Scale Analysis of the Formation and Evolution of Polygonal Fault Systems

volume change and alteration to the stress path leads to the development of localised faulting, the characteristics of which once more correlate well with seismic observation of shallow intraformational fault systems.

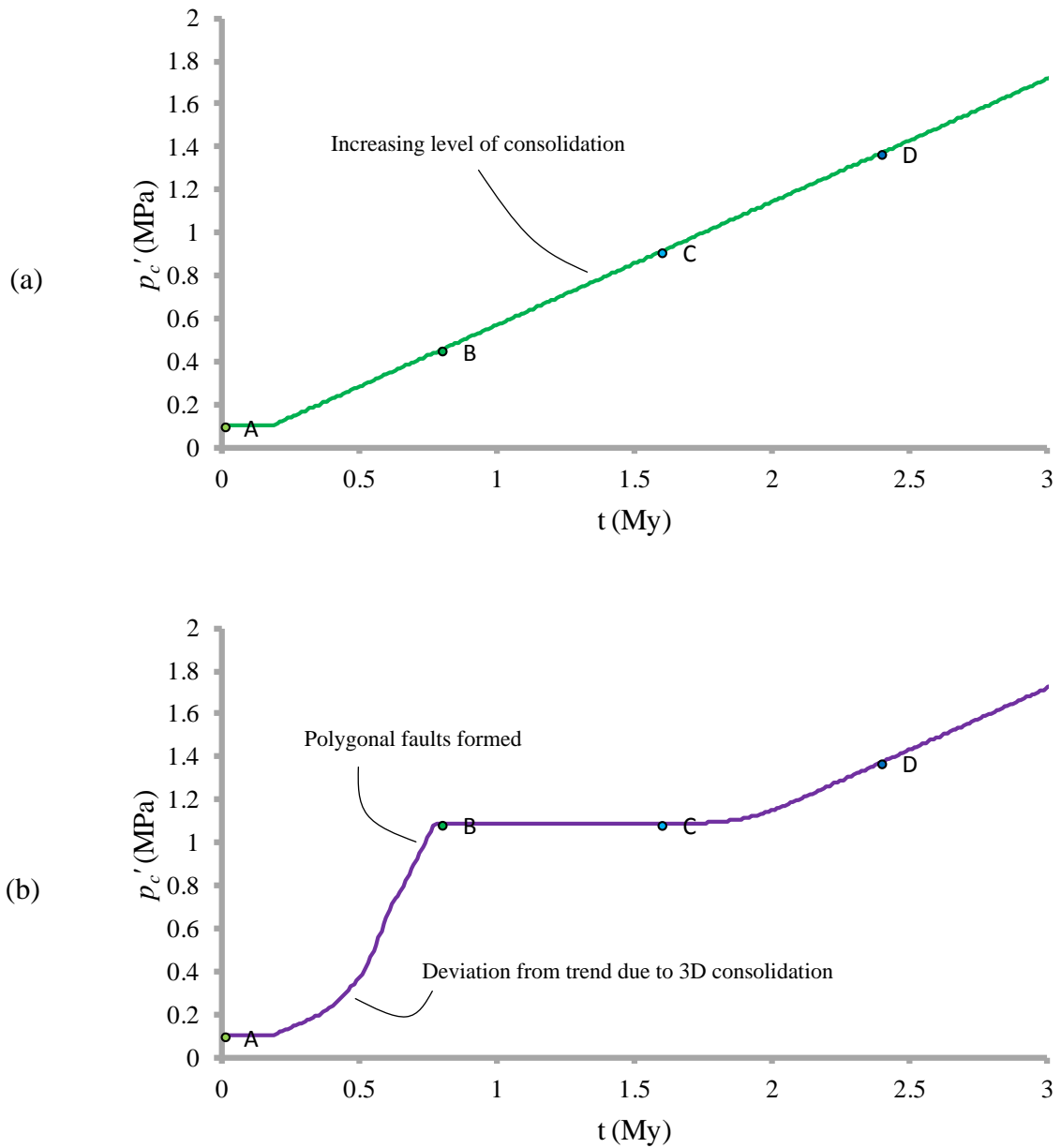


Figure 5-32: Evolution of preconsolidation pressure (a) conventional consolidation (b) three-dimensional consolidation.

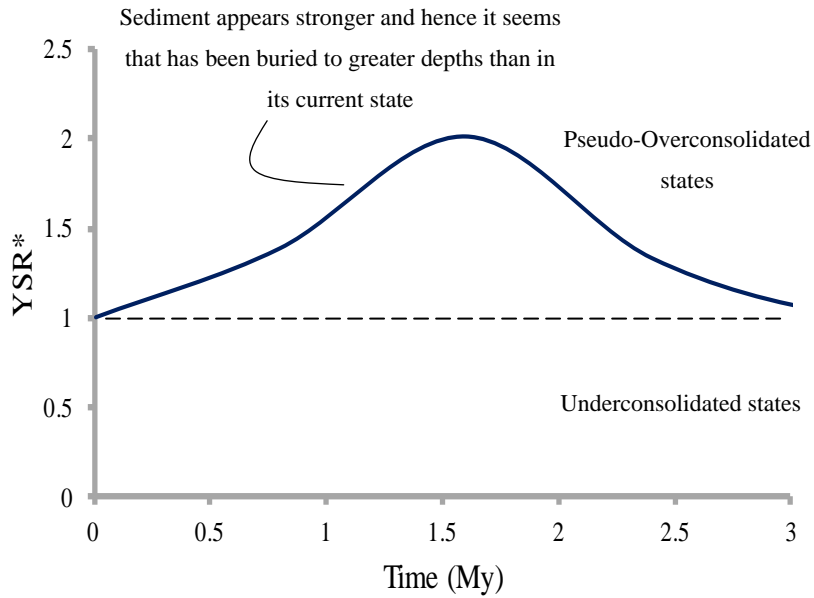


Figure 5-33: Evolution of Yield Stress Ratio (YSR*). Note that as the three-dimensional consolidation begins the material appears to be more consolidated. As this process moves to completion the sediment tends back to the normal consolidation trend.

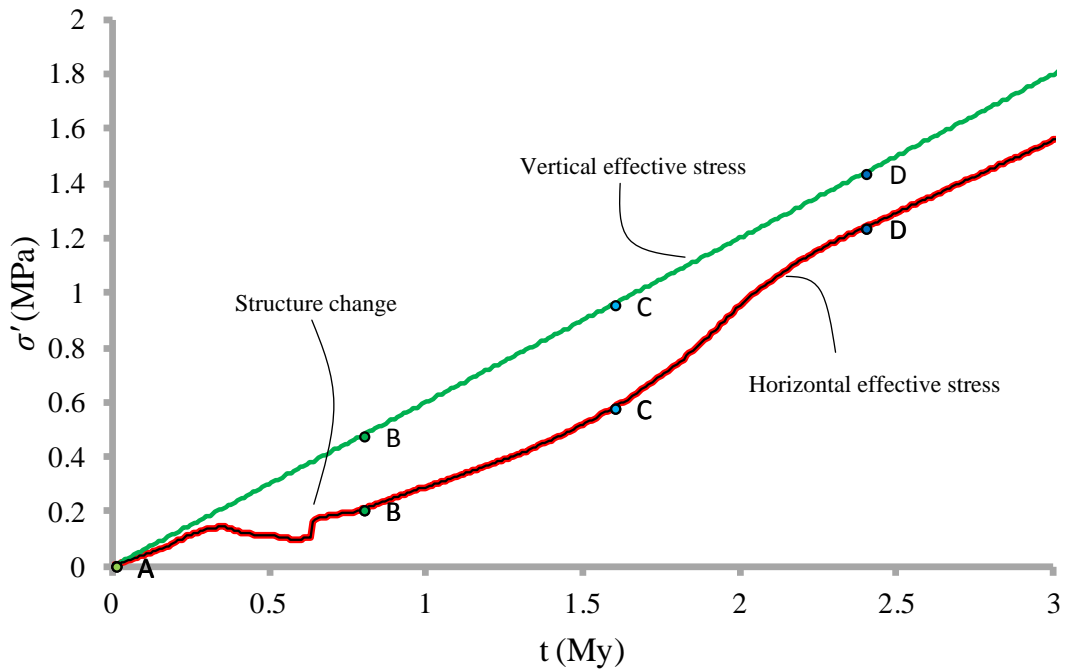


Figure 5-34: Stress evolution for shallow case. Note that the process is completed within the first 1My and after just over 2My the value of K_0 has increased to approximately 0.8.

5.4 Summary and Discussion

5.4.1 The Diagenetic Model for Genesis of Polygonal Faults

5.4.1.1 Opal A/CT Transformation

The results presented in section 5.1 indicate that the influence of dissolution-reprecipitation processes such as the Opal A/CT transformation may lead to localised shear failure. This was achieved without the need to invoke additional mechanisms such as differential compaction. It is however noted that subtle differential stress arising from irregular topology of the tier base or reaction front would likely bias fault spacing and potentially explain the higher density of faulting predicted in the models.

Comparison for model predictions with seismic observation (Ireland, 2011) is favourable both in terms of the depth at which faulting is developed and fault style. The density data observations indicate that porosity loss may be more rapid than replicated by the model, but the overconsolidation due to the diagenetic process and subsequent inhibited porosity loss is captured well by the model. It is worth noting that the faulting is triggered well before the reaction is completed. Many of the characteristics of the modelled fault network agree with criteria outlined for identifying polygonal fault systems (Cartwright and Dewhurst, 1998).

It was highlighted that the Opal A/CT seems an unlikely candidate for explaining all instances of polygonal fault formation, notably because there is evidence in many cases that faulting occurs some distance above this transformation boundary.

5.4.1.2 Controls on Fault Genesis and Tier Structure Derived from Sensitivity Study

The sensitivity study aimed at establishing the key aspects of a more generic diagenetic model for polygonal fault genesis showed that;

- 1 2D and 3D sensitivity models featuring progressive sedimentation recover layer-bound systems of faults whose characteristics agree with the Cartwright and Dewhurst criteria.
- 2 In the right conditions and at sufficiently shallow depth, polygonal faults may nucleate and grow for smaller diagenetic volume changes. Results indicate that a 5% change in porosity would be sufficient given a high thermal gradient and quick reaction rate. For fast reaction rates and a comparatively slow sedimentation rate, which is typical of most polygonal fault systems, it is shown that the chemical volume reduction has more significant implications for the evolution of stress and material state, and hence determines deformation style. Given the slow sedimentation rates and the general

reluctance of smectite rich and biosiliceous sediments to consolidate, this conclusion would seem reasonable.

- 3 Expression of the volume reduction as fully isotropic i.e. hydrostatic volume reduction, is important in determining deformation style. This further supports the inferred requirement for a truly three-dimensional volumetric strain. It is suggested that chemical compaction dominates and this type of volume reduction, where zones of the sediment are subjected to strong dissolution, will differ from volume loss due to clay particle rotation during conventional consolidation. It is also stressed that the types of sediments that are often observed to host polygonal faults, such as biosiliceous chalks and muds and smectitic claystones have high porosities and possess distinct, random fabrics. Therefore, dissolution during burial diagenesis seems likely to result in a significant horizontal stress reduction.
- 4 The thermal gradient is important in controlling the rate of visco-plastic deformation. Where thermal gradients are high the chemical process may be operating at a rate that is more significant than the volume change due to conventional consolidation. This facilitated an earlier change in horizontal stress and failure of the sediment.
- 5 Low residual friction facilitates high displacement on growing faults, which is consistent with the work of Shin (2009). Simulations using low residual friction lead to more listric fault geometries when they are observed in section. Faults that are gently listric are often associated with deeply buried tiers, or where the host sediments are dominantly biosiliceous (Cartwright, 2011). These results indicate that at the residual state the biosiliceous sediments may, potentially, have extremely low residual friction values.
- 6 Simulations of tier structures with sand intervals lead to pronounced decoupling of deformation above and below the sand layers. This behaviour arises from the more conventional consolidation behaviour of the strong sand, where stress conditions are not favourable for shear and continued fault propagation. These observations are consistent with those reported from many PFS tiers and reinforces the potential for using polygonal faults to locate deep-water sand bodies for exploration purposes.
- 7 The diagenetic reaction (Figure 5-24(a)) can lead to a pseudo-overconsolidated state and it is interesting to note that this behaviour is also seen in the Nankai data (see Figure 4-4) as well as being observed for the Opal CT case. It is therefore argued that this is a

Field Scale Analysis of the Formation and Evolution of Polygonal Fault Systems

signature of a post-sedimentation process such as diagenesis. In the Nankai case it seems more than coincidental that the interval observed to have the anomalous porosity trend is also the host of a polygonal fault system.

The above comments may explain the presence of shallow polygonal faults in locations where the crust is, or was, relatively young and hot, such as the Nankai Trough or the Vøring Basin, and there is growing evidence for diagenetic mechanisms to reconcile the presence of polygonal faults in many other settings. A network of polygonal faults in the Sanzhou Sag, Songliao Basin has been tentatively attributed to the influence of diagenesis (Ding et al., 2013). Comparison of diagenetic textures is shown in Figure 5-35.

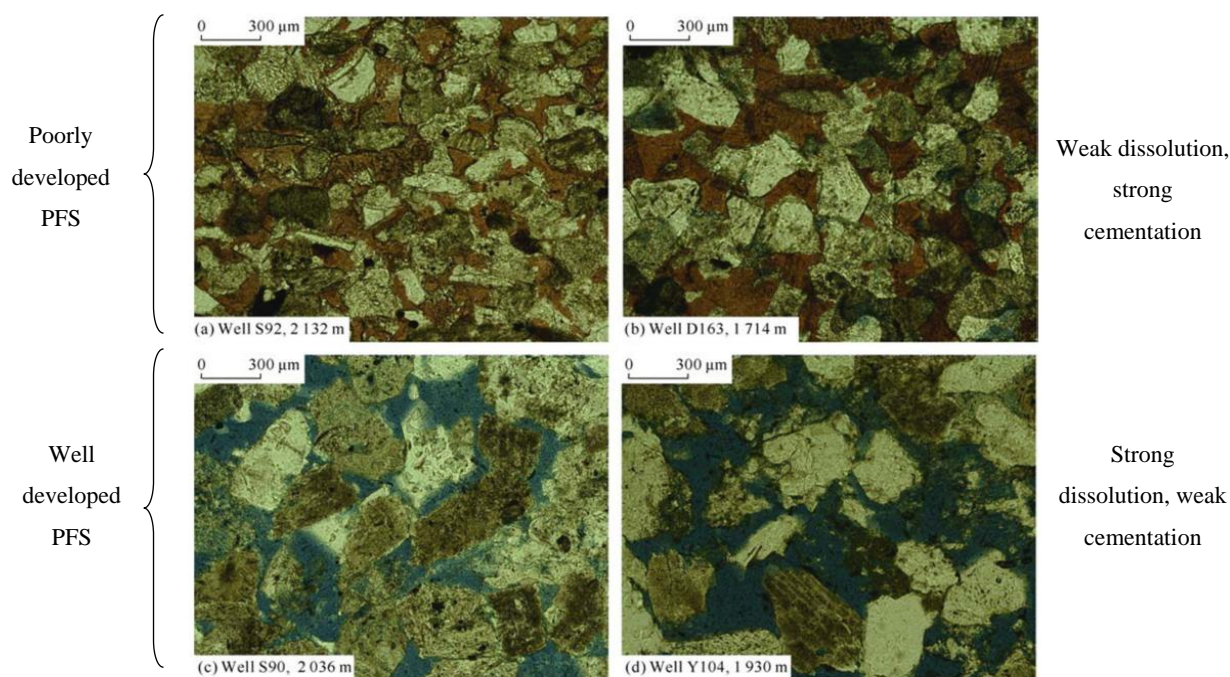


Figure 5-35: Correlation between diagenetic textures and intensity of polygonal faulting in the Sanzhou Sag (Ding et al., 2013).

The arrangement of clastic grains in the upper images is inferred to correspond to a strong level of cementation. These zones are noted to correspond to a lower intensity of faulting than zones where dissolution was much higher, as shown in the bottom images. Results presented in this chapter indicate that the rate of diagenetic reaction relative to sedimentation is important in determining whether shear failure is predicted. Subtle changes in mineralogy and other local factors may also be key in determining deformation style. It is reasonable to also assume that in some locations there may be additional, subtle cementation i.e. with

negligible influence on sediment volume but sufficient to produce a more marked pseudo-overconsolidation. This may have the affect of inhibiting faulting as the sediment response is essentially very stiff and elastic to substantial burial depths, thus arresting fault development (Croizé et al., 2010). Introducing such variations would make for interesting additional work.

5.4.2 Fault Development at Shallow Depth

Results presented in section 5.3 shows that the framework may be extended to a more generic "3-D consolidation" process that has similar implications for stress and state boundary surface evolution. For example, a characterised weak clay was shown to become pervasively polygonally faulted within the first 80m of burial.

The simulation results indicate that even though the porosity difference between the two consolidation styles is negligible, the resulting deformation is quite different. The 3-D consolidation results in an apparent pseudo-overconsolidation. Specifically, the material would indicate that the material had been buried to a greater depth. This observation compares favourably with observations made of some near-surface clays and mudstones. Diatomaceous sediments offshore Peru are noted to appear to be more consolidated near surface and tend towards a normally consolidated state at depth - see Figure 5-36. The implications of this are that shallow sediments are noted to be pervasively deformed by decimetre-scale localised shear fractures whereas more deeply buried sediments exhibit diffuse scaly cleavage. The reasons for this anomalous behaviour are not fully understood, but early diagenetic processes such as microbial sulphate reduction or dolomitization, or the possibility that some sediments naturally lie in a condition denser than critical state are offered as potential explanations (Hill and Marsters, 1990). The fractures could also be the expression of regional volume reduction as observed for Boom Clay (Dehandschutter et al., 2005) that takes place at a shallow depth which in some locations manifests itself as larger scale, seismically-observable faults.

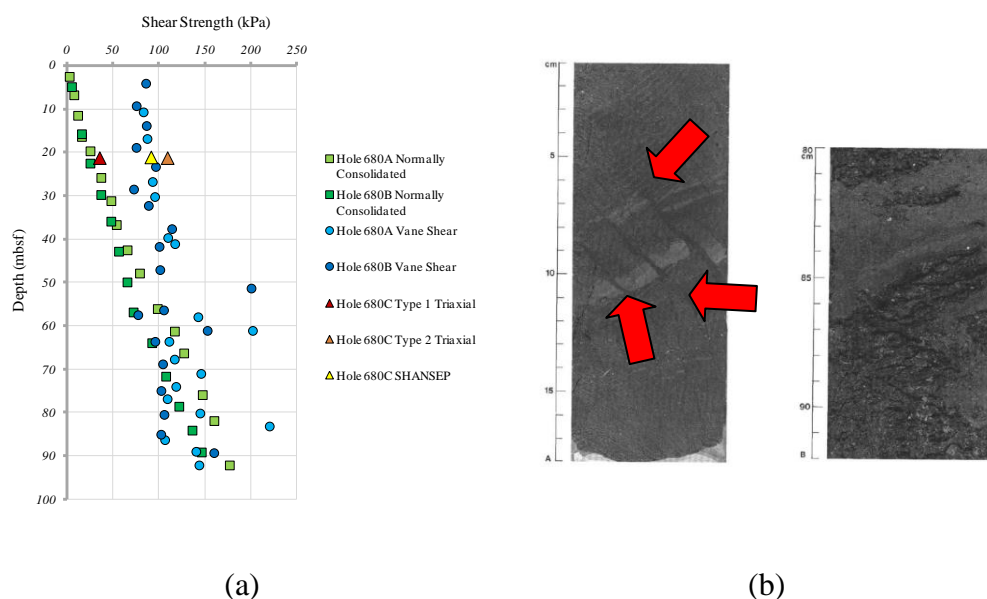


Figure 5-36: Diatomaceous sediments on the Peruvian continental margin. (a) Expected and observed consolidation styles showing apparent overconsolidation in the first 80 metres (Lee et al., 1990) (b) Images of core samples - note the shallow sample (left) exhibits decimetre scale shear fractures indicated by red arrows (Hill and Marsters, 1990).

Further evidence comes from Lake Superior where sediments appear to be overconsolidated to a ratio of between 3 and 4 (A. Bolton - unpublished manuscript). However, there is no evidence that the sediments have been unloaded to the extent required to achieve this OCR. The sediment is also pervasively fractured at the centimetre scale as shown in Figure 5-37.

As noted, it seems unlikely that diagenesis is the triggering mechanism here and creep could be a candidate. Creep may be "volumetric" in sediments with high organic contents due to the breakdown of organic matter. Also, rate dependency is widely acknowledged in fine grained sediments but rarely observed for sand, as creep in poorly consolidated sediments is known to be strongly dependent on clay fraction (Zoback, 2007). When coupled with the slow sedimentation rates observed for most tiers, creep appears to be another candidate genetic mechanism whose implications for constitutive response have strong parallels with the diagenetic model i.e. both are examples of volume reducing post-sedimentation processes. It is also stressed that there is an overlap between creep and diagenesis as many creep processes are sensitive to elevated temperatures.

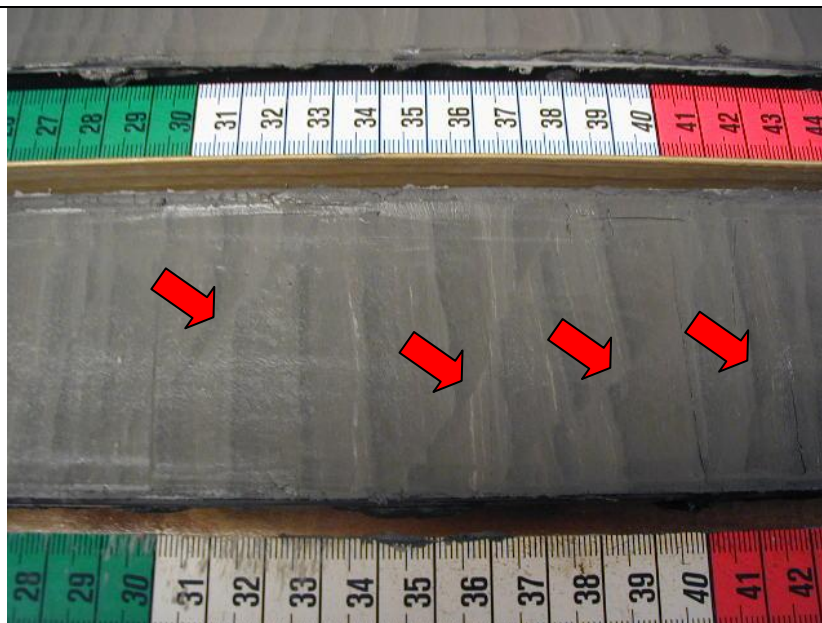


Figure 5-37: Core photographs from Lake Superior (A. Bolton - unpublished manuscript). Note the decimetre scale shear fractures (red arrows).

5.4.3 Horizontal Stress Reduction Hypotheses

The magnitude of horizontal stress reduction becomes quite pronounced in some simulations, particularly where the reaction is rapid and the mechanical response to further loading is driven by the elastic response. The magnitude of the horizontal stress reduction is broadly in the range reported in the conceptual experimental models of Shin et al., (2008).

It is argued in some cases that horizontal stress measurements with strata hosting PFS using Leak-Off Tests (LOT) do not correlate with hypotheses requiring horizontal stress reduction. For example, data from Miocene age sediments in the North Sea are presented by Gouly and Swarbrick (2005), with LOT data estimating the stress ratio to be in the range 0.7 to 0.8. The Miocene sediments are however fairly deeply buried, with the polygonal fault tiers located between 1718 and 2437mbsf i.e. at total vertical stresses lying between 35 and 50MPa. The results presented in this chapter indicate that once shear failure is triggered via the horizontal stress reduction and the process moves to completion, recovery to the K_0 condition is predicted, as also demonstrated by Shin et al., (2008). Therefore, as demonstrated by the simulation results within this chapter, the stress state at the depths noted by Gouly and Swarbrick (2005) would still be compatible with the evolutionary models where horizontal stress reduction is observed during the reaction.

It is also argued by Gouly and Swarbrick (2005) that K_0 is a lithology specific constant and

that reductions in horizontal stress ratio are not corroborated by experimental testing. It is argued here that horizontal stresses are not frequently monitored during oedometer or modified triaxial testing so it is difficult to assess the evolution of horizontal stresses. Furthermore, and crucially, experimental tests are not performed over geological time-frames. However, where the value of K_0 is measured in such tests there is evidence to suggest the following;

- 1 The value of K_0 may be quite low where the response is governed by the elastic behaviour (Karig and Ask, 2003; Ask and Morgan, 2010). The value drops further for low values of ν i.e. where cementation is inferred to be strong.
- 2 Re-sedimentation of Gulf of Mexico poorly consolidated clays has indicated that the value of K_0 changes depending on the level of consolidation (Casey et al., 2014). The samples tested closely resemble London Clay and have a high smectite content. Samples consolidated to less than 1MPa had K_0 values of less than 0.6, but for effective stresses in excess of 10MPa the value of K_0 was observed to be in the anticipated range of 0.7 to 0.8. Similar trends are also observed for the friction angle which reduced from more than 40° to approximately 12° for some specimens. The change in K_0 is attributed to the breakdown of an initial fabric (the sample appears overconsolidated).
- 3 Testing of chalks, which are also known to host PFS, under K_0 boundary conditions indicates that the stress ratio may be rate sensitive (Omdal, 2010). Specifically, when specimens are loaded quickly they have a higher inferred K_0 value. Specimens loaded more slowly are noted to have lower K_0 values and lie in close proximity to the critical state line. When samples are loaded quickly and left to creep they tend towards the slow (or rate independent) trend. Importantly, to maintain the uniaxial strain boundary conditions the horizontal stresses during testing had to be increased. This unusual behaviour is linked to the micro-scale structure of chalk i.e. a framework of interlocking coccoliths which exert a control on deformation style as they are broken down and the load is redistributed.

5.4.4 Appraisal of Modelling Approach and Progression

The recovery of polygonal fault systems which closely resemble those observed on seismic provides confidence in the geomechanical argument and the abilities of the finite-strain modelling approach. The key implication of this chapter is again stressed;

"the demonstration of the influence of post-sedimentation processes on the stress and material state during early burial, which in optimal conditions leads to macro-scale, localised deformation and the genesis of polygonal faults."

The outcome of the presented investigations is the suggestion that the genesis of polygonal faults might not necessarily be governed by any one specific mechanism, and instead may be controlled by a variety of processes who share similar characteristics and lead to similar constitutive responses. The model output shows that the signature of such processes might be a seemingly higher level of consolidation than expected, which is in agreement with observation in some shallow PFS.

In the introductory chapter the recovery of polygonal faults in both 2D and 3D numerical models whose characteristics satisfied the Cartwright and Dewhurst criteria was identified as the key objective of this study. This has been accomplished for a range of scenarios and depths, and the models illustrate how the diagenetic mechanism can predict large-scale fault networks with characteristics that strongly resemble those of many polygonal fault systems.

In the following chapter the approach is used to investigate how mechanical controls influence the polygonal planform geometry.

5.5 References

- Ask, M. V. S., and J. K. Morgan, 2010, Projection of mechanical properties from shallow to greater depths seaward of the Nankai accretionary prism: *Tectonophysics*, v. 482, no. 1-4, p. 50–64.
- Baudon, C., and J. A. Cartwright, 2008, Early stage evolution of growth faults: 3D seismic insights from the Levant Basin, Eastern Mediterranean: *Journal of Structural Geology*, v. 30, p. 888–898.
- BGS, 2010, FORGE Report: Review of Boom Clay and Opalinus Clay parameters: 16 p.
- Carruthers, T. D., 2012, Interaction of polygonal fault systems with salt diapirs: Unpublished PhD Thesis - Cardiff University, p. 526.
- Cartwright, J. A., 2011, Diagenetically induced shear failure of fine-grained sediments and the development of polygonal fault systems, *in Marine and Petroleum Geology*: Elsevier Ltd, p. 1593–1610.
- Cartwright, J. A., and D. N. Dewhurst, 1998, Layer-bound compaction faults in fine-grained sediments: *Geological Society of America Bulletin*, v. 110, no. 10, p. 1242–1257.
- Cartwright, J. A., and L. Lonergan, 1996, Volumetric contraction during the compaction of mudrocks: a mechanism for the development of regional-scale polygonal fault systems: *Basin Research*, v. 8, no. 2, p. 183–193.
- Cartwright, J. A., N. J. Watrus, D. E. Rausch, and A. Bolton, 2004, Recognition of an early Holocene polygonal fault system in Lake Superior: Implications for the compaction of fine-grained sediments: *Geology*, v. 32, no. 3, p. 253–256.
- Casey, B., B. P. Fahy, P. B. Flemings, and J. T. Germaine, 2014, Shear Strength of Two Gulf of Mexico Mudrocks and a Comparison with Other Sediments, *in Fourth EAGE Shale Workshop. Shales: What do they have in common?*
- Croizé, D., S. N. Ehrenberg, K. Bjørlykke, F. Renard, and J. Jahren, 2010, Petrophysical properties of bioclastic platform carbonates: implications for porosity controls during burial: *Marine and Petroleum Geology*, v. 27, no. 8, p. 1765–1774.
- Davies, R. J., and M. T. Ireland, 2011, Initiation and propagation of polygonal fault arrays by thermally triggered volume reduction reactions in siliceous sediment: *Marine Geology*, v. 289, no. 1-4, p. 150–158.
- Dehandschutter, B., P. Gaviglo, J. P. Sizun, M. Sintubin, S. Vandycke, N. Vandenberghe, and L. Wouters, 2005, Volumetric matrix strain related to intraformational faulting in argillaceous sediments: *Journal of the Geological Society*, v. 162, p. 801–813.

- Dewhurst, D. N., J. A. Cartwright, and L. Lonergan, 1999, The development of polygonal fault systems by syneresis of colloidal sediments: *Marine and Petroleum Geology*, v. 16, no. 8, p. 793–810.
- Ding, X., G. Liu, M. Sun, and P. Wang, 2013, Origin of polygonal fault systems: A case from the Sanzhao sag in the Songliao Basin, East China: *Petroleum Exploration and Development*, v. 40, no. 3, p. 333–343.
- Gay, A., M. Lopez, P. Cochonat, and G. Sermondadaz, 2004, Polygonal faults-furrows system related to early stages of compaction - upper Miocene to recent sediments of the Lower Congo Basin: *Basin Research*, v. 16, no. 1, p. 101–116.
- Goult, N. R., 2008, Geomechanics of polygonal fault systems: a review: *Petroleum Geoscience*, v. 14, no. 4, p. 389–397.
- Goult, N. R., and R. E. Swarbrick, 2005, Development of polygonal fault systems: a test of hypotheses: *Journal of the Geological Society*, v. 162, no. 4, p. 587–590.
- Hansen, D. M., J. W. Shimeld, M. A. Williamson, and H. Lykke-Andersen, 2004, Development of a major polygonal fault system in Upper Cretaceous chalk and Cenozoic mudrocks of the Sable Subbasin, Canadian Atlantic margin: *Marine and Petroleum Geology*, v. 21, no. 9, p. 1205–1219.
- Henry, P., T. Kanamatsu, K. T. Moe, and M. Strasser, 2012, IODP Expedition 333: Return to Nankai Trough Subduction Inputs Sites and Coring of Mass Transport Deposits: *Scientific Drilling*, no. 14, September 2012, p. 4–17.
- Hibsch, C., J. Cartwright, D. M. Hansen, P. Gaviglio, G. Andre, M. Cushing, P. Bracq, P. Juignet, P. Benoit, and J. Allouc, 2003, Normal faulting in chalk: tectonic stresses vs. compaction-related polygonal faulting: Geological Society, London, Special Publications, v. 216, no. 1, p. 291–308.
- Hill, P. R., and J. C. Marsters, 1990, 41. Controls on physical properties of Peru continental margin sediments and their relationship to deformation styles, *in* Proceedings of the Ocean Drilling Program, Scientific Results, Vol. 112: p. 623–632.
- Ireland, M. T., 2011, 3-D seismic investigation of the diagenesis and deformation of Cenozoic sediments on the Eastern Atlantic Margin: Unpublished PhD thesis - Durham University, p. 185.
- Jackson, C. A. L., D. Carruthers, S. N. Mahlo, and O. Briggs, 2014, Can polygonal faults help locate deepwater reservoirs?: *AAPG Bulletin*, no. May, doi:10.1306/03131413104.
- Jackson, C. A.-L., S. N. Mahlo, O. Briggs, and T. D. Carruthers, 2013, Role of Polygonal Fault Mapping in De-Risking Deepwater Reservoir Presence: A 3-D Seismic Reflection Case Study from Offshore Norway, *in* AAPG Annual Convention and Exhibition, Pittsburgh, Pennsylvania.

-
- Jennings, R. H., and J. M. Mazzullo, 1977, 36. Shallow burial diagenesis of chalks and related sediments at Site 550 on the Goban Spur: Proceedings of the Ocean Drilling Program, Scientific Results, p. 853–861.
- Karig, D. E., and M. V. S. Ask, 2003, Geological perspectives on consolidation of clay-rich marine sediments: *Journal of Geophysical Research*, v. 108, p. 1–14, doi:10.1029/2001JB000652.
- Lee, H. J., R. E. Kayen, and W. G. McArthur, 1990, 43. Consolidation, triaxial shear-strength, and index-property characteristics of organic-rich sediment from the Peru continental margin: Results from leg 112, *in* Proceedings of the Ocean Drilling Program, Scientific Results, Vol. 112: p. 639–651.
- Omdal, E., 2010, The Mechanical Behavior of Chalk under Laboratory Conditions Simulating Reservoir Operations: Unpublished PhD Thesis - University of Stavanger, p. 88.
- Shin, H., 2009, Development of Discontinuities in Granular Media: Georgia Institute of Technology, p. 158.
- Shin, H., J. C. Santamarina, and J. A. Cartwright, 2008, Contraction-driven shear failure in compacting uncemented sediments: *Geology*, v. 36, no. 12, p. 931.
- Shin, H., J. C. Santamarina, and J. A. Cartwright, 2010, Displacement field in contraction-driven faults: *Journal of Geophysical Research*, v. 115, no. B7, p. B07408.
- De Souza Neto, E. A., D. Peric, and D. R. J. Owen, 2008, Computational methods for plasticity: Theory and applications: Wiley-Blackwell, p. 814.
- Thornton, D. A., and A. J. L. Crook, 2013, Predictive Modeling of the Evolution of Fault Structure: 3-D Modeling and Coupled Geomechanical/Flow Simulation, *in* 47th ARMA Rock Mechanics and Geomechanics Symposium, San Francisco, California.
- Thornton, D. A., and A. J. L. Crook, 2014, Predictive Modeling of the Evolution of Fault Structure: 3-D Modeling and Coupled Geomechanical/Flow Simulation: Rock Mechanics and Rock Engineering.
- Volpi, V., A. Camerlenghi, C. Hillenbrand, M. Rebesco, and R. Ivaldiz, 2003, Effects of biogenic silica on sediment compaction and slope stability on the Pacific margin of the Antarctic Peninsula: *Basin Research*, v. 15, p. 339–363.
- Wattrus, N. J., D. E. Rausch, and J. A. Cartwright, 2003, Soft-sediment deformation in Lake Superior: Evidence for an immature Polygonal Fault System?, *in* P. Van Rensberger, R. R. Hillis, A. J. Maltman, and C. K. Morley, eds., *Subsurface Sediment Mobilization*: Geological Society, London, Special Publications, p. 323–334.
- Wood, D. M., 1990, Soil Behaviour and Critical State Soil Mechanics: Cambridge University Press, p. 488.

Zoback, M. D., 2007, Reservoir Geomechanics: Cambridge, p. 461.

Chapter 6

POLYGONAL FAULTS AND THE INFLUENCE OF HORIZONTAL STRESS ANISOTROPY

Results presented in Chapter 5 show that the model based on the proposed geomechanical argument predicts the natural formation of a system of polygonal faults. This is a significant step and validates the proposed argument as well as providing confidence in the chosen modelling approach. This chapter seeks to investigate how PFS interact with other tectonic structures and subsurface features by further developing models from the previous chapter. The aim is to evaluate the potential for PFS to constrain subsurface paleostress distributions. Relationships that help quantify paleostress would be beneficial in terms of helping understand interactions between polygonal faults and dynamic structures such as salt diapirs. This is important as these might be attractive exploration targets and PFS may shed light on their evolution over geological time by acting as 'paleostress piezometers' (Cartwright, 2011; Carruthers et al., 2013).

6.1 Examples of Planform Geometry Polarisation Due to Horizontal Stress Anisotropy

6.1.1 Tectonic Faults

The interactions between tectonic faults and polygonal faults has been recognised for some time (Hansen et al., 2004), and it is acknowledged that they may be useful in constraining fault activity. For example, Figure 6-1(a) shows a region where a set of polygonal faults is cross-cut by large tectonic faults. It is apparent that the polygonal faults are orthogonal to the fault where they are in close proximity. The image shown in Figure 6-1(b) is from a tier in the same region but in this case it is clear that there is no polarisation of the planform geometry with no obvious orthogonal intersections near the tectonic fault. The inference from these observations is that the tier in Figure 6-1(a) was active at the same time as the tectonic fault was growing and responded to the resulting stress perturbation by aligning parallel to the intermediate principal stress. The tier in Figure 6-1(b) is assumed to have formed prior to the formation of the tectonic fault as no reorientation of the planform geometry is observed. Thus, the timing of the fault can be neatly constrained to the period between the formation of

Polygonal Faults and the Influence of Horizontal Stress Anisotropy

the two tiers. Similar observations have been made in the Sable Basin (Hansen et al., 2004), offshore Nova Scotia where polygonal faults are observed to meet larger tectonic faults at approximately 90° , as shown in Figure 6-1(c-d).

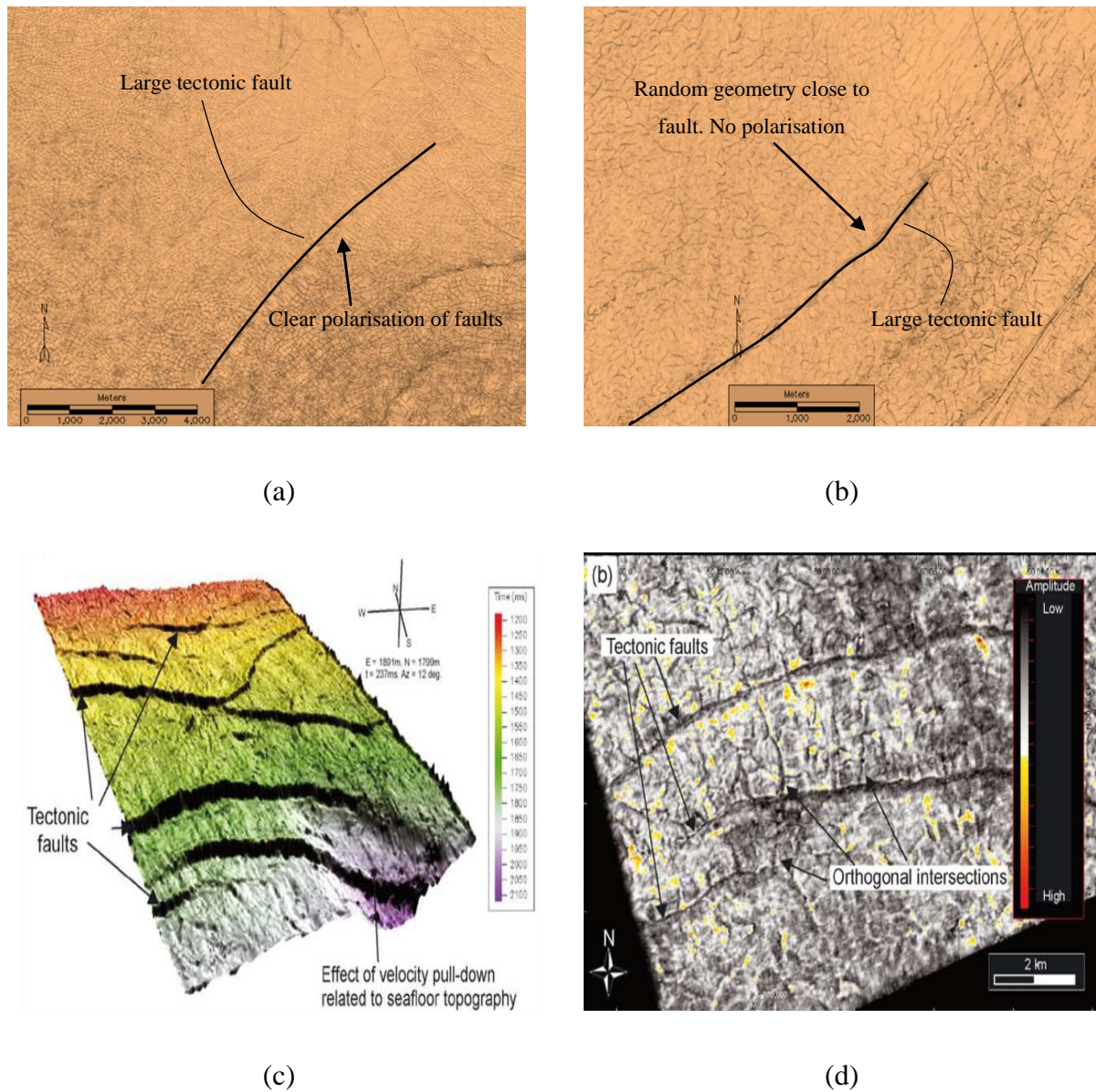


Figure 6-1: (a-b) Polygonal faults interacting with tectonic faults. Images used with permission from J. Cartwright (c-d) 3D view of Eocene horizon and seismic attribute map from the Sable Basin, offshore Nova Scotia showing interactions between polygonal faults and larger tectonic faults (Hansen et al., 2004).

It is worth noting that similar observations are made for joint sets e.g. Lachenbruch, 1963; Rawnsley et al., 1992. Often secondary joint ladders are observed to meet primary joint

ladders at 90° . It is argued that this might imply a local stress change close to the primary joint set in a similar way to the interaction between tectonic and polygonal faults, as opposed to a complete regional stress rotation (Bai et al., 2002).

6.1.2 Slopes

Figure 6-2 provides two examples of planform geometry modification due to a slope at the base of the tier. Figure 6-2(a) shows a PFS from the Faroe-Shetland Basin (Cartwright, 2011) featuring a slope which trends approximately NW-SE. In the northwest of the image the slope is gentle and the stress state is inferred to be near isotropic. In this zone the fault azimuths appear random, the spacing is slightly tighter (smaller distances between adjacent faults), and the length of individual faults is modest (approximately in the range 100m to 500m). Referring to the region with a more pronounced slope it appears that the fault pattern is strongly polarised with most faults aligned orthogonal to the slope direction. Faults appear to be spaced slightly further apart and that faults that are aligned parallel to the slope are significantly longer, striking for several kilometres in some cases. Many other examples show preferential alignment of faults orthogonal to slope (Cartwright, 2011 and references therein).

Figure 6-2(b) shows a system of polygonal faults in the Nankai Trough (Heffernan et al., 2004). A slope is once again present, with inclination of about 5° as one moves from the axial trench zone in the South East to the proto-thrust zone in the North West. The rose diagrams indicate that the vast majority of faults overlying the basement lows are aligned orthogonal to the slope direction and strike SW-NE. Faults overlying the basement highs exhibit a wider range of azimuths due to irregular topology.

6.1.3 Salt Structures

The low permeability of salt masses within halokinetic structures and the structural traps that they form combine to make such structures attractive exploration targets (Fossen, 2010). The complex stress state around salt leads to frequent drilling problems and there is great interest in understanding and modelling these stress perturbations (Dusseault et al., 2004; Koupriantchik et al., 2004; Nikolinakou, 2011). The relationship between salt structures and PFS is also well documented (Davison et al., 2000; Stewart, 2006; Carruthers, 2012; Carruthers et al., 2013). Figure 6-3(a) shows the North Pierce salt diapir piercing polygonally faulted Miocene age sediments in the North Sea (Carruthers, 2012).

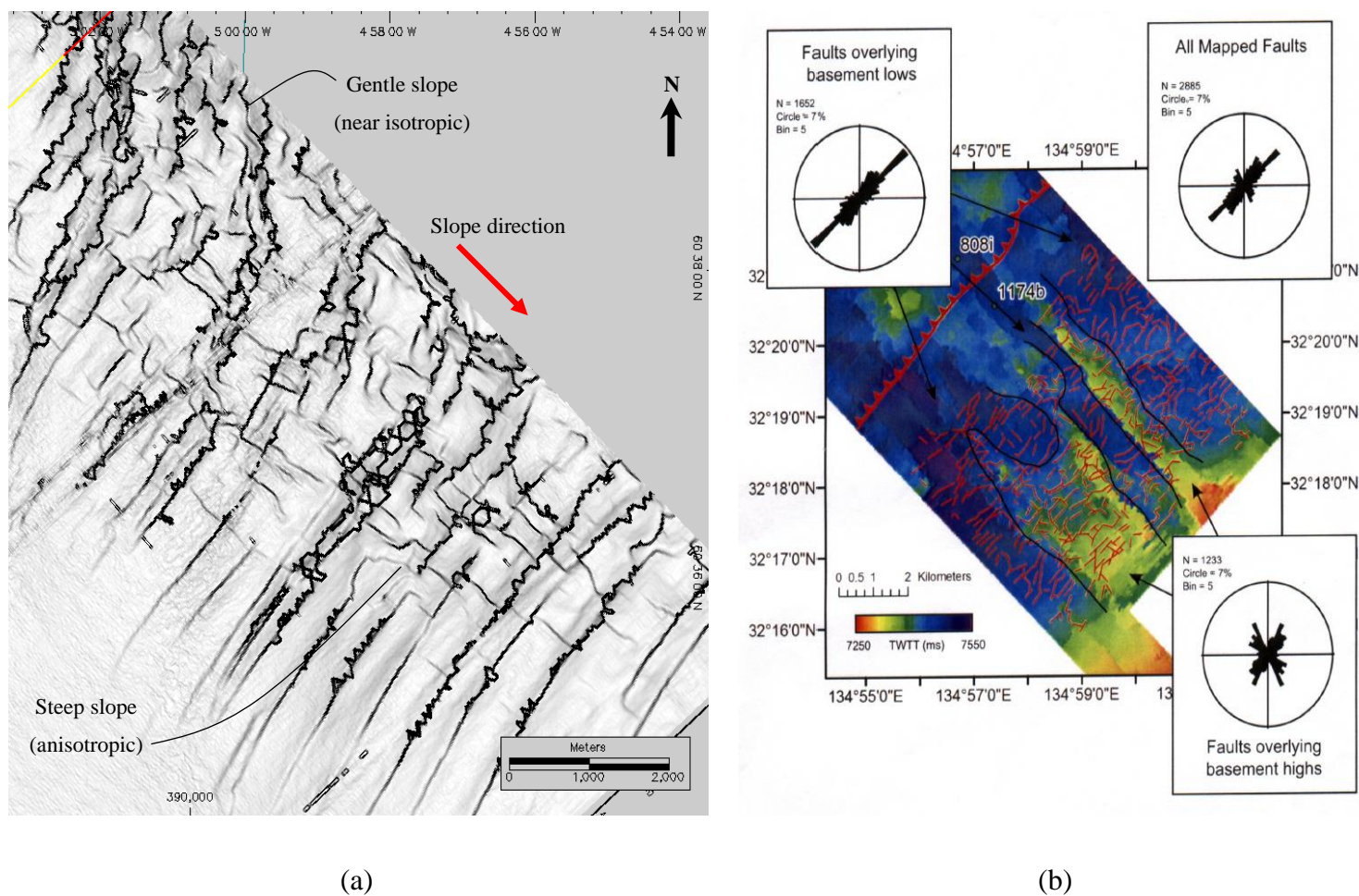


Figure 6-2: Modification of polygonal planform geometry due to a sloping base (a) Planform geometry for a PFS in Faroe-Shetland Basin (Cartwright, 2011) (b) Planform geometry for a PFS in Nankai Trough (Heffernan et al., 2004).

The red dashed line marks the so-called 'transition boundary' which delimits horizontally anisotropic and isotropic stress states. Both the North Pierce and South Pierce diapirs pierce several separate tiers and the position of the transition boundary relative to the salt diapir is observed to vary. This relationship is observed for several North Sea diapirs, but is not fully understood.

Whilst arching of the overburden during diapir growth may contribute, the favoured mechanism to explain this relationship for the North and South Pierce diapirs is increased loading of the adjacent sediment due to the inability of the salt to sustain deviatoric stresses (Carruthers et al., 2013). Figure 6-3(b) provides a further example of this interaction and shows the transition boundary in a shallow PFS relative to a diapir, offshore West Africa.

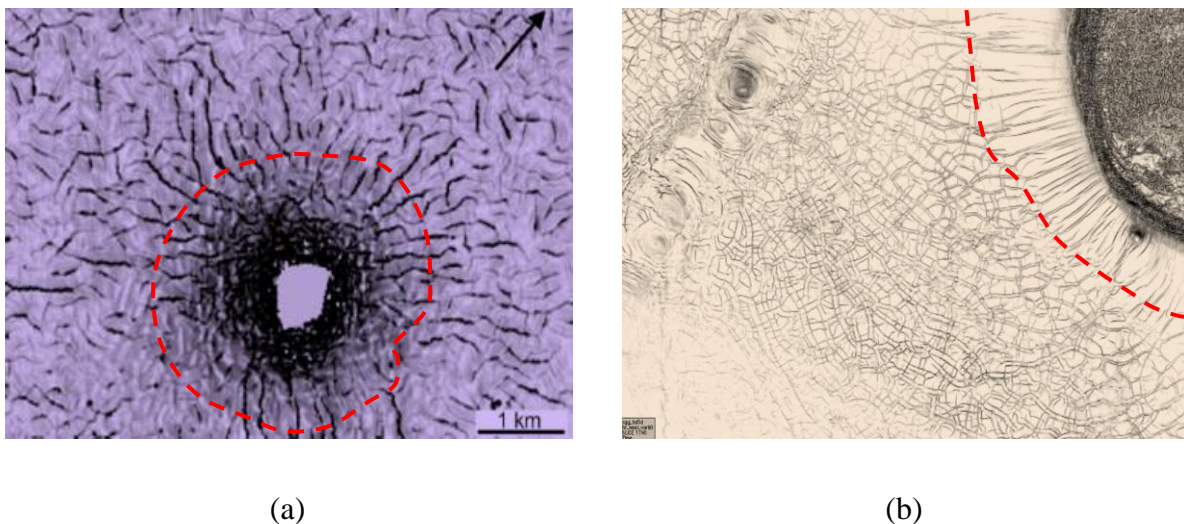


Figure 6-3: Interactions between polygonal fault systems and salt structures (a) North Pierce salt diapir, North Sea (Carruthers, 2012) (b) Offshore West Africa (used with permission from J. Cartwright). Note how the planform geometry changes close to the salt diapirs in both examples. Fault length also appears to change in response to the anisotropic stress field, yet spacing of faults is consistent. Transition boundary is shown via the dashed red line.

6.1.4 Anticlines and Fold Belts

Anticlines and folds represent another appealing target for exploration as hydrocarbons are often accumulated in the anticline crest. Understanding fracture distributions and top seal integrity is important in this case as the flexure and horizontal stress reduction associated with anticline formation may lead to large scale crestal grabens (Rance et al., 2013) or to

intense fracturing of reservoir units on the sub-seismic scale.

Few cases of the interaction between polygonal faults and folds/anticlines are reported. One such case from South East Asia is however shown in Figure 6-4 (Morley et al., 2014). The green triangle indicates a region where the planform geometry indicates a horizontally isotropic stress state. The yellow triangle shows the approximate location of a NNW-SSE trending fold. The faults in close proximity to the fold are interpreted to be polygonal faults responding to the stress anisotropy caused as the faults entered the deformation front. It is noted that, if a well developed polygonal fault system was not located nearby, the faults overlying the anticline might commonly be attributed to having an exogenic origin. It is also noted that these faults lie orthogonal to any crestal normal faults that might be expected to develop over the fold and hence impose different potential fluid migration pathways (Morley et al., 2014).

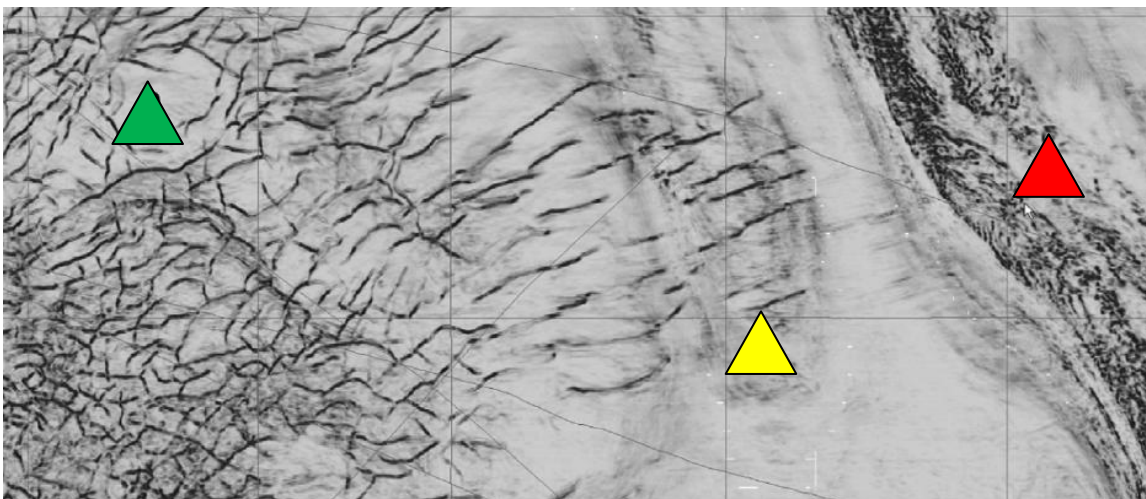


Figure 6-4: Planform geometry polarisation in a deepwater fold and thrust belt, SE Asia, modified after (Morley et al., 2014). Faults become polarised as they enter the deformation front associated with the fold belt. A fold is present below the shown horizon with a N-S to NNW-SSE trending axis. The green triangle marks the inferred isotropic region and the yellow triangle marks the region polarised by the underlying fold. The red triangle indicates another anticline but in a region not associated with polygonal faulting. Note marked change in fault length.

6.1.5 Comments

The cases discussed above have demonstrated an intimate relationship between polygonal faults and adjacent structures and topology variations. An important point is that in all cases the polygonal planform geometry is modified as a result of a change from a near-isotropic horizontal state of stress to an anisotropic state of stress. This is summarised in Figure 6-5(a-d) and shows the orientation of the minimum and intermediate principal stresses which in the normal faulting regime lie in the horizontal plane (Anderson, 1951; Zoback, 2007). As noted previously, these relationships suggest polygonal faults are useful indicators of paleostress and attempts to better understand and quantify this relationship are the principal objectives of this chapter.

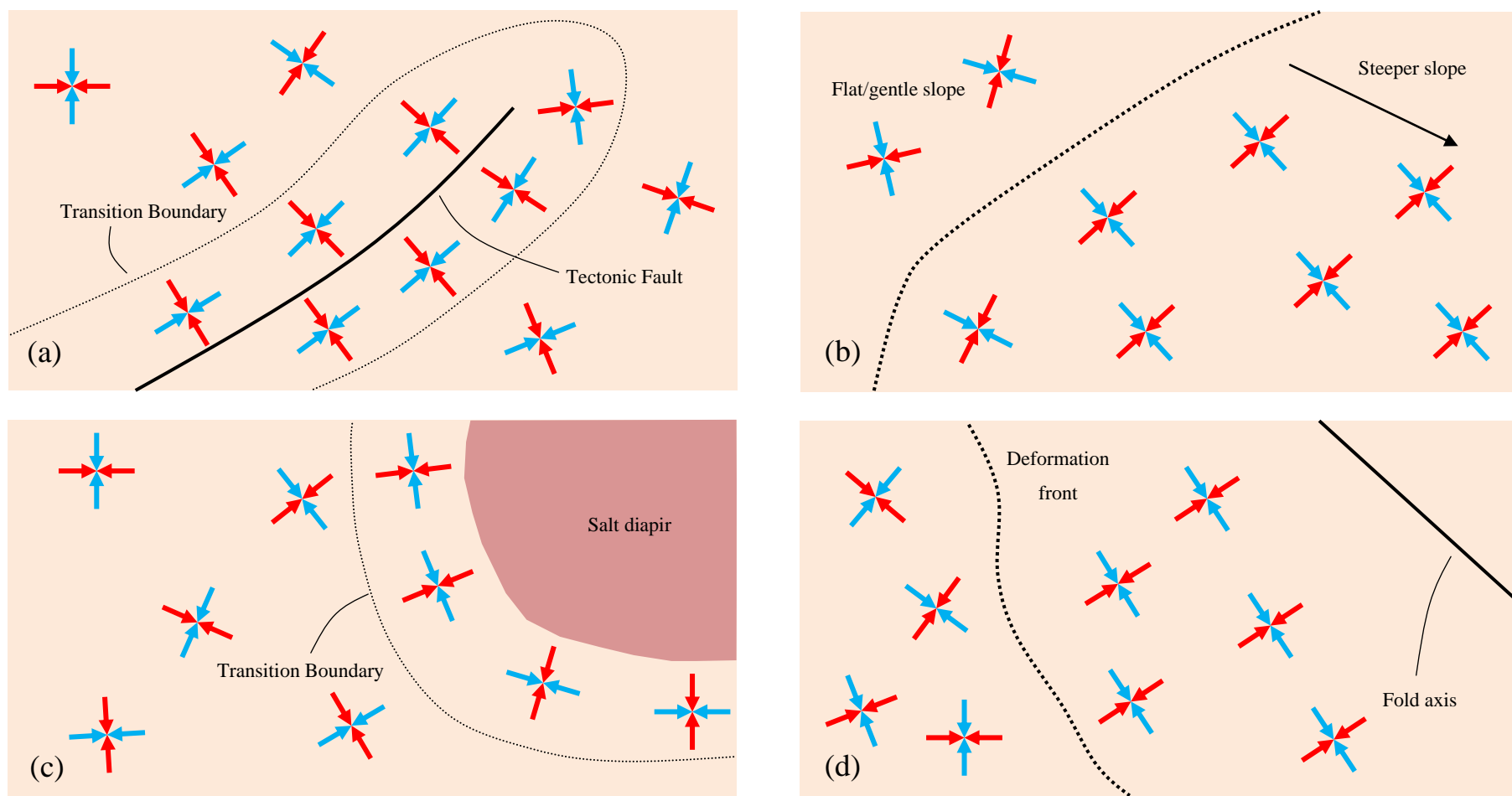


Figure 6-5: Summary of polarisation of polygonal planform geometry from various forms of horizontal stress anisotropy. Red arrows indicate orientation of $S_{H,max}$ and blue arrows indicate orientation of $S_{h,min}$. Inferred horizontal stress state is shown along with boundary marking transition from isotropic to anisotropic stress states. (a) tectonic faults (b) slopes (c) salt diapirs (d) anticlines/fold belts.

6.2 Strategy for Conceptual Investigation

To investigate the relationship between planform geometry and horizontal stress anisotropy, the evolutionary models discussed in Chapter 5 are extended by modifying the boundary conditions in order to induce subtle stress anisotropy. The setup for the models is shown in Figure 6-6. The size of the domain is increased for these models which leads to significantly more computational time being required. This decision was made due to the following considerations;

- 1 The boundary conditions may exert too much of a control on the resulting planform geometry. By extending the size of the domain the influence of the boundary will be reduced. Ideally, a larger domain than the 2km x 2km size adopted would be used, but memory usage and computational time considerations impose some constraints.
- 2 The increased size of the domain facilitates development of a larger number of polygonal faults. This allows the relationship between fault number and stress anisotropy to be derived with increased confidence.

Clearly this greatly increases the number of elements required and the presented models contain between 12 and 20 million finite elements, making efficient solution using domain-decomposition and solution in parallel essential. More detail on the initialisation, deposition rates, thermal gradients, material characterisations and layer thicknesses is provided in Section 5.2.

During the deposition of the chemically active layers, one of the side boundaries is gradually displaced at a constant velocity in order to induce anisotropy in the horizontal stresses. The influence of applying half the total displacement (strain) to both boundaries, as adopted in other publications e.g. Olson et al., (2007), was investigated in addition to applying the total displacement to just one boundary as shown in Figure 6-6. The comparison between the two cases revealed little difference and as such applying the load to just one boundary was judged to be an appropriate method.

Table 6-1 shows a summary of the loading conditions and measured stress anisotropy. In scenario 0 there is no displacement applied to the side boundary and this case therefore represents the horizontally isotropic scenario. This can be considered as the control model against which the influence of horizontal stress anisotropy is evaluated.

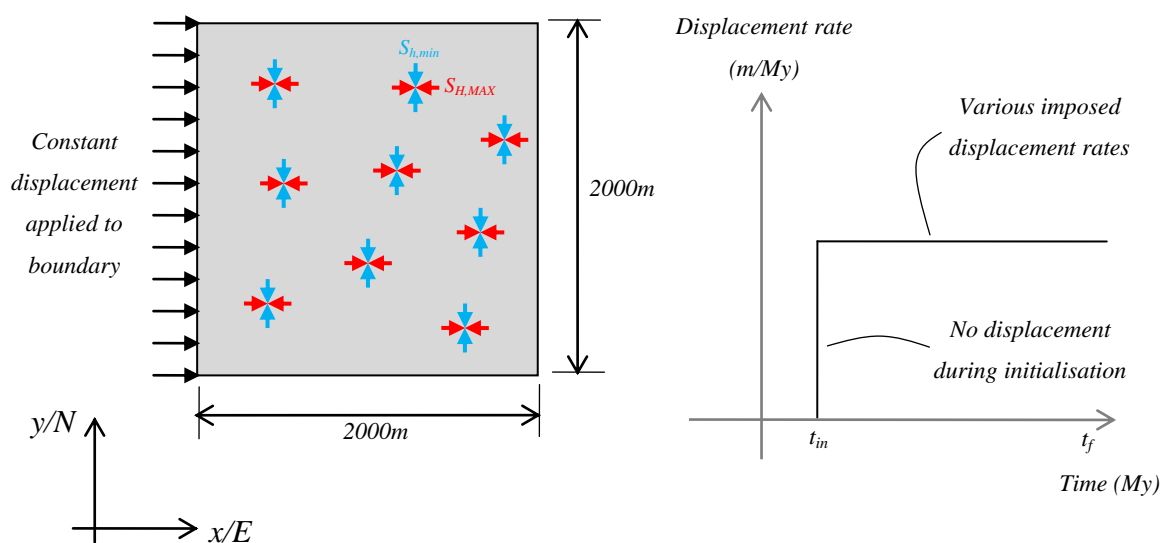


Figure 6-6: Plan view of model domain showing setup for conceptual investigation for stress anisotropy study. For comparison with rose diagrams the x and y directions correspond to EW and NS respectively. The z direction lies in the plane - see Section 5.2.2 for more detail regarding model setup.

Prior to fault development a sample of points at the level of the H1 horizon are used to assess the level of anisotropy. Specifically, the horizontal stress ratio H is shown which is calculated using Equation 6-1.

$$H = \frac{\sigma'_{H,max}}{\sigma'_{h,min}} = \frac{\sigma'_{xx}}{\sigma'_{yy}} \quad 6-1$$

Scenario	Loading type	Displacement rate (m/My)	Av. Horizontal stress ratio (H)	$\sigma'_{H,MAX}$ relative to $\sigma'_{h,min}$ prior to fault development (%)
0	Isotropic	0.00	1.000141	+0.01
1	Anisotropic	0.14	1.001899	+0.19
2	Anisotropic	3.33	1.018261	+1.83
3	Anisotropic	6.67	1.030478	+3.05

Table 6-1: Summary of imposed horizontally anisotropy stress states. In case 1, no displacements are applied to the model boundary and hence the averaged horizontal stress ratio is close to unity.

The value of H for all the sample points for each scenario is shown in Figure 6-7 and these values are averaged to give the values shown in Table 6-1. Note that for scenario 0 where the boundary is not displaced has a range of horizontal stress ratios that lie very close to 1,

therefore reflecting horizontal stress isotropy. For anisotropic scenario 1, the modest extension results in a very slight anisotropy, with the averaged $\sigma'_{H,MAX}$ value being about 0.2% larger than the averaged $\sigma'_{h,min}$. Anisotropic scenarios 2 and 3 feature larger imposed displacements and by referring to Figure 6-7 and Figure 6-8 the difference between the two horizontal stresses is more significant. For anisotropic cases 2 and 3 the maximum difference between the horizontal stresses is approximately 1.83% and 3.05%.

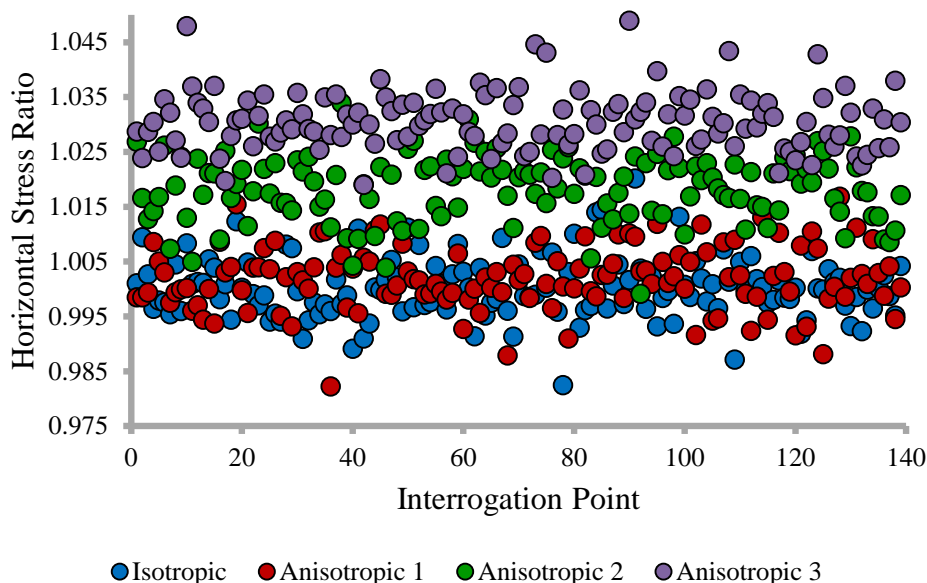


Figure 6-7: Horizontal stress ratio for a selection of 140 interrogation points on the H1 horizon prior to the development of the polygonal faults. The values shown for each scenario were used to calculate the average HSR as shown in Table 6-1.

6.3 Results and Analysis

Considering comments made in the Section 6.1, four criterion are chosen for identifying any potential relationships:

- 1 Intensity of faulting - the number of faults observed per unit area in mapview.
- 2 Fault spacing - the distance between midpoints of adjacent polygonal faults in mapview.
- 3 Fault strike direction - the azimuth of faults in mapview.
- 4 Fault length - the interrogated length of the faults in mapview.

The significance of any identified relationships is presented and discussed in Section 6.4, and some considerations for incorporating the findings into a workflow for paleostress estimation

are outlined in Section 6.5.

Remarks 1 The influence of stress anisotropy information is interpreted within this section using a selection of the tools available in the online software package Visible Geology (<http://app.visiblegeology.com/>).

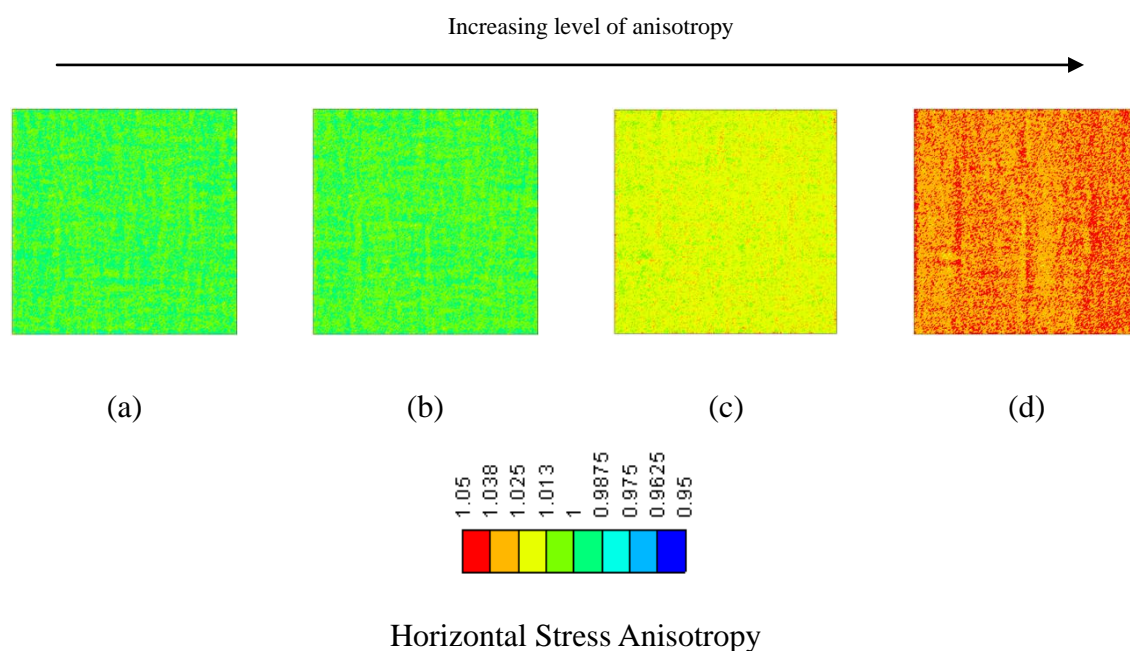


Figure 6-8: Variation in the degree of horizontal stress anisotropy. Note that in case (a) the contours indicate that the Horizontal Stress Ratio is very close to 1. There is only a very slight change in case (b) reflecting extremely subtle anisotropy. As the imposed displacements increase the contours indicate that the level of anisotropy grows larger, as shown in (c) and (d)

6.3.1 Intensity of Faulting

Intensity of faulting is investigated by counting the number of zones of intense plastic straining, analogous to fault development, at a horizon some distance above the location of maximum throw. The measurements for each sensitivity are made at the same horizon due to the fact that, as highlighted in Section 5.22, the intensity of faulting may vary vertically through a tier. The identification of an individual fault is made based on the intensity of plastic straining and the observed fault structure in 3D. Visual inspection of the planform geometry for the various sensitivities in Figure 6-11 to Figure 6-14 indicates a clear relationship between horizontal stress anisotropy and the number of faults per unit area. For

Polygonal Faults and the Influence of Horizontal Stress Anisotropy

the 4km² section modelled the total number of faults within this area is observed to fall from 47 in the isotropic case to approximately 13 in scenario 3 featuring the most pronounced anisotropy (Table 6-2).

Scenario	Loading type	Number of faults observed
0	Isotropic	47
1	Anisotropic	31
2	Anisotropic	18
3	Anisotropic	13

Table 6-2: Number of faults observed for various levels of horizontal stress anisotropy.

A plot of the number of observed faults against the magnitude of horizontal stress anisotropy, as presented in Figure 6-9, shows that the number of faults appears to be proportional to the logarithm of the difference between the horizontal stresses. This observation appears to be consistent with observation from a range of polygonal fault systems where horizontal stress anisotropy is thought to be significant - see Figure 6-2, Figure 6-3 and Figure 6-4 for example.

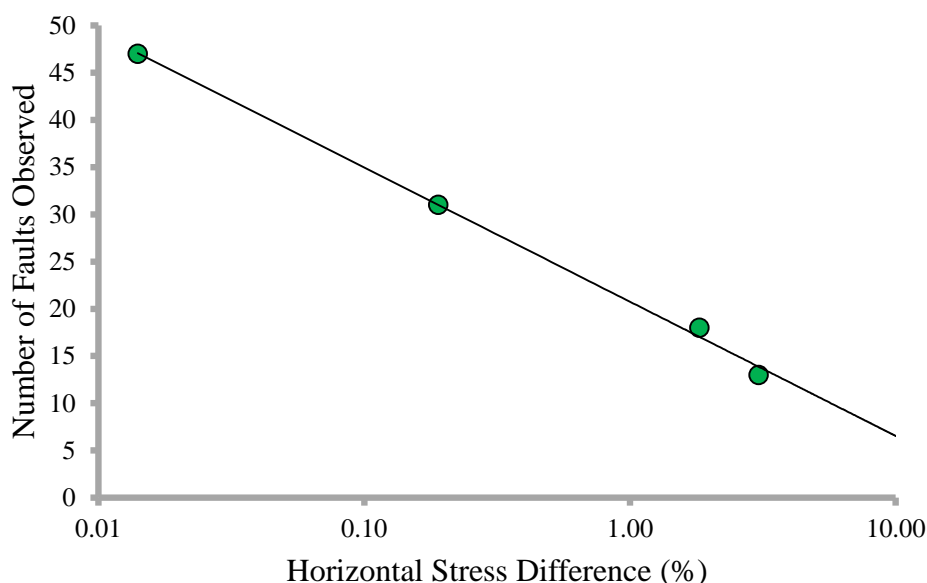


Figure 6-9: Variation of intensity of faulting with horizontal stress anisotropy. Note that as the horizontal stress difference increases the number of faults observed decreases.

6.3.2 Fault Spacing

From inspection of the interpreted planform geometries it is clear that fault spacing is variable in all cases, though it appears that the spacing is slightly 'looser' as anisotropy

Polygonal Faults and the Influence of Horizontal Stress Anisotropy

increases. Fault spacing is quantified following the approach adopted by Carruthers (2012) in which the distance between the midpoint on adjacent faults is estimated. The spacing between a representative selection of faults whose characteristics are suitable for assessment is evaluated using the aforementioned method, and this data is shown in Figure 6-10. Referring to Figure 6-10 the spacing of faults in the isotropic case appears slightly tighter, likely due to the range in strike directions which invariably leads to faults being slightly closer to one another. Despite the gradually decreasing density of faulting in the anisotropic cases, however, the spacing is still variable and does not appear to change appreciably. The inference is that, despite increased horizontal stress anisotropy and reduction in fault intensity, the spacing of faults does not markedly differ relative to the isotropic case. Once again this observation is consistent with reported cases. For example, studies of the spacing between radially aligned faults around North Sea salt structures and adjacent polygonal faults indicates that the spacing is broadly equivalent (Davison et al., 2000; Carruthers et al., 2013), hence the inference that the radial faults are in fact polarised polygonal faults responding to the diapir stress field. Considering this, it seems that although the spacing between the isotropic and anisotropic cases may differ slightly, the data presented in Figure 6-10 shows that there is no strong correlation between horizontal stress anisotropy and fault spacing, which in both the model output and seismic observation is typically highly variable. In conclusion, it is suggested that fault spacing is potentially a weak candidate for assessing and quantifying paleostress anisotropy and incorporating it into a workflow for paleostress estimation is perhaps unwise.

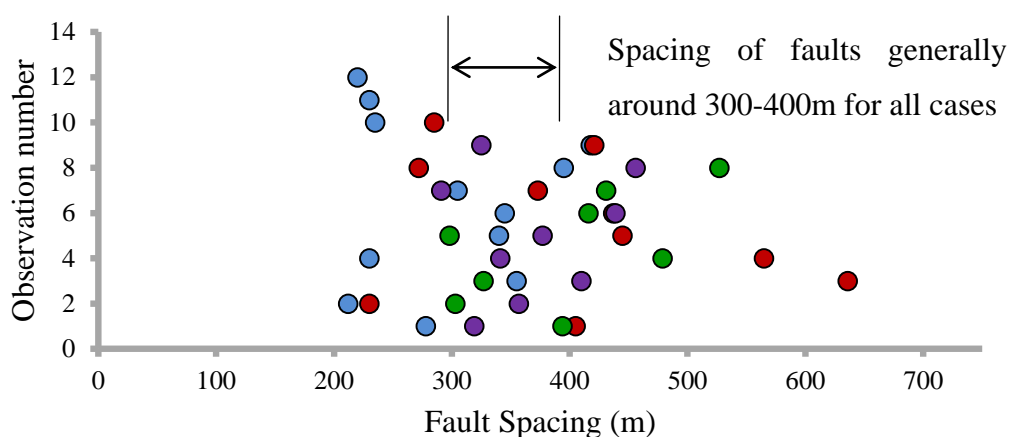


Figure 6-10: Variation of fault spacing with level of horizontal stress anisotropy. The spacing varies widely regardless of the magnitude of the horizontal stress difference.

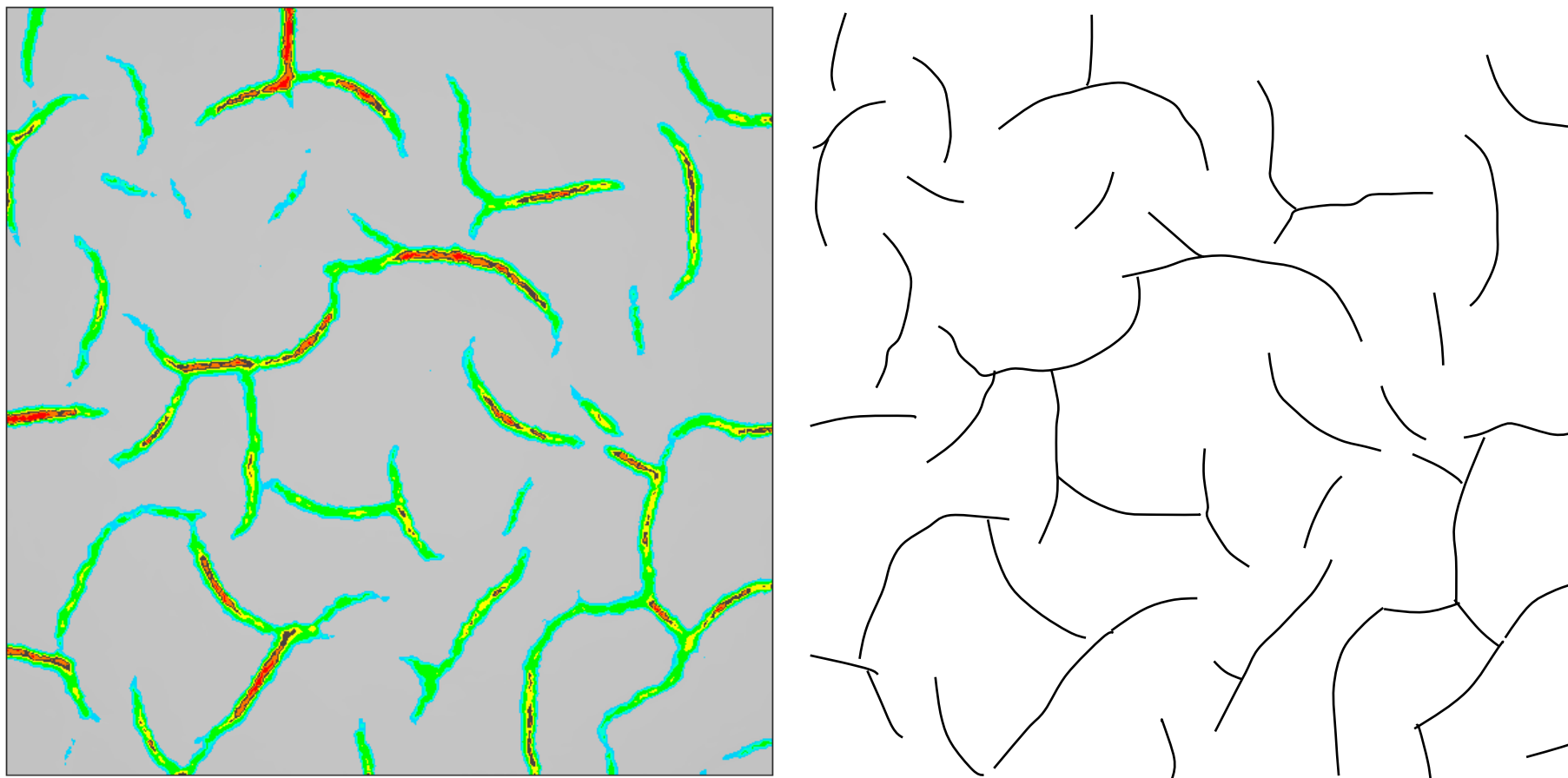


Figure 6-11: Horizontally isotropic case (a) Contours of effective plastic strain at the end of the simulation (b) Interpreted polygonal planform geometry at the end of the simulation.

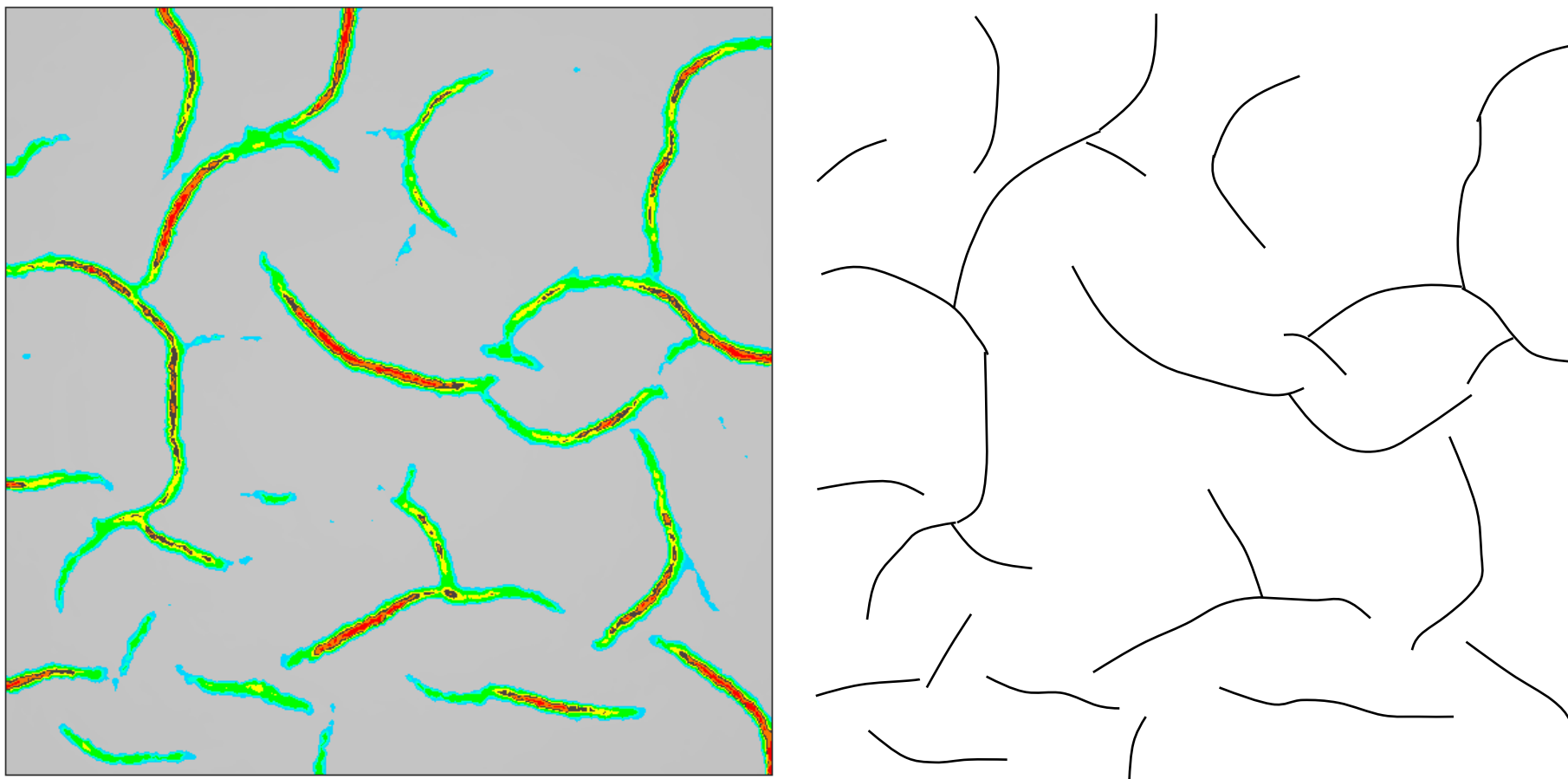


Figure 6-12: Horizontal stress anisotropy scenario 1 (a) Contours of effective plastic strain at the end of the simulation (b) Interpreted polygonal planform geometry at the end of the simulation.

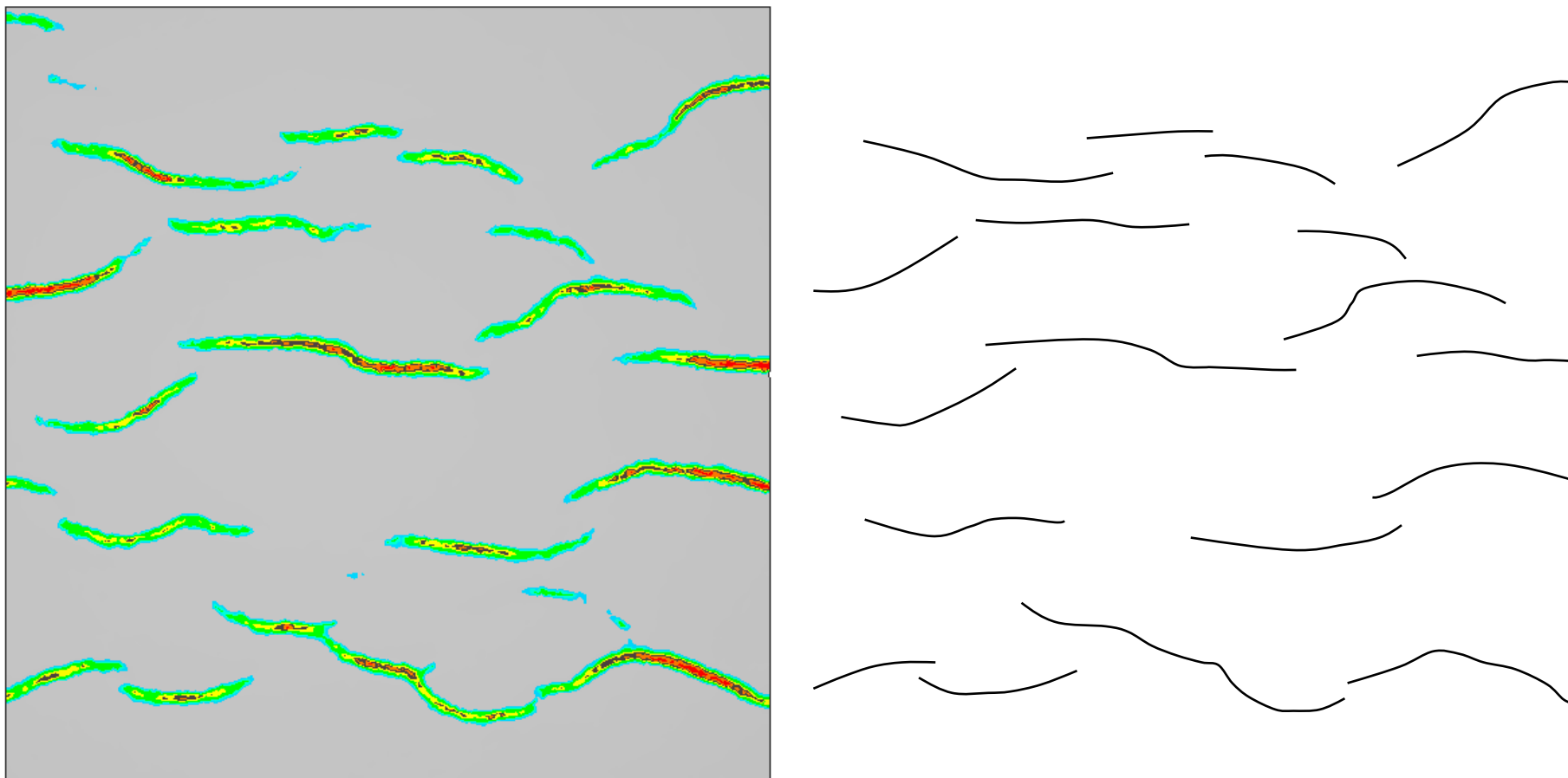


Figure 6-13: Horizontal stress anisotropy scenario 2 (a) Contours of effective plastic strain at the end of the simulation (b) Interpreted polygonal planform geometry at the end of the simulation.

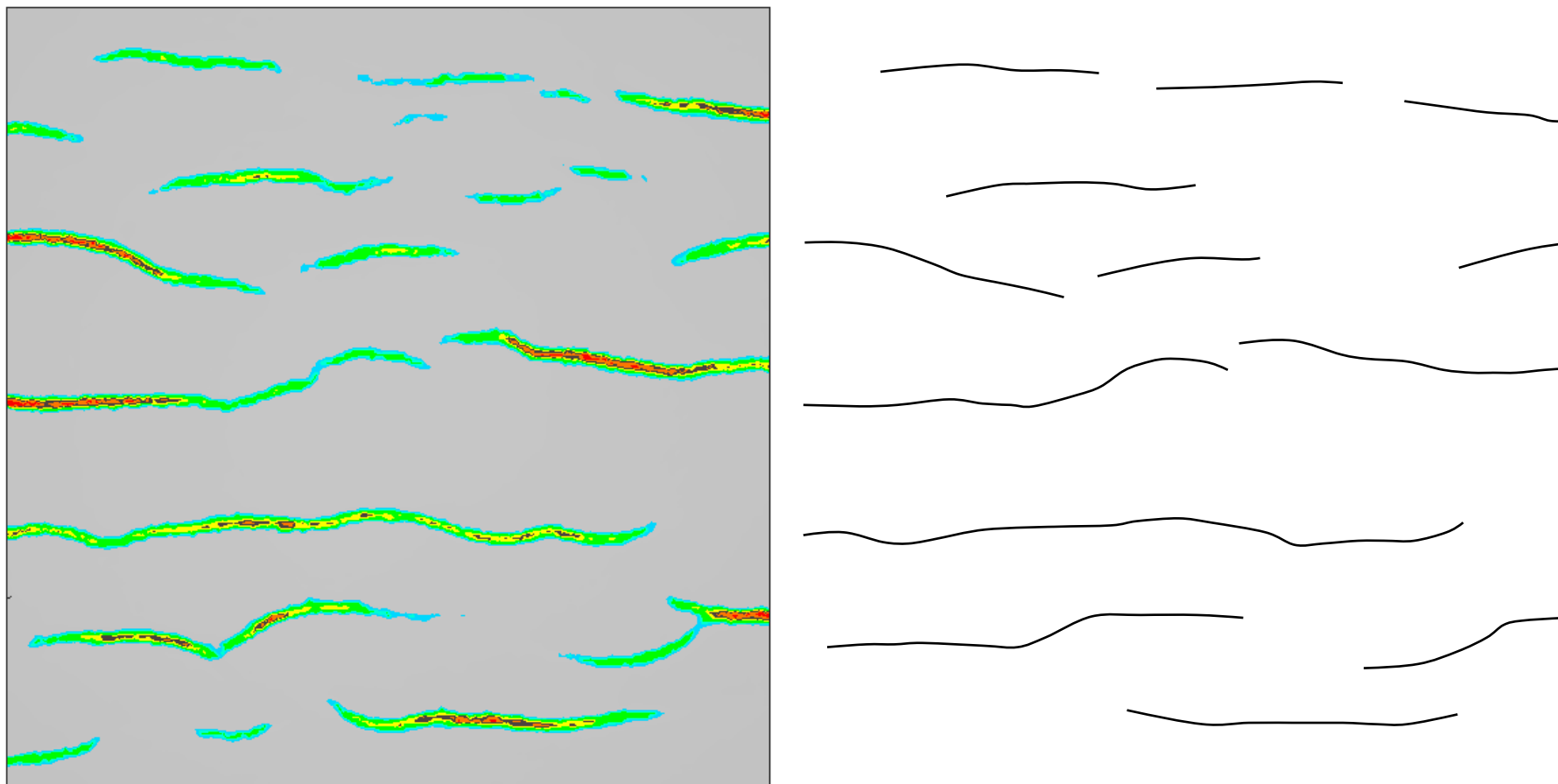


Figure 6-14: Horizontal stress anisotropy scenario 3 (a) Contours of effective plastic strain at the end of the simulation (b) Interpreted polygonal planform geometry at the end of the simulation.

6.3.3 Fault Strike

From inspection of Figure 6-11(a-b) to Figure 6-14(a-b) it is clear that there is a marked change to the polygonal planform geometry in terms of fault azimuth. As the anisotropy is increased a larger number of faults align parallel to the direction of compression. Rose diagrams, such as those in Figure 6-15 and Figure 6-16, are a useful means of interpreting this change. Note that, due to the cusp-shaped fault profiles in planview, it is difficult to obtain a consistent strike value and in some cases an approximation of strike is used.

The rose diagram in Figure 6-15(a) represents the isotropic case and exhibits no obvious preference in terms of the strike direction, though it can be argued that there are slightly more faults striking NW-SE. Note how there is a minimum of three faults striking in any given direction, confirming fault formation in a horizontally isotropic stress state. Figure 6-15(b) demonstrates the influence of anisotropy as faults start to become preferentially aligned and tend towards preferential strike in the East-West direction. The extent of the realignment in this case is remarkable given that the estimated difference in the horizontal stresses prior to fault formation is only 0.2%.

Referring to Figure 6-16(a) and (b), the magnitude of horizontal stress anisotropy is more pronounced, yet it is still estimated to be at a maximum of approximately 3%. In Figure 6-16(a) rarely are faults noted to deviate from the E-W direction by more than $\pm 20^\circ$. It is stressed that even in this case the horizontal stress difference is on average only 1.83%. Figure 6-16(b) clearly demonstrates that when this value exceeds approximately 3% all faults are observed to strike to within $\pm 20^\circ$ of the direction of most compressive horizontal stress. An alternative means of interpreting this data is by way of histograms, which can be found in Figure 6-17. The progressive bias in fault direction is again quite clear until all faults are close to E-W, and the data is finally concisely summarised in table.

Scenario	Horizontal Stress Difference (%)	Faults observed to be striking within $\pm 10^\circ$ of E-W direction (%)
0	0.01	8.5
1	0.19	12.9
2	1.83	61.1
3	3.05	81.8

Table 6-3: Summary of fault strike relationships. As the horizontal stress difference becomes more pronounced an increasing percentage of faults begin to strike in the direction of the intermediate principal stress.

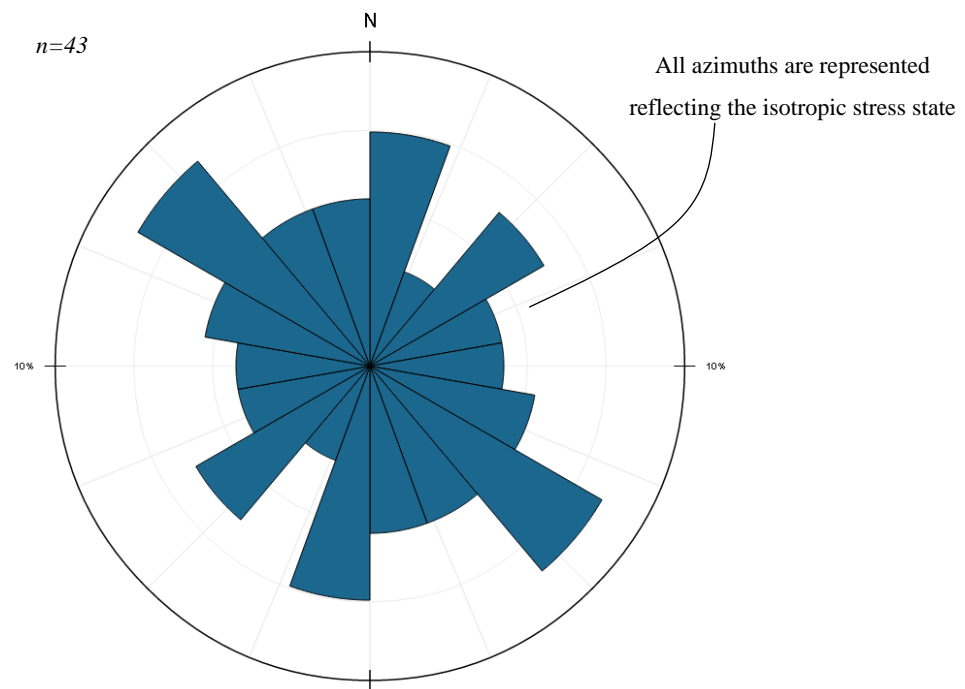
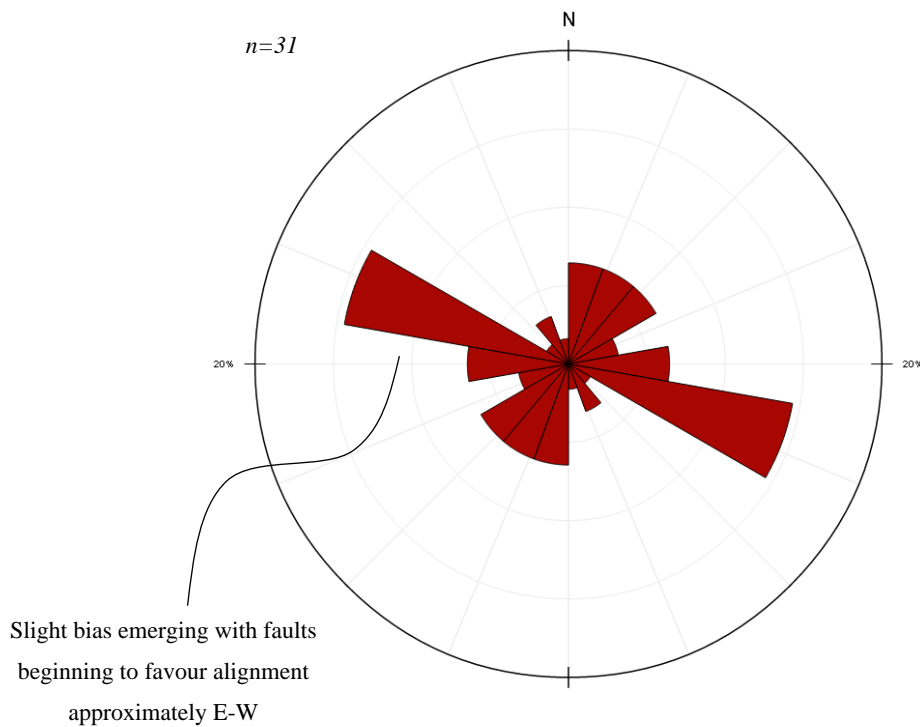
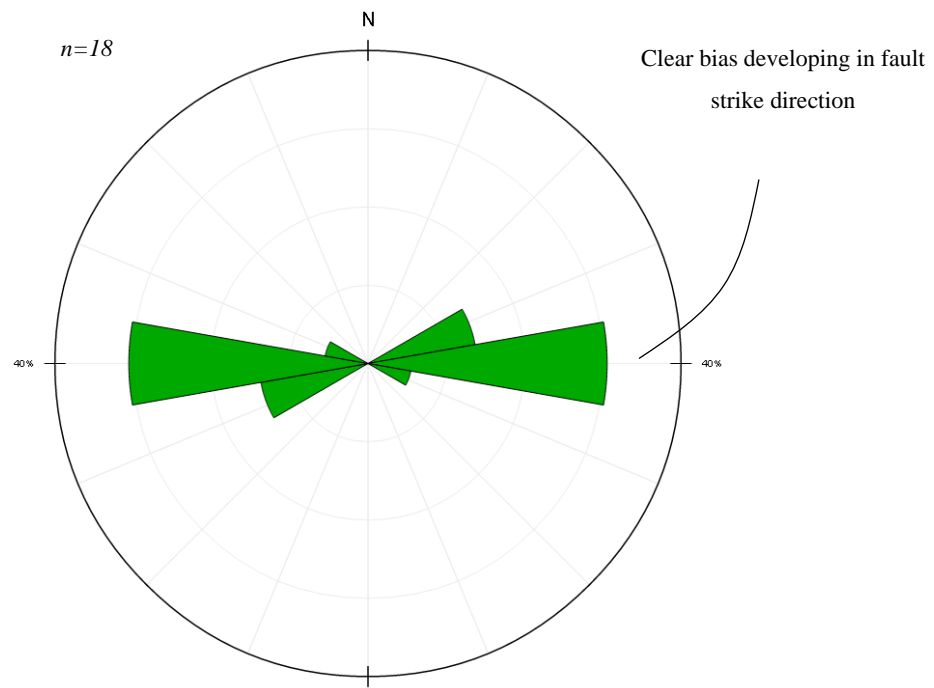
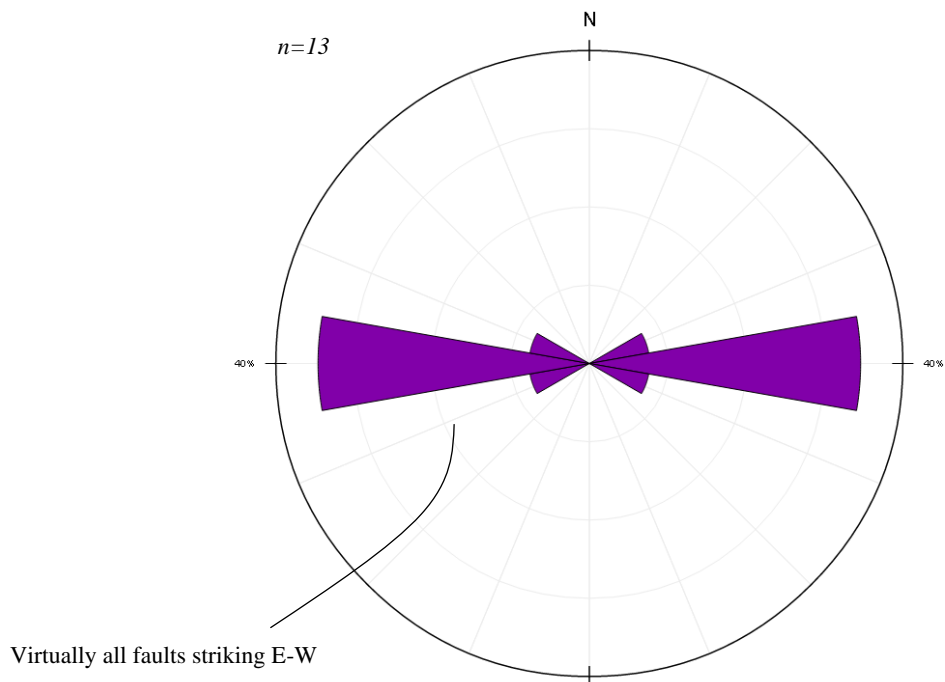
(a) *Horizontal stress difference of 0.01%*(b) *Horizontal stress difference of 0.19%*

Figure 6-15: Rose diagrams as visualisation of fault strike directions for various degrees of horizontal stress anisotropy. Note the marked reorientation of faults in (b).



(a) *Horizontal stress difference of 1.83%*



(b) *Horizontal stress difference of 3.05%*

Figure 6-16: Rose diagrams as visualisation of fault strike directions for various degrees of horizontal stress anisotropy. Note how virtually all faults strike East-West.

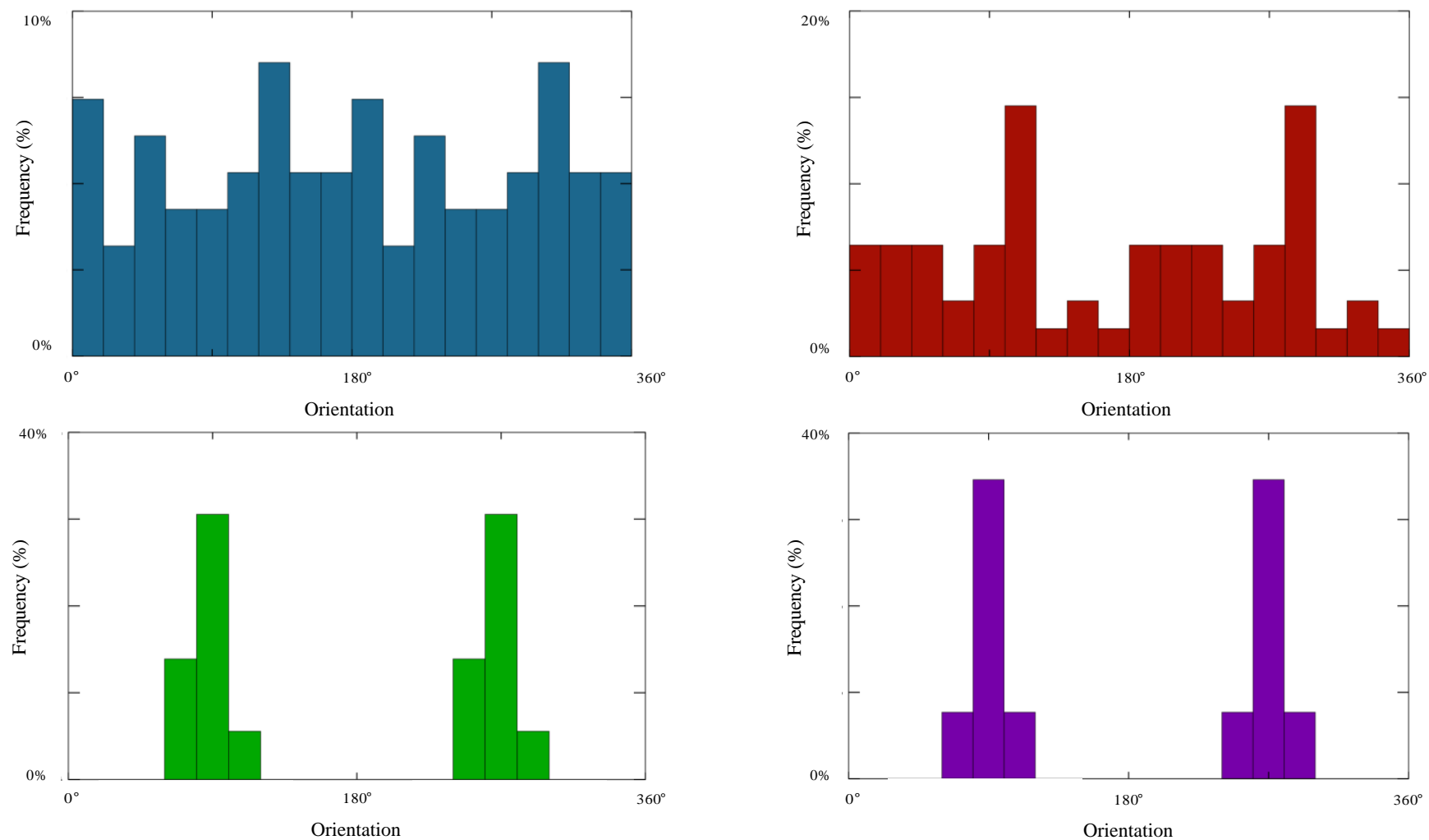


Figure 6-17: Data displayed in Figure 6-15 and presented in the form of histograms. For the isotropic case there is no obvious bias in fault azimuth. A progressive transition towards faults striking approximately East-West is observed.

Once more, the numerical predictions appear to be in good agreement with seismic observation related to polarisation of strike direction due to horizontal stress anisotropy and the relationship between fault strike azimuth and magnitude of anisotropy is compelling. It is therefore argued that this is potentially the strongest criterion for indicating and approximating paleostress orientations and magnitudes.

6.3.4 Fault Length

6.3.4.1 General Observations

Fault length is also noted to be related to the difference in the horizontal stress magnitudes. Inspection of the planform geometry for the isotropic case shows that fault segments have generally quite modest lengths (Figure 6-11).

Fault lengths have been interrogated at this horizon and the results are presented for this case in Figure 6-18(a). The lengths of faults rarely exceeds more than 500m and the vast majority are within 200 and 350m in length. It should be noted that these values are in excellent agreement for observations made of polygonal fault tiers of equivalent thickness in the North Sea where the stress state is nearly isotropic (Carruthers, 2012; Carruthers et al., 2013) as well as in many other reported cases. The average fault length in the isotropic scenario is 305m.

Incorporating subtle anisotropy results in a reduction in the total number of faults, as noted in Section 6.3.1, and it can be argued there is a subtle change in the length characteristics - see Figure 6-18(b). There is little change in the observed maximum or minimum lengths but it does appear that a greater number of faults have lengths in the range 350 to 500m. The average length for anisotropic scenario 1 is slightly higher at 376m.

For scenario 2, with approximately 1.85% horizontal stress difference prior to faulting, the combination of strike direction and increased length is more noticeable (Figure 6-13). The interrogated lengths of each of the faults at this level are displayed in Figure 6-18(c). The data is shifted more noticeably than the previous cases due to the general increase in length, and a larger proportion of the faults have lengths in excess of 500m. Maximum fault length is now approximately 950m, compared to around 700m for the previous two cases, and the average length is 518m.

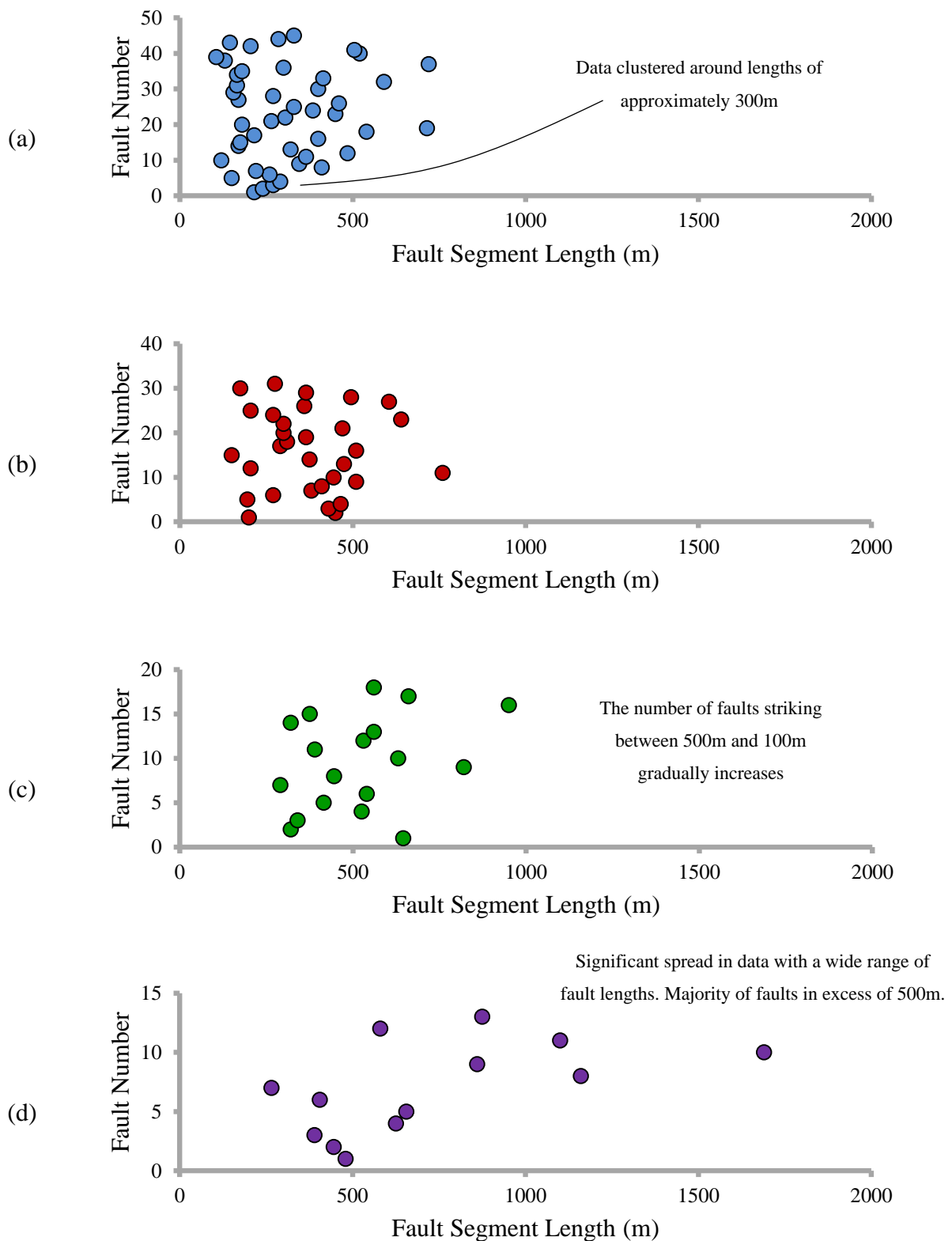


Figure 6-18: Variation of approximated fault lengths for all faults in each sensitivity. Horizontal stress differences are (a) 0.01% (b) 0.19% (c) 1.83% (d) 3.05%. Note how the range of fault lengths is much wider where anisotropy is greatest.

Polygonal Faults and the Influence of Horizontal Stress Anisotropy

The most significant changes in fault length are unsurprisingly found in scenario 3 where the horizontal stress difference is most marked. Figure 6-14 reveals a number of very large faults with some almost traversing the entire width of the domain. Figure 6-18(d) reveals that the range of observed fault lengths has increased substantially, ranging from a minimum of 300m to a maximum length of over 1500m. The majority of faults exceed 500m with several in excess of 1km, the average length is 733m.

6.3.4.2 Insights into Fault Growth from Length Data

The relationships presented in Figure 6-18 are analysed further in Figure 6-19. Figure 6-19(a) shows the minimum fault length observed as a function of the horizontal stress difference. The spread of the data is quite contained, and the minimum fault length for each case is generally between 150 and 250m. This could reinforce suggestions that the fault segment length is an intrinsic property.

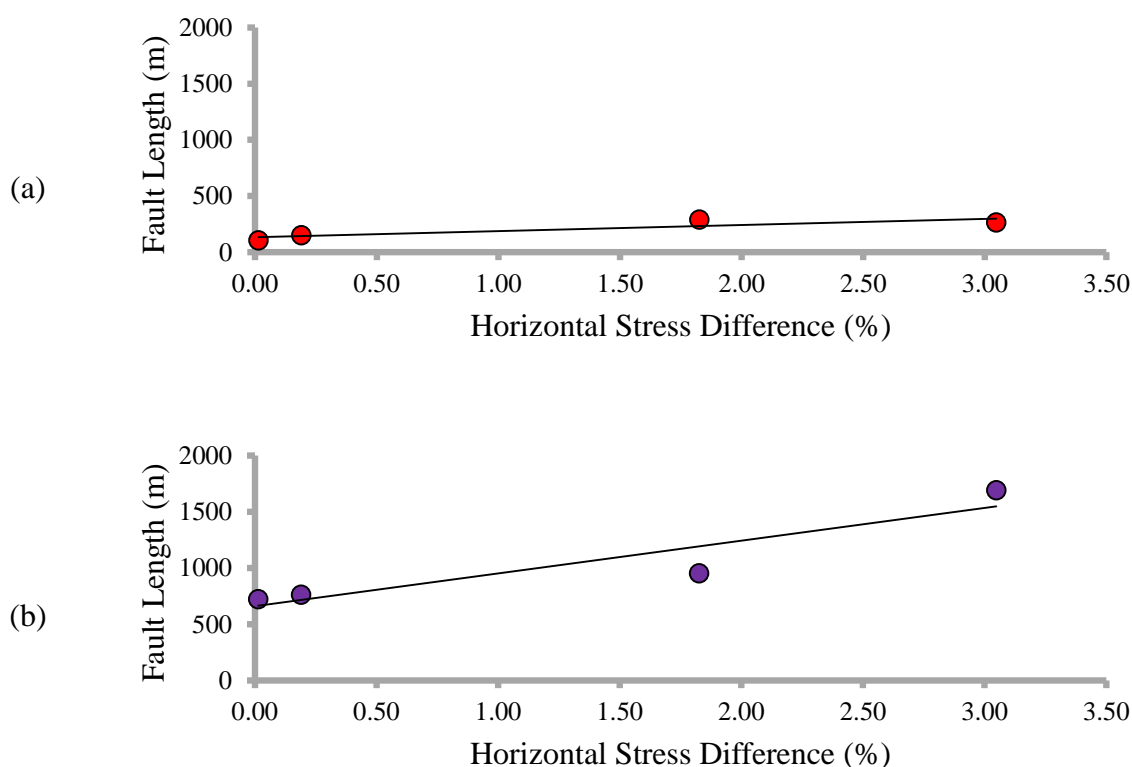


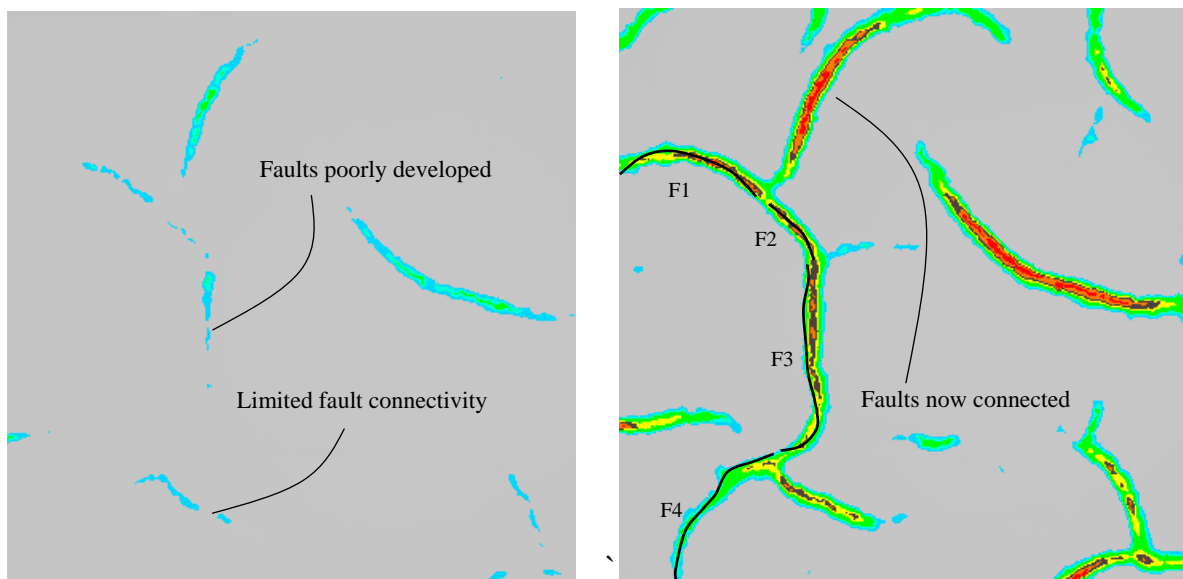
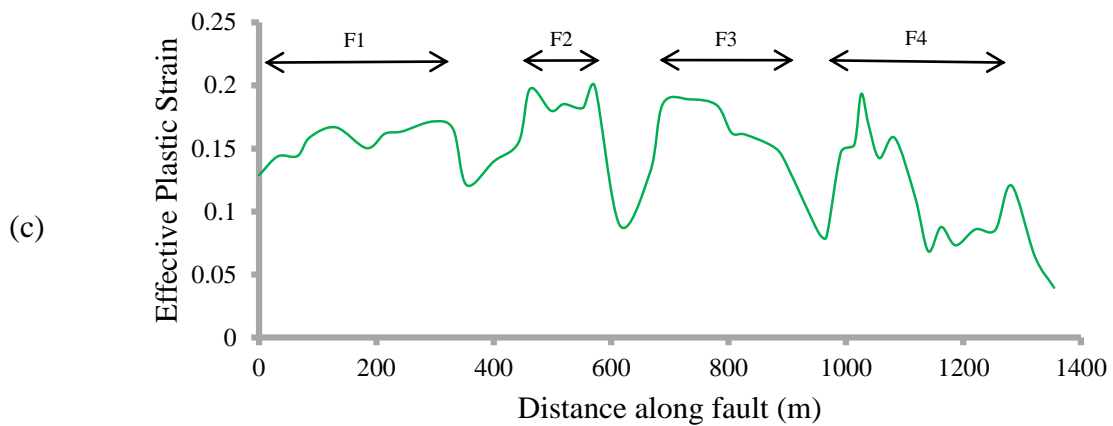
Figure 6-19: (a) Variation in minimum fault length in metres as a function of horizontal stress anisotropy (b) Variation in maximum fault length in metres as a function of horizontal stress anisotropy.

When viewed in contrast with the plot of Figure 6-19(b), which shows the maximum fault length for each case, it appears that the larger range in maximum fault lengths might be explained by the coalescence of smaller faults.

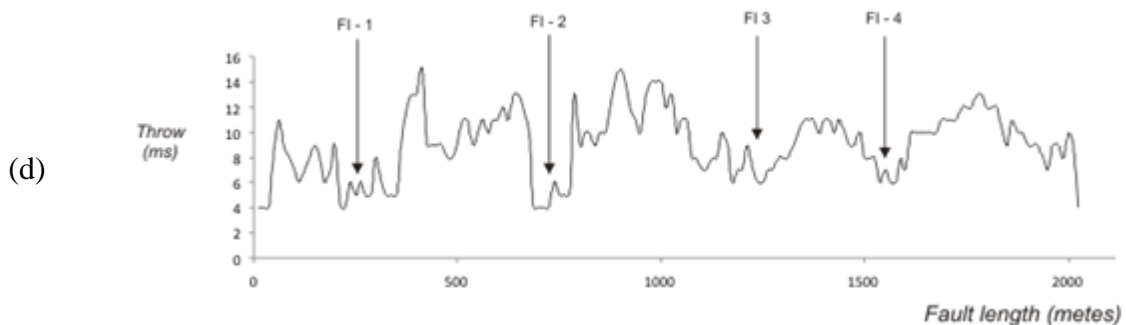
Studying the transient development of the faults adds weight to this assertion. Figure 6-20(a) shows an early stage of fault development where initially only a small number of faults are observed. The poor development of the faults is evidenced by unconnected tips (Cartwright, 2011) and the lack of any appreciable accumulated effective plastic strain. In Figure 6-20(b) the faults are now well developed and fault connectivity reflects a more mature fault system. Study of the faults systems in Chapter 5, as well as those described here, indicates a relationship between effective plastic strain and throw. Specifically, the region of most intense plastic straining coincides with the location of maximum throw. Figure 6-20(c) shows how effective plastic strain varies along the transect highlighted in Figure 6-20(b).

Where the faults are well developed the plastic strain is higher and hence the throw is more pronounced. Small values of effective plastic strain, and therefore throw, are observed where growing faults have radially propagated towards each other and particularly at intersections with faults whose orientation is normal. These comments satisfy those made regarding polygonal faults in the Central North Sea (Carruthers and Cartwright, 2010). Figure 6-20(d) presents data for a fault transect from this region. The thickness of the tier is comparable. Throw on the faults is modest and rarely exceeds more than 15m or so, and is also observed to be highly variable.

The similarities between the plots in (c) and (d) suggest that the style of propagation in the models likely bears a strong resemblance to contraction-driven intraformational faults in the field. As throw maxima are commonly interpreted to represent the nucleation site of a fault (Cartwright and Mansfield, 1998), it is argued by the same logic that minima, as noted in (d), represent orthogonal fault intersections or joining of faults via strike linkage (Carruthers, 2012). These are exactly the cases where throw minima are observed in the computational models, clearly adding support to this hypothesis.

(a) $t=5.1My$ (b) $t=6.1My$ 

(c)



(d)

Figure 6-20: Development of faults for one sensitivity (a) Initial fault development (b) developed and connected faults (c) effective plastic strain along the transect shown in (b) (d) transect taken along faults in the CNS (Carruthers and Cartwright, 2010).

Considering these arguments leads to an explanation for the increased maximum fault length in the cases with more pronounced horizontal stress anisotropy. Figure 6-21(a) highlights two of the largest faults that were observed in Figure 6-14. The fault on the left clearly incorporates a smaller fault via strike linkage (point A). A similar scenario appears as though it may occur at B if fault propagation continues or the faults are reactivated. Figure 6-21(b) demonstrates faults that have not managed to link (at C) and another successful linkage at D. Where faults do link a slight 'kink' is observed that clearly indicates a subtle change in strike as faults seek to become joined. These patterns have been noticed in extensional systems as evidence of normal fault propagation and linkage. Examples have been described in the Canyonlands national park where thin-skinned extension over a ductile detachment leads to similar kinked fault arrangements (Trudgill and Cartwright, 1994; Cartwright et al., 1995). Importantly, these patterns are also noted where polygonal faults are polarised due to imposed horizontal stress anisotropy. Such a scenario is shown in Figure 6-21(c) which shows kinked faults present around a large salt diapir in the Espirito Santo Basin (Carruthers, 2012).

The increased length of the faults where anisotropy is greatest is therefore explained by linkage of faults that are optimally orientated due to the alignment of the intermediate principal stress (maximum horizontal stress). The random orientation of faults in the horizontally isotropic case means that faults are less likely to be optimally orientated for fault linkage, and propagation in planview is likely to be arrested, or at least limited, due to intersection with other growing faults. Therefore, where anisotropy is subtle maximum fault lengths are likely to be smaller.

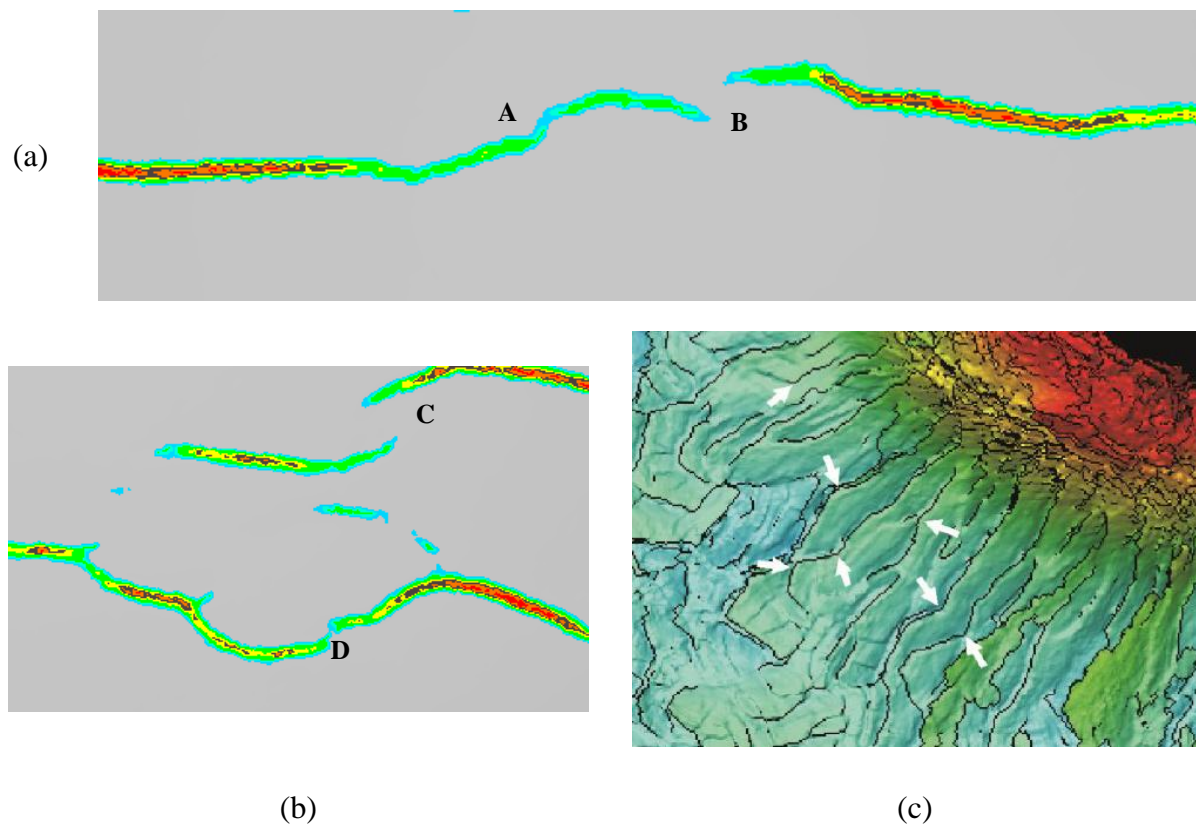


Figure 6-21: (a-b) Coalescence of faults observed in models leading to the formation of 'kinks' (c) Radial fault traces around a fault diapir in the Espirito Santo Basin (Carruthers, 2012).

6.4 Discussion

This chapter has investigated how the polygonal planform geometry responds to anisotropic horizontal stress states. The models described in Chapter 5 were augmented by introducing simple boundary conditions that induce varying degrees of stress anisotropy. The simulation results show that:

- 1 Changes to the polygonal planform geometry are clearly demonstrated and are pronounced even for subtle degrees of horizontal stress anisotropy. The magnitude of stress anisotropy required to produce strong re-alignment of faults may represent a difference in minimum and intermediate principal stresses of less than 1 or 2%. This correlates with previous findings as, for example, realignment of polygonal faults is observed for slopes of less than 1° (Cartwright, 2011), even though this corresponds to an approximate 1% anisotropy between the smallest and intermediate principal stresses (Crans et al., 1980). This observation reinforces the assertion that polygonal faults are

extremely sensitive to even small measures of horizontal stress anisotropy, and by extension are useful paleostress indicators.

- 2 From inspection of planform geometry it is obvious that the intensity of faults, defined as the number of faults per unit area, decreases with increasing horizontal stress anisotropy. This is consistent with observation, for example in Figure 6-4. Additional evidence for this relationship may be found in Figure 6-22 where polygonal faults respond to polarisation of the stress field due to a growing tectonic fault. The green and purple boxes in the figure are of equal area and are located in regions of inferred horizontally anisotropic and isotropic stress states respectively. Note that where the stress state is horizontally anisotropic the number of faults is smaller than in the isotropic case. Similar relationships are observed for tensile fracturing in deeply buried sandstones - Figure 6-23.
- 3 As horizontal stress anisotropy increases the azimuth of faults in the models becomes increasingly biased, until the majority of faults are aligned parallel to the intermediate principal stress. For example, Figure 6-13 and Table 6-3 indicate that for a horizontal stress difference prior to fault development of approximately 1.83%, the percentage of faults striking in the direction of the maximum horizontal stress is 61.1%. This value rises to 81.8% when the difference in horizontal stresses is just over 3%. This is also consistent with the field examples discussed in the introduction to this chapter. The arrangement of the faults in Figure 6-2, Figure 6-3 and Figure 6-4 and also with other published cases such as the work of Olson et al., (2007) - see Figure 6-23.
- 4 Fault spacing is observed to vary widely for each tier and despite the increasing difference in horizontal stresses the spacing was not observed to increase significantly. This observation is supported by observations of radial faults around North Sea salt structures that, due to similar spacing, are interpreted to be polarised polygonal faults (Carruthers, 2012).
- 5 Minimum fault length for all cases investigated was observed to be in the range of approximately 250 to 350m. Maximum fault length varied more widely and for the strongest horizontal stress anisotropy faults were observed to approach 2km in length. Investigation reveals that the increased fault length results from fault linkage of preferentially aligned faults and fewer intersections with faults striking in an orthogonal direction. Fault alignment where the stress state is isotropic does not favour a larger

number of long faults. Again these observations are consistent with observations of fault length around salt structures (Cartwright, 2011; Carruthers, 2012; Ho et al., 2013), tectonic faults (Hansen et al., 2004), and on slopes (Heffernan et al., 2004; Cartwright, 2011; Ireland et al., 2011).

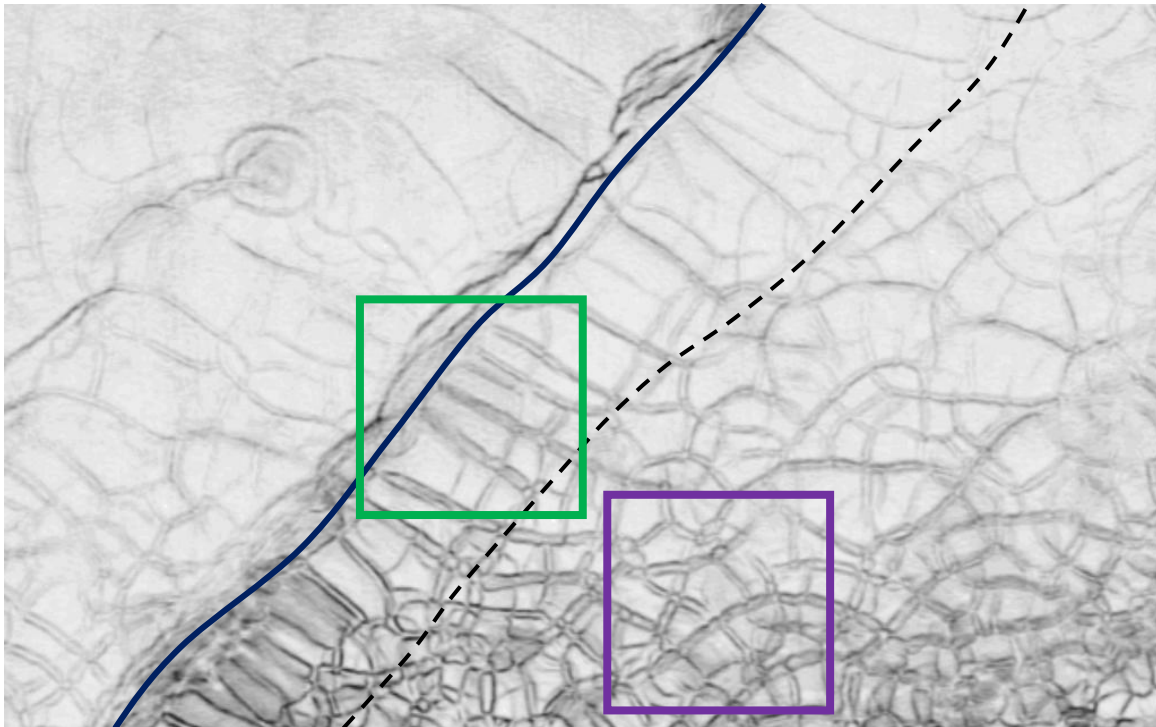


Figure 6-22: Polygonal faults developing in the hanging wall of a large tectonic fault (used and modified with permission from J. Cartwright). The solid black line indicates the location of the fault and the dashed black line indicates the inferred boundary between horizontally isotropic and anisotropic stress states. The green and purple boxes are of equal area and demonstrate the difference in fault intensity in the anisotropic and isotropic regions respectively. Note the changes in fault intensity between the two regions, and also the modification of fault length and strike direction.

To summarise, the relationships highlighted in this section confirm the suspected close relationship between planform geometry and differences in the orientations and magnitudes of the horizontal stresses. Of the four indicators of planform geometry chosen for assessing the influence of horizontal stress anisotropy, fault intensity, azimuth and length are the best geometric indicators based on the results of this study. Fault spacing is found to not strongly correlate with increasing horizontal stress difference.

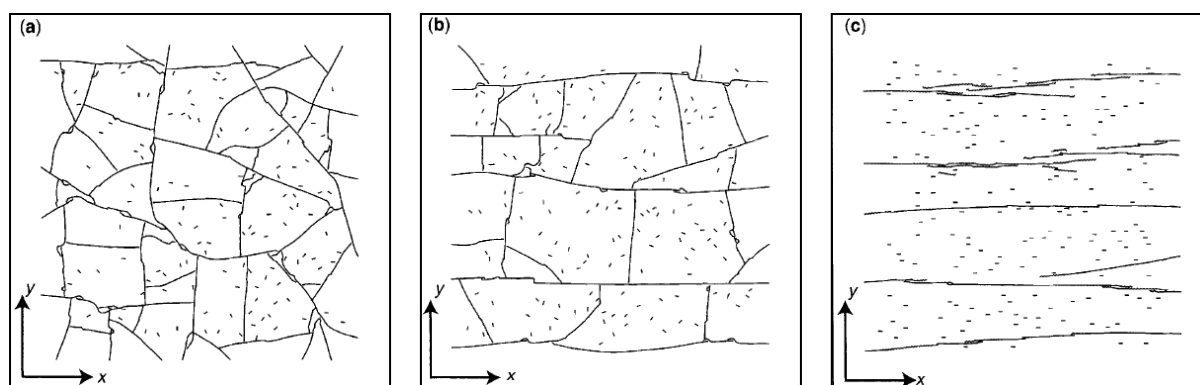


Figure 6-23: Fracture patterns in deeply buried sandstones created via application of (a) isotropic strain imposed at boundaries (b) moderate anisotropic strain imposed at boundaries which is larger in the x direction (c) strong anisotropic strain imposed at boundaries which is larger in the x direction (Olson et al., 2007). Note how the intensity and strike direction of the fractures changes in response to horizontal stress anisotropy.

6.5 Estimating Paleostress

The analysis of the previous sections indicates relationships between polygonal planform geometry and horizontal stress anisotropy. It is now proposed that these may be used in a workflow for establishing stress anisotropy purely by inspection of the planform geometry.

6.5.1 Concepts for a Workflow to Estimate Paleostress

A potential methodology for estimating paleostress magnitudes could take the following form. In keeping with the theme of this thesis, the domain could be discretised into zones of equal area. The size of these regions would naturally need to take into account the size of the polygonal fault system. The identification of a region where the stress state is essentially isotropic would comprise an important first step, and establishing the intensity, lengths and fault azimuth in this zone is key. By establishing each criterion for every region over the basin, these zones could be weighted against the isotropic region, and therefore the stress state could be evaluated for any location where the faults are present. This is shown conceptually in Figure 6-24(a) where an isotropic region is established (green) and then adjacent regions are assessed relative to this region. Red colours indicate regions where attributes indicate anisotropy.

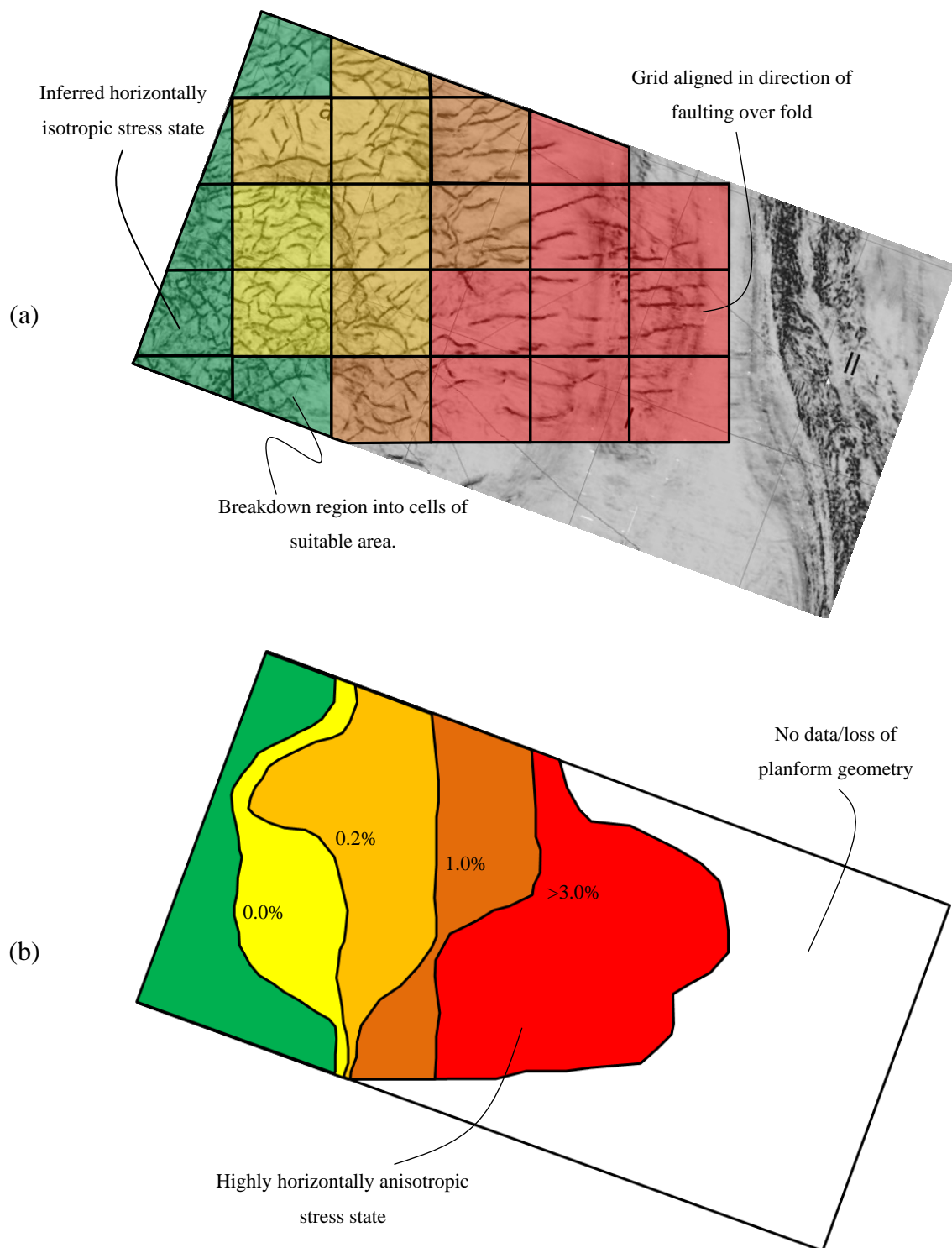


Figure 6-24: Potential approach for using planform geometry to estimate paleostress using image modified after Morley et al., (2014). In (a) the domain is broken down into cells. Azimuth, spacing and length relationships are established for each cell and by comparing to a reference region with an approximately isotropic stress state, a contour map of stress anisotropy could then be created as shown in (b).

By carrying out this procedure using the relationships outlined in Sections 6.3.1, 6.3.3, and 6.3.4 a map of anisotropy could be established for the region and this is shown in Figure 6-24(b). The loss of the planform geometry in Figure 6-24(b) could represent very marked horizontal stress differences and result in reduced fault intensity. However, in the absence of any concrete evidence to support this assertion, this could equally represent non-mechanical controls on planform geometry, and the significance of these controls is discussed in the following section.

6.5.2 Constraints on Use

Whilst the preceding discussion regarding the using polygonal faults as paleostress indicators is generally positive, and there is potential in the conceptual methodology in Section 6.5.1, it is noted that the following points should be considered carefully.

6.5.2.1 Lithological Controls

The constitutive properties of the hosting sediments is thought to be the key to polygonal fault development, with fine-grain size identified as being essential (Cartwright and Dewhurst, 1998; Dewhurst et al., 1999). Lateral facies variations and in particular transitions from predominantly fine-grained to coarse-grained sequences results in variation in spacing and intensity of faulting, with occasional complete loss of the planform geometry (Cartwright, 2011; Jackson et al., 2013, 2014). Furthermore, variation in the expression of the inferred diagenetic processes that control PFS genesis i.e. relative amounts of dissolution and cementation, is also envisaged to alter spatial distribution of faults (Hansen et al., 2004; Ding et al., 2013), as shown in Figure 6-25. It is worth noting that this investigation has focused on varying the mechanical controls, and there has been no sensitivity analysis within this chapter based on the constitutive properties of the material. For example, the perturbation of the stress field around a salt structure is noted to be variable and dependent on the constitutive properties of the host sediments (Bowers, 2007), particularly stiffness and Poisson's ratio. Whilst the stiffness at the time of genesis of the faults can be assumed to be fairly low, due to the reduction in effective mean stress from mineral dissolution and the high porosity of the hosting sediments, establishing the extents to which the stress field is perturbed would make for interesting future study.

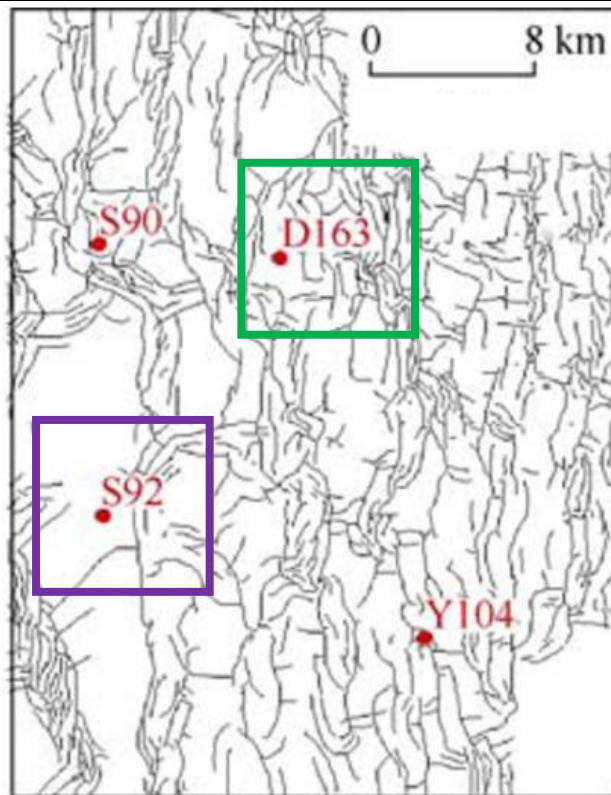


Figure 6-25: Lithological influence on planform geometry, modified after Ding et al., (2013). At locations S90 and D163 the diagenetic reaction is associated with a strong dissolution and minor re-precipitation and here faulting is well developed and numerous (green box). At locations S92 and Y104 the reaction is associated with weak dissolution and stronger cementation, coinciding with a reduction in the number of faults (purple box). Locations shown correspond to images in Figure 5.34. This situation could be misinterpreted as resulting from changes in stress conditions.

6.5.2.2 Maturity and Tier Structure

Fault spacing is thought to crudely scale with tier thickness (Carruthers, 2012; Ho et al., 2013): where tiers are thin the fault spacing is normally observed to be tighter. Consequently, where there are thickness variations there is a possibility for fault spacing to change, although it seems unlikely that these changes would occur over small intervals. Occasionally the tier may thin and pinchout so that faults are no longer observed, clearly this would represent a progressive change in planform geometry (Ho et al., 2013). Additionally, if the system is still developing in some regions and faulting is not well connected this could also be mistaken for changes in stress anisotropy.

6.5.2.3 Reactivation of Faults and Diachronous Growth

There is potential for polygonal faults to become reactivated and therefore the attributes of the faults at or during genesis may be different from the present day (Carruthers, 2012). Additionally, in some instances, the present planform geometry is thought to have resulted from two or more separate periods of faulting, indicative of 'diachronous' development. Such behaviour is reported in shallow diatomaceous sediments offshore Angola, where 'ladder' planform geometries are noted which feature dominant faults that strike for several kilometres linked by small scale faults running orthogonal to them (Ho et al., 2013). The pattern is suggested to result from two phases of growth, where the elongate faults develop first in a weakly anisotropic stress state, prior to the development of the smaller scale faulting in a secondary phase.

6.5.2.4 Pockmarks and Complex Local Stress States

The planform geometry may become influenced by small scale structures such as pockmarks, resulting in a local realignment of faults (Andresen and Huuse, 2011; Cartwright, 2011; Ho et al., 2013). In these instances the pockmark may only be between 250 and 300m in width, yet the polygonal faults become organised into a strong radial pattern. Crucially, although from inspection of the planform geometry reveals the obvious influence of horizontal stress anisotropy the use of the indicators suggested in Section 6.3 may not confirm this. This is because in this particular case there may not be significant changes in fault length or fault intensity, and the radial pattern would not reveal a preferred strike direction. Therefore the subtleties of complex local stress states may be lost with the suggested workflow.

6.5.3 Validation

Validation of the proposed strategy is important but is not straightforward. Considering the points made in Section 6.5.2, in order to use the polygonal faults as paleostress indicators the hosting tier would ideally be uniform in thickness and have no significant lateral facies variation. Crucially, to avoid having to consider reactivation and multiple growth phases it would need to be fairly young and at shallow depth. Obtaining data for such a region would likely be difficult as logging of data by companies exploring the region would probably focus on deeper zones around a targeted formation.

However, if the properties of the sediment can be approximated, the near-surface stress field could be approximated in a current-day stress analysis. This process is routine in the oil and

Polygonal Faults and the Influence of Horizontal Stress Anisotropy

gas industry for establishing optimal well trajectories and for obtaining initial conditions for reservoir depletion scenario analyses (Henk, 2005; Kristiansen and Plischke, 2010). A current day stress analysis around a North Sea salt diapir undertaken with the ELFEN geomechanical modelling code is shown in Figure 6-26. Figure 6-26(a) shows the ratio of the intermediate and principal stresses adjacent to the diapir, and as expected the ratio decays as one moves away from the structure. Figure 6-26(b) shows this data interpreted in a similar way to Figure 6-24(b). If polygonal faults were present at this level, and the stress state at the present day is inferred to not have differed greatly from the stress state imposed when faulting was triggered, then this stress state could be used to validate the relationships outlined in Section 6.3. Then using this one validated structure the stress state could be extrapolated over the entire polygonal fault system, obviously factoring in the caveats noted in Section 6.5.2.

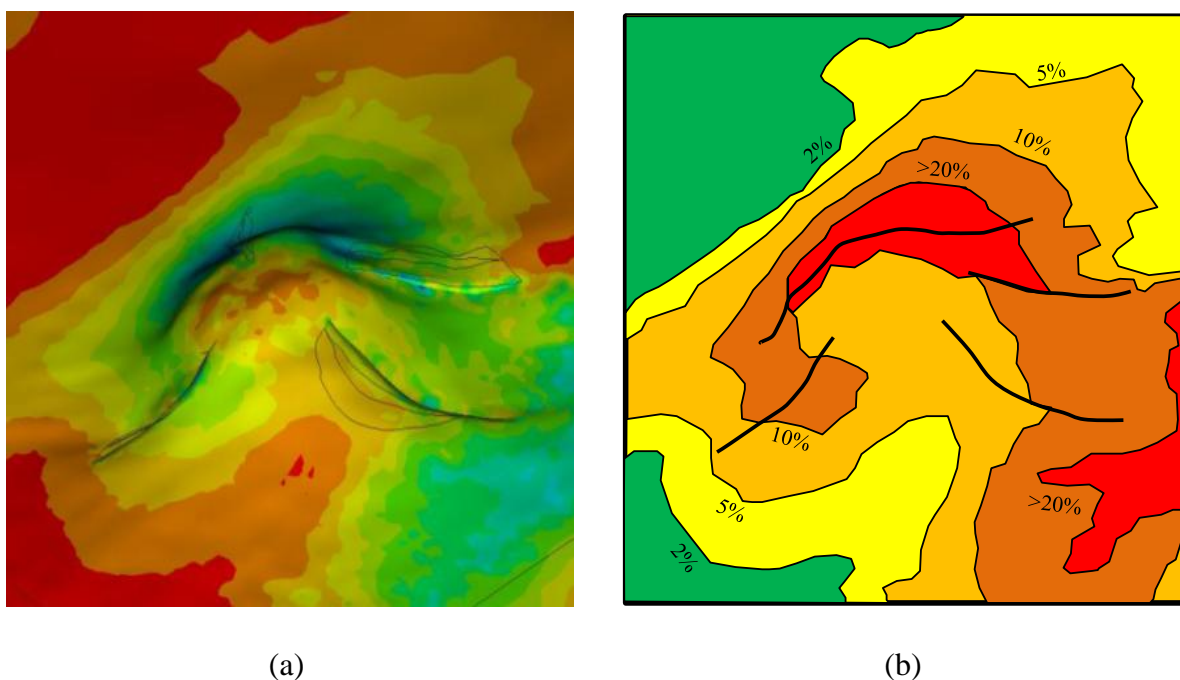


Figure 6-26: (a) Ratio between minimum and intermediate principal stresses at a horizon pierced by a salt diapir, North Sea (Rockfield, 2012). Red colours indicate isotropy, blue indicates anisotropy (b) Interpretation of (a) using similar contour bands to Figure 6-24(b). Note how there is very high horizontal stress anisotropy near the diapir but that within approximately 1-2 diapir radii this has decayed almost exponentially to a value of less than 2%.

It is important to emphasise that the polygonal faults themselves are not the only indicators of

paleostress orientations, and other novel methods using different geological indicators could also be used to assist in validation of the proposed framework. An interesting example is presented by Bureau et al., (2013) that uses the geometry of sandstone intrusions to estimate paleostress magnitudes and orientations. The intrusions evolve due to elevated pore pressures that develop in an underlying parent sand layer, which results in liquefaction and injection of sand through Oligocene/Eocene age polygonal faults. The geometry of the intrusion can then help to constrain the paleostress magnitude. The issue with adopting this case for validation is that the intrusions developed in the Miocene, sometime after the development of the faults, and as a result the stress state likely differs between fault development and injection of the intrusions. However, in general, where other local indicators can be identified that correspond to a similar time period as the fault development, these may also be useful validation tools. A potential example might be core information that detail dominant trends in sub-seismic fracture or vein orientations, or inferences made possible from analysis of sediment fabric (Ask and Morgan, 2010).

6.6 Closing Comments

The implication of the points raised during the discussion is that whilst use of polygonal faults to constrain stress states might present an intuitive and novel approach, it should only be used to obtain approximate values. Importantly, the regional geology and stratigraphy need to be mapped carefully and fully understood. This will avoid lithological changes to planform geometry being wrongly interpreted as having mechanical origins. This is only possible with high quality 3D seismic data. It is, therefore, suggested that the tools developed here might form part of a multi-disciplinary approach and compliment the conventional use of 3D seismic data in constraining paleostress using polygonal fault systems. Future work could focus on continuing the development and validation of this methodology.

6.7 References

- Anderson, E. M., 1951, *The Dynamics of Faulting and Dyke Formation with Applications to Britain*: Oliver and Boyd, Edinburgh, p. 206.
- Andresen, K. J., and M. Huuse, 2011, “Bulls-eye” pockmarks and polygonal faulting in the Lower Congo Basin: Relative timing and implications for fluid expulsion during shallow burial: *Marine Geology*, v. 279, no. 1-4, p. 111–127.
- Ask, M. V. S., and J. K. Morgan, 2010, Projection of mechanical properties from shallow to greater depths seaward of the Nankai accretionary prism: *Tectonophysics*, v. 482, no. 1-4, p. 50–64.
- Bai, T., L. Maerten, M. R. Gross, and A. Aydin, 2002, Orthogonal cross joints: do they imply a regional stress rotation?: *Journal of Structural Geology*, v. 24, no. 1, p. 77–88.
- Bowers, G. L., 2007, Effect of inelastic sediment behavior on near-salt stresses and pore pressures: *The Leading Edge*, v. 26, no. 11, p. 1462.
- Bureau, D., R. Mourgues, J. Cartwright, M. Foschi, and M. M. Abdelmalak, 2013, Characterisation of interactions between a pre-existing polygonal fault system and sandstone intrusions and the determination of paleo-stresses in the Faroe-Shetland basin: *Journal of Structural Geology*, v. 46, p. 186–199.
- Carruthers, T. D., 2012, *Interaction of polygonal fault systems with salt diapirs*: Unpublished PhD Thesis - Cardiff University, p. 526.
- Carruthers, D., and J. Cartwright, 2010, Using polygonal fault systems as a tool for reconstructing the state of stress associated with salt diapirs, *in* *Salt tectonics, sediments and prospectivity* - Geological Society of London.
- Carruthers, D., J. A. Cartwright, M. P. A. Jackson, and P. Schutjens, 2013, Origin and timing of layer-bound radial faulting around North Sea salt stocks: New insights into the evolving stress state around rising diapirs: *Marine and Petroleum Geology*, v. 48, p. 130–148.
- Cartwright, J. A., 2011, Diagenetically induced shear failure of fine-grained sediments and the development of polygonal fault systems, *in* *Marine and Petroleum Geology*: Elsevier Ltd, p. 1593–1610.
- Cartwright, J. A., and D. N. Dewhurst, 1998, Layer-bound compaction faults in fine-grained sediments: *Geological Society of America Bulletin*, v. 110, no. 10, p. 1242–1257.
- Cartwright, J. A., and C. S. Mansfield, 1998, Lateral displacement variation and lateral tip geometry of normal faults in the Canyonlands National Park, Utah: *Journal of Structural Geology*, v. 20, no. 1, p. 3–19.

-
- Cartwright, J. A., B. D. Trudgill, and C. S. Mansfield, 1995, Fault growth by segment linkage: an explanation for scatter in maximum displacement and trace length data from the Canyonlands Grabens of SE Utah: *Journal of Structural Geology*, v. 17, no. 9, p. 1319–1326.
- Crans, W., G. Mandl, and J. Haremboure, 1980, On the theory of growth faulting*: A geomechanical delta model based on gravity sliding: *Journal of Petroleum Geology*, v. 2, no. 3, p. 265–307.
- Davison, I., I. Alsop, P. Birch, C. Elders, N. Evans, H. Nicholson, P. Rorison, D. Wade, J. Woodward, and M. Young, 2000, Geometry and late-stage structural evolution of Central Graben salt diapirs, North Sea: *Marine and Petroleum Geology*, v. 17, no. 4, p. 499–522.
- Dewhurst, D. N., J. A. Cartwright, and L. Lonergan, 1999, The development of polygonal fault systems by syneresis of colloidal sediments: *Marine and Petroleum Geology*, v. 16, no. 8, p. 793–810.
- Ding, X., G. Liu, M. Sun, and P. Wang, 2013, Origin of polygonal fault systems: A case from the Sanzhao sag in the Songliao Basin, East China: *Petroleum Exploration and Development*, v. 40, no. 3, p. 333–343.
- Dusseault, M. B., V. Maury, and F. Sanfilippo, 2004, Drilling Around Salt : Risks , Stresses , And Uncertainties: *Stress: The International Journal on the Biology of Stress*.
- Fossen, H., 2010, *Structural Geology*: p. 480.
- Hansen, D. M., J. W. Shimeld, M. A. Williamson, and H. Lykke-Andersen, 2004, Development of a major polygonal fault system in Upper Cretaceous chalk and Cenozoic mudrocks of the Sable Subbasin, Canadian Atlantic margin: *Marine and Petroleum Geology*, v. 21, no. 9, p. 1205–1219.
- Heffernan, A. S., J. C. Moore, N. L. Bangs, G. F. Moore, and T. H. Shipley, 2004, Initial deformation in a subduction thrust system: Polygonal normal faulting in the incoming sedimentary sequences of the Nankai subduction zone, Southwestern Japan., *in* Davies, R.J., Cartwright, J.A., Stewart, S.A., Underhill, J.R., Lappin, M. (Eds.), *3D Seismic Technology: Application to the Exploration of Sedimentary Basins*: Geological Society, London, p. 457–472.
- Henk, A., 2005, Pre-drilling prediction of the tectonic stress field with geomechanical models: *First Break*, v. 23, no. November, p. 53–57.
- Ho, S., T. D. Carruthers, P. Imbert, and J. Cartwright, 2013, Spatial Variations in Geometries of Polygonal Faults Due to Stress Perturbations & Interplay with Fluid Venting Features, *in* 75th EAGE Conference and Exhibition incorporating EUROPEC, London, 10-13 June 2013: p. 1–5.

- Ireland, M. T., N. R. Goult, and R. J. Davies, 2011, Influence of stratigraphic setting and simple shear on layer-bound compaction faults offshore Mauritania: *Journal of Structural Geology*, v. 33, no. 4, p. 487–499.
- Jackson, C. A. L., D. Carruthers, S. N. Mahlo, and O. Briggs, 2014, Can polygonal faults help locate deepwater reservoirs?: *AAPG Bulletin*, no. May, doi:10.1306/03131413104.
- Jackson, C. A.-L., S. N. Mahlo, O. Briggs, and T. D. Carruthers, 2013, Role of Polygonal Fault Mapping in De-Risking Deepwater Reservoir Presence: A 3-D Seismic Reflection Case Study from Offshore Norway, *in AAPG Annual Convention and Exhibition*, Pittsburgh, Pennsylvania.
- Koupriantchik, D., S. P. Hunt, P. J. Boulton, and A. G. Meyers, 2004, Geomechanical modelling of salt diapirs : 3D salt structure from the Officer Basin , South Australia: *Science And Technology*.
- Kristiansen, T., and P. Plischke, 2010, History Matched Full Field Geomechanics Model of the Valhall Field Including Water Weakening, *in 72nd EAGE Conference & Exhibition*: p. 14–17.
- Lachenbruch, A. H., 1963, Mechanics of thermal contraction cracks and ice-wedge polygons in permafrost. *Geological Society of America: Geological Society of America Special Papers.*, v. 70, p. 1–66.
- Morley, C. K., J. Warren, M. Tingay, P. Boonyasaknanon, and A. Julapour, 2014, Comparison of modern fluid distribution, pressure and flow in sediments associated with anticlines growing in deepwater (Brunei) and continental environments (Iran): *Marine and Petroleum Geology*, v. 51, p. 210–229.
- Nikolinakou, M. A., 2011, Geomechanical Modeling of Stresses Adjacent to Salt Bodies : 2 . Poro-Elasto-Plasticity and Coupled Overpressures: *AAPG Bulletin*.
- Olson, J. E., S. E. Laubach, and R. H. Lander, 2007, Combining diagenesis and mechanics to quantify fracture aperture distributions and fracture pattern permeability: *Geological Society, London, Special Publications*, v. 270, no. 1, p. 101–116.
- Rance, J. M., M. L. Profit, S. J. Dee, and D. T. Roberts, 2013, Predicting the Paleo Evolution of Overpressured Geological Structures, *in 47th ARMA Rock Mechanics and Geomechanics Symposium*, San Francisco, California.
- Rawnsley, K. D., T. Rives, and J. Petit, 1992, Joint development in perturbed stress fields near faults: *Journal of Structural Geology*, v. 14, no. 8/9, p. 939–951.
- Rockfield, 2012, *Rockfield - A world leader in advanced geomechanical modelling*: 29 p.
- Stewart, S., 2006, Implications of passive salt diapir kinematics for reservoir segmentation by radial and concentric faults: *Marine and Petroleum Geology*, v. 23, no. 8, p. 843–853.

Trudgill, B., and J. Cartwright, 1994, Geological Society of America Bulletin Relay-ramp forms and normal-fault linkages , Canyonlands National Park , Utah: Geological Society of America Bulletin, v. 106, no. 9, p. 1143–1157, doi:10.1130/0016-7606(1994)106<1143.

Zoback, M. D., 2007, Reservoir Geomechanics: Cambridge, p. 461.

Chapter 7

CONCLUSIONS AND SUGGESTIONS FOR FUTURE INVESTIGATION

The example of the Qiongdangnan Basin in the introductory chapter demonstrated the potential for polygonal faults to potentially act as seal-bypass systems and compromise the integrity of caprocks. In the case of the Niobrara formation, Colorado, the polygonally faulted interval is itself the targeted reservoir formation. Furthermore, it appears that natural fracture networks within the Niobrara formation, which seem likely to be strongly related to the presence of the polygonal faults, are instrumental in providing sufficient connectivity and porosity in order for the play to be economically viable (Sonnenberg and Underwood, 2012). These cases demonstrate that understanding the development and growth of these faults has important implications for hydrocarbon and unconventional resources exploration, and this research has been primarily focused on examining the geomechanical conditions controlling the development of polygonal faults with the aid of computational modelling tools.

This chapter aims to summarise the key points highlighted within the thesis that contribute to the collective understanding of the nature and significance of polygonal fault systems. A concise summary of each chapter is provided and the approach adopted is justified. A brief discussion is also offered as a synthesis of the results contained which serves to compliment the comprehensive discussions provided at the end of Chapters 4 through 6. Finally, a review of potential limitations and future work is considered.

7.1 Approach for Investigating the Genesis and Evolution of Polygonal Faults

7.1.1 Chapter 2: Analysing the Behaviour of Sediments During Early Burial

Chapter 2 focused on understanding the behaviour of sediments during early burial. Typically studies of the geomechanical evolution of a sediment consider only the depositional porosity and how this becomes modified during burial. Recently, focus has been given to the fabric and bonding of sediments, which is commonly derived from processes occurring during or after sedimentation. Processes that alter structure have important implications for the behaviour of sediments both in compaction and in shear, and may include the nature of the

depositional environment, creep, cementation and diagenesis, all of which were discussed.

7.1.2 Chapter 3: Utilising Computational Geomechanics

Investigations of polygonal faults are dominated by the use of seismic data. 3D seismic has allowed for both identification of polygonal faults in many basins globally, and the establishing of some key controls and characteristics that govern their evolution. The complex constitutive response that underlies their formation means that studying them using kinematic restoration and/or bench scale modelling is limited, and this explains the reluctance for researchers to adopt these techniques. The deficiencies in traditional modelling approaches suggest the requirement for an alternative methodology for analysing the formation and evolution of polygonal fault systems. Therefore, the approach adopted within this work is to utilise computational geomechanics. Chapter 3 provided a basic and uncomplicated discussion of the approaches used in previous forward modelling studies. With reference to polygonal faults, some important considerations were shown to be;

- 1 A flexible, robust computational framework that can treat irregular or evolving topologies and the finite deformation associated with the development of the localised faults in both two and three dimensions. The adaptive finite element framework used by the forward modelling code ELFEN was shown to satisfy these requirements.
- 2 A material model with a suitable level of sophistication was necessary in order to replicate both the shear and compactive behaviour of soils and soft rocks. A strength based constitutive model using the critical state concept was identified as most suitable. Material models that are conventionally used to describe soil/rock behaviour, such as Mohr-Coulomb, are limited in their ability to capture all deformation styles and importantly struggle to consistently deal with the transition between brittle and ductile states.

7.2 Chapter 4: The Diagenetic Mechanism for Polygonal Fault Formation

Chapter 4 focused on how the influence of burial diagenesis may be built into the elastoplastic SR3 constitutive model. A discussion on the influence of thermally driven chemical volume reductions and influence on stress and material state was provided with reference to case studies, conceptual models and experimental studies of dissolution-driven shear failure. The enhancement of the constitutive model with a simple empirical law for chemical compaction was outlined based on a previous study (Crook, 2010) and was shown to adopt a sequential implementation, whereby a short term mechanical update is performed first before

the influence of chemical compaction is considered. A stress update is required to accommodate diagenetically sourced deformation and this has been modified in this work so that the chemical volume reduction may be expressed orthotropically or isotropically, dependent on the reaction and sediment type. Tracking of the level of cementation structure due to the precipitation of cements was also added and was consistently tracked so that it can also be mechanically removed. The Opal A/CT transformation was specifically targeted due to recent evidence suggesting a coincidence between this diagenetic boundary and PFS. The functionality of enhancements to the code was exhibited in a suite of tests that involved differing magnitudes and expressions of chemical volume change. A trend of horizontal stress reduction until completion of the chemical process was observed before recovery to the K_0 condition. A satisfactory qualitative agreement with experimental studies of dissolution by Shin et al., (2008) provided confidence in both the geomechanical argument and the modelling approach.

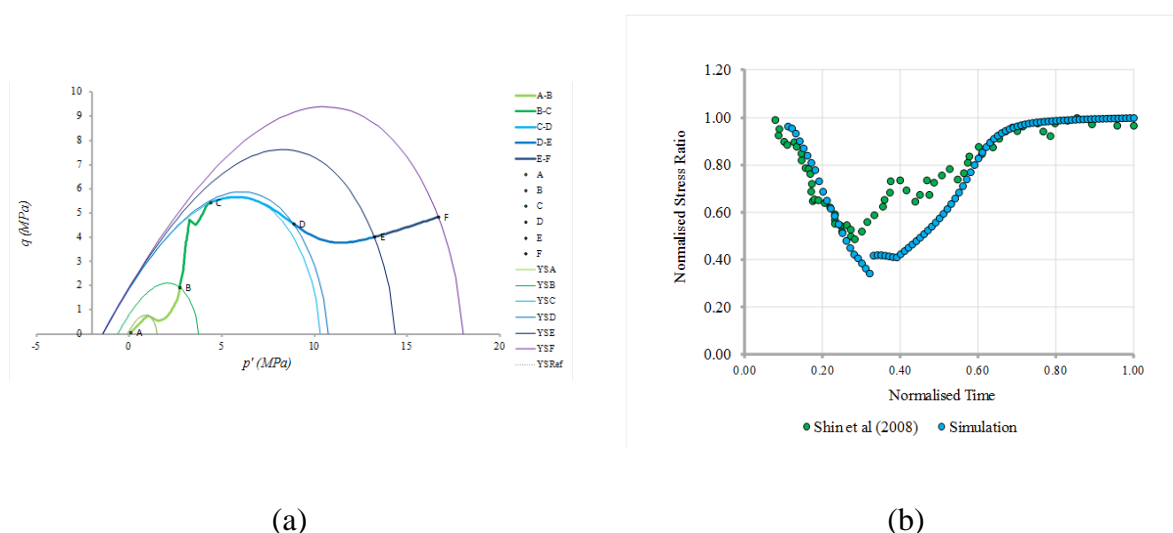


Figure 7-1: Results from Chapter 4 (a) Stress path and state boundary surface evolution for a chemical porosity change of 10% (b) Corresponding evolution of K_0 and comparison with experimental data. Note data is normalised to allow for qualitative comparison.

7.3 Chapter 5: Field Scale Modelling of the Formation and Evolution of a PFS

Chapter 5 aimed to assess whether diagenetically-induced shear led to localised failure and the development of polygonal faults at the field scale. The principal findings of the chapter are summarised below.

-
- 1 The Opal A/CT could be a candidate for PFS formation as it was demonstrated that the characterised material exhibited localised shear failure and the formation of faults that strongly resembled many polygonal faults and matched criterion for identifying these fault systems. The results would appear to reinforce the suggestions of Davies and Ireland (2011) who proposed that thermally triggered volume reduction that is not necessarily near surface may trigger polygonal fault formation at more substantial depths. It was however noted that although this reaction is unlikely to be a universal explanation for polygonal fault formation. Although some evidence suggests a strong relationship between polygonal faults and the Opal A/CT transition boundary, this is not necessarily causal and may just enhance the expression of pre-existing faults (Neagu et al., 2010; Cartwright, 2011).
 - 2 A sensitivity study was undertaken that indicated that given quick reaction rates the genesis of polygonal faults may be associated with more subtle diagenetic volume reductions. This might reinforce the diagenesis of volcanic ash as a strong candidate as the reaction is thought to potentially be associated with a smaller volume change than the Opal A/CT transformation. It was also demonstrated that the expression of the volume reduction was key, as also indicated in the single element testing of Chapter 4.
 - 3 A near-surface study was undertaken to demonstrate that the volume reduction is the key driver for polygonal fault formation. The motivation for this study was that in some cases the formation of faults appears to be very near surface, in a realm that is potentially incompatible with many reactions. Faults were shown to form within 50m of the sediment-water interface. The changes to material state resulted in an apparent overconsolidation, or increased strength, at shallow depths which arrested further consolidation.

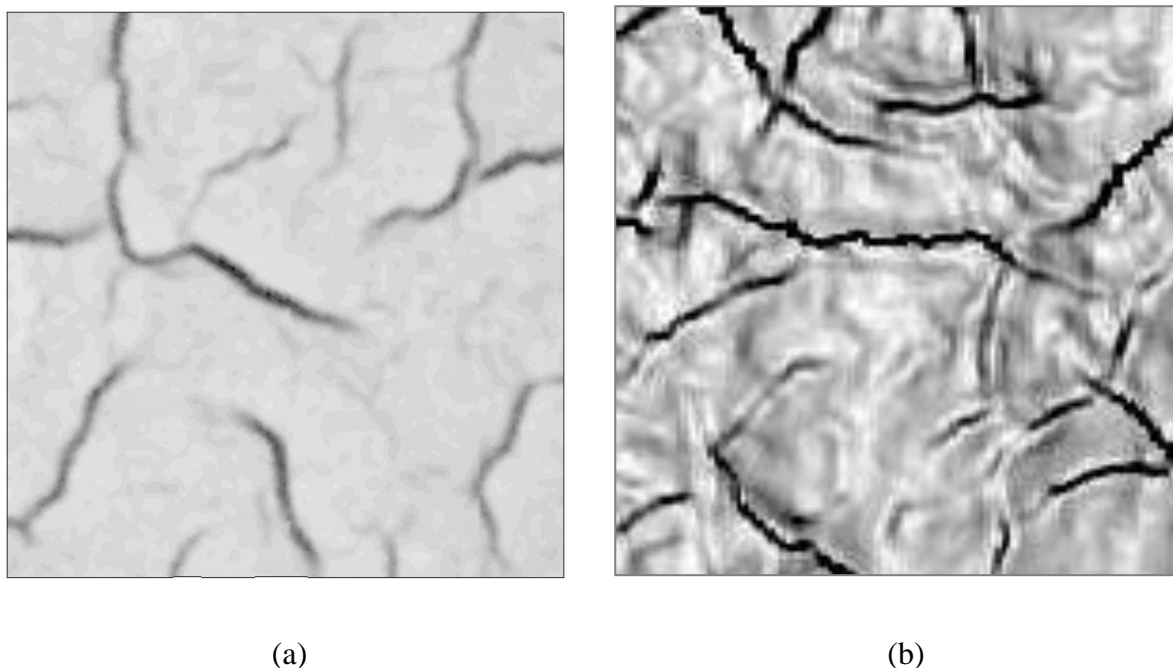


Figure 7-2: Results from Chapter 5 (a) Successful recovery of the polygonal planform geometry from 3D sensitivity study (b) coherence slice showing polygonal fault system in North Sea (used with permission from J. Cartwright). Note the strong resemblance between model output and an actual polygonal fault system.

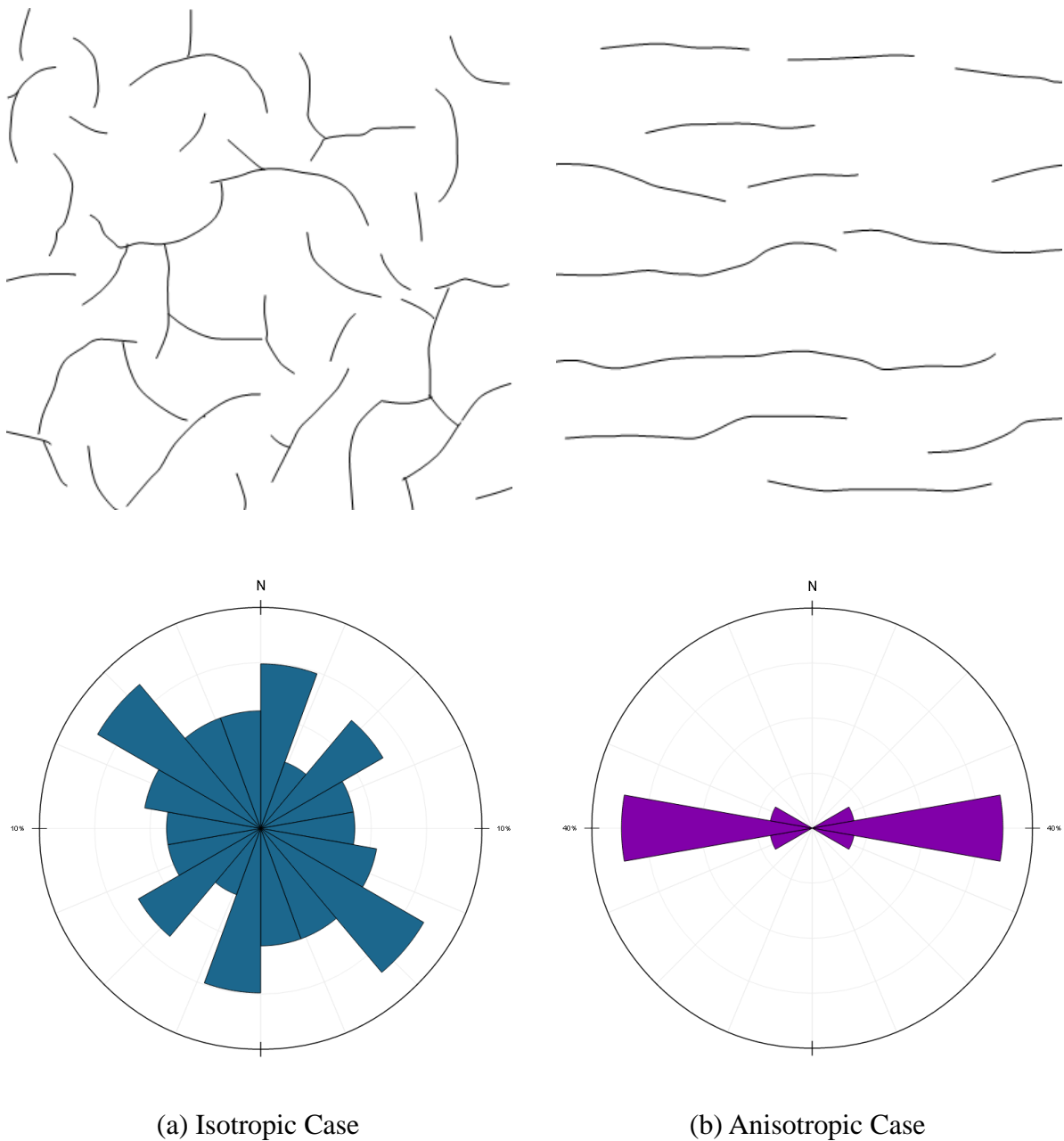
7.4 Chapter 6: Polygonal Fault Formation and Horizontally Anisotropic Stress States

The objective of Chapter 6 was to further develop the work of Chapters 4 and 5 in a study of the response of polygonal fault systems to regional horizontal stress anisotropy. The relationship between the planform geometry is well documented from a qualitative perspective, and faults are known to become polarised when in proximity to tectonic faults, slopes, diapirs and folds as a result of local perturbations of the regional stress field. Therefore, polygonal faults may be useful tools in assessment of paleostress magnitudes and orientations. To assess the influence of horizontal stress anisotropy, simple conceptual models were developed by modifying the 3D models of Chapter 5 and applying displacements to the model boundaries. A selection of the results presented in Chapter 6 are shown in Figure 7-3. The key discussion points made in this Chapter are;

- 1 Even for relatively small horizontal stress differences the changes to the planform geometry were quite pronounced, which reinforces the fact that polygonal faults are

extremely sensitive to very small amounts of horizontal stress anisotropy. In particular, fault azimuth changes considerably as the horizontal stress difference becomes more pronounced as shown in Figure 7-3(b). In this case the horizontal stress difference is just over 3% but over 80% of faults strike in the E-W direction.

- 2 The spacing of the faults does not significantly change with increasing horizontal stress anisotropy, and in all cases was observed to be varied. This result is perhaps expected as, for instance, the spacing of radial faults around many salt structures is similar to that of nearby polygonal faults; leading to the postulation that the radial faults are in fact polarised polygonal faults.
- 3 Fault intensity changes and the number of faults observed per unit area decreases as horizontal stress anisotropy increases. It is believed that this occurs because faults are restricted in the orientations they can assume and fault linkage is promoted, resulting in a smaller number of faults. This same reasoning is suggested for the observed general trend of increasing maximum fault length with increased horizontal stress anisotropy.



Horizontal stress difference of 0.01%

Horizontal stress difference of 3.05%

Figure 7-3: Results from Chapter 6 (a) Planform geometry and rose diagram for horizontally isotropic case (b) Planform geometry and rose diagram for horizontally anisotropic case (c-d) relationships between anisotropy and fault intensity and length respectively. The results indicate that even small differences in the magnitude of the horizontal stresses is sufficient to cause dramatic changes to the planform geometry, as displayed in the two rose diagrams. Note also the changes in the number and length of the faults.

7.5 Discussion

7.5.1 Diagenesis as a Trigger for Polygonal Fault Genesis

The favourable comparison between the single element testing in Chapter 4 and experimental studies (Shin et al., 2008) showed that despite the quite basic implementation, the modelling is able to capture some of the envisaged key physical impacts arising from diagenetic processes on sediment evolution. The nature of the reaction and the influence on the chemical flow rule was shown to also control the change in stress state. This is particularly significant as it indicates that the composition and fabric of the sediment are important, and that the diagenetic volume reduction might be expressed in a fundamentally different way to normal consolidation (Roberts et al., 2013).

Key observations demonstrated that fault throw and displacement was strongly controlled by the residual friction of the sediment as well as the presence of stiff and competent sand sequences, in good agreement with observations in the North Sea for example (Jackson et al., 2013, 2014). Collectively these observations may help to constrain the specific reactions and conditions that trigger faulting. Importantly, this has demonstrated that discounting the significance of residual friction (Gouly, 2008) is unwise as it almost certainly has a first order bearing on the evolution, if not genesis, of a polygonal fault system (Cartwright, 2011). Finally, the mechanical barrier provided by stiff sand sequences adds weight to the argument that many polygonal fault systems have stopped growing and are inactive (Cartwright et al., 2003).

7.5.2 The Influence of Early Diagenesis and Brittle-Ductile Transitions

The focus of this thesis has been on attempts to capture the response of clay rich sediments to mechanical and chemical changes during early burial. Perhaps the fundamental result contained within this work is the demonstration of the influence of an early brittle-ductile transition facilitated by diagenesis.

The diagenetic process modelled in Chapter 5 (and particularly in the sensitivity study) showed that a quick reaction rate relative to sedimentation resulted in a marked pseudo-overconsolidation and intersection of the yield surface on the dry side of critical state. This is a fundamental observation as it potentially provides a potential marker for evidence of post-sedimentation processes and is consistent with analysis from several polygonal fault systems and what is known of the behaviour of hemiplealgalic sediments at shallow depths (Hill and Marsters, 1990; Lee et al., 1990). Collectively, the models of Chapter 5 demonstrated that

potentially volume reducing mechanisms can operate over a range of depths and in all cases the horizontal stress reduction and change to the material state resulted in polygonal faulting. This agrees with the hypothesis that a range of reactions might provide suitable conditions for genesis of polygonal faults (Cartwright, 2011), which seems reasonable given the variability of tiers in terms of age, fault type e.g. linear, curvilinear (Carruthers, 2012), and host sediment composition.

The consequence of the change in material and stress state was localised shear failure even in K_0 conditions. It should be once again highlighted that the thermal gradient was quite high for the sensitivity study but was representative of regions like the Nankai trough. In other settings where polygonal faults are found at shallow depths the thermal gradient is likely to be far more modest. In reality other factors exert a control on transformation processes such as those studied e.g. pore fluid chemistry. The work of Tribble and Wilkens (1994) which studied the alteration of volcanic ash indicated that in fact this process is accentuated where there are depositional hiatuses and/or slow deposition rates, which are common in regions containing PFS (see Chapter 2). This is due to the more efficient exchange between pore waters and seawater. This therefore appears to be a reinforcement of the arguments presented here regarding the rates and contributions of mechanical and chemical processes. It is worth restating that the current implementation requires continuous deposition in order to further advance the diagenetic process. Future work could seek to investigate the limitations of this existing implementation.

The illustration of a complex evolution of stress and material state within this thesis highlights the potential danger in making inferences regarding the genetic mechanism for polygonal fault formation based on the present-day condition and behaviour of specimens. It is likely that due to secondary consolidation processes such as creep, dissolution and precipitation the nature of the sediment at the time of deposition and indeed at the time of fault formation may be markedly different. For example the high smectite content in some specimens is likely authigenic (Tribble and Wilkens, 1994; Cartwright, 2011) and the weakness associated with smectite rich specimens e.g. in the North Sea (Wensaas et al., 1998) perhaps reflects a diagenetically altered state rather than depositional state.

The recent work on the behaviour of smectite-rich mudrocks over large stress ranges that was discussed in Chapter 5 showed how the stress state changed as the sediment consolidated (Casey, 2014; Casey et al., 2014). These sediments exhibit similar behaviour to London Clay,

which is known to host polygonal fault networks in the North Sea. At shallow depths the re-sedimented samples exhibited a notably lower K_0 value which increased as the specimen was exposed to increasing stresses. Another curious aspect is that the angle of the critical state line is observed to change; it is higher at lower stresses but reduces with consolidation. Such an observation is also broadly in agreement with the brittle-ductile transition discussed here and, similarly, it explains the perhaps curious presence of localised faulting in comparatively weak sediments located in regions of low activity. It would also explain how the faults are able to nucleate at shallow depth but then accumulate throws of up to 100m at still relatively modest depths (Shin et al., 2010). Detailed experimental studies of lithologies known to host polygonal faults can be used for future constitutive model development (see Section 7.7.1).

7.5.3 Trigger Beds

An assumption has been made that the material within the polygonally faulted interval is essentially homogeneous. Whilst this is clearly a simplification, and noting that the models are deliberately conceptual, this does appear valid in some cases. For example the constant porosity of sediments noted in the Nankai Trough sediments indicates some degree of homogeneity. Furthermore, as discussed in the discussion of Chapter 5 the volcanic ash that is in various stages of alteration appears to be widely dispersed throughout the polygonally faulted (White et al., 2011), indicating that the whole tier is susceptible to diagenetic processes.

A preliminary exercise into the significance of 'trigger beds' that might act to nucleate deformation has been undertaken but is not included as part of this thesis. An interesting conclusion has so far shown that it is important for the diagenetically induced stress change to take place throughout the tier, as presented within the thesis, in order to allow for continued fault propagation. The only exception to this case is where a thin section which undergoes diagenetically-induced shear failure is bounded by extremely weak sediment. This weak sediment is presently modelled with a Mohr-Coulomb material model with significant reduction in cohesion, friction angle and dilatancy angle. This potentially suggests that only thin sections of the tier might be needed to undergo diagenetic shear failure but more research effort is required. Again, this might suggest a combination of mechanisms that includes diagenesis but also the weak nature and low residual strength of mudstones known to host polygonal faults.

7.5.4 Polygonal Faults and Paleostress Estimation

A potential workflow for estimating paleostress with polygonal faults was proposed using the observations made in Chapter 6. Whilst the derived relationships are encouraging and certainly compare favourably with trends noted in 3D seismic data, it is noted that other factors such as facies variation, tier thickness and the maturity of the fault system might facilitate non-mechanical changes to the planform geometry (Carruthers, 2012). Therefore, an appreciation of the regional stratigraphy, tier structure and regional structural evolution is considering pre-requisite for any exercise in estimating paleostress anisotropy. The extreme sensitivity of the polygonal fault orientation to even subtle horizontal stress anisotropy does perhaps mean that application in meaningful paleo-stress analyses may prove difficult.

7.6 Research Limitations

7.6.1 Subsurface Uncertainty and Validation

In any study, particularly one that is focused on modelling of complex physical processes, it is critical to be mindful of the assumptions and limitations of the output and interpretation.

The early genesis of polygonal faults and difficulties identifying them for analysis in the field means that conclusively establishing genetic mechanisms will likely always be difficult and therefore will be strongly debated. It is difficult to conclusively validate some of the conceptual arguments presented here. Where possible validation of the geomechanical argument has been attempted by comparison with seismic data or geomechanical testing. The assumption that material properties are essentially homogenous throughout the tier is likely unrealistic and there will undoubtedly be significant variations in constitutive behaviour on a variety of scales throughout the tier. For simplicity such issues have been ignored, and clearly there is a finite resolution that can be achieved given the scale of the faulting.

Recent studies in the Western Desert, Egypt have discovered what appears to be a PFS within the Cretaceous Khoman chalk (Tewksbury et al., 2011). Such outcrops might allow for detailed field investigation, although given the age and inferred pre-erosion depths of the Khoman chalk it seems possible that any signatures of the cause of the fault formation may have been overprinted, and it is debatable that the Khoman Chalk represents the level at which faulting was initiated. Regardless, analysis of field-analogues such as the Khoman Chalk PFS will certainly prove useful in constraining timing of fault formation through geochemical analysis (Cartwright, 2014; Tewksbury et al., 2014). Once this is firmly

established then this information can be used in geomechanical models such as those presented within this work in order to further constrain which mechanisms are physically reasonable.

The availability of high quality material data with which to populate both the mechanical and chemical parameters of the SR3 constitutive model is also limited. Where possible data has been sourced from the small number of publications and ODP wells that target the sediments known to host polygonal faults. It is stressed that high quality material data is difficult to source, and that the characterisations presented are of a standard that meets or exceeds those in many other publications with a similar focus (Nikolinakou et al., 2014; Thornton and Crook, 2014). Whilst there is confidence that the characterisations are reasonably representative of the sediments that they model a more focused drilling project with an emphasis on high quality geotechnical characterisation of sediments known to be polygonally faulted would be beneficial for continued geomechanical forward modelling work.

7.6.2 Complexity of Diagenetic Processes

Whilst the results presented have attempted to capture the mechanical-chemical behaviour of sediments during early burial, it is clear that such processes are extremely complex. Frequently, the reactions involve phase transformations and may feature mass transport over fairly large distances (Addis and Jones, 1985). Transient changes in pore-fluid composition may also occur, and the diagenetic boundary may not be regular over the entire basin leading to an element of differential compaction (Davies and Ireland, 2011).

Additional precipitation of cements associated with fairly small volume changes might serve to strengthen the rock substantially. All these factors suggest that over geological time the nature of diagenetic processes is invariably complicated and non-linear. It is very difficult however to constrain the exact individual contributions of these factors.

7.6.3 Use of Geomechanical Forward Modelling

The limitations of incorporating complicated diagenetic processes into the constitutive model has been explained in the preceding section. Regardless, the work presented here has indicated that geomechanical forward modelling is a new and potentially very exciting tool for exploring the genesis and development of polygonal faults. The adopted approach is considered state-of-the-art as it can deal with finite-strains and the material models have sufficient complexity to adequately address the constitutive response of the sediments.

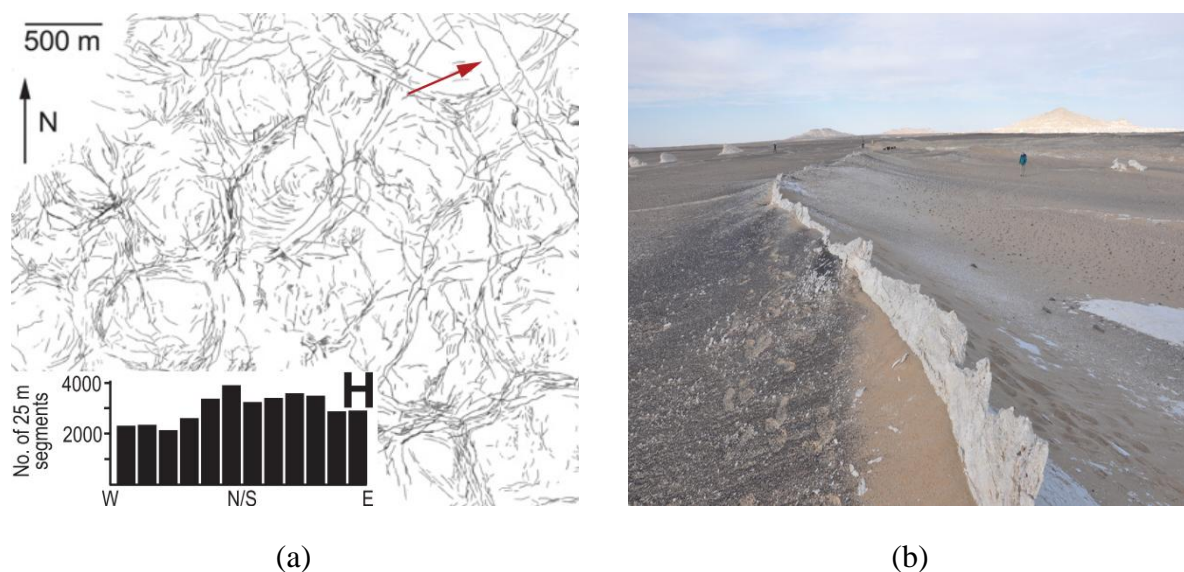


Figure 7-4: Inferred polygonal fault system in the exposed Khoman Chalk, Egypt (a) Detailed interpretation of planform geometry (Tewksbury et al., 2014), (b) Calcite fins indicate that at some point the faults were transmitting fluids and help to define the locations of faults. It is uncertain as to whether this indicates early dewatering or fluid migration after the faults had formed (Tewksbury et al., 2011).

However, as indicated in the previous chapters there are some disadvantages in adopting this approach. The most notable disadvantage is the attainable resolution. Networks of polygonal faults are observed over vast distances and individual fault traces can vary from between 100m to several kilometres. Therefore, as shown, reasonably large domains are required, but there must be sufficient resolution to capture the comparatively thin tiers and importantly the small throws that are observed. In two-dimensions fairly large domains can be treated quite easily with a fairly fine mesh, with most simulations generally having less than 300,000 finite elements. The extension to 3D and adoption of the ANV strain tetrahedral element dramatically increases the number of elements. Typically, the simulations adopted used between 3,000,000 and 25,000,000 elements even with a coarser mesh size. Whilst progress is continually being made on computational efficiency via parallel computing it is likely that there the computational time necessary will always impose restrictions on the size of domains that can be modelled.

7.7 Extension of the Study and Future Work

7.7.1 Alternative Mechanisms and Improved Constitutive Modelling

This study has focused on the diagenetic mechanism, whilst also acknowledging the

influence of residual friction, and other similar post-sedimentation processes such as creep. As highlighted previously, creep behaviour is strongly dependent on clay fraction. Reports of visco-plastic behaviour in sands is limited, and only observed where there is a discernible clay fraction. Sediments known to host polygonal faults are known to be sensitive to creep (D. Dewhurst, private communication) and the high clay fractions again supports this.

Therefore, whilst the parallels between diagenesis and creep have been acknowledged and explored in a limited sense, a more focused investigation of creep over paleo-time would be interesting. It is important to reiterate that extended creep testing is rare, and like diagenesis, over geological time it remains poorly understood. Furthermore, separating the influence of separate post-sedimentation processes may be difficult. The interest in fine-grained sediments for HLW disposal over extended timeframes does however mean that our understanding of such processes is continually expanding.

7.7.2 Influence of Overpressure and Contribution from Diagenesis

The work presented in Chapters 4, 5, and 6 has made the assumption that the sediments behave in a drained fashion. This effectively means that the sediment is loaded sufficiently slowly and the permeability is sufficiently high for the sediments to consolidate normally and pore pressures remain hydrostatic. It would appear that this is a reasonable assumption given that;

- 1 Polygonal fault systems are associated with sediments that have been deposited very slowly. Deposition rates that rarely exceed 100m/My (or 0.1mm/yr) and are frequently much lower than this as detailed in Chapter 2.
- 2 Polygonal faults are thought to form at shallow depths, where the sediment has quite high porosities. Therefore it is probable that the sediment has sufficient permeability to permit fluids to escape and to efficiently de-water.

However, as shown in Figure 7-5(a), sediment permeability is controlled by the fraction of clay size particles (Yang and Aplin, 2010). As sediments known to host polygonal faults are observed to contain high proportions of clay size particles (see Chapter 2) there is at least a possibility for sediments to become slightly overpressured. Furthermore, developed faults might act as fluid migration pathways and locally raise the pore-pressures around their growing upper-tips. This would act to reduce the effective mean stress in this zone and allow for easier fault propagation.

Such scenarios would make for interesting future work, and the framework for such investigations is already developed and has been utilised in the study of the formation of an overpressured anticline (Rance et al., 2013) and deepwater fold and thrust belts (Thornton and Crook, 2014). Such procedures are more complex, and necessitate a good appreciation of the physics of mechanical-seepage problems. For example, the mechanical response is governed by the momentum balance equation in Equation 7-1 and stipulates that the divergence of the effective stresses must be balanced by the body forces for equilibrium to be maintained. Equation 7-2 represents the equation for single phase Darcy flow. The solution procedure adopted within ELFEN is staggered, such that the pore pressure is implicitly evaluated at a set number of timesteps in the seepage code and then passed to the mechanical code. Updated topology and material state is then passed back to the seepage code and the process continues.

As clearly shown by Equations 7-1 and 7-2, and reinforced by Figure 7-5(b), the coupling is therefore strong in an algorithmic sense as the fluid pressure defines the effective stress calculated in the mechanical field. The volume strain rate that is passed to the seepage code is dependent on the effective stress and the fluid pressure and the resulting pore fluid pressure is dependent on the volumetric strain rate. The importance of the rate of loading is represented by the volume strain rate term. Equation 7-3 demonstrates that the total volume strain rate may be additively decomposed into the contributions from elastic, plastic, creep, chemical and elastic thermal strains respectively.

$$\mathbf{L}^T (\boldsymbol{\sigma}' - \alpha(\phi) \mathbf{m} p_f) + \rho_b \mathbf{g} = 0 \quad 7-1$$

$$\underbrace{\text{div} \left(\frac{\mathbf{k}(\phi)}{\mu_f(T)} (\nabla p_f - \rho_f(T) \mathbf{g}) \right)}_{\text{Permeability}} = \underbrace{\left(\frac{\phi}{K_f} + \frac{(\alpha(\phi) - \phi)}{K_s} \right)}_{\text{Storativity}} \frac{\partial p_f}{\partial t} - \underbrace{\left(\alpha \frac{\partial \varepsilon_v}{\partial t} \right)}_{\text{Volume strain rate}} \quad 7-2$$

$$\Delta \varepsilon_v = \Delta \varepsilon_e + \Delta \varepsilon_{mech}^p + \Delta \varepsilon_{mech}^c + \Delta \varepsilon_{chem}^c + \Delta \varepsilon^T \quad 7-3$$

This leads to the interesting and developing topic of chemically induced overpressure, as the volume change due to diagenesis will ultimately contribute to the generation of pore pressures greater than hydrostatic. This occurs because of the dominant influence of the volume strain rate term on overpressure generation. An example of such a scenario is discussed by Nordgård Bolås et al., (2008), where it is suggested that the observed

overpressures in Jurassic sandstones result from diagenetic processes. The framework within ELFEN has been used to investigate this previously and is shown in Figure 7-5(c) and (d). It is clear that both the modelled porosity depth trend and the magnitude of overpressures are both in good agreement with published data.

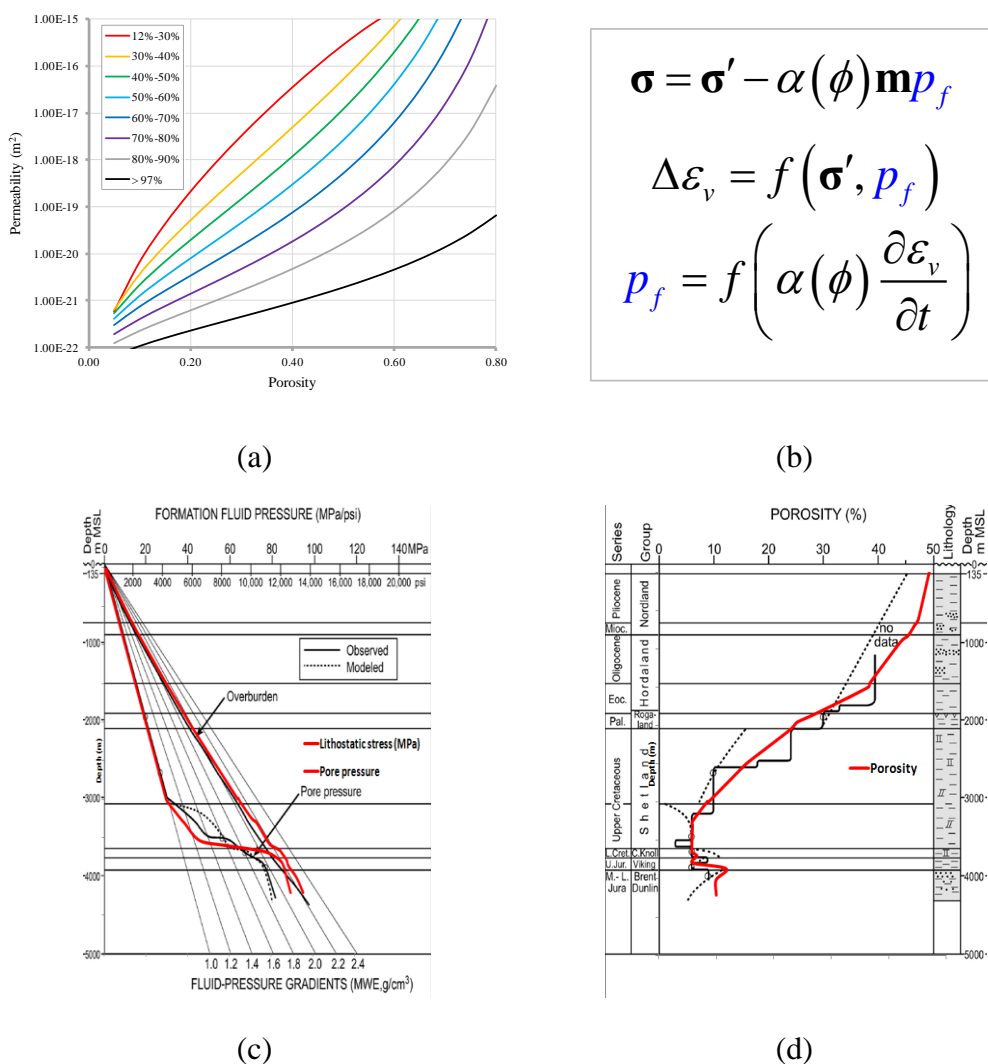


Figure 7-5: Concepts of a proposed future coupled study (a) Dependency of mudstone and claystone permeability on clay fraction, modified after Yang and Aplin, (2010) (b) Strong algorithmic coupling between mechanical and seepage fields (c, d) Previous utilisation of chemical compaction laws to investigate chemically induced overpressures in Jurassic sandstones, North Sea (Crook, 2010).

Whilst such studies offer much potential insight into non-mechanical overpressure generation, it is stressed that the relationship between mechanical and chemical behaviour is likely to be more strongly coupled than realised in previous studies, or indeed within this thesis. This is

highlighted in several publications, e.g. Goultly et al., (2012), where it is suggested that porosity loss from dissolution might lead to overpressure generation, but further porosity loss might be inhibited by the increasing contribution from the pore fluid.

With consideration of the results of Chapter 5, the modelled fault planes had dips of between 40° and 50°. This is certainly in agreement with some polygonal fault systems however there are many cases, particularly where the system has not been buried deeply, in which the fault dip is very steep and in the range 60° to 80°. This could possibly be explained by a combination of mechanisms and the volume reducing process also leading to overpressure generation. This would act to reduce the effective mean stress and change where the stress path intersects the state boundary surface, as shown in Figure 7-6. Intersection of the yield surface at low effective mean stress is often associated with highly extensional plastic flow with near axial splitting (jointing) and/or high angle shear bands (Kato, 2010).

7.7.3 A Unified Study Incorporating Explicit Modelling of Salt Diapir Growth

Chapter 6 highlighted that the polarisation of the polygonal planform geometry has been recognised for some time, particularly where salt structures are inferred to be the cause. An aim of this study was to begin developing methods to use the planform geometry to quantify horizontal paleo-stress magnitudes and orientations. This was achieved in Chapter 6 by using the modelling tools with simple boundary conditions to understand how local and regional compression alters the planform geometry. A natural extension of the work presented in this thesis would be to develop models where the salt structure is modelled explicitly (Thornton et al., 2011) using an appropriate visco-plastic constitutive law (Dawson and Munson, 1983; Munson, 1997; Fredrich et al., 2007).

The stress perturbation around salt structures has been studied for some time and explored by allowing relaxation of visco-elastic salt and studying how this changes the stresses in adjacent sediments (Koupriantchik et al., 2004; Luo et al., 2011; Nikolinakou, 2011). Recent work has used *ELFEN* to understand how stresses may evolve as diapirs grow (Nikolinakou et al., 2014). It would be interesting to explore the relationship between modes of diapir growth and the distance of the transition boundary. This might help to distinguish between whether the relaxation of the salt onto adjacent overburden due to the inability of the salt to sustain deviatoric stresses or arching of the overburden exerts the biggest control on the distance from the diapir to the transition boundary. Such a study would likely require a large domain and therefore potentially a significant number of finite elements. Whilst large

numbers of elements can be treated as noted in section 6.2, it is important to stress that a large amount of computational time in this case may be spent dealing with excessive element distortion and remeshing the problem domain.

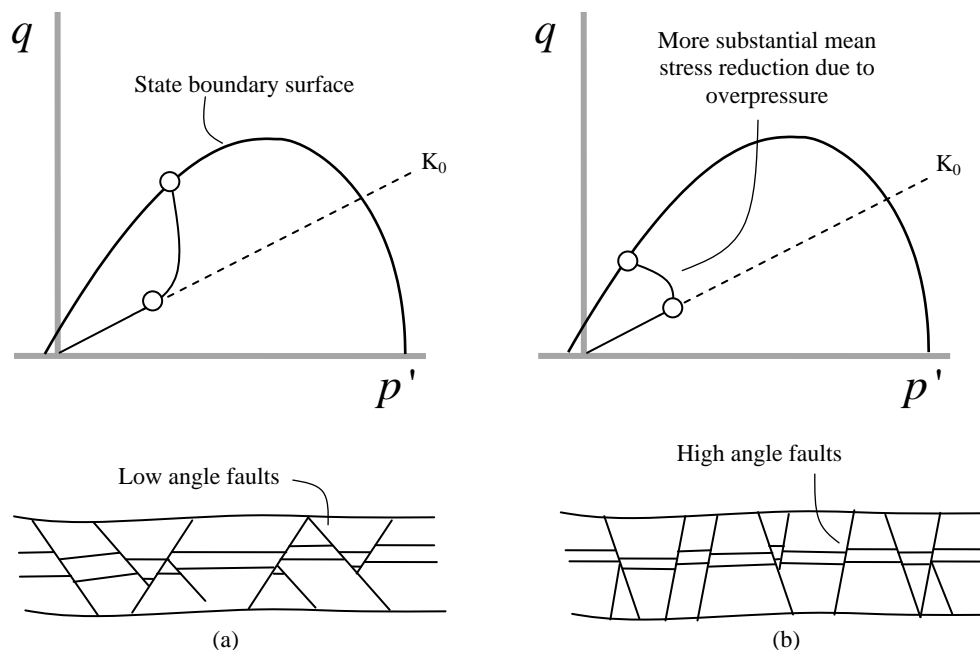


Figure 7-6: Potential stress paths and faulting style for (a) diagenetically induced shear failure with hydrostatic pore pressure (b) diagenetically induced shear failure with development of overpressure.

7.8 Closing Comments

Polygonal faults are unique in that the scale over which they are consistently observed is far beyond any other conventional fault type, and despite extensive study they remain relatively poorly understood. Echoing comments recently made by Jackson et al., (2013) it is stressed that these faults are not just an academic curiosity; understanding polygonal faults is key for several areas related to the role of fine-grained sediments in hydrocarbon exploration. Geomechanical forward modelling offers insight into what conditions are suitable for genesis and growth of these faults. This research project is the first known that attempts to study the evolution of these faults with sophisticated geomechanical forward modelling tools.

As suggested by Cartwright (2014), the key to unlocking the mysteries of polygonal fault systems lies with multidisciplinary approaches which incorporate field based study, 3D seismic data and detailed geochemical analysis. This work hopefully demonstrates that

geomechanical modelling can also form part of this collective approach. The successful development of polygonal faults arising naturally from the models has been shown, which was identified as the key objective in the introductory chapter. This adds weight to the diagenetic argument although the parallels between this and other volume reducing models was discussed. This work also demonstrates a fundamental but often overlooked truth; the evolution of sediments is invariably complex and frequently the influence of post-sedimentation processes is frequently not accorded sufficient importance. In the fine-grained, chemically active sediments studied here it is argued that such processes may exert more control on behaviour than increasing burial stresses. The influence of diagenesis on sediment behaviour and overpressure is an emerging and rapidly developing field, of which this thesis is part, and as highlighted there is significant scope for the study to be extended into a number of directions in future.

7.9 References

- Addis, M. A., and M. E. Jones, 1985, Volume changes during diagenesis: Marine and Petroleum Geology, v. 2, no. March, p. 241–246.
- Carruthers, T. D., 2012, Interaction of polygonal fault systems with salt diapirs: Unpublished PhD Thesis - Cardiff University, p. 526.
- Cartwright, J., 2014, Are outcrop studies the key to understanding the origins of polygonal fault systems?: Geology, v. 42, no. 6, p. 559–560.
- Cartwright, J. A., 2011, Diagenetically induced shear failure of fine-grained sediments and the development of polygonal fault systems, *in* Marine and Petroleum Geology: Elsevier Ltd, p. 1593–1610.
- Cartwright, J. A., D. James, and A. Bolton, 2003, The genesis of polygonal fault systems: a review: Geological Society, London, Special Publications, v. 216, no. 1, p. 223–243.
- Casey, B., 2014, The Consolidation and Strength Behavior of Mechanically Compressed-Fine Grained Sediments: Unpublished PhD Thesis - Massachusetts Institute of Technology, p. 259.
- Casey, B., B. P. Fahy, P. B. Flemings, and J. T. Germaine, 2014, Shear Strength of Two Gulf of Mexico Mudrocks and a Comparison with Other Sediments, *in* Fourth EAGE Shale Workshop. Shales: What do they have in common?
- Crook, A. J. L., 2010, Supplementary Compaction for Geological Applications: 87 p.
- Davies, R. J., and M. T. Ireland, 2011, Initiation and propagation of polygonal fault arrays by thermally triggered volume reduction reactions in siliceous sediment: Marine Geology, v. 289, no. 1-4, p. 150–158.
- Dawson, P. R., and D. . Munson, 1983, Numerical Simulation of Creep Deformations Around a Room in a Deep Potash Mine *: International Journal of Rock Mechanics and Mining Sciences & Geomechanics Abstracts, v. 20, no. 1.
- Fredrich, J., A. Fossum, and R. Hickman, 2007, Mineralogy of deepwater Gulf of Mexico salt formations and implications for constitutive behavior: Journal of Petroleum Science and Engineering, v. 57, no. 3-4, p. 354–374.
- Goult, N. R., 2008, Geomechanics of polygonal fault systems: a review: Petroleum Geoscience, v. 14, no. 4, p. 389–397.
- Goult, N. R., A. M. Ramdhan, and S. J. Jones, 2012, Chemical compaction of mudrocks in the presences of overpressure: Petroleum Geoscience, v. 18, p. 471–479.

-
- Hill, P. R., and J. C. Marsters, 1990, 41. Controls on physical properties of Peru continental margin sediments and their relationship to deformation styles, *in* Proceedings of the Ocean Drilling Program, Scientific Results, Vol. 112: p. 623–632.
- Jackson, C. A. L., D. Carruthers, S. N. Mahlo, and O. Briggs, 2014, Can polygonal faults help locate deepwater reservoirs?: AAPG Bulletin, no. May, doi:10.1306/03131413104.
- Jackson, C. A.-L., S. N. Mahlo, O. Briggs, and T. D. Carruthers, 2013, Role of Polygonal Fault Mapping in De-risking Deepwater Reservoir Presence: A 3-D Seismic Reflection Case Study from Offshore Norway, *in* AAPG Annual Convention and Exhibition, Pittsburgh, Pennsylvania.
- Kato, J., 2010, Computational Strategies for Predicting Localisations in Forward Modelling of Geological Structures: Unpublished PhD Thesis - Swansea University.
- Koupriantchik, D., S. P. Hunt, P. J. Boulton, and A. G. Meyers, 2004, Geomechanical modelling of salt diapirs : 3D salt structure from the Officer Basin , South Australia: Science And Technology.
- Lee, H. J., R. E. Kayen, and W. G. McArthur, 1990, 43. Consolidation, triaxial shear-strength, and index-property characteristics of organic-rich sediment from the Peru continental margin: Results from leg 112, *in* Proceedings of the Ocean Drilling Program, Scientific Results, Vol. 112: p. 639–651.
- Luo, G., M. A. Nikolinakou, P. B. Flemings, and M. R. Hudec, 2011, Geomechanical modeling of stresses adjacent to salt bodies : 1 . Uncoupled models.
- Munson, D. ., 1997, Constitutive Model of Creep in Rock Salt Applied to Underground Room Closure: International Journal of Rock Mechanics and Mining Sciences & Geomechanics Abstracts, v. 34, no. 2, p. 233–247.
- Neagu, R. C., J. A. Cartwright, and R. J. Davies, 2010, Measurement of diagenetic compaction strain from quantitative analysis of fault plane dip: Journal of Structural Geology, v. 32, no. 5, p. 641–655.
- Nikolinakou, M. A., 2011, Geomechanical Modeling of Stresses Adjacent to Salt Bodies : 2 . Poro-Elasto-Plasticity and Coupled Overpressures: AAPG Bulletin.
- Nikolinakou, M. A., P. B. Flemings, and M. R. Hudec, 2014, Modeling stress evolution around a rising salt diapir: Marine and Petroleum Geology, v. 51, p. 230–238.
- Nordgård Bolås, H. M., C. Hermanrud, T. A. Schutter, and G. M. Grimsmo Teige, 2008, Is stress-insensitive chemical compaction responsible for high overpressures in deeply buried North Sea chalks?: Marine and Petroleum Geology, v. 25, no. 7, p. 565–587.

-
- Rance, J. M., M. L. Profit, S. J. Dee, and D. T. Roberts, 2013, Predicting the Paleo Evolution of Overpressured Geological Structures, *in* 47th ARMA Rock Mechanics and Geomechanics Symposium, San Francisco, California.
- Roberts, D. T., A. J. L. Crook, M. L. Profit, J. M. Rance, and J. A. Cartwright, 2013, Geomechanical Forward Modelling of the Genesis of Polygonal Fault Systems, *in* 1st EAGE Workshop on Geomechanics and Energy.
- Shin, H., J. C. Santamarina, and J. A. Cartwright, 2008, Contraction-driven shear failure in compacting uncemented sediments: *Geology*, v. 36, no. 12, p. 931.
- Shin, H., J. C. Santamarina, and J. A. Cartwright, 2010, Displacement field in contraction-driven faults: *Journal of Geophysical Research*, v. 115, no. B7, p. B07408.
- Sonnenberg, S. A., and D. Underwood, 2012, Polygonal fault systems: A new structural style for the Niobrara formation, Denver Basin, Colorado, *in* AAPG Annual Convention and Exhibition, Long Beach, California.
- Tewksbury, B. J., J. P. Hogan, S. a. Kattenhorn, C. J. Mehrtens, and E. a. Tarabees, 2014, Polygonal faults in chalk: Insights from extensive exposures of the Khoman Formation, Western Desert, Egypt: *Geology*, v. 42, no. 6, p. 479–482.
- Tewksbury, B., S. Kattenhorn, C. Sayler, C. Tewksbury-Christle, and D. Saint-Jacques, 2011, Polygonal patterns and desert eyes: Reconnaissance satellite image study of fold and fault structures in Late Cretaceous and Early Tertiary Limestones of the Western Desert, Egypt, *in* Geological Society of America Conference, Minneapolis, MN, USA.
- Thornton, D. A., and A. J. L. Crook, 2014, Predictive Modeling of the Evolution of Fault Structure: 3-D Modeling and Coupled Geomechanical/Flow Simulation: *Rock Mechanics and Rock Engineering*.
- Thornton, D. A., D. T. Roberts, A. J. L. Crook, and J. G. Yu, 2011, Regional-Scale Salt Tectonics Modelling: Bench-Scale Validation and Extension to Field-Scale Predictions, *in* Geological Society of America Conference.
- Tribble, J. S., and R. O. Y. H. Wilkens, 1994, Microfabric of Altered Ash Layers, ODP Leg 131, Nankai Trough: *Clays and Clay Minerals*, v. 42, no. 4, p. 428–436.
- Wensaas, L., P. Aagaard, T. Berre, and E. Roaldset, 1998, Mechanical properties of North Sea Tertiary mudrocks " investigations by triaxial testing of side-wall cores: *Clay Minerals*, v. 33, p. 171–183.
- White, R. J., G. A. Spinelli, P. S. Mozley, and N. W. Dunbar, 2011, Importance of volcanic glass alteration to sediment stabilization: offshore Japan: *Sedimentology*, v. 58, no. 5, p. 1138–1154.
- Yang, Y., and A. C. Aplin, 2010, A permeability–porosity relationship for mudstones: *Marine and Petroleum Geology*, v. 27, no. 8, p. 1692–1697.

Appendix

QUASI-STATIC EXPLICIT ADAPTIVE FINITE ELEMENT FRAMEWORK AND APPLICATION TO PROBLEMS IN STRUCTURAL GEOLOGY

Explicit treatment of quasi-static problems is advantageous for studying the forward modelling of geological structures on a large scale as;

- An explicit algorithm is fairly straightforward to implement (Gray et al., 2014) compared to an implicit approach.
- It is easy to implement for parallel processing and therefore well suited for the efficient solution of computationally large problems (Thornton and Crook, 2014).
- It may be applied to problems that are inherently unstable.
- Extremely large strains or topology changes may be readily accommodated (Peric and Crook, 2004).

This Appendix contains a brief overview of the explicit solution of the finite element governing equations with direct application to the evolution of geological structures. The location of the code modifications made in Chapter 4 is also highlighted.

Explicit Finite Element Framework

Governing Equations and Semi-Discretisation by Finite Elements

Consider a deformable body, Ω with boundary, $\partial\Omega$ in the spatial configuration as shown in Figure A-1. Applied loads are equivalent to resultant inertial forces according to *Newton's second law of motion*, giving,

$$\int_{\partial\Omega} \mathbf{t}dA + \int_{\Omega} \rho \mathbf{b}dV = \int_{\Omega} \rho \ddot{\mathbf{u}}dV \quad \text{A-1}$$

where \mathbf{t} is a traction vector of force per unit area acting on the boundary $\partial\Omega$, \mathbf{b} is a vector field of body force per unit mass, ρ is the current material density, dA is a differential surface area, dV is a differential volume and \mathbf{u} is the displacement vector field.

Using Gauss theorem, the first part of Equation A-1 can also be expressed as a volume integral;

$$\int_{\Omega} \nabla \cdot \boldsymbol{\sigma} dV + \int_{\Omega} \rho \mathbf{b} dV = \int_{\Omega} \rho \ddot{\mathbf{u}} dV \quad \text{A-2}$$

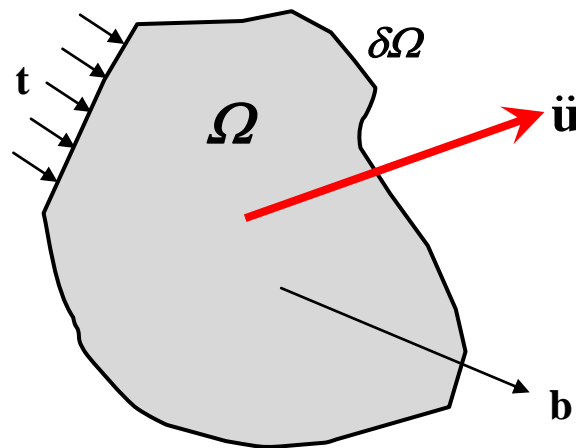


Figure A-1: The conservation of momentum balance.

Invoking the Principle of Virtual Work allows for the strong form of Equation A-2 to be recast into a weak form that is more suitable for discretisation by finite elements. This is achieved by considering the influence of an arbitrary fictitious velocity increment, $\delta \mathbf{v}$ on the body in Figure A-1;

$$\delta W = \int_{\Omega} \rho \ddot{\mathbf{u}} \cdot \delta \mathbf{v} dV + \left(\int_{\Omega} \boldsymbol{\sigma} : \delta \mathbf{d} dV - \int_{\delta\Omega} \mathbf{t} \cdot \delta \mathbf{v} dA \right) - \int_{\Omega} \rho \mathbf{b} \cdot \delta \mathbf{v} dV = 0 \quad \text{A-3}$$

Where $\delta \mathbf{d}$ is a virtual increment of the rate of deformation tensor, \mathbf{d} – see Bonet and Wood, 2008 for more detail on work conjugacy between nonlinear stress and strain tensors. The terms on the right hand side of Equation A-3 represent the inertial, internal and external work terms respectively;

$$\delta W = \delta W^{inert} + \delta W^{int} - \delta W^{ext} = 0 \quad \text{A-4}$$

The spatial discretisation of a system expresses the local equilibrium equations in terms of a finite number of degrees of freedom. The degrees of freedom are realised at discrete points

within a continuum known as nodes, the connectivity of these nodes defines finite polygonal volumes known as elements. The 3D continuum domain is now expressed as the summation of the elements within the domain;

$$\Omega \cong \sum_{e=1}^{nelem} {}^e\Omega \quad \mathbf{A-5}$$

The variation of nodal quantities within an element is defined by polynomial functions known as interpolation or shape functions, N_i . Shape functions are usually defined with respect to a natural coordinate system resulting in an isoparametric description (Zienkiewicz and Taylor, 2005; Zienkiewicz et al., 2005). The mapping from the natural coordinate system to the global coordinate system is defined by the Jacobian. It is required that shape functions ensure continuity of the nodal displacements. The element displacements and velocities may respectively be written using the shape functions as;

$${}^e\mathbf{u}(t) \cong \sum_{i=1}^{nnode} N_i {}^e\mathbf{u}_i(t) = \sum_{i=1}^{nnode} N_i \begin{bmatrix} \mathbf{u}_{x_i}(t) \\ \mathbf{u}_{y_i}(t) \\ \mathbf{u}_{z_i}(t) \end{bmatrix} \quad \mathbf{A-6}$$

$${}^e\mathbf{v}(t) \cong \sum_{i=1}^{nnode} N_i {}^e\mathbf{v}_i(t) = \sum_{i=1}^{nnode} N_i \begin{bmatrix} \mathbf{v}_{x_i}(t) \\ \mathbf{v}_{y_i}(t) \\ \mathbf{v}_{z_i}(t) \end{bmatrix}$$

Clearly the spatial distribution of nodes and the order of shape functions determines the ability of a discretisation to resolve a system response i.e. the accuracy is dependent on the fineness of the finite element mesh and the order of the shape functions – low order elements and coarse meshes are less computationally expensive but are also less accurate. The work terms of Equation A-4 may now be written using the shape functions;

$$\begin{aligned}
\delta W^{inert} &= \int_{\Omega} \rho \ddot{\mathbf{u}} \cdot \delta \mathbf{v} dV \\
&\cong \sum_{e=1}^{nelem} \int_{e\Omega} \rho \left(\sum_{i=1}^{nnode} N_i {}^e \ddot{\mathbf{u}}_i \right) \cdot \left(\sum_{i=1}^{nnode} N_i {}^e \delta \mathbf{v}_i \right) dV \\
&\cong \sum_{e=1}^{nelem} \sum_{i=1}^{nnode} {}^e \delta \mathbf{v}_i \cdot \int_{e\Omega} \rho N_i^T [N_1, N_2, \dots, N_{nnode}] [{}^e \ddot{\mathbf{u}}_1^T, {}^e \ddot{\mathbf{u}}_2^T, \dots, {}^e \ddot{\mathbf{u}}_{nnode}^T]^T dV \\
&\cong \sum_{e=1}^{nelem} \sum_{i=1}^{nnode} {}^e \delta \mathbf{v}_i \cdot \mathbf{f}_i^{inert}
\end{aligned}$$

$$\begin{aligned}
\delta W^{int} &= \int_{\Omega} \boldsymbol{\sigma} : \delta \mathbf{d} dV \equiv \int_V \boldsymbol{\sigma} : \delta \mathbf{l} dV \\
&\cong \sum_{e=1}^{nelem} \int_{e\Omega} \boldsymbol{\sigma} : \left(\sum_{i=1}^{nnode} {}^e \delta \mathbf{v}_i \otimes \nabla_x N_i \right) dV \\
&\cong \sum_{e=1}^{nelem} \sum_{i=1}^{nnode} {}^e \delta \mathbf{v}_i \cdot \int_{e\Omega} \boldsymbol{\sigma} \nabla_x N_i dV \\
&\cong \sum_{e=1}^{nelem} \sum_{i=1}^{nnode} {}^e \delta \mathbf{v}_i \cdot \mathbf{f}_i^{int}
\end{aligned}$$

A-7

$$\begin{aligned}
\delta W^{ext} &= \int_{\partial\Omega} \mathbf{t} \cdot \delta \mathbf{v} dA + \int_{\Omega} \rho \mathbf{b} \cdot \delta \mathbf{v} dV \\
&\cong \sum_{e=1}^{nelem} \int_{e\partial\Omega} \mathbf{t} \cdot \left(\sum_{i=1}^{nnode} N_i {}^e \delta \mathbf{v}_i \right) dA + \sum_{e=1}^{nelem} \int_{e\Omega} \rho \mathbf{b} \cdot \left(\sum_{i=1}^{nnode} N_i {}^e \delta \mathbf{v}_i \right) dV \\
&\cong \sum_{e=1}^{nelem} \sum_{i=1}^{nnode} {}^e \delta \mathbf{v}_i \cdot \left(\int_{e\partial\Omega} N_i \mathbf{t} dA + \int_{e\Omega} N_i \rho \mathbf{b} dV \right) \\
&\cong \sum_{e=1}^{nelem} \sum_{i=1}^{nnode} {}^e \delta \mathbf{v}_i \cdot \mathbf{f}_i^{ext}
\end{aligned}$$

Therefore, by considering the arbitrary choice of a virtual velocity increment;

$$\delta W \cong \sum_{e=1}^{nelem} \sum_{i=1}^{nnode} {}^e \delta \mathbf{v}_i \cdot \left(\mathbf{f}_i^{inert} + \mathbf{f}_i^{int} - \mathbf{f}_i^{ext} \right) \equiv \sum_{e=1}^{nelem} \sum_{i=1}^{nnode} \left(\mathbf{f}_i^{inert} + \mathbf{f}_i^{int} - \mathbf{f}_i^{ext} \right) = 0 \quad \text{A-8}$$

We have now assembled a system of ordinary differential equations that are second order in time. This spatial discretisation process provides the semi-discretised finite element equations that render the entire system as a function of time dependent nodal displacement vector \mathbf{u} ,

$$\mathbf{f}^{ext}(\mathbf{u}(t)) - \mathbf{f}^{int}(\mathbf{u}(t)) = \mathbf{M}\ddot{\mathbf{u}}(t) \quad \mathbf{A-9}$$

where \mathbf{M} is the consistent mass matrix, $\ddot{\mathbf{u}}$ is the global acceleration vector (second time derivative of the displacement vector \mathbf{u}). The global *external load vector* \mathbf{f}^{ext} represents the nodal forces arising from body loads and tractions on the boundary. The global *internal load vector* \mathbf{f}^{int} represents the forces arising from the constitutive response.

Central Difference Time Integration

The preferred approach for advancing the solution in time is the so called *central difference* method, which is popular in explicit computational mechanics (Belytschko et al., 2014). The approach firstly evaluates the internal and external forces at time t subject to the imposed initial and boundary conditions. At $t=0$ the initial stresses, boundary displacements and state variables must be initialised.

$${}^t\mathbf{f}^{ext} = \mathbf{f}^{ext}(t), \quad {}^t\mathbf{f}^{ext} = \mathbf{f}^{ext}(t, \mathbf{u}) \quad \mathbf{A-10}$$

The acceleration at time t may be evaluated as;

$${}^t\ddot{\mathbf{u}} = \mathbf{M}^{-1}({}^t\mathbf{f}^{ext} - {}^t\mathbf{f}^{int}) \quad \mathbf{A-11}$$

This implies an inversion of the global mass matrix is required, which is a computationally expensive task. Consequently, the mass and damping (if required) matrices are defined as diagonal matrices by the process of ‘mass lumping’, which effectively assigns fractions of the mass to each element node. This allows the equations to be integrated as single degree of freedom equations at each node i ;

$$\ddot{u}_i = \frac{1}{M_i} (f_i^{ext} - f_i^{int}) \quad \mathbf{A-12}$$

So the assembled diagonal mass matrix \mathbf{M} may be written as (Klerck, 2000);

$$\mathbf{M} = \mathbf{A} \sum_{e=1}^{nelem} \sum_{i=1}^{nnode} \sum_{j=1}^{nnode} \int_{eV} {}^e\rho \mathbf{N}_i^T [\mathbf{N}_1, \mathbf{N}_2, \dots, \mathbf{N}_{nnode}] \delta_{ij} dV \equiv \mathbf{A} \sum_{e=1}^{nelem} \sum_{i=1}^{nnode} \sum_{j=1}^{nnode} \int_{eV} \frac{{}^e\rho \delta_{ij}}{nnode} dV \quad \mathbf{A-13}$$

The acceleration nodal vector may then be used in evaluation of the velocity at the midpoint;

$${}^{t+\Delta t/2}\dot{\mathbf{u}} = {}^{t-\Delta t/2}\dot{\mathbf{u}} + {}^t\ddot{\mathbf{u}}\Delta t_m \quad \mathbf{A-14}$$

The displacement nodal vector at the new timestep are given by;

$${}^{t+\Delta t}\mathbf{u} = {}^t\mathbf{u} + {}^{t+\Delta t/2}\dot{\mathbf{u}}\Delta t \quad \mathbf{A-15}$$

Finally, coordinate nodal vector at the new timestep are evaluated as;

$${}^{t+\Delta t}\mathbf{x} = {}^t\mathbf{x} + {}^{t+\Delta t/2}\dot{\mathbf{u}}\Delta t \quad \mathbf{A-16}$$

Now the displacements and spatial position of each node in the domain have been evaluated at the new timestep. The internal force vectors are updated at this stage based on the constitutive response, and the energy balance is evaluated. The influence of irrecoverable deformation, which is not known a priori, is made post-solution. It is at this stage that the material stress update (Chapter 3) and subsequent chemical compaction stress update (Chapter 4) are made. The energies are then re-evaluated to factor energy dissipated from the system through plasticity.

By setting $t + \Delta t \rightarrow t$ the steps outlined can be repeated and the solution can continue to progress through time until the analysis is completed. The time integration is summarised in Figure A-2. This approach, in combination with diagonal mass matrices, means that the time integration of the discretised momentum equations does not require the exact solution of any governing equations.

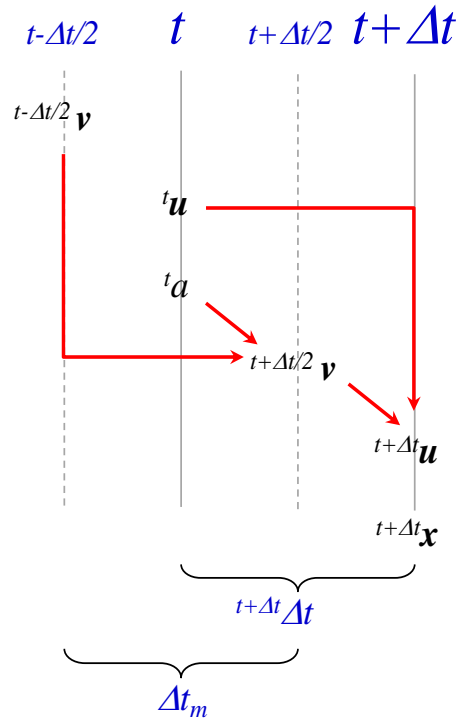


Figure A-2: Central difference integration scheme.

Stability Considerations and Mass Scaling

An issue with adoption of the central difference integration scheme is that it is only conditionally stable. The critical timestep, Δt_{crit}^e , for a single finite element is dependent on factors such as the element formulation, damping etc, but may be approximated as;

$$\Delta t_{crit}^e = \left| \frac{l^e}{c^e} \right|, \text{ with } c^e \approx \sqrt{\frac{E^e}{\rho^e}} \quad \mathbf{A-17}$$

where l^e represents the element characteristic length, c^e is the wave speed propagating through the element, and ρ^e is the element density. Consideration of the entire system of equilibrium equations therefore returns n critical timesteps, which for an unstructured mesh are usually unequal. Therefore, the critical timestep is evaluated as;

$$\Delta t_{crit} = \min \left| l^e \sqrt{\frac{\rho^e}{E^e}} \right| \quad \mathbf{A-18}$$

This ensures that the smallest timestep of any element in the domain is adopted to ensure that stability is maintained. With specific consideration to modelling the evolution of sediments over geological time it is clear that as the sediment consolidates it will become both stiffer and denser, and hence the timestep will gradually reduce over the analysis. The loss of volume would also reduce the element characteristic length, though this can be remedied to an extent via adaptivity. Loading in the context of geological structure evolution represents deposition and/or basal and tectonic movement over millions of years. As the application of the loading is therefore very slow, the problem is classed as *quasi-static*. As such, the contribution from the inertial forces can essentially be neglected and the mass matrix may be optimised in order to obtain a solution in the desired number of timesteps. Importantly, this type of mass scaling does not affect the self-weight. Where a small number of small finite elements control the timestep, these may also be scaled more substantially without affecting the overall solution, though the influence of doing so must be carefully assessed via comparison of the global system strain and kinetic energies. In general the strain energy should be two orders of magnitude higher than the kinetic energy. It should be noted however that some strain energy is dissipated through plasticity.

Remeshing Strategy

Chapter 3 outlined various computational frameworks, and noted that due to the Lagrangian reference frame a robust adaptive remeshing strategy is essential. Additionally, with reference to the evolution of localisations, remeshing is required to resolve heavy distortion around faults and provide sufficient kinematic freedom for their evolution. The key components of the adaptive remeshing strategy adopted for this thesis are described below.

Entity-based model definition

An adaptive strategy necessitates that all process data (e.g. loads, constraints, contact, etc.) must be defined independently of the finite element mesh, as the discretisation of the domain changes with each remeshing step. This is achieved by using a hierarchical model database constructed using points, lines, surface and volume entities that are defined via the pre-processor. All process data is defined on these geometrical entities rather than the finite element mesh, and the hierarchical model is then evolved throughout the simulation using the geometry defined by the current deformed state.

Remeshing indicators

The approach adopted by the Zienkiewicz-Zhu type error estimation method centres around obtaining an error measure, by comparing the Gauss point value of a suitable error indicator with a more accurate distribution of the error indicator obtained by a smoothing procedure. The method is therefore flexible, allowing incorporation of many different error indicators and is computationally efficient, as the more accurate solution is obtained directly from the current solution variables. For this thesis the so called $L2$ Norm has been adopted;

$$\mathbf{I}^e = \int_{V_e} \boldsymbol{\sigma} \mathbf{D}^{-1} \boldsymbol{\sigma} dv \quad \mathbf{A-19}$$

where $\boldsymbol{\sigma}$ is the stress vector and \mathbf{D} is the modulus matrix. Additionally, another indicator is used which is based on a measure of element distortion. The distortion error at time $t + \Delta t$.

$$\xi_{dist} = \frac{{}^{t+\Delta t}A - {}^0A}{{}^0A} \times 100 \quad \mathbf{A-20}$$

Where A is the element triangle area and superscript 0 denotes the initial value for the mesh. The error is checked over a specified number of timesteps and will be triggered when $\xi_{dist} > \xi_{allowable}$. This is particularly useful for capturing large shear deformations around faults or within viscous, flowing structures such as salt or mud diapirs.

Regeneration of the Mesh and Mapping Procedure

The new mesh is generated using an advancing front algorithm. After creating the new mesh, the transfer of displacement, velocity and history-dependent variables from the old mesh to a new mesh is required. The rate form of the explicit algorithm, so that the solution state on the current mesh h and time t_n is defined by;

$${}^h\boldsymbol{\Lambda}_n = \left({}^h v_{n-1/2}, {}^h x_n, {}^h \boldsymbol{\sigma}_n, {}^h q_n \right) \quad \mathbf{A-21}$$

Where ${}^h v_{n-1/2}$, ${}^h x_n$, ${}^h \boldsymbol{\sigma}_n$, ${}^h q_n$ denote values of the velocity, updated coordinates, stresses and a vector of internal variables at time t not $t_{n-1/2}$ for the mesh h . Assuming that the estimated error of the solutions ${}^h \boldsymbol{\Lambda}_n$ is within the prescribed criteria while they are violated by the solution ${}^h \boldsymbol{\Lambda}_{n+1}$, a new mesh $h+1$ is generated and a new solution ${}^{h+1} \boldsymbol{\Lambda}_{n+1}$ must be computed.

For the explicit solution algorithm adopted in this thesis, the timestep is very small giving rise to relatively small changes in material state between time steps. Consequently, in the explicit transfer strategy the solution is directly mapped from ${}^h\mathbf{\Lambda}_{n+1}$ to ${}^{h+1}\mathbf{\Lambda}_{n+1}$ in the deformed configuration. This updated state is evaluated using the Gauss point transfer operator T_G i.e.

$${}^{h+1}q_{n+1} = T_G \left[{}^h q_{n+1} \right], \quad {}^{h+1}\boldsymbol{\sigma}_{n+1} = T_G \left[{}^h \boldsymbol{\sigma}_{n+1} \right] \quad \text{A-22}$$

And the nodal transfer operator T_N to compute the velocity on the new mesh i.e.

$${}^{h+1}v_{n+1/2} = T_N \left[{}^h v_{n+1/2} \right] \quad \text{A-23}$$

As the nodal information is continuous at the element boundaries, the nodal operator T_N uses the element shape functions to interpolate data between the mesh h and $h+1$. The Gauss point information is not continuous and may vary strongly between adjacent elements.

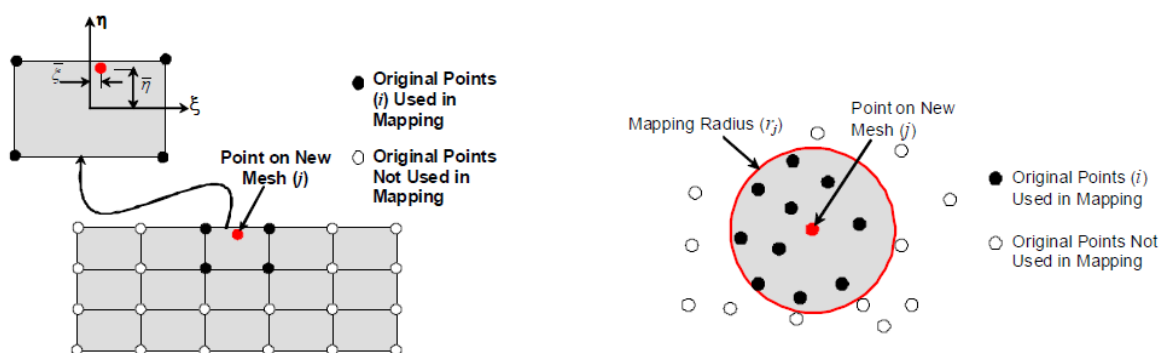


Figure A-3: Mapping procedures for nodal and Gauss point information (Kato, 2010).

Left image shows shape function interpolation for mapping nodal information. Right image shows weighted least square mapping for Gauss point information.

Consequently, rather than averaging data to the nodes to create a continuous field, the Gauss point data is directly interpolated to the Gauss points in the new mesh. This is achieved by a least squares mapping procedure. The approach for transferring nodal and Gauss point information is shown in Figure A-3.

References

- Belytschko, T., K. L. Liu, B. Moran, and K. I. Elkhodary, 2014, *Nonlinear Finite Elements for Continua and Structures*: Wiley, p. 832.
- Bonet, J., and R. D. Wood, 2008, *Nonlinear Continuum Mechanics for Finite Element Analysis*: p. 340.
- Gray, G. G., J. K. Morgan, and P. F. Sanz, 2014, Overview of continuum and particle dynamics methods for mechanical modeling of contractional geologic structures: *Journal of Structural Geology*, v. 59, p. 19–36.
- Kato, J., 2010, *Computational Strategies for Predicting Localisations in Forward Modelling of Geological Structures*: Unpublished PhD Thesis - Swansea University.
- Klerck, P. A., 2000, *The Finite Element Modelling of Discrete Fracture in Quasi-Brittle Materials*: Unpublished PhD Thesis - Swansea University, p. 200.
- Peric, D., and A. J. L. Crook, 2004, Computational strategies for predictive geology with reference to salt tectonics: *Computer Methods in Applied Mechanics and Engineering*, v. 193, no. 48-51, p. 5195–5222.
- Thornton, D. A., and A. J. L. Crook, 2014, *Predictive Modeling of the Evolution of Fault Structure: 3-D Modeling and Coupled Geomechanical/Flow Simulation*: Rock Mechanics and Rock Engineering.
- Zienkiewicz, O. C., and R. L. Taylor, 2005, *The Finite Element Method For Solid and Structural Mechanics*: Elsevier, p. 631.
- Zienkiewicz, O. C., R. L. Taylor, and J. Z. Zhu, 2005, *The Finite Element Method: It's Basis and Fundamentals*: Elsevier, p. 733.